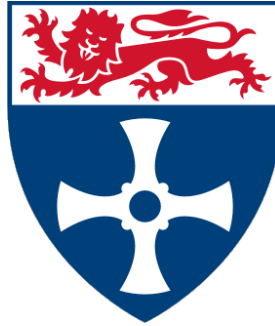


Synchronous Reluctance Motors with Fractional Slot-Concentrated Windings



Christopher Michael Donaghy-Spargo

School of Electrical and Electronic Engineering

Newcastle University

A thesis submitted for the degree of

Doctor of Philosophy

To my wife and my family.

Declaration

I hereby declare that except where specific reference is made to the work of others, the contents of this thesis are original and have not been submitted in whole or in part for consideration for any other degree or qualification in this, or any other University. This thesis is the result of my own work and includes nothing which is the outcome of work done in collaboration, except where specifically indicated in the text. This dissertation contains less than 80,000 words including appendices, bibliography, footnotes, tables and equations and has less than 150 figures. This thesis has been typeset using L^AT_EX.

Christopher Michael Donaghy-Spargo

© May 2016

Acknowledgements

Firstly, I would like to thank my supervisor Prof. Barrie Mecrow for his generous support and encouragement throughout this work. I would also like to thank Dr. James Widmer for his kind support and assistance in many technical and non-technical matters related to this work. Many thanks must also be given to Dr. Chris Morton for assisting in test rig set-up, as well as his much appreciated technical guidance. Gratitude must also go to the Mechanical Workshop for their advice and assistance during the construction of the prototype machine. Financial assistance was provided by the UK Engineering and Physical Sciences Research Council (EPSRC) in the form of a Doctoral Training Award and additional financial assistance was kindly provided by Cummins Generator Technologies, Stamford, UK, through industrial sponsorship of this work, for which I am grateful.

My wife, Laura, has given me unwavering love and support throughout the course of this PhD and has displayed great patience on many a missed evening or weekend due to the long working hours, especially when writing up this thesis and simultaneously working at Dyson. For this I am eternally grateful, thank you. Without this, and the continued support of my family, it would have made the journey from being a graduate 'BEng student' to 'a PhD' a whole lot more difficult. Thank you all for your kindness and patience.

A token of appreciation must also go to the late Oliver Heaviside, the eminent '*electromagnetician*', for his great inspiration to me over the years, whose writings and achievements captured my imagination and catapulted my quest for knowledge and understanding;

"Nearly all the millions, or rather billions, of human beings who have peopled this earth have been content to go through life taking things as they found them, and without any desire to understand what is going on around them."

- OLIVER HEAVISIDE, ELECTROMAGNETIC THEORY VOL. I. PP.11, 1893

Awards Received

During the course of this PhD degree, I have been fortunate to be awarded three prestigious accolades in relation to the research contained within this thesis and my wider contribution to STEM ambassadorial work and services to the engineering community. All of the extracurricular activities undertaken throughout these four years have made completing the PhD degree more difficult, but at the same time, more worthwhile and rewarding - the experience has been fantastic and I would do it all again. The awards bestowed onto me during this period are;

- SIR HENRY ROYCE MEDAL - *Awarded jointly by Institution of Engineering and Technology (IET) and the Sir Henry Royce Memorial Foundation*, November 2014
- BRONZE MEDAL IN ENGINEERING - SET for BRITAIN Exhibition - *Awarded by the UK Parliamentary and Scientific Committee and the Royal Academy of Engineering*, March 2014
- POSTGRADUATE SCHOLARSHIP FOR RESEARCH - *Awarded by the Institution of Engineering and Technology (IET)*, October 2012

I would therefore like to thank the IET, the Sir Henry Royce Memorial Foundation, the Royal Academy of Engineering and the UK Parliament for these awards, their support and their recognition. Thank you.

Abstract

Today, high efficiency and high torque density electrical machines are a growing research interest and machines that contain no permanent magnet material are increasingly sought. Despite the lack of interest over the last twenty years, the permanent magnet-free synchronous reluctance machine is undergoing a revival and has become a research focus due to its magnet-free construction, high efficiency and robustness. They are now considered a potential future technology for future industrial variable speed drive applications and even electric vehicles. This thesis presents for the first time a synchronous reluctance motor with fractional slot-concentrated windings, utilizing non-overlapping single tooth wound coils, for high efficiency and high torque density permanent magnet-free electric drives. It presents all stages of the design and validation process from the initial concept stage through the design of such a machine, to the test and validation of a constructed prototype motor. The prototype machine utilizes a segmented stator core back iron arrangement for ease of winding and facilitating high slot fill factors. The conventional synchronous reluctance motor topology utilizes distributed winding systems with a large number of stator slots, presenting some limitations and challenges when considering high efficiency, high torque density electrical machines with low cost. This thesis aims to present an advancement in synchronous reluctance technology by identifying limitations and improving the design of synchronous reluctance motors through development of a novel machine topology. With the presented novel fractional slot concentrated winding machine design, additional challenges such as high torque ripple and low power factor arise, they are explored and analysed - the design modified to minimise any unwanted parasitic effects. The electrical and electromagnetic characteristics of the developed machine are also explored and compared with that of a conventional machine. A novel FEA post-processing technique is developed to analyse individual air-gap field harmonic torque contributions and the machines dq theory also modified in order to account for additional effects. The developed machine is found to be lower cost, lower mass and higher efficiency than an equivalent induction or conventional synchronous reluctance motor, but does suffer higher torque ripples and lower power factor. The prototype is validated using static and dynamic testing with the results showing a good match with finite element predictions. The work contained within this thesis can be considered as a first step to developing commercial technology based on the concept for variable speed drive applications.

Contents

Contents	i
List of Figures	vii
List of Tables	xi
1 Introduction	1
1.1 Research Challenges	7
1.1.1 Low/No Permanent Magnet Electrical Machines	7
1.1.2 High Efficiency Electrical Energy Conversion	8
1.2 Reluctance Machines	10
1.2.1 Low/No Permanent Magnet Electrical Machines	10
1.2.2 High Efficiency Electrical Energy Conversion	11
1.2.3 Advantages and Disadvantages	12
1.2.4 SynRM or SRM?	13
1.3 Literature	15
1.4 Overview of SynRM Motor Technology	16
1.4.1 Brief History	16
1.4.2 Operating Principle	17
1.4.3 Machine Modelling	17
1.4.4 Figures of Merit	20
1.4.5 Rotor Designs	21
1.4.6 Challenges	23
1.5 References	25
2 Motor Concept Development	32
2.1 Alternative Winding Arrangements	32
2.1.1 Fractional Conductor Windings	32
2.1.2 Toroidal Windings (Gramme-Ring Winding)	35
2.1.3 Fractional Slot-Concentrated Windings	37
2.1.4 Comparison and Conclusion	38
2.2 General Winding Considerations	39
2.2.1 Machine Losses	39

2.2.2	Slot Fill Factor	39
2.2.3	End Windings	41
2.2.4	Winding Mass / Conductor Material	42
2.2.5	Thermal Aspect	43
2.2.6	Summary	44
2.3	Application of FSCW to the SynRM	45
2.3.1	Fundamental Topology	45
2.3.2	Single vs. Double Layer	46
2.3.3	Winding End Region Lengths	47
2.3.3.1	Average End Turn Length	47
2.3.3.2	End Winding Axial Extent	47
2.3.4	Winding Factors and MMF Harmonics	48
2.3.4.1	Winding Factor Comparison	49
2.3.4.2	Applicable Slot-Pole Combinations	50
2.3.4.3	Magnetomotive Force Waves	51
2.3.5	Iron Loss	52
2.3.6	Torque Ripple	53
2.3.7	Inductances	53
2.3.7.1	Magnetizing Inductance	54
2.3.7.2	Leakage Inductance	54
2.3.7.3	Leakage Inductance Effects on Saliency Ratio and Power Factor	55
2.3.8	Manufacturing	57
2.3.8.1	Mechanical Arrangement of Higher Pole SynRMs	58
2.4	Conclusion	59
2.5	References	61
3	Prototype: Design and Performance	63
3.1	Machine Sizing and Stator Electromagnetic Design	63
3.1.1	Key Dimensions	64
3.1.2	Stator Segmentation	65
3.1.3	Winding Design and Configuration	66
3.1.4	End Length and AC Losses	71
3.2	Rotor Electromagnetic Design	72
3.2.1	Number of Flux Barriers (Flux Guides)	72
3.2.2	Tangential and Radial Rib Width	75
3.2.3	cSynRM Rotor Design	76
3.2.4	Final Rotor Lamination Profile	78
3.3	Analytical Inductances	79
3.3.1	Airgap Length	79
3.3.2	Magnetizing Inductances	79

3.3.2.1	Direct-Axis Inductance	80
3.3.2.2	Quadrature-Axis Inductance	80
3.3.3	Stator Leakage Inductances	81
3.3.3.1	Stator Slot Leakage	81
3.3.3.2	Tooth Tip Leakage	82
3.3.3.3	End Winding Leakage	83
3.3.3.4	Airgap Harmonic Leakage	83
3.3.4	Summary and Saliency Ratio Calculations	84
3.3.5	Note On Analytical Inductance Calculation	85
3.4	Final Design Performance Analysis	85
3.4.1	Rated Load Performance	85
3.4.2	FEA Torque vs Speed Curve	88
3.4.3	FEA Calculated Inductances	88
3.4.4	Note on cSynRM Inductances	91
3.5	Influence of Slot Wedges and Rotor Skew	91
3.5.1	Semi-Magnetic Slot Wedges	91
3.5.2	Skewing Effects	93
3.6	3D Effects	95
3.7	Rotordynamic Calculations	97
3.7.1	Rotor Stress, Deformation and Safety Factor	98
3.7.1.1	5000 rpm (Maximum Speed)	98
3.7.1.2	10,000 rpm (2x Maximum Speed)	100
3.7.2	Rotor Resonant Modes	100
3.7.2.1	First Bending Mode - The First Critical Speed	102
3.7.2.2	Rotordynamic Torsional Modes	103
3.8	FEA Machine Comparisons	104
3.8.1	Commercial Induction Motor	104
3.8.2	Equivalent Synchronous Reluctance Motor	105
3.8.3	Constant Loss Operation	108
3.8.4	cSynRM with Increased Fill Factor	109
3.8.5	Axial Extents	111
3.8.6	Machine Mass and Cost	111
3.9	Conclusion	112
3.10	References	114
4	Prototype: Fabrication and Assembly	116
4.1	Stator Stack Manufacture	117
4.2	Electro-Discharge-Machining Technique	117
4.3	Coil Manufacture and Stator Assembly	118
4.3.1	Slot Fill Factor	118
4.3.2	Stator Segment Coil Winding	119

4.3.3	End Winding Supports	121
4.3.4	Stator Stack Assembly	122
4.3.5	Stator Coil Terminations	122
4.4	Rotor Stack Manufacture and Assembly	124
4.4.1	First Rotor Stack	124
4.4.2	Final Rotor Stack	125
4.5	Mass Manufacturability	126
4.6	Conclusion	127
5	Prototype: Testing and Verification	128
5.1	Insulation System	128
5.2	Locked Rotor DC Testing	129
5.2.1	Equipment and Setup	129
5.2.2	Static (DC) Torque Tests	131
5.2.2.1	Measurement and FEA Comparison	131
5.2.2.2	Fundamental Component of Torque	134
5.2.2.3	Mean Cyclic Torque	134
5.2.2.4	Torque Index Estimation	135
5.2.3	Flux Linkages	135
5.2.4	3D Effects of Q-Axis Inductance	138
5.2.5	Inductances	140
5.2.6	Saliency Ratio	141
5.3	Locked Rotor AC Testing	141
5.3.1	Equipment and Setup	142
5.3.2	AC Magnetization	144
5.3.3	Inductances	144
5.4	Stator Leakage Inductance	146
5.4.1	Removed Rotor Test	146
5.4.2	Leakage Inductance	148
5.4.2.1	Lumped End Winding Inductance	148
5.4.2.2	Finite Element Modeling	149
5.4.2.3	Measurements	150
5.4.2.4	Results Comparison	150
5.5	Summary of Results	151
5.5.1	Result Comparison	151
5.5.2	Machine Performance	152
5.6	DC Thermal Testing	152
5.7	Full Running Testing	153
5.7.1	Equipment and Setup	153
5.7.2	Rated Speed and Current	154
5.7.3	Rated Speed and Torque	155

5.7.4	Torque vs. Speed	156
5.8	Conclusion	157
5.9	References	158
6	Novel Harmonic Torque Analysis Technique	159
6.1	Introduction	159
6.2	Airgap Maxwell Stresses	160
6.2.1	Stator Magnetomotive Force Waves	160
6.2.2	Conventional Stress Theory	161
6.3	Field Post-Processing	162
6.3.1	Harmonic Decomposition	163
6.3.2	SynRM and cSynRM MMF Spectra	164
6.3.3	SynRM and cSynRM Airgap Field Spectra	164
6.3.3.1	3D Airgap Field Maps	165
6.3.3.2	Even Airgap Harmonics	167
6.4	Harmonic Stress Components	168
6.5	Torque Analysis	169
6.5.1	Harmonic Torque Calculation	169
6.5.2	Implementation	171
6.6	FSCW Synchronous Reluctance Machine	172
6.6.1	Initial Machine Design	172
6.6.2	Initial Rotor Design and Iterations	175
6.6.3	Prototype Machine Design	180
6.6.4	Accuracy of Post-Processed Solutions	182
6.7	Conclusions	183
6.8	References	184
7	Inductance Characteristics and Modified dq Machine Model	185
7.1	dq Theory Review	185
7.1.1	Winding Distribution	187
7.2	Flux Linkage Harmonics	187
7.2.1	cSynRM Phase Flux Linkages	187
7.2.2	SynRM Phase Flux Linkages	189
7.3	Machine Characteristics	190
7.3.1	Flux Linkages	190
7.3.1.1	Post Transformation Harmonic Content	192
7.3.2	Inductances	193
7.3.2.1	Saliency Ratios	197
7.3.3	Summary	198
7.4	Flux-Linkage Functions	199
7.4.1	Reciprocity	200

7.4.2	Cross Coupling vs Cross Saturation	200
7.4.3	Inductance vs Flux Linkage	200
7.4.4	Flux Linkage Total Derivatives	201
7.4.5	Revision of SynRM <i>abc</i> -Frame Circuit Equations	201
7.5	Modified <i>dq</i> Circuit Equations	202
7.5.1	Orthogonal Axis Equivalent Circuits	203
7.5.1.1	Implications for the cSynRM	203
7.6	Electromagnetic Torque Expressions	205
7.6.1	Development of Torque Expression	205
7.6.2	Expansion To Machine Inductances	206
7.6.3	Torque Harmonics	207
7.6.4	Other Methods of Torque Calculation	207
7.6.4.1	Numerical Derivatives	208
7.6.5	Comparison of Torque Calculations	208
7.6.6	Summary	211
7.7	Applicability of DQ Theory	211
7.8	Conclusion	213
7.9	References	214
8	Conclusion and Further Work	216
8.1	General Conclusions	217
8.1.1	Motor Concept	217
8.1.2	Design and Performance	218
8.1.3	Prototyping and Experimental Verification	219
8.1.4	Analysis	219
8.2	Suggested Further Work	220
8.3	Closing Remarks	221
A	Prototype: Mechanical Drawings	223

List of Figures

1.1	IEC efficiency curves for 4-pole 50Hz induction motors	9
1.2	Simple reluctance motor	11
1.3	Left: Synchronous Reluctance Machine; Right: Switched Reluctance Machine	13
1.4	Above: SynRM VSI; Below: Switched Reluctance Machine AHB	14
1.5	Steady state phasor diagram of the synchronous reluctance machine . . .	17
1.6	Kosto's design (top) and other SynRM rotor topologies [36, 105]	22
2.1	Four pole distributed winding [13] and over-lapping end windings [29] . .	33
2.2	A stator of a two pole machine with a fractional conductor winding [1] . .	33
2.3	Toroidal coils wrapped around the core back [6]	36
2.4	Four pole double layer fractional slot-concentrated winding [13] and short end windings [30]	37
2.5	Fill factor effect on copper losses	40
2.6	Fill factor effect on slot thermal conductivity (air cavity and copper winding)	44
2.7	Distributed and FSCW winding topologies	45
2.8	Comparison of end winding axial extents between distributed and FSCW	48
2.9	Winding factors of double layer distributed winding, $Q_s = 36$ & $p = 4$. .	49
2.10	Winding factors of double layer FSCW, $Q_s = 6$ & $p = 4$	50
2.11	MMF of Distributed winding, $Q_s = 36$ & $p = 2$	51
2.12	MMF of double layer FSCW, $Q_s = 6$ & $p = 2$	52
2.13	True saliency ratio as a function of leakage inductance	55
2.14	Maximum power factor as a function of leakage inductance; $\xi_{mag} = 16$.	56
2.15	Mecrow <i>et al</i> "Segmental Stator" arrangement [28]	57
2.16	Radial and Tangential Ribs of the Rotor	58
3.1	Complete stator segment dimensions	65
3.2	Effect of interface gaps	65
3.3	Inter-segment airgap flux plots with inter-segments gaps of 0mm, 0.03mm and 0.05mm (top to bottom)	67
3.4	Winding factors and 3ph MMF harmonic spectrum	68
3.5	Winding layout showing each phase coil sides	68
3.6	Three phase MMF distribution for various three phase current instants . .	69

3.8	Key performance criteria variation with N_b	73
3.7	Barrier Number Visualisation, 1 to 5 barriers and 5 barriers with cut-out, equivalent to 3 to 12 layers	74
3.9	Depiction of the rotor tangential and radial ribs	75
3.10	$L_{d,q} = f(i)$ for radial (top) and tangential (bottom) rib thickness variation	76
3.11	6-slot 4-pole cSynRM 2D cross-section	77
3.12	Comparison of torque waveforms (SynRM and cSynRM)	77
3.13	Initial rotor design	78
3.14	Slot dimensions in relation to the slot leakage permanence	82
3.15	2D FEA plot of the designed machine at rated operating point	87
3.16	Torque and power vs speed curves for rated current limit	88
3.17	FEA calculated d - and q -axis inductances	89
3.18	Flux plots in the d - and q -axis rotor positions	90
3.19	Semi-magnetic wedge model	91
3.20	Semi-magnetic wedge B-H and relative permeability curves	92
3.21	Machine performance criteria variation for different slot wedge materials	93
3.22	Skew factors with skew angle	94
3.23	3D model of the prototype machine end windings	96
3.24	3D vs 2D FEA Torque Waveforms	96
3.25	von-Mises stress distribution at 5000rpm (exaggerated deformation)	99
3.26	Deformation distribution at 5000rpm (exaggerated)	99
3.27	von-Mises stress distribution at 10,000rpm (exaggerated deformation)	101
3.28	Deformation distribution at 10,000rpm (exaggerated)	101
3.29	Exaggerated deformation characteristic for mode $\nu = 1$	104
3.30	Induction motor before teardown	105
3.31	Induction and SynRM lamination profiles with FEA realisation	106
4.1	3D CAD model of prototype cSynRM	116
4.2	Conductor placements in the slot	118
4.3	Stator segment with end pieces and winding jig	119
4.4	Close-up of a stator coil being wound	120
4.5	Two trial coils in the mock stator	121
4.6	Segmental end winding support	122
4.7	End turns and winding supports on completed stator	123
4.8	Stator terminal ring and stator coil terminations of the prototype machine	123
4.9	The complete first rotor lamination stack (partial cut) at the contractor	124
4.10	The first rotor lamination stack - partial cut of failed manufacture	125
4.11	Completed prototype rotor stack and shaft assembly	126
5.1	DC Testing Winding Configuration	130
5.2	Locked rotor DC test rig	130

5.3	Static Torque - 5A	132
5.4	Static Torque - 10A	132
5.5	Static Torque - 15A	133
5.6	Static Torque - 20A	133
5.7	Static Torque - 20A with Fundamental and Harmonic Spectrum	134
5.8	Averaged Torque vs Current	135
5.9	Measured Voltage and Current Data with Calculated Flux Linkage Wave- form	136
5.10	Algorithm for Flux Linkage Calculation from DC Testing	137
5.11	Orthogonal Axis Flux Linkages (Direct Current Method)	138
5.12	Measured and FEA flux linkages with rotor angle and current (surfaces)	139
5.13	d - q axis Inductances (Measured and FEA)	140
5.14	Algorithm for Inductance Calculation from AC Testing	142
5.15	AC Testing Winding Configuration	143
5.16	Locked rotor AC test rig	143
5.17	AC Test Waveforms	144
5.18	d -axis (left) and q -axis (right) AC magnetization curves	145
5.19	Inductance Comparison (AC, DC and FEA data)	145
5.20	Ideal search coil design and placement [16]	147
5.21	Removed rotor testing of the prototype machine showing search coil	148
5.22	Representative 3D FEA End Winding Model	149
5.23	Removed Rotor FEA showing search coil	149
5.24	Measured temperature rise of prototype cSynRM for 300W winding loss	153
5.25	Full running rig showing instrumentation and the test bed	154
5.26	Applied current waveform at rated speed and RMS line current	155
5.27	Measured and FEA torque speed curves; Blue: FEA Red: Measured	156
6.1	Cylindrical co-ordinate system use to evaluate the stress tensor	161
6.2	Stresses in the air gap of a loaded machine	162
6.3	3ph MMF Harmonic Spectra	164
6.4	Top to bottom: Radial field, radial field harmonic spectrum, tangential field, tangential field harmonic spectrum; Left: SynRM, Right: cSynRM	165
6.5	Distributed machine; Top: Radial field, Bottom: Tangential field	166
6.6	FSCW machine; Top: Radial field, Bottom: Tangential field	167
6.7	Resultant radial and tangential stresses (force densities); Top: SynRM, Bottom: cSynRM	169
6.8	Design cycle implementation	171
6.9	6-slot 4-pole cSynRM - Initial motor cross-section	172
6.10	Initial machine design; Top: Reconstructed and FE torque waveforms Bottom: Selected torque space harmonic components	173
6.11	8 pole field for maximum (upper) and zero (lower) torque positions	174

6.12	Initial rotor design (9 flux barriers)	175
6.13	q-axis cutout rotor designs	176
6.14	Iterative rotor designs a) through f)	177
6.15	Iterative designs g) and h) with the final rotor design i)	178
6.16	Torque quality comparison	180
6.17	6-slot 4-pole cSynRM - Prototype machine 2D model	180
6.18	Prototyped machine; Top: Reconstructed and FE torque waveforms; Bot- tom: Selected torque harmonic components	181
7.1	cSynRM MMF harmonic spectrum with and without even harmonics	188
7.2	cSynRM 3ph flux linkage waveforms and corresponding harmonic spectra	188
7.3	3ph flux linkage waveforms of the SynRM and corresponding harmonics	189
7.4	cSynRM flux linkages in the $dq0$ reference frame (rated current with a current angle of 45 degrees)	191
7.5	cSynRM flux linkage harmonics in the $dq0$ reference frame	191
7.6	SynRM flux linkages in the $dq0$ reference frame (rated current with a current angle of 45 degrees)	192
7.7	cSynRM - spatial variation of L_d with rotor angle	195
7.8	cSynRM - Spatial variation of L_q with rotor angle	195
7.9	SynRM - spatial variation of L_d with rotor angle	196
7.10	SynRM - spatial variation of L_q with rotor angle	196
7.11	cSynRM - spatial variation of ξ_{true} with rotor angle	197
7.12	cSynRM - maximum, minimum and average ξ_{true}	198
7.13	SynRM - ξ_{true} of the distributed winding motor	198
7.14	Modified dq equivalent circuits for the cSynRM	204
7.15	Torque per pole pair using only $\Psi_{i_q} - \Psi_{q i_d}$	208
7.16	Torque due to the d -axis flux linkage spatial partial derivative	209
7.17	Torque due to the q -axis flux linkage spatial partial derivative	209
7.18	Torque component waveforms	210
7.19	Torque waveform comparison (computed results)	211

List of Tables

1.1	Synchronous and switched reluctance machine differences	14
2.1	Comparison of conventional and fractional conductor windings	35
2.2	Comparison of selected winding types	39
2.3	Resistivity-density products	42
2.4	Typical thermal conductivities of common engineering materials	44
2.5	FSCW vs. Distributed Winding	46
2.6	Single Layer vs. Double Layer	46
2.7	Fundamental winding factors of applicable double layer FSCW slot-pole combinations	51
2.8	Airgap harmonic leakage factors - adapted from [27]	55
3.1	Fixed Machine Specifications	64
3.2	Summary of prototype inductances and calculated rotor saliency	84
3.3	cSynRM Performance at 1500rpm with $I_s = 21.2A$ (340W loss)	86
3.4	Semi-magnetic wedge mechanical properties	92
3.5	3D vs 2D FEA Iron Losses	97
3.6	Mechanical properties of M250-35A	98
3.7	Rotor critical speeds	103
3.8	Induction machine specification	105
3.9	IM, SynRM and cSynRM machine volumes and masses	106
3.10	IM, SynRM and cSynRM machine specifications	107
3.11	Constant loss performance of the IM, SynRM and the cSynRM	108
3.12	cSynRM increased fill factor performance (340W loss)	110
3.13	Comparison of mass and costs of motor components	111
4.1	Calculated and measured coil parameters	120
5.1	Saliency Ratio (DC Flux Linkage Tests)	141
5.2	Summary of the Stator Leakage Inductance Results	150
5.3	Summary of static test results	151
5.4	Rated speed and current measurement comparison with FEA	155
5.5	Results at stator line current to achieve rated torque	155

6.1	Effect of cutout depth on mean torque and torque ripple	176
6.2	Design iteration mean and ripple torque with rotor fitness	179
7.1	abc to $dq0$ harmonic ordinate transformations	193
7.2	Flux linkage functional relationships	199
7.3	Machine performance comparison between averaged dq and FEA	212

Chapter 1

Introduction

This chapter outlines the organisation of this thesis, its contributions to scientific and engineering knowledge and its associated publications. This chapter also serves to introduce the selected research challenges in electrical machine design, it provides an overview of the synchronous reluctance motor and proposes a route of investigation that forms the main text of this thesis. The aim of the introduction is to inform the reader of the key outcomes of this work and the state of the art in synchronous reluctance motors.

Organisation of Thesis

Chapter 1 identifies research challenges and suggests the reluctance type of machine as an avenue of further investigation. A comprehensive review of synchronous reluctance technology and its relation to switched reluctance technology is presented. The operating principles, a brief history, current literature and the standard machine mathematical model and common figures of merit are presented. This chapter allows the work in subsequent chapters to be contextualised.

Chapter 2 surveys potential winding configurations and topologies for performance improvements in synchronous reluctance motors. The theory behind the chosen fractional slot concentrated windings (FSCW) is reviewed and the development of the concept of the concentrated winding synchronous reluctance motor (cSynRM) is described. The ramifications of the application of FSCW to synchronous reluctance machines are explored, with both the advantages and drawbacks considered. The synthesis of fractional slot concentrated windings and synchronous reluctance machines is presented in the form of a novel machine topology.

Chapter 3 details the analytical design, finite element analysis and performance calculations for the cSynRM prototype machine. Mechanical analysis (rotor first bending mode, torsional modes and stresses) complements the electromagnetic analysis and optimisation. Leakage inductance is explored and the dominant leakage component is identified; this chapter also presents a brief comparison of performance between

induction machines (IM), conventional synchronous reluctance machines (SynRM) and the novel machine for high energy conversion efficiency and high torque density applications.

Chapter 4 describes the fabrication and assembly of a prototype synchronous reluctance motor with fractional slot concentrated windings, as designed in Chapter 3

Chapter 5 presents the static and dynamic testing and experimental verification of the prototype fractional slot concentrated winding synchronous reluctance machine. Experimental rigs and testing regimes/methods are documented with the obtained results presented and compared with analytical and finite element calculations. Various tests are reported including DC and AC stand still testing, full rotating testing and removed rotor tests. The results of a thermal soak is also presented.

Chapter 6 develops a novel finite element post processing method to compute the contribution of individual air-gap field harmonics on rotor electromagnetic torque. New information on the composition of the torque waveform is and therefore the sources of torque ripple in synchronous machines is identified. The conventional synchronous reluctance motor and the developed cSynRM are compared and the optimal design for torque ripple reduction of the finalised rotor design is presented.

Chapter 7 the conventional $d-q$ theory is assessed with respect to the developed machine topology it is expanded for fractional slot concentrated winding synchronous reluctance machines. Selected inductance characteristics of the cSynRM machine are also investigated and compared with a conventionally wound machine. Equivalent circuits for the cSynRM are developed and torque expressions based on the modified $d-q$ theory are derived and their results compared to FEA studies.

Chapter 8 concludes the work in this thesis and sets the scene for further research in this area by suggesting subsequent projects and avenues of investigation.

Scientific Contribution to Knowledge

An outline of all published materials and original contributions to scientific knowledge related to this thesis is presented here. The work contained within this thesis has been widely disseminated through the following publications:

Peer-reviewed Publications

The original work in this thesis has yielded a number of peer-reviewed journal and conference publications;

Journal Publications

1. Spargo, C.M.; Mecrow, B.C.; Widmer, J.D.; Morton, C., "*Design and Validation of a Synchronous Reluctance Motor with Single Tooth Windings*", Energy Conversion, IEEE Transactions on, vol. 30, no. 2, pp. 795, 805, 2015
2. Spargo, C.M.; Mecrow, B.C.; Widmer, J.D.; Morton, C., "*Application of Fractional Slot-Concentrated Windings to Synchronous Reluctance Motors*" Industry Applications, IEEE Transactions on, vol.51, no.2, pp.1446,1455, 2015
3. Spargo, C.M.; Mecrow, B.C.; Widmer, J.D., "*A Semi-numerical Finite-Element Post-processing Torque Ripple Analysis Technique for Synchronous Electric Machines Utilizing the Air-Gap Maxwell Stress Tensor*" Magnetics, IEEE Transactions on , vol.50, no.5, pp.1,9, May 2014

Conference Publications

1. Spargo, Christopher; Mecrow, Barrie; Widmer, James, "*Design of a Synchronous Reluctance Motor with Non-Overlapping Fractional-Slot Concentrated Windings*" Energy Conversion Congress and Exposition (ECCE), 2014 IEEE , vol., no., pp.1393,1399, 14-18 Sept. 2014
2. Spargo, Christopher; Mecrow, Barrie; Widmer, James, "*Synchronous Reluctance Motors with Toroidal Windings*" Energy Conversion Congress and Exposition (ECCE), 2014 IEEE , vol., no., pp.1374,1378, 14-18 Sept. 2014
3. Spargo, C.M.; Mecrow, B.C.; Widmer, J.D., "*Computationally Efficient Skew Effect Calculation in Electric Machines Utilising Harmonic Maxwellian Stress Decomposition*" Electrical Machines (ICEM), 2014 International Conference on, vol., no., pp.1044,1049, 2-5 Sept. 2014
4. Spargo, C.M.; Mecrow, B.C.; Widmer, J.D., "*Higher Pole Number Synchronous Reluctance Machines with Fractional Slot Concentrated Windings*" Power Electronics, Machines and Drives (PEMD 2014), 7th IET International Conference on , vol., no., pp.1,6, 8-10 April 2014
5. Spargo, C.M.; Mecrow, B.C.; Widmer, J.D., "*Application of Fractional Slot Concentrated Windings to Synchronous Reluctance Machines*" Electric Machines & Drives Conference (IEMDC), 2013 IEEE International , vol., no., pp.618,625, 12-15 May 2013

In Preparation

1. Spargo, C.M.; Mecrow, B.C.; Widmer, J.D., "*On The Stator Leakage Inductance of Fractional Slot Concentrated Wound Synchronous Reluctance Machines*", Magnetics, IEEE Transactions on, Q2 2016 submission expected

2. Spargo, C.M.; Mecrow, B.C.; Widmer, J.D., “*Inductance Characteristics and Machine Model for Synchronous Reluctance Machines with Fractional Slot Concentrated Windings*”, Magnetics, IEEE Transactions on, Q2 2016 submission expected

Other Publications

During the course of this research programme (Oct 2011 to Oct 2014), a number of co-authored papers and magazine articles on related topics were also published in peer-reviewed sources;

1. Widmer, J.D.; Spargo, C.M.; Atkinson, G.J.; Mecrow, B.C., “*Solar Plane Propulsion Motors With Precompressed Aluminum Stator Windings*” Energy Conversion, IEEE Transactions on, vol.29, no.3, pp.681,688, Sept. 2014
2. Morton, C.; Spargo, C.M.; Pickert, V., “*Electrified Hydraulic Power Steering System in Hybrid Electric Heavy Trucks*” Electrical Systems in Transportation, IET, vol.4, no.3, pp.70,77, September 2014
3. Spargo, C. M., “Synchronous Reluctance Technology: Part II”, MagNews, Spring 2014, UK Magnetics Society, ISSN: 1354-817
4. Spargo, C. M., “Synchronous Reluctance Technology: Part I”, MagNews, Winter 2013, UK Magnetics Society, ISSN: 1354-817
5. Widmer, J.D.; Martin, R.; Spargo, C.M.; Mecrow, B.C.; Celik, T., “*Winding Configurations for a Six Phase Switched Reluctance Machine*” Electrical Machines (ICEM), 2012 XXth International Conference on, pp.532,538, 2-5 Sept. 2012
6. Widmer, J.D.; Mecrow, B.C.; Spargo, C.M.; Martin, R.; Celik, T., “*Use of a 3 Phase Full Bridge Converter to Drive a 6 phase Switched Reluctance Machine*” Power Electronics, Machines and Drives (PEMD 2012), 6th IET International Conference on, pp.1,6, 27-29 March 2012

Key Contributions

Chapter 1

- Presenting the case for synthesising a new synchronous reluctance motor topology for high torque and high electrical energy efficiency applications
- Providing a literature review of current SynRM technology and identifying a shortfall in research in this area

Chapter 2

- Presenting for the first time the concept of the Fractional Slot Concentrated Winding Synchronous Reluctance Motor (cSynRM)
- Exploring the advantages and disadvantages for adopting such a winding scheme in this type of machine
- Presenting the criteria for the design of such a machine - design guidelines

Chapter 3

- The first design and FEA analysis of a cSynRM type motor is presented
- An optimised multiple flux barrier rotor design to reduce torque ripple is developed
- Identification of the dominant stator leakage inductance component in this type of machine and its impact on motor performance is described
- Mechanical stress and rotor-dynamic analysis of the novel rotor design with respect to its fine features is presented
- Presentation of a comparison of the designed cSynRM motor with current technology and showing that its performance and construction make it an attractive alternative

Chapter 4

- The methods and processes for fabricating a segmental stator with single tooth windings and complex rotor core of a prototype cSynRM motor is described in detail

Chapter 5

- Verification of the FEA magnetic model of the novel cSynRM through different DC and AC standstill tests on a static test bed is completed
- Experimental verification of the machine under dynamic operation at full rated torque and speed on a dynamometer
- Identification of the challenges associated with measuring stator leakage inductance via the removed rotor test in machines with fractional slot concentrated windings

Chapter 6

- Development of a novel FEA post-processing method to calculate the direct torque contribution of each airgap magnetic field space harmonic
- Comparison of a conventional synchronous reluctance motor and the novel cSynRM in terms of airgap field harmonics and airgap shear stress distributions is made
- Post-processing of the FEA field identifies a backwards rotating 8-pole field causes significant torque ripple in the novel cSynRM due to the rich airgap space harmonic content
- Development of a optimised multiple flux barrier rotor design to reduce torque ripple due to the offending airgap space harmonic field is presented
- A comparison of the initial rotor design with the optimised rotor design showing a reduction in torque ripple due to the 8-pole field contribution

Chapter 7

- Identification of inadequacies in the synchronous reluctance motor $d-q$ model due to the parasitic effects introduced by adopting fractional slot concentrated windings is performed and necessary modifications the model are made accordingly
- For the first time, the inductance variation with rotor position in the synchronous reluctance motor with fractional slot concentrated windings is explored
- A new $d-q$ axis equivalent circuit for the cSynRM motor topology based on the modified $d-q$ model is presented
- Following the new equivalent circuit, new torque expressions for the cSynRM motor topology are developed and validated through FEA studies

1.1 Research Challenges

Currently, in 2016, there is a research emphasis on electrical machines with low volumes of rare earth magnetic material, which has been reported in the worlds media [1-6]. There is also an emphasis on very high efficiency, known as *super-premium efficiency* in IEC¹ terminology, electrical machines in the industrial sector [7-10]. These research areas are driven by differing factors; the former is driven by the growth in the electric vehicle automotive market, coupled with various supply issues surrounding the permanent magnet material. The latter is driven by the light and heavy industrial sectors, coupled with government legislation, to effect a reduction in energy usage and world CO₂ emissions [11,12]. Both of these exciting research streams will now be explored to justify and contextualise the work in this thesis.

1.1.1 Low/No Permanent Magnet Electrical Machines

“Rare Earth” or “RE” elements are a collection of seventeen elements from the periodic table [13], that despite their name, are relatively abundant in the Earth’s crust. These elements are used in numerous applications, such as permanent magnets, lasers, battery electrodes and camera lenses. However, due to their geochemical properties, they are typically dispersed throughout the Earth’s crust and deposits of concentrated ore are not usually found; it is therefore usually uneconomical to perform extraction [14]. The origins of so called “Rare Earth” elements date back to 1787 with the discovery of Gadolinium [15], but despite their high relative abundance, rare earth minerals are more difficult to mine and extract than equivalent sources of transition metals [16]. Deposits are known to exist in China, the United States, Canada, Australia, India and Brazil, among others. The geographical distribution of the RE ore within the earth is naturally occurring, deposited during the formation of the earth. Despite the numerous geographical locations, in 2010, China was producing 95 percent of the world’s RE supply with only 37 percent of the world’s proven reserves [17]. In 2012, China reportedly slipped in the rankings and now produces approximately 90% of the proven reserve [18]. It has recently been discovered that Japan may have a large reserve of RE material, approximately 6.8 million tons [19]. It will however take a significant amount of time to construct economical mining and processing facilities. In 2010 there was a price surge for Neodymium Oxide of over 300%, where the average cost increased from 75 USD/kg to 325 USD/kg in a 10 month time frame [20]. The price had actually been increasing from July 2009 when the pricing was just 25 USD/kg; current pricing as of early 2016 is around 100 USD/kg. The cost has significantly dropped since 2011 to levels just above the 2010 value, however this surge has induced shock into the emerging automotive markets. As well as the price surge, a number of other issues arise when using rare earth metals. The mining and processing of RE’s have serious environmental consequences if not properly managed. Hazards that

¹International Electrotechnical Commission

pose a risk to wildlife, miners and plant workers such as radioactive slurry resulting from the common occurrence of Thorium and Uranium in rare earth element ores [21] and toxic acids that are required during the refining process [17] are key issues that must be considered. Along with the environmental impact of operations, China has officially cited reserve depletion as the main reasoning for a significant reduction of its rare earth mineral production sector [22] and the export ban [21].

A major emerging marketplace that may in future rely on vast amounts of Rare Earth elements is the electric vehicles market. As of early 2016 the majority of marketed electric vehicles contain interior permanent magnet machines, with varying permanent magnet weights of between 1.5-2kg; the *Nissan Leaf* interior permanent magnet motor has 1.9kg of rotor magnet [24], very few include induction machine technology [25] or wound field synchronous motor technology [26]. In the EU alone, the prediction for the numbers of electric vehicles to be sold in 2020 is to be 9% of the market share [23]. On current figures of 900,000 vehicle registrations per year, that equates to some 81,000 hybrid/electric vehicles and assuming a single traction motor, equates to 81,000 electric motors with potentially around 162 metric tonnes of rare earth permanent magnets being required for the automotive sector alone. If the US and Japanese markets are considered also, this figure triples to approximately 500 metric tonnes at current estimates. This is actually a small amount in relation to the global production of approximately 105,000 tonnes of NdFeB magnets per year. However, even though the mass of the permanent magnet material is low relative to the other components within the motor, it is a major contributor to the cost. If the price boom of 2010 was to re-occur, the production cost of the permanent magnet electric motors in such a volume may become economically non-viable. This is a very undesirable position for the future automotive market and thus research into permanent magnet-less or low volume permanent magnet machines has become an area of great research interest.

Rare earth permanent magnets are used in electrical machines due to their high remnant flux density and coercive force that enables high torque density, efficiency and inverter utilization. However, due to the high cost, political and environmental issues associated with the material, alternative machines with reduced or no Rare Earth material are a current area of great research interest. This thesis contributes to the effort to advance motor technology without the use of permanent magnet materials, thus acting to help alleviate the dependence on the rare earth magnets for future applications.

1.1.2 High Efficiency Electrical Energy Conversion

Between 43% and 46% of the 16TW [27, 28] of the globally consumed electrical power goes directly into electric motors for applications from industrial fan, pump and mill type loads to consumer goods such as vacuum cleaners, hand dryers and refrigeration/central

heating pumps. Approximately 90% of the motors that use this power are induction motors, governed by the IEC 600034-30 efficiency standards from the International Electrotechnical Commission (IEC). This usage is due to their low price, good availability with simple construction & high reliability and typically a full load power factor of 0.9. These are usually of the low voltage, 4-pole, totally enclosed fan ventilated type, that are designed for continuous duty. The current efficiency standard is the IE2 high efficiency standard which limits the minimum efficiency of these motors, based on their power rating. However, due to the global effort to reduce energy usage and carbon emissions, new EU legislation, by Commission Regulation (EC) No 640/2009, implementing Directive 2005/32/EC, with the exception of some special applications, industrial motors must at some point in time conform to the following [29,30];

- IE2 standard by June 16, 2011
- IE3 standard by January 1, 2015 (for motors ≥ 7.5 to 375 kW & IE2 only in combination with an adjustable speed drive)
- IE3 standard for all motors by January 1, 2017, (for motors from 0.75 to 375 kW & IE2 only in combination with an adjustable speed drive)

The IE3 standard is known as Premium Efficiency, there is also scope in the legislation setting out the IE4 super-premium efficiency standard. Between each standard there is usually a 3-4% change in minimum efficiency, depending on power rating and pole number. The various IEC efficiency ratings for 4-pole 50Hz induction machines are presented in Fig. 1.1.

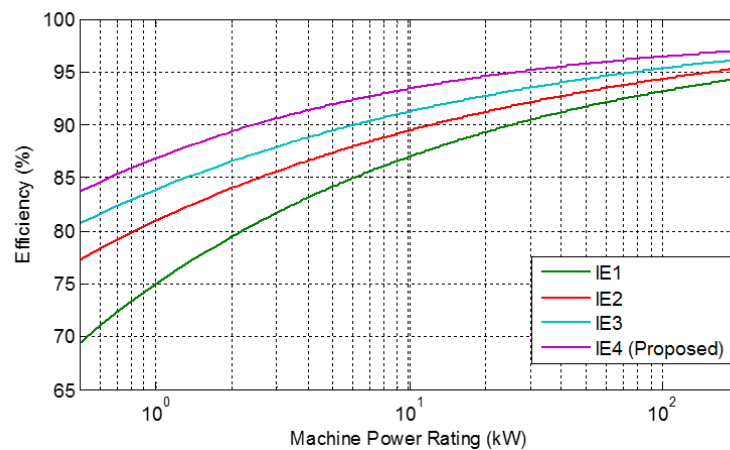


Figure 1.1: IEC efficiency curves for 4-pole 50Hz induction motors

This concern for higher energy efficiency is pushing electrical machine design further, with cast-copper induction machine rotors giving a efficiency increase somewhere between 1% and 5%. With copper cages the material cost rises, but the winding loss and thermal stress is reduced [31]. Cast copper induction motors are currently used by the US

military for traction applications [32]. There are also equivalent efficiency ratings and legislations in the USA, regulated by the US National Electrical Manufacturers Association (NEMA). The IE3 IEC rating is equivalent to the NEMA Premium Efficiency rating and the IE4 IEC rating is equivalent to the NEMA Super-premium efficiency rating.

In 2011, competition to the traditional induction motor was brought to market in the form of the first mass produced IE4 rated synchronous reluctance machine, marketed for common industrial loads such as fan, pump and mill type applications, introduced by ABB [33]. Two variants of the ABB drive-package exist, a IE4 super-premium efficiency motor and a IE3 high output motor, both coupled with advanced ABB drives controlling the machines with direct torque control [34]. Although by legislation variable frequency controlled drives are limited to a minimum of IE2 improved efficiency standard (as inverter fed machine typically have lower efficiency due to inverter effects on the machine), these are the first motors, and the first synchronous reluctance machines to achieve the future IE4 super premium efficiency rating and are key step in realising very high efficiency electrical machines for the industrial sector. Detailed information on the IEC efficiency ratings can be found in the IEC/TS 60034-27-2:2012 standard [35]. This thesis contributes to this research stream by aiming to improve machine efficiency even further through novel machine design of synchronous reluctance motors; concentrating on machines for variable speed drive (VFD) applications. Comparison with the standard induction motor is key to understand the commercial viability of synchronous reluctance technology.

1.2 Reluctance Machines

An overview of reluctance machines and their potential to address the research challenges outlined in the preceding section is presented. An exploration of topological options is briefly explored and a decision is made concerning the topology of choice for further research that forms the theme of the work in this thesis.

1.2.1 Low/No Permanent Magnet Electrical Machines

So called *Reluctance* machines do not inherently contain permanent magnet material and all rotor electromagnetic torque is produced by rotor saliency, *i.e.* rotors with non-isotropic magnetic reluctance that interacts with a stator magneto-motive force. Energy minimisation is a key principle and in any electromechanical system, forces and torques are produced to act on the system with the aim to minimise the stored energy, in this case stored magnetic energy. Movement of a high permeability rotor component to minimise the reluctance path and maximise the mutual inductance of the rotor core and the energised coil is the basic principle of operation for a simple reluctance machine. Machines that operate on this principle date back to around 1842, with a locomotive traction motor designed by Scottish inventor Robert Davidson for the Edinburgh-Glasgow railway line

[36], which was also the first electric locomotive. Due to their lack of permanent magnets, the principal materials required to construct a reluctance machine are electrical steel and copper wire, leading to low cost, robust and supply chain friendly designs. These reluctance machines therefore are an alternative to permanent magnet machines, if high torque density and other qualifying requirements are met, for future automotive applications and high efficiency industrial application motors. To-date, the simple synchronous reluctance motor has not found widespread use like the induction motor. This is typically due to its lower power factor and lack of line-start capability. Figure 1.2 shows a simple doubly salient structure that forms a simple reluctance machine: a coil is energised by current i causing an electromagnetic torque T .

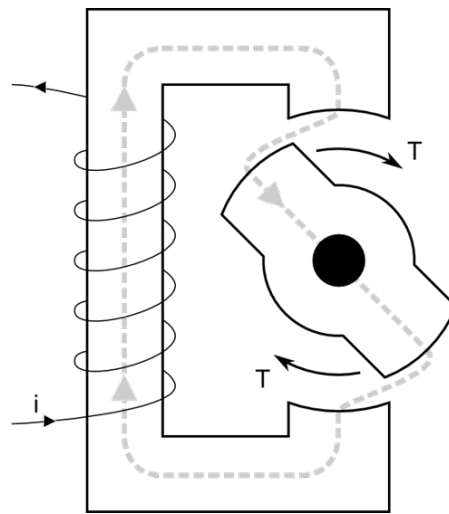


Figure 1.2: Simple reluctance motor

1.2.2 High Efficiency Electrical Energy Conversion

A type of reluctance machine, namely the synchronous reluctance machine, has recently (late 2011) been introduced to the mass market by the ABB as a *super-premium efficiency* motor for fan, mill and pump variable speed drive applications conforming to the future IE4 efficiency standard [35]. These machines do not have rotor copper loss or operate asynchronously like the induction motor, so there are no losses associated with rotor slip. Therefore, the synchronous reluctance machine has an efficiency advantage over the induction machine typically used in these types of industrial applications. This performance increase depends upon the rotor design, but it is perfectly feasible to design a rotor that enables the synchronous reluctance motor to outperform the induction motor in terms of torque and power density [33], with ABB offering a so called HO (High Output) option that claims higher power ratings in a lower frame size. Again, these reluctance machines show promise for high electrical energy efficiency that conforms to legislation aimed at reducing energy consumption and carbon emissions as well as exhibiting a relatively high torque density. The synchronous reluctance motor is suited mostly for operation in variable speed drive applications as they have no direct on-line starting capability; this thesis

will focus on such operation.

1.2.3 Advantages and Disadvantages

The synchronous reluctance machine (SynRM) has some inherent advantages over induction machine (IM) and permanent magnet synchronous machine (PMSM) technologies. The most obvious benefits of reluctance technology are:

- Rotor synchronisation (over IM) for applications where many machines and their plant are required to be synchronous
- No permanent magnets (over PMSM) - which means no magnet losses or demagnetization and the design is lower cost
- No rotor conductors (over IM) which can lead to thermal improvements, lower maintenance requirements, cost and/or easier manufacture
- The design can have a lower rotor inertia leading to faster speed dynamics
- Ease of control, no slip estimator is required

However, with these advantages there are obviously associated disadvantages;

- Moderate torque density ($IM \leq SynRM < PMSM$)
- Lower technological maturity / familiarity compared to induction machine and PM technologies
- Lower power factor than both the induction motor and the PM machine
- No line start capability like the induction machine for DOL applications (additional starting cage is required in the design)
- Low availability, currently only ABB manufacture on a large scale, as far as the author is aware

The induction machine and the permanent magnet machine technologies will still play important roles in the future; however, the reluctance machine has high potential for some applications. With the advantages and disadvantages in mind, the type of reluctance machine must be determined for further research which each have their own positive and negative attributes; these are explored further in the next section. Under certain conditions, i.e. the rotor saliency is sufficiently high, the synchronous reluctance machine is known to have a higher torque density with lower loss per unit torque than the induction machine [50]. The rugged nature of the synchronous reluctance machine, with no rotor copper losses and control simplicity has merits over both the IM and the PMSM; however care must be taken in the design and number of the small saturable ribs (radial and tangential) required in common rotor topologies. In terms of torque transients, the SynRM

typically would have a rotor with lower inertia, and can be controlled for maximum speed torque transients [51], making the synchronous reluctance machine an attractive alternative for fast and robust servo drives. The synchronous reluctance machine stands out as a machine that has high potential and thus will be the focus of this thesis.

1.2.4 SynRM or SRM?

Essentially, there are two main types of rotary electrical machine that operate solely on the reluctance principle and therefore develop only a reluctance torque. They are the:

- Synchronous Reluctance (SynRM)
- Switched Reluctance (SRM)

The synchronous reluctance machine is commonly attributed to Kostko who published in 1923 [37], however history of the machine can be taken back even further to an invention by *Nikola Tesla*, who published a paper by the American Institute of Electrical Engineers in 1888 and patents [38] regarding three motor inventions; the self starting induction motor, the synchronous reluctance motor and a wound rotor synchronous motor. The switched reluctance machine has a heritage back to the 1840's [36]. Typical machine topologies are presented in Figure. 1.3. There are a number of differences between the construction and operation of these two variants, presented in Table 1.1

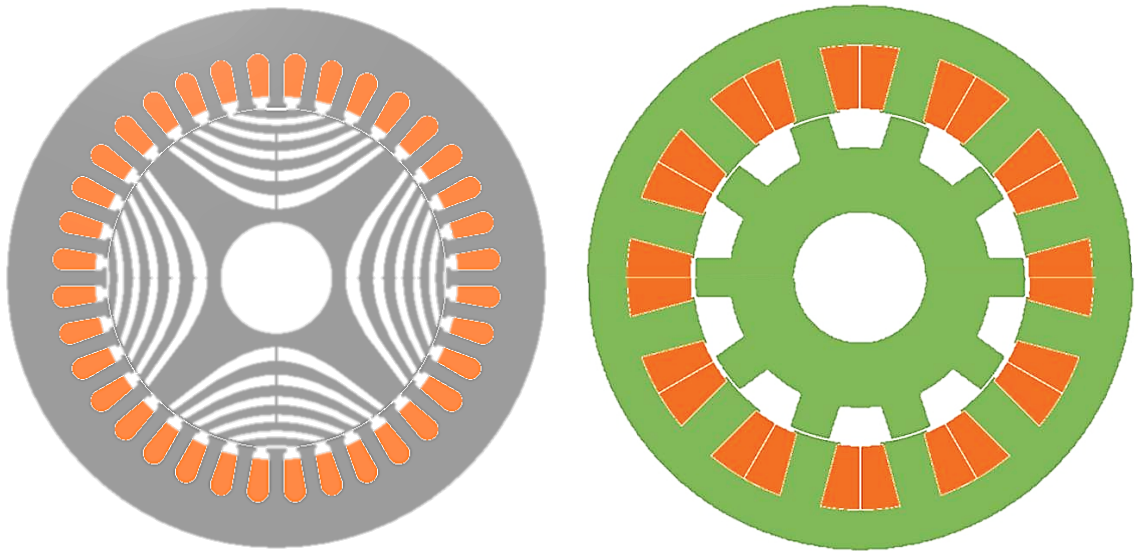


Figure 1.3: Left: Synchronous Reluctance Machine; Right: Switched Reluctance Machine

	SYNRM	SRM
<i>Stator</i>	Smooth bore except for slotting	Salient poles
<i>Rotor</i>	Arrangement of internal flux guides	Salient poles
<i>Winding</i>	Polyphase distributed winding	Tooth concentrated coils
<i>Excitation</i>	Balanced polyphase currents	Sequence of DC current pulses
<i>Inductance</i>	Sinusoidal	Triangular / Trapezoidal
<i>Converter</i>	Standard Voltage Source Inverter (VSI)	Non-standard

Table 1.1: Synchronous and switched reluctance machine differences

The synchronous reluctance machine resembles an AC induction motor: the same stator but with a different rotor - without rotor bars or windings; The switched reluctance machine, which is not a true AC rotating field machine, is of a less conventional construction. The switched reluctance machine has the benefit of single tooth coils with short end windings but requires a non-standard converter, the Asymmetric Half-Bridge (AHB). A drive topology schematic comparison is presented in Fig. 1.4.

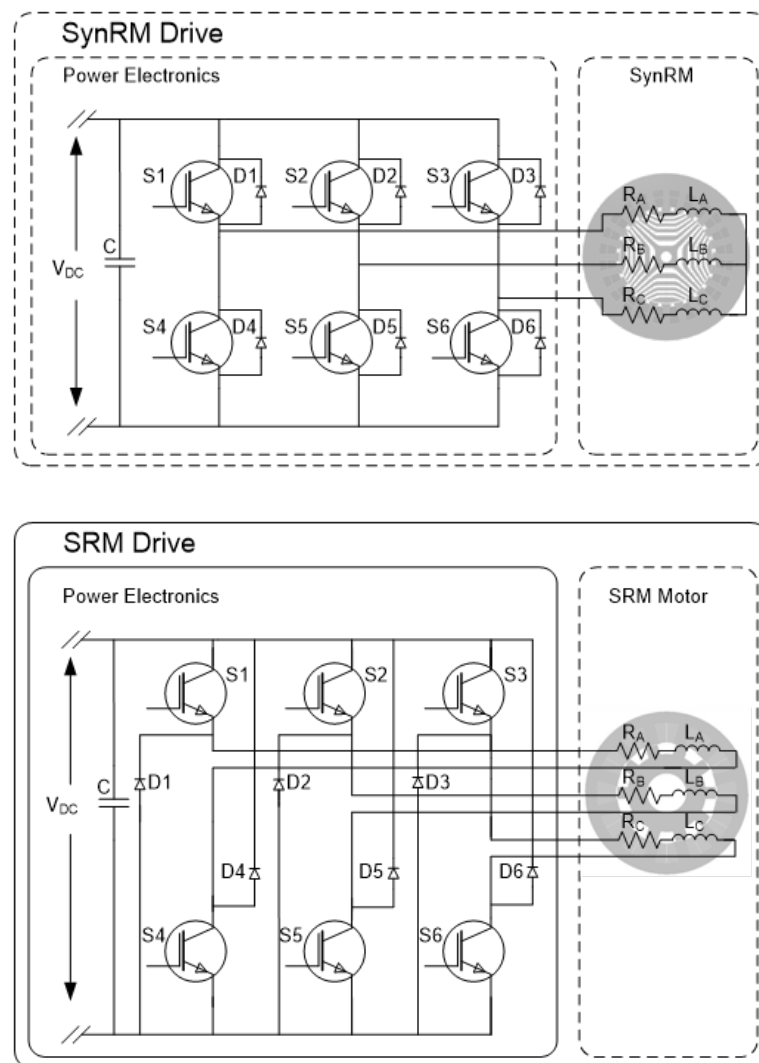


Figure 1.4: Above: SynRM VSI; Below: Switched Reluctance Machine AHB

The non-standard converter used by the SRM is not available “off the shelf”, it requires additional current sensors and motor connecting leads. Switched reluctance motor technology is well known for its high torque ripple, acoustic noise and vibration [36], which are undesirable characteristics. The switched reluctance motor has undergone a great amount of research in recent times [39-43] and has been a large area of research for the research group in which this thesis is written [43-47], notably in the invention of the segmental rotor switched reluctance machine [48,49] which exhibits superior performance due to better utilization of the magnetic and electric loadings. The synchronous reluctance machine has been somewhat neglected relative to the continued research of IM and PM machines, and also of late, the switched reluctance machine.

1.3 Literature

As of April 2015 and within the last 10 years, according to the *IEEE* and the *IET* there are over 2,258 conference and journal papers concerning the switched reluctance machine, there are approximately only 1000 for the synchronous reluctance motor, but over 13,396 articles for the permanent magnet motor. The induction machine has a similar level of contribution as the PM motor with 11,951 conference and journal articles being published. Thus the research in the last decade has clearly focussed on the permanent magnet and induction motor technologies, with half the research into reluctance based machines in the field of the synchronous reluctance motor compared to the switched reluctance motor. There are many papers, old and new, dealing with synchronous technology [37, 51-79]. Electromagnetic design and optimisation of synchronous reluctance machine rotors is dealt with extensively [37, 51-64] which was popular from the 50s right through to the present. In this time many landmark papers deal with the details of designing a rotor with a very high saliency ratio [57], leading to high efficiency and high power factor. The design of transverse laminated and axially laminated rotors is now well documented. Other papers deal specifically with torque ripple minimisation in synchronous reluctance machines [53, 61, 65-67], and novel concepts are still being presented [61, 68]. Field weakening performance of synchronous reluctance machines [69-71] and their control [72-74] have also been a large research area. Recently a theoretical and experimental re-evaluation of the synchronous reluctance motor has been presented [75] and most efforts are concerned with high speed [76] or design modifications for high saliency ratios and inclusion of PM material for power factor improvement and drive size reduction [77-79]. However, the switched reluctance machine has attracted more interest for vehicle applications [39, 80-83]. The vast majority of the published synchronous reluctance machine papers assume polyphase distributed windings, identical to that of the induction machine. Permanent magnet machine research has, however, made use of fractional slot concentrated windings due to the inherent benefits [84] (such as short end windings and high fill factors) for vehicular [85-88] and high efficiency [89] applications. Some induction ma-

chines have also included these fractional slot concentrated windings [90 & 91]. Switched reluctance machines include single tooth windings as they are intrinsic to their topology [92]. In terms of traction motors for vehicular applications, the vast majority have been interior permanent magnet or induction machine technologies, with synchronous reluctance being neglected. Recent developments such as IPM (interior permanent magnet) motors with ferrite magnets and Permanent magnet assisted synchronous reluctance motors [93-96] have been considered for vehicular and high efficiency applications. According to the available literature, there has been no detailed analysis, synthesis, prototype and validation of a fractional slot concentrated winding synchronous reluctance motor. This thesis attempts to fill the knowledge gap and contribute to the scientific community through detailed exploration and synthesis of fractional slot concentrated windings with the synchronous reluctance machine.

1.4 Overview of SynRM Motor Technology

Here, an overview of conventional (a machine with polyphase distributed windings) synchronous reluctance technology is presented. Firstly the development of the synchronous reluctance machine is briefly traced from a historical perspective, the basic operating principle is discussed and the machine mathematical model in the synchronous $d-q$ frame is presented. Common figures of merit and typical values are presented and an overview of rotor designs is also presented.

1.4.1 Brief History

As mentioned previously, the synchronous reluctance machine can trace its roots back to an invention of Nikola Tesla in 1887 but was first published in its modern form by J. K. Kostko in 1923. The synchronous reluctance machine gained interest after Kostko's publication engineers such as Tricky [97] continued the work on synchronous reluctance motors, developing performance analysis techniques. However, the synchronous reluctance machine did not really gain wide interest until the 1960s. In Lawernson's work [98-100], synchronous reluctance motor technology found acceptance in variable speed and multiple synchronised machine applications such as in paper mills. Due to advancements in control and power electronics technology in the 1980s and the commercialisation of rare-earth permanent magnets around this time, the permanent magnet synchronous machine (PMSM) became the research topic of choice due to its inherent high torque density and high efficiency [101]. In the 1990's an interest in synchronous reluctance motors was reignited by the work of Stanton and Miller [102-104], however, PM machines research has dominated until recently, where a resurgence in reluctance technology is under way.

1.4.2 Operating Principle

The synchronous reluctance machine produces only a reluctance torque. Rotor magnetic anisotropy (*i.e.* rotor *saliency*) is the cause of significant torque production. A tangential Maxwell stress is produced in the airgap by the interaction with and relative position of the stator currents and the rotor saliency. In a synchronous reluctance machine with a magnetically anisotropic rotor, the air-gap magnetic field is produced by the stator conductors, distributed around the stator core periphery. It links the rotor through the air gap, as in a wound synchronous machine or induction machine. Tangential Maxwell stress in the air gap is formed due to the anisotropic nature of the rotor and positioning of the magnetic field by means of control. The stress manifests the torque based on the load angle and it is generally considered that the current angle in the machine, defined as the angle between the current vector and the d -axis of the rotor, is used to control this tangential stress and therefore the torque production. The rotor anisotropic nature is determined by an axis of lowest magnetic reluctance (d -axis) and an axis of greatest magnetic reluctance (q -axis). The d -axis is π electrical degrees displaced from the q -axis of the rotor. The axis convention in the SynRM is the opposite to that of PM machines as the main flux path is provided by permanent magnets, typically in the q -axis when referring to the SynRM axis convention.

1.4.3 Machine Modelling

The following equations are based on steady state operation of the synchronous reluctance motor. Machine variables in the abc frame are transformed into the synchronously rotating reference frame by a $dq0$ transformation. The steady state phasor diagram of the synchronous reluctance motor is presented in Figure. 1.5.

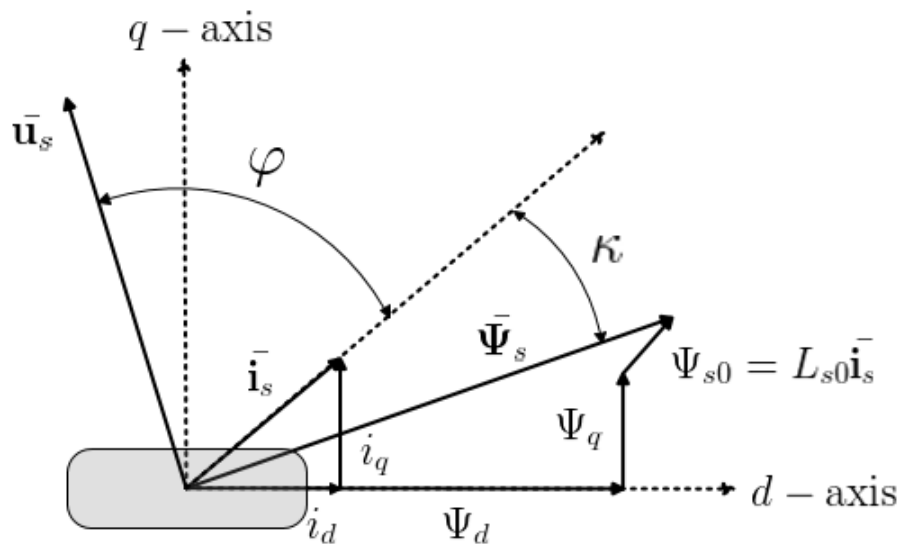


Figure 1.5: Steady state phasor diagram of the synchronous reluctance machine

The machine mathematical model in phase (abc) coordinates, expressed in matrix

form can be written;

$$\mathbf{u}_{abc} = \mathbf{R}_s \mathbf{i}_{abc} + \frac{d\Psi_{abc}}{dt} \quad (1.1)$$

Where;

$$\mathbf{u}_{abc} = \begin{bmatrix} u_a \\ u_b \\ u_c \end{bmatrix} \quad \mathbf{i}_{abc} = \begin{bmatrix} i_a \\ i_b \\ i_c \end{bmatrix} \quad \Psi_{abc} = \begin{bmatrix} \Psi_a \\ \Psi_b \\ \Psi_c \end{bmatrix} \quad \mathbf{R}_s = \begin{bmatrix} R_a & 0 & 0 \\ 0 & R_b & 0 \\ 0 & 0 & R_c \end{bmatrix} \quad (1.2)$$

are the voltage vector \mathbf{u}_{abc} , the current vector \mathbf{i}_{abc} , the flux linkage vector Ψ_{abc} and the phase resistance matrix \mathbf{R}_s respectively. In Fig. 1.5, the angle φ is the power factor angle between the voltage and current vectors, κ is the current angle between the current vector and the flux linkage vector and the subscripts d and q indicate the axis components of the respective vector. The term Ψ_{s0} is the stator leakage flux linkage and L_{s0} the associate stator leakage inductance. The current vector \mathbf{i}_{abc} forms a set of balanced sinusoidal currents corresponding to the current phasor \mathbf{i}_s ;

$$\begin{bmatrix} i_a \\ i_b \\ i_c \end{bmatrix} = \sqrt{2}I_s \begin{bmatrix} \cos(\omega t) \\ \cos(\omega t - \frac{2\pi}{3}) \\ \cos(\omega t + \frac{2\pi}{3}) \end{bmatrix} \quad (1.3)$$

Where I_s is the RMS current and $\omega = 2\pi f_s$ is its electrical frequency. Now in order to develop a model compatible with control development, the stator phase coordinate time dependant frame must transformed into the synchronous $dq0$ time-independent reference frame using the Park-Blondel power invariant transformation [15]. The transformation matrix \mathbf{T}^{-1} is written;

$$\mathbf{T}^{-1} = \sqrt{\frac{2}{3}} \begin{bmatrix} \cos(\theta) & \cos(\theta - \frac{2\pi}{3}) & \cos(\theta + \frac{2\pi}{3}) \\ -\sin(\theta) & -\sin(\theta - \frac{2\pi}{3}) & -\sin(\theta + \frac{2\pi}{3}) \\ \frac{1}{\sqrt{2}} & \frac{1}{\sqrt{2}} & \frac{1}{\sqrt{2}} \end{bmatrix} \quad (1.4)$$

The angle $\theta = \omega t + \beta$, where β is an initial phase angle based on the location of the d -axis. The machine equations are then transformed into the following set, where the voltage vector \mathbf{u}_{dq} corresponds to the voltage phasor \mathbf{u}_s ;

$$\mathbf{u}_{dq} = \mathbf{R} \mathbf{i}_{dq} + \mathbf{L}_{dq} \frac{d\mathbf{i}_{dq}}{dt} + p\omega \Lambda \Psi_{dq} \quad (1.5)$$

Where;

$$\mathbf{u}_{dq} = \begin{bmatrix} u_d \\ u_q \end{bmatrix} \quad \mathbf{i}_{dq} = \begin{bmatrix} i_d \\ i_q \end{bmatrix} \quad \Psi_{dq} = \begin{bmatrix} \Psi_d \\ \Psi_q \end{bmatrix} \quad \mathbf{R} = \begin{bmatrix} R_s & 0 \\ 0 & R_s \end{bmatrix} \quad (1.6)$$

$$\Lambda = \begin{bmatrix} 0 & -1 \\ 1 & 0 \end{bmatrix} \quad \mathbf{L}_{dq} = \begin{bmatrix} L_d & 0 \\ 0 & L_q \end{bmatrix} \quad (1.7)$$

are the transformed voltage vector \mathbf{u}_{dq} , the current vector \mathbf{i}_{dq} , the flux linkage vector Ψ_{dq} , resistance matrix \mathbf{R} , the cross coupling matrix Λ and the inductance matrix from left to right \mathbf{L}_{dq} . Here p is the number of pole pairs. The 0 -axis component is taken as zero as we assume that if the machine is star-connected then at the star-point $\sum i = 0$ and $i_0 = \sqrt{\frac{2}{3}} \frac{1}{\sqrt{2}} (i_a + i_b + i_c) = 0$. The inductance elements in the matrix \mathbf{L}_{dq} are usually considered as constant, though this is not generally the case as is explored in subsequent chapters. It must also be noted that the null elements in the inductance matrix are not always null, cross coupling inductances can also exist however they are generally considered to be zero. This current phasor sets up the stator flux phasor Ψ_s which comprises of magnetising components along the dq axes and a stator leakage component.

$$\Psi_s = \Psi_{md} + j\Psi_{mq} + L_{s\sigma}\mathbf{i}_s \quad (1.8)$$

Here, Ψ_{md} is the direct axis magnetizing component and Ψ_{mq} is the quadrature axis magnetizing component with $L_{s\sigma}\mathbf{i}_s$ the stator leakage flux determined by the stator leakage inductance $L_{s\sigma}$. As well as the voltage equations, another equation that is required to predict performance is the torque equation. The machine electromagnetic power in the synchronous reference frame can be expressed if we consider multiplying the voltage equation through by \mathbf{i}_{dq}^T and from an equation that has the following form;

$$\underbrace{\mathbf{u}_{dq}\mathbf{i}_{dq}^T}_{\text{Total}} = \underbrace{\mathbf{R}\mathbf{i}_{dq}\mathbf{i}_{dq}^T}_{\text{Loss}} + \underbrace{\mathbf{L}_{dq}\frac{d\mathbf{i}_{dq}}{dt}\mathbf{i}_{dq}^T}_{\text{Stored}} + \underbrace{p\omega\Lambda\Psi_{dq}\mathbf{i}_{dq}^T}_{\text{Mechanical}} \quad (1.9)$$

$$p_t = v_d i_d + v_q i_q = p_{loss} + p_{stored} + p_{mech} \quad (1.10)$$

It is the mechanical power p_{mech} developed by the machine that is translated into rotor electromagnetic torque. Therefore interest is in the terms that contain $\frac{d\theta}{dt} = \omega$, thus the torque can be expressed;

$$\tau_{em(dq0)} = p(\Psi_d i_q - \Psi_q i_d) = p(\Psi_{dq} \times \mathbf{i}_{dq}) \quad (1.11)$$

Here $\Psi_{dq} \times \mathbf{i}_{dq}$ is a vector cross product and by using the relation $\Psi_{dq} = \mathbf{L}_{dq}\mathbf{i}_{dq}$, the torque equation can be reduced to;

$$\tau_{em(dq0)} = p(L_d - L_q) i_d i_q \quad (1.12)$$

Here L_d and L_q are the direct and quadrature axis inductances respectively. Utilizing

expression of the dq equivalent currents as the stator current in the stationary abc frame², this torque equation can be rewritten;

$$\tau_{em(dq0)} = \frac{1}{2}p (L_d - L_q) i_s^2 \sin(2\kappa) \quad (1.13)$$

Where κ is termed the *current angle*, the angle between the current vector and the stator flux vector. These equations form an electrical dynamic model of the synchronous reluctance machine in the synchronous reference frame that can be used to evaluate the machine performance. The main control strategy for synchronous reluctance machines is current angle control, where the machine can be controlled for maximum torque per Ampere (MTPA) or maximum power factor (MPFC). It is evident from the torque equation Eq. 1.13 that for maximum torque per Ampere, $\sin(2\kappa) = 1$, thus $\kappa = \frac{\pi}{4}$. Under this control, the torque equation reduces to;

$$\tau_{em(dq0)} = \frac{i_s^2}{2}p \{L_d - L_q\} \quad (1.14)$$

The power factor for any current angle can be found by inspection of the steady state phasor diagram as;

$$\cos(\phi) = \frac{\xi - 1}{\sqrt{2}} \sqrt{\frac{\sin(2\kappa)}{\xi^2 \cot(\kappa) + \tan(\kappa)}} \quad (1.15)$$

Where $\xi = \frac{L_d}{L_q}$ is the saliency ratio of the machine. Under MTPA, the power factor equation reduces to;

$$\cos(\phi) = \frac{\xi - 1}{\sqrt{2}} \sqrt{\frac{1}{\xi^2 + 1}} \quad (1.16)$$

Clearly under MTPA the power factor is limited to 0.707 regardless of the magnitude of the saliency ratio as; $\lim_{\xi \rightarrow \infty} \left\{ \frac{\xi - 1}{\sqrt{2}} \sqrt{\frac{1}{\xi^2 + 1}} \right\} = \frac{1}{\sqrt{2}}$.

1.4.4 Figures of Merit

Along with the relevant model, three *figures of merit* can be used with synchronous reluctance motors to gauge their performance potential.

- *Saliency Ratio*, ξ , is the ratio of the d -axis to the q -axis inductance, physically relating to the level of anisotropic magnetic reluctance of the rotor, governing the power factor and ultimately the overall performance of the machine. It also known as the *true* saliency ratio, as it takes into account the stator leakage components $L_{s\sigma}$, a similar figure of merit can also be defined that ignores the leakage and is termed

²The current vector is written; $\begin{bmatrix} i_d \\ i_q \end{bmatrix} = I_s \begin{bmatrix} \cos(\kappa) & 0 \\ 0 & \sin(\kappa) \end{bmatrix}$, thus the current phasor magnitude is $|I_s| = \sqrt{i_d^2 + i_q^2}$ and the angle between the d -axis and the current phasor is then written $\kappa = \arctan\left(\frac{i_q}{i_d}\right)$

the *magnetising* saliency ratio.

$$\xi = \frac{L_d}{L_q} = \frac{L_{md} + L_{s\sigma}}{L_{mq} + L_{s\sigma}} \quad (1.17)$$

Where L_{md} , L_{mq} and $L_{s\sigma}$ are the magnetizing and stator leakage inductances respectively. The saliency ratio indicates the level of anisotropic magnetic reluctance in the rotor component, which is of great interest as the higher the saliency ratio, the greater the general machine performance. An increased stator leakage inductance acts to reduce the true saliency ratio of the machine, impairing performance.

- The *Torque Index*, Θ , is the difference in the d -axis and q -axis inductances;

$$\Theta = L_d - L_q = L_{md} - L_{mq} \quad (1.18)$$

The torque index is another important figure of merit pertaining to the torque capability of the machine. The higher the torque index, the higher the torque density of the machine. The stator leakage inductance is important in the saliency ratio of the machine, however it does not affect the torque index.

- These are complimented by the *Inverter Utilization*, Y , which indicates the kVA/kW requirement of the attached voltage source inverter (VSI).

$$Y = \eta \cdot \cos(\phi) \quad (1.19)$$

Where η is the machine efficiency and $\cos(\phi)$ the machine power factor. These figures of merit give an indication as to the level of performance of a synchronous reluctance machine. Higher values indicate higher performance, with the main figure of merit the saliency ratio.

1.4.5 Rotor Designs

The stator of a synchronous reluctance machine may be identical to that of the induction machine. Various synchronous reluctance machine rotors are presented in Figure 1.6 with their typical achievable saliency figures of merit, the higher the better. The early rotors were constructed from simple salient poles which had a very poor performance due to their poor saliency ratio ξ . Improvements were made by modifying induction motor rotors, the rotor bars removed and slots linking the rotor bar slots were stamped in order to develop a higher degree of saliency for increased performance over the simply salient type. From this, the rotor evolved into a segmental arrangement, like Kostko's original in 1923, which increased the saliency. Further developments led to the flux guide rotor, where flux guides directed flux in the magnetizing axis (d -axis) and reduced the flux in the orthogonal axis (q -axis) leading to high saliency. These rotors are of the transverse lamination (TLA) type, *i.e.* they are laminated as conventional induction machines. Another type, the axially laminated variant where the laminations are oriented axially, provides the

highest saliency and therefore the highest performance in terms of torque capability and power factor, however, due to the axial lamination, eddy-current losses can be significant. This eddy current problem and their construction difficulty have appeared to prevent further development and adoption such that the TLA flux guide rotor is the rotor topology of choice for synchronous reluctance machine design engineer.

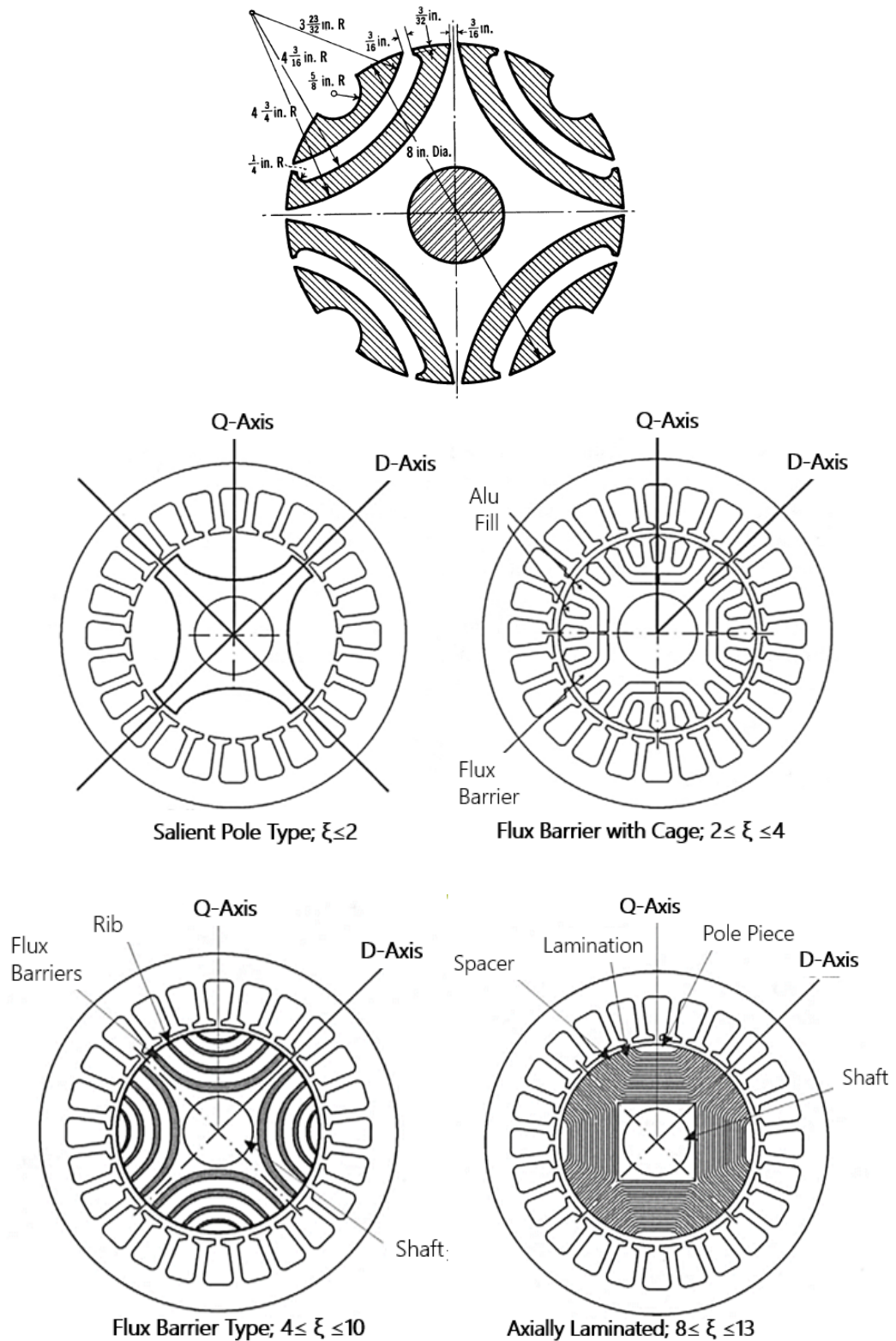


Figure 1.6: Kosto's design (top) and other SynRM rotor topologies [36, 105]

The synchronous reluctance machine under these rotor types, if direct on-line, is not self starting and generally requires a variable speed drive to get up to synchronous speed. Historically however, direct on-line synchronous reluctance machines have incorporated a cage, otherwise known as a starting cage, to get the machine to synchronous speed and attain synchronous performance [106]. The transverse laminated flux barrier rotor showing details of its construction are shown in the lower left hand corner of Figure. 1.6. It is this rotor type that will be considered in this thesis due to the attainable high saliency ratios and ease of manufacture. In order to obtain good machine performance, the saliency ratio must be maximised. The saliency ratio of the machine is mainly dictated by the electromagnetic design of the rotor. The stator leakage inductance also has an effect, as shown by Eq. 1.17. It is usually low compared to the magnetizing components in polyphase distributed winding machines; a sentiment which cannot be carried over to the machine proposed in this thesis, as will be explained in due course.

1.4.6 Challenges

Based on the current literature in Section 1.3, conventional SynRM technology is deemed a viable technology with many advantages, but it does have some undesirable characteristics. These are as follows;

1. Long end windings (Polyphase distributed windings)
 - (a) Long axial extent
 - (b) Long average turn length
 - (c) Overlapping phases
2. Low fill factor, between 30-40% typically
 - (a) Low power / torque density
 - (b) Poor slot thermal conductivity
3. Complex Winding Arrangements
 - (a) Labour intensive
 - (b) Costly
4. Requires Magnetization by Stator MMF
 - (a) Low power factor
 - (b) Low inverter utilization

This thesis aims to tackle some of these challenges, pushing synchronous reluctance machine technology toward high torque density and high efficiency electric motors that outperform the current technology induction machine and bring reluctance technology closer to that of high performance permanent magnet machines. If synthesis of the synchronous reluctance machine and the topological merits of the switched reluctance could be realised, a novel machine topology that addresses some of the identified challenges would result and would be applicable to both of the identified research challenges set out at the beginning of this chapter.

1.5 References

1. <http://www.bloomberg.com/news/2011-01-14/toyota-readying-electric-motors-that-don-t-use-rare-earths.htm>
2. <http://gigaom.com/2012/11/21/an-electric-motor-thats-ditched-the-rare-earth-materials/>
3. <http://evworld.com/news.cfm?newsid=24925>
4. <http://www.reuters.com/article/2012/06/22/us-rareearths-alternatives-idUSBRE85L0YB20120622>
5. <http://www.bbc.co.uk/programmes/b00scY0d>
6. <http://www.economist.com/news/science-and-technology/21566613-electric-motor-does-not-need-expensive-rare-earth-magnets-reluctant-heroes>
7. <http://www.esi-africa.com/node/16839>
8. <http://www.4-traders.com/KSB-AG-436319/news/KSB-AG-KSB-launches-promotion-programme-for-building-services-17269803/>
9. <http://www.pacetoday.com.au/news/lack-of-regulatory-enforcement-results-in-slow-ado>
10. <http://www.eurekamagazine.co.uk/design-engineering-features/technology/super-premium-defines-efficiency/36080/>
11. http://ec.europa.eu/clima/policies/transport/vehicles/index_en.htm
12. Commission Regulation (EU) No 63/2011
13. Nomenclature of Inorganic Chemistry IUPAC Recommendation, 2005
14. Rare earth elements critical resources for high technology, US geological survey, 2006, fact sheet USGS 087-02
15. 1787-1987, 200 years of rare earth, RE information centre IPRT, North Holland
16. F.H Spedding & A.H. Daane, 'The Rare Earths', John Wiley & Sons, 1961
17. http://www.nytimes.com/2010/10/30/business/global/30rare.html?pagewanted=all&_r=0
18. <http://www.bbc.co.uk/news/business-18516461>
19. <http://www.extremetech.com/extreme/151513-japan-discovers-large-quantity-of-rare-earth-hopes-to-break-chinas-chokehold-on-supply>
20. <http://www.marketoracle.co.uk/Article33315.html>
21. <http://www.technologyreview.com/news/421472/can-the-us-rare-earth-industry-rebound/>
22. <http://www.reuters.com/article/2011/09/06/china-rare-earth-idUSL3E7K620P20110906>
23. 'VW joins rush into electric vehicles', Financial Times, March 8, 2010
24. Tim Burgess, 'Benchmarking of Competitive Technologies', Oakridge National Laboratory, 2012
25. 'About the size of a water melon, with a lot more juice', Tesla Motors

26. 'Renault Fluence Z.E.', Renault, <http://www.renault.com/en/vehicules/aujourd'hui/renault-vehicules-electriques/pages/fluence-ze.aspx>
27. Wolfson, R., 'The Future of Energy', http://www.insightcruises.com/pdf/sa11_slides/Wolfson/Future_of_energy.pdf
28. Waide, P. and Conrad, B., 'Energy-efficiency policy opportunities for electric motor-driven systems', International Energy Agency, 2011 Working Paper in the Energy Efficiency Series, OECD/IEA 2011
29. Commission Regulation (EC) No 640/2009
30. EU Directive 2005/32/EC
31. Peters, D.T.; Brush, E.F.; Kirtley, J.L., "Die-cast copper rotors as strategy for improving induction motor efficiency," Electrical Insulation Conference and Electrical Manufacturing Expo, 2007, vol., no., pp.322,327, 22-24 Oct. 2007
32. 'Copper Motor Rotors Give Army Trucks a Boost', Machine Design, <http://machinedesign.com/news/copper-motor-rotors-give-army-trucks-boost>
33. 'ABB's synchronous reluctance motor and drive package wins 2011 Automation Award', ABB UK, <http://www.abb.co.uk/cawp/seitp202/87688c289d52378cc125796e0045f0f5.aspx>
34. 'Low voltage IE4 synchronous reluctance motor and drive package for pump and fan applications', ABB, 2013, [http://www05.abb.com/global/scot/scot234.nsf/veritydisplay/23fcebcbcd9f0286c1257bd500217837/\\$file/Catalog_IE4_SynRM_EN%2006-2013_9AKK105828_LOWRES.pdf](http://www05.abb.com/global/scot/scot234.nsf/veritydisplay/23fcebcbcd9f0286c1257bd500217837/$file/Catalog_IE4_SynRM_EN%2006-2013_9AKK105828_LOWRES.pdf)
35. PD IEC/TS 60034-27-2:2012, British Standards Institution, 2013
36. J. Reid, 'Robert Davidson – Pioneer Electrician', The Scientific Tourist: Aberdeen, Aberdeen University
37. Kostko, J.K., "Polyphase reaction synchronous motors," American Institute of Electrical Engineers, Journal of the, vol.42, no.11, pp.1162,1168, Nov. 1923
38. Tesla, N., "A New System of Alternate Current Motors and Transformers," American Institute of Electrical Engineers, Transactions of the, vol.V, no.10, pp.308,327, July 1888
39. Santos, F.L.M.; Anthonis, J.; Naclerio, F.; Gyselinck, J.J.C.; Van der Auweraer, H.; Goes, L.C.S., "Multiphysics NVH Modeling: Simulation of a Switched Reluctance Motor for an Electric Vehicle," Industrial Electronics, IEEE Transactions on, vol.61, no.1, pp.469,476, Jan. 2014
40. Widmer, J.D.; Martin, R.; Mecrow, B.C., "Optimisation of an 80kW Segmental Rotor Switched Reluctance Machine for automotive traction," Electric Machines & Drives Conference (IEMDC), 2013 IEEE International, vol., no., pp.427,433, 12-15 May 2013
41. Haghbin, S.; Rabiei, A.; Grunditz, E., "Switched reluctance motor in electric or hybrid vehicle applications: A status review," Industrial Electronics and Applications (ICIEA), 2013 8th IEEE Conference on, vol., no., pp.1017,1022, 19-21 June 2013
42. Singh, S.K.; Tripathi, R.K., "Minimization of torque ripples in SRM drive using DITC for electrical vehicle application," Engineering and Systems (SCES), 2013 Students Conference on, vol., no., pp.1,5, 12-14 April 2013

43. Bateman, C.J.; Mecrow, B.C.; Clothier, A.C.; Acarnley, P.P.; Tuftnell, N.D., "Sensorless Operation of an Ultra-High-Speed Switched Reluctance Machine," *Industry Applications, IEEE Transactions on* , vol.46, no.6, pp.2329,2337, Nov.-Dec. 2010
44. Widmer, J.D.; Mecrow, B.C., "Optimized Segmental Rotor Switched Reluctance Machines With a Greater Number of Rotor Segments Than Stator Slots," *Industry Applications, IEEE Transactions on* , vol.49, no.4, pp.1491,1498, July-Aug. 2013
45. Widmer, J. D.; Martin, R.; Spargo, C. M.; Mecrow, B. C.; Celik, T., "Winding configurations for a six phase switched reluctance machine," *Electrical Machines (ICEM), 2012 XXth International Conference on* , vol., no., pp.532,538, 2-5 Sept. 2012
46. Widmer, J. D.; Mecrow, B. C.; Spargo, C. M.; Martin, R.; Celik, T., "Use of a 3 phase full bridge converter to drive a 6 phase switched reluctance machine," *Power Electronics, Machines and Drives (PEMD 2012), 6th IET International Conference on* , vol., no., pp.1,6, 27-29 March 2012
47. Mecrow, B. C.; Finch, J. W.; El-Kharashi, E. A.; Jack, A. G., "Switched reluctance motors with segmental rotors," *Electric Power Applications, IEE Proceedings -* , vol.149, no.4, pp.245,254, July 2002
48. Mecrow, Barrie Charles , "Control of a Switched Reluctance Drive" , Patent No. 7205694
49. Lipo T.A.: " Synchronous reluctance machines – a viable alternative for AC drives ," *Electr Mach Power Syst*, vol. 19, pp. 659-671, 1991 49I. Boldea, 'Reluctance Synchronous Machines and Drives', Clarendon Press, 1996
50. Cruickshank, A. J O; Anderson, A. F.; Menzies, R.W., "Theory and performance of reluctance motors with axially laminated anisotropic rotors," *Electrical Engineers, Proceedings of the Institution of* , vol.118, no.7, pp.887,894, July 1971
51. Boglietti, A.; Pastorelli, M., "Induction and synchronous reluctance motors comparison," *Industrial Electronics, 2008. IECON 2008. 34th Annual Conference of IEEE* , vol., no., pp.2041,2044, 10-13 Nov. 2008
52. Honsinger, V.B., "The Inductances L_d and L_q of Reluctance Machines," *Power Apparatus and Systems, IEEE Transactions on* , vol.PAS-90, no.1, pp.298,304, Jan. 1971
53. Vagati, A.; Pastorelli, M.; Francheschini, G.; Petrache, S.C., "Design of low-torque-ripple synchronous reluctance motors," *Industry Applications, IEEE Transactions on* , vol.34, no.4, pp.758,765, Jul/Aug 1998
54. Matsuo, T.; Lipo, T.A., "Rotor design optimization of synchronous reluctance machine," *Energy Conversion, IEEE Transactions on* , vol.9, no.2, pp.359,365, Jun 1994
55. Lawrenson, P.J.; Gupta, S.K., "Developments in the performance and theory of segmental-rotor reluctance motors," *Electrical Engineers, Proceedings of the Institution of* , vol.114, no.5, pp.645,653, May 1967
56. Lawrenson, P.J.; Agu, L.A., "Theory and performance of polyphase reluctance machines," *Electrical Engineers, Proceedings of the Institution of* , vol.111, no.8, pp.1435,1445, August 1964
57. Staton, D.A.; Miller, T.J.E.; Wood, S.E., "Maximising the saliency ratio of the synchronous reluctance motor," *Electric Power Applications, IEE Proceedings B* , vol.140, no.4, pp.249,259, Jul 1993

58. Staton, D.A.; Miller, T.J.E.; Wood, S.E., "Optimisation of the synchronous reluctance motor geometry," *Electrical Machines and Drives*, 1991. Fifth International Conference on (Conf. Publ. No. 341) , vol., no., pp.156,160, 11-13 Sep 1991
59. Miller, T.J.E.; Hutton, A.; Cossar, C.; Staton, D.A., "Design of a synchronous reluctance motor drive," *Industry Applications*, IEEE Transactions on , vol.27, no.4, pp.741,749, Jul/Aug 1991
60. Alotto, P.; Barcaro, M.; Bianchi, N.; Guarnieri, M., "Optimization of Interior PM Motors With Machaon Rotor Flux Barriers," *Magnetics*, IEEE Transactions on , vol.47, no.5, pp.958,961, May 2011
61. Bianchi, N.; Bolognani, S.; Bon, D.; Pre, M.D., "Torque Harmonic Compensation in a Synchronous Reluctance Motor," *Power Electronics Specialists Conference*, 2006. PESC '06. 37th IEEE , vol., no., pp.1,6, 18-22 June 2006
62. Bianchi, N.; Chalmers, B.J., "Axially laminated reluctance motor: analytical and finite-element methods for magnetic analysis," *Magnetics*, IEEE Transactions on , vol.38, no.1, pp.239,245, Jan 2002
63. Moghaddam, Reza R.; Magnussen, F.; Sadarangani, C., "Novel rotor design optimization of synchronous reluctance machine for high torque density," *Power Electronics, Machines and Drives (PEMD 2012)*, 6th IET International Conference on , vol., no., pp.1,4, 27-29 March 2012
64. Moghaddam, R.; Gyllensten, F., "Novel High Performance SynRM Design Method, an Easy Approach for a Complicated Rotor Topology," *Industrial Electronics*, IEEE Transactions on , vol.PP, no.99, pp.1,1, 2014
65. Sanada, M.; Hiramoto, K.; Morimoto, S.; Takeda, Y., "Torque ripple improvement for synchronous reluctance motor using an asymmetric flux barrier arrangement," *Industry Applications*, IEEE Transactions on , vol.40, no.4, pp.1076,1082, July-Aug. 2004
66. Moghaddam, R.-R.; Magnussen, F.; Sadarangani, C., "Novel rotor design optimization of Synchronous Reluctance Machine for low torque ripple," *Electrical Machines (ICEM)*, 2012 XXth International Conference on , vol., no., pp.720,724, 2-5 Sept. 2012
67. Fratta, A.; Toglia, G.P.; Vagati, A.; Villata, F., "Ripple evaluation of high-performance synchronous reluctance machines," *Industry Applications Magazine*, IEEE , vol.1, no.4, pp.14,22, Jul/Aug 1995
68. Ferrari, M.; Bianchi, N.; Doria, A.; Fornasiero, E., "Design of synchronous reluctance motor for hybrid electric vehicles," *Electric Machines & Drives Conference (IEMDC)*, 2013 IEEE International , vol., no., pp.1058,1065, 12-15 May 2013
69. Soong, W.L.; Miller, T.J.E., "Field-weakening performance of brushless synchronous AC motor drives," *Electric Power Applications*, IEE Proceedings - , vol.141, no.6, pp.331,340, Nov 1994
70. Chalmers, B.J.; Musaba, L., "Design and field-weakening performance of a synchronous reluctance motor with axially-laminated rotor," *Industry Applications Conference*, 1997. Thirty-Second IAS Annual Meeting, IAS '97., Conference Record of the 1997 IEEE , vol.1, no., pp.271,278 vol.1, 5-9 Oct 1997
71. Ahn, J.; Lim, S.-B.; Kim, K.-C.; Lee, J.; Choi, J.-H.; Kim, S.; Hong, J. -P, "Field weakening control of synchronous reluctance motor for electric power steering," *Electric Power Applications*, IET , vol.1, no.4, pp.565,570, July 2007

72. Tuovinen, T.; Hinkkanen, M.; Luomi, J., "Analysis and Design of a Position Observer With Resistance Adaptation for Synchronous Reluctance Motor Drives," *Industry Applications, IEEE Transactions on* , vol.49, no.1, pp.66,73, Jan.-Feb. 2013
73. Zengcai Qu; Hinkkanen, M., "Loss-minimizing control of synchronous reluctance motors — A review," *Industrial Technology (ICIT), 2013 IEEE International Conference on* , vol., no., pp.350,355, 25-28 Feb. 2013
74. Boroujeni, S.S.; Markadeh, G.R.A.; Soltani, J.; Abjadi, N. R., "Flux and torque control of synchronous reluctance motor based on second order sliding mode method," *Control, Instrumentation and Automation (ICCIA), 2011 2nd International Conference on* , vol., no., pp.490,495, 27-29 Dec. 2011
75. Moghaddam, R.R.; Magnussen, F.; Sadarangani, C., "Theoretical and Experimental Reevaluation of Synchronous Reluctance Machine," *Industrial Electronics, IEEE Transactions on* , vol.57, no.1, pp.6,13, Jan. 2010
76. Ikaheimo, J.; Kolehmainen, J.; Kansakangas, T.; Kivela, V.; Moghaddam, R., "Synchronous High-Speed Reluctance Machine with Novel Rotor Construction," *Industrial Electronics, IEEE Transactions on* , vol.PP, no.99, pp.1,1, 0
77. Vartanian, R.; Deshpande, Y.; Toliyat, H.A., "Performance analysis of a rare earth magnet based NEMA frame Permanent Magnet assisted Synchronous Reluctance Machine with different magnet type and quantity," *Electric Machines & Drives Conference (IEMDC), 2013 IEEE International* , vol., no., pp.476,483, 12-15 May 2013
78. Chuang, Tzu-shien, "A high-efficiency PM-assisted synchronous reluctance motor drive," *Applied Power Electronics Conference and Exposition (APEC), 2013 Twenty-Eighth Annual IEEE* , vol., no., pp.3180,3185, 17-21 March 2013
79. Vartanian, R.; Toliyat, H.A.; Akin, B.; Poley, R., "Power factor improvement of synchronous reluctance motors (SynRM) using permanent magnets for drive size reduction," *Applied Power Electronics Conference and Exposition (APEC), 2012 Twenty-Seventh Annual IEEE* , vol., no., pp.628,633, 5-9 Feb. 2012
80. Widmer, J.D.; Martin, R.; Mecrow, B.C., "Optimisation of an 80kW Segmental Rotor Switched Reluctance Machine for automotive traction," *Electric Machines & Drives Conference (IEMDC), 2013 IEEE International* , vol., no., pp.427,433, 12-15 May 2013
81. Kiyota, K.; Kakishima, T.; Sugimoto, H.; Chiba, A., "Comparison of the Test Result and 3D-FEM Analysis at the Knee Point of a 60 kW SRM for a HEV," *Magnetics, IEEE Transactions on* , vol.49, no.5, pp.2291,2294, May 2013
82. Singh, S.K.; Tripathi, R.K., "Minimization of torque ripples in SRM drive using DITC for electrical vehicle application," *Engineering and Systems (SCES), 2013 Students Conference on* , vol., no., pp.1,5, 12-14 April 2013
83. Haghbin, S.; Rabiei, A.; Grunditz, E., "Switched reluctance motor in electric or hybrid vehicle applications: A status review," *Industrial Electronics and Applications (ICIEA), 2013 8th IEEE Conference on* , vol., no., pp.1017,1022, 19-21 June 2013
84. El-Refaie, A.M., "Fractional-Slot Concentrated-Windings Synchronous Permanent Magnet Machines: Opportunities and Challenges," *Industrial Electronics, IEEE Transactions on* , vol.57, no.1, pp.107,121, Jan. 2010

85. Jiabin Wang; Xibo Yuan; Atallah, K., "Design Optimization of a Surface-Mounted Permanent-Magnet Motor With Concentrated Windings for Electric Vehicle Applications," *Vehicular Technology*, IEEE Transactions on , vol.62, no.3, pp.1053,1064, March 2013
86. Guohai Liu; Junqin Yang; Wenxiang Zhao; Jinghua Ji; Qian Chen; Wensheng Gong, "Design and Analysis of a New Fault-Tolerant Permanent-Magnet Vernier Machine for Electric Vehicles," *Magnetics*, IEEE Transactions on , vol.48, no.11, pp.4176,4179, Nov. 2012
87. Reddy, P.B.; Kum-Kang Huh; El-Refaie, A., "Effect of stator shifting on harmonic cancellation and flux weakening performance of interior PM machines equipped with fractional-slot concentrated windings for hybrid traction applications," *Energy Conversion Congress and Exposition (ECCE)*, 2012 IEEE , vol., no., pp.525,533, 15-20 Sept. 2012
88. Reddy, P.B.; EL-Refaie, A.M.; Kum-Kang Huh; Tangudu, J.K.; Jahns, T.M., "Comparison of Interior and Surface PM Machines Equipped With Fractional-Slot Concentrated Windings for Hybrid Traction Applications," *Energy Conversion*, IEEE Transactions on , vol.27, no.3, pp.593,602, Sept. 2012
89. El-Refaie, A., "Fractional-slot concentrated-windings: A paradigm shift in electrical machines," *Electrical Machines Design Control and Diagnosis (WEMDCD)*, 2013 IEEE Workshop on , vol., no., pp.24,32, 11-12 March 2013
90. Abdel-Khalik, A.S.; Ahmed, S., "Performance Evaluation of a Five-Phase Modular Winding Induction Machine," *Industrial Electronics*, IEEE Transactions on , vol.59, no.6, pp.2654,2669, June 2012
91. El-Refaie, A.M.; Shah, M.R., "Comparison of Induction Machine Performance with Distributed and Fractional-Slot Concentrated Windings," *Industry Applications Society Annual Meeting*, 2008. IAS '08. IEEE , vol., no., pp.1,8, 5-9 Oct. 2008
92. Miller. T, J. E; 'Electronic Control of Switched Reluctance Machines', Newnes, 2001
93. Vagati, A.; Boazzo, B.; Guglielmi, P.; Pellegrino, G., "Ferrite assisted synchronous reluctance machines: A general approach," *Electrical Machines (ICEM)*, 2012 XXth International Conference on , vol., no., pp.1315,1321, 2-5 Sept. 2012
94. Ishii, S.; Hasegawa, Y.; Nakamura, K.; Ichinokura, O., "Characteristics of novel flux barrier type outer rotor IPM motor with rare-earth and ferrite magnets," *Renewable Energy Research and Applications (ICRERA)*, 2012 International Conference on , vol., no., pp.1,4, 11-14 Nov. 2012
95. Bianchi, N., "Synchronous reluctance and interior permanent magnet motors," *Electrical Machines Design Control and Diagnosis (WEMDCD)*, 2013 IEEE Workshop on , vol., no., pp.75,84, 11-12 March 2013
96. Barcaro, M.; Bianchi, N., "Interior PM Machines using Ferrite to Replace Rare-Earth Surface PM Machines," *Industry Applications*, IEEE Transactions on , vol.PP, no.99, pp.1,1, 0
97. Talebi, S.; Niazi, P.; Toliyat, H.A., "Design of Permanent Magnet-Assisted Synchronous Reluctance Motors Made Easy," *Industry Applications Conference*, 2007. 42nd IAS Annual Meeting. Conference Record of the 2007 IEEE , vol., no., pp.2242,2248, 23-27 Sept. 2007
98. Trickey, P. H., "Performance Calculations on Polyphase Reluctance Motors (Synchronous Motors Without Field Excitation)," *American Institute of Electrical Engineers*, Transactions of the , vol.65, no.4, pp.191,193, April 1946

99. Lawrenson, P.J.; Mathur, R. M.; Murthy Vamaraju, S.R., "Importance of winding and permeance harmonics in the prediction of reluctance-motor performance," *Electrical Engineers, Proceedings of the Institution of* , vol.116, no.5, pp.781,787, May 1969
100. Lawrenson, P.J.; Agu, L.A., "Theory and performance of polyphase reluctance machines," *Electrical Engineers, Proceedings of the Institution of* , vol.111, no.8, pp.1435,1445, August 1964
101. Lawrenson, P.J.; Agu, L.A., "Reluctance machines," *Electronics and Power* , vol.10, no.8, pp.264,265, August 1964
102. Zhu, Z.Q.; Howe, D., "Electrical Machines and Drives for Electric, Hybrid, and Fuel Cell Vehicles," *Proceedings of the IEEE* , vol.95, no.4, pp.746,765, April 2007
103. Miller, T.J.E.; Hutton, A.; Cossar, C.; Staton, D.A., "Design of a synchronous reluctance motor drive," *Industry Applications, IEEE Transactions on* , vol.27, no.4, pp.741,749, Jul/Aug 1991
104. Staton, D.A.; Deodhar, R.P.; Soong, W.L.; Miller, T.J.E., "Torque prediction using the flux-MMF diagram in AC, DC, and reluctance motors," *Industry Applications, IEEE Transactions on* , vol.32, no.1, pp.180,188, Jan/Feb 1996
105. Staton, D.A.; Miller, T.J.E.; Wood, S.E., "Maximising the saliency ratio of the synchronous reluctance motor," *Electric Power Applications, IEE Proceedings B* , vol.140, no.4, pp.249,259, Jul 1993
106. Betz Robert Eric, 'Modeling and Control of Synchronous Reluctance Machines', *Control in Power Electronics Selected Problems*, Academic Press, USA, 251-299 (2002)
107. I. Boldea, 'Reluctance Synchronous Machines and Drives', Clarendon Press, 1996

Chapter 2

Motor Concept Development

This chapter outlines the key considerations in developing a novel machine to advance synchronous reluctance motor technology. The aim is to explore the possibilities and set the course for the design of a prototype machine.

2.1 Alternative Winding Arrangements

In developing a synchronous reluctance motor concept that advances the technology and performance of such machines, different stator winding arrangements are briefly explored. Here, the stator topology and different winding types are investigated as the two rotor types, the transversely laminated (TLA) and axially laminated types (ALA), have been the source of intensive and comprehensive research in the past. In addition, the literature consists solely of polyphase distributed winding stator synchronous reluctance motors and in industry the stator stampings are usually those designed for caged induction motors. Firstly the use of *Fractional Conductor Windings* to fine tune machine performance is briefly explored, then a *Toroidal Stator Winding* arrangement is considered and finally the use of *Fractional Slot-Concentrated Windings* is considered and advocated for further investigation. A detailed further investigation into the use of Fractional Slot Concentrated Windings in Synchronous Reluctance Machines is then presented.

2.1.1 Fractional Conductor Windings

The essence of Fractional Conductor Windings [1-3] is to enable the machine designer to have increased control over the harmonic content of the airgap flux density. This is achieved by not constraining the mean number of conductors per slot to a positive integer. By assigning differing numbers of conductors from the same phase to different slots, it is possible to achieve the condition where the mean number of conductors per slot is fractional. This simply means that coils having different number of integer conductors can be used in a phase group of coils. This way the airgap magneto-motive force (MMF) can be finely controlled so that the magnitudes of applicable field harmonics can be further

refined. Fine tuning through the use of fractional conductor windings can positively affect both the magnetising and leakage reactances of the machine, through control of the winding factors. This type of winding is essentially identical in construction to a conventional distributed winding which has long end windings. Figure 2.1 shows the distributed winding topology where the coils follow the periphery of the stator core-back through one rotor pole pitch if the coils are of the fully pitched type, this is slightly shorter if the coils are short pitched.

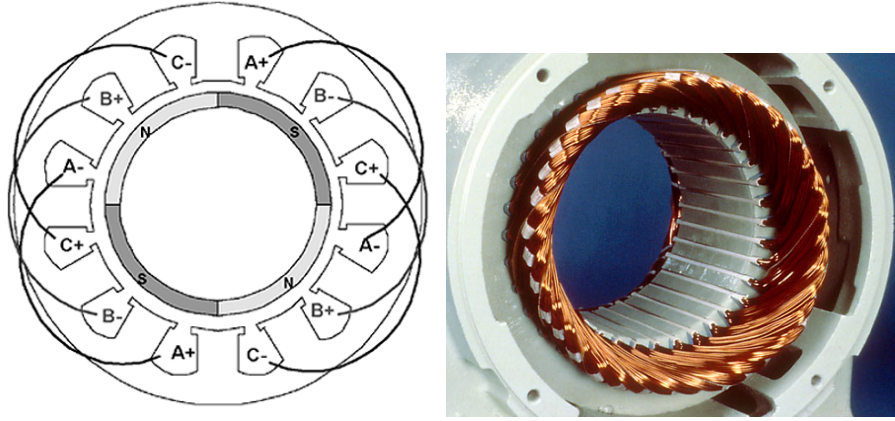


Figure 2.1: Four pole distributed winding [13] and over-lapping end windings [29]

There is very little literature on the fractional conductor winding, Figure 2.2 shows the layout of the *Fractional Conductor Winding* in one phase group with different turns per coil.

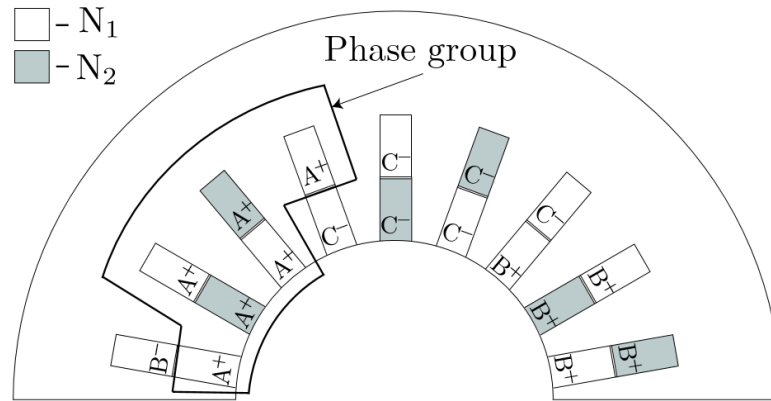


Figure 2.2: A stator of a two pole machine with a fractional conductor winding [1]

In Figure 2.2 some coils have a number of turns N_1 and some with N_2 turns. In an m phase fractional conductor winding the number of slots per pole per phase q can be expressed [1];

$$q = q_1 + q_2 = \frac{Q_s}{2mp} \quad (2.1)$$

Where q_1 is the number of coils in half a slot with N_1 turns, q_2 the number of coils in half a slot with N_2 turns, implying a double layer winding and the number of pole pairs of the winding p . The effective or mean number of conductors per slot for a winding with number of layers n_l can be defined [1];

$$N_{se} \triangleq n_l \frac{q_1 N_1 + q_2 N_2}{q} \quad (2.2)$$

Conventionally, distributed windings are simply defined by the number of slots per pole per phase and the value is either fractional or an integer;

$$q = \frac{Q_s}{2mp} \in \mathbb{Q} \quad (2.3)$$

With a fractional conductor winding, the shape of the airgap MMF wave can be finely adjusted, giving a more sinusoidal distribution and leading to reduced harmonic content or acting to increase the fundamental winding factor. However, if a fractional conductor winding is inappropriately selected, even harmonics could potentially occur. In [1] the theoretical details such as the airgap MMF harmonics, winding factors and applicable windings are discussed. Leakage inductances are explored in [2] and the design process in [3]. Here, it is sufficient to summarize the main findings based on the literature;

- Use of fractional conductor windings can minimize the spatial harmonics spectrum of a winding
- In some cases a marginally higher fundamental winding factor can be achieved
- Even harmonics can be generated if irregular phase group patterns are used
- High performance achieved with the q_2 coils placed either side of the phase group [1]

From the geometry of the winding, there are a number of observations –

- End winding length is linked to the rotor pole pitch and the winding chording
- The coils are overlapping
- The coils are complex in geometry and numerous and therefore are difficult to manufacture when compared to simpler coil types
- Conductors are distributed sinusoidally around the airgap periphery

Therefore, although fine tuning of the machine parameters may be possible with fractional conductor windings, the overall scheme of the winding remains identical to that of the conventional distributed winding (long overlapping end windings). As an example (taken from [1]), a two pole $p = 1$ machine with $Q_s = 36$ is considered. The best arrangement is chosen such that the q_2 coils are placed either side of the phase group. With $N_1 = 2$ and

$N_2 = 1$ and for $q = 6$ and $q_2 = 2$, an effective or mean number of conductors per slot is calculated as $N_{se} = \frac{10}{3}$, the winding factors are compared to a conventional winding of $q = 6$ in Table. 2.1.

	Conventional	Fractional Conductor	Change
q	6	6	-
q_2	0	2	-
k_{w1}	0.956	0.97	+1.46%
k_{w5}	0.19	0.35	+84.20%
k_{w7}	0.14	0.02	-92.85%
k_{w11}	0.11	0.13	+18.18%
k_{w13}	0.09	0.05	-44.44%

Table 2.1: Comparison of conventional and fractional conductor windings

From Table 2.1 it is easy to see that the machine will have a higher torque producing capability as the fundamental winding factor has been increased, although only by 1.46%. However, the 5th and 11th harmonics have increased, though the 7th and 13th have reduced. Different configurations give differing results, but with such minor gains possible and some associated drawbacks, including increased manufacturing processes, this type of winding is questionable for advancing SynRM technology. In this winding, the long end turns still exist and overlap. They are required to be manufactured in the same manner as a conventional winding, making the changes have a minimal effect on machine performance, cost or manufacturability. The fill factor is identical to that of conventional windings, around $S_{FF} \approx 0.35$, the net gains are very low, at the expense of a more complicated winding procedure.

2.1.2 Toroidal Windings (Gramme-Ring Winding)

Another type of winding, that is non-overlapping and has short end windings, is the toroidal winding [4] or Gramme-Ring winding, in which a coil is wrapped toroidally around the core-back of the machine. This type of winding was first presented in 1968 in a patent [5] for induction machines and subsequent work has shown its effectiveness [6]. Toroidal windings have also been investigated for double rotor permanent magnet machines [7] and the switched reluctance (SRM) [8] as well as having a variant often employed in axial flux machines [9]. The winding number of slots per pole per phase is to be defined identical to that of conventional distributed or fractional conductor windings;

$$q = \frac{Q_s}{2mp} \in \mathbb{Q} \quad (2.4)$$

This is because at the airgap periphery the winding appears to be a conventionally distributed winding. Figure 2.3 shows the winding topology of the *Toroidal Winding*

scheme.

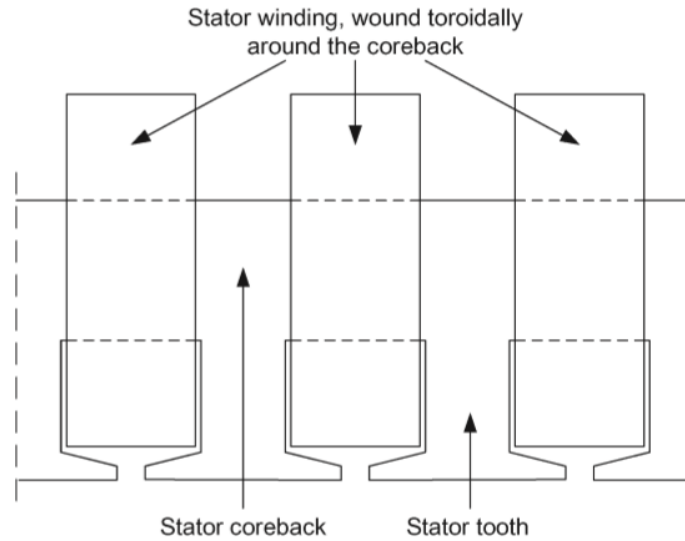


Figure 2.3: Toroidal coils wrapped around the core back [6]

From the geometry of the winding, there are a number of observations –

- End winding length is linked to the coreback depth and hence the rotor pole number
- The outer diameter of the machine is increased to accommodate the conductors and a special casing will be required (for the return conductors)
- Conductors appear as distributed windings at the stator bore – maintaining winding factor and low space harmonic MMF content
- The stator leakage inductance will increase due to stray fields of the return conductors

It is not immediately obvious that short end windings exist when compared to the distributed winding. Although the coils are similar to the fractional slot concentrated winding (see Section 2.1.3), if applied to a machine with a traditional aspect ratio (outer diameter < stack length) the inactive part of the winding around the core-back is longer than the active part of the winding. However, if the aspect ratio of the machine is changed to a more suitable 'pancake' type (outer diameter > stack length), it has been shown that a smaller overall stator phase resistance can be achieved than would be possible with distributed windings [4,6], leading to lower coil length and copper loss. The outer diameter of the machine is required to be increased due to the return path conductors, which is a disadvantage and a special stator core insertion technique/arrangement will be required as to not damage those bundles of conductors.

Only odd harmonics exist in the MMF and airgap waveforms due to the quasi-distributed nature of the conductors/coils. Here, any even harmonics are eliminated. The toroidal

winding could potentially increase machine efficiency though copper loss reductions, but increased manufacturing and limited applicable aspect ratios are a major hindrance to this type of winding. The leakage factor of the machine would be expected to increase due to stray fields caused by the return conductors, these also have the possibility of interacting strongly with any casing causing eddy current losses. The fill factor is again identical to that of conventional and fractional conductor windings, around $S_{FF} \approx 0.35$, but with more complicated manufacture and application limitations.

2.1.3 Fractional Slot-Concentrated Windings

Fractional Slot-Concentrated Windings are another alternative topology to the conventional technology. Here, like the toroidal winding, short end windings result as the coils are wrapped around a single tooth. Thus, the end winding spans a tooth pitch rather than a whole rotor pole pitch, tending to reduce both winding mass and copper loss. The synchronous reluctance motor has, in the literature, consisted solely of poly-phase distributed wound stators [10-12]. PM based machines and SRM drives typically utilize fractional slot-concentrated windings (FSCW) due to their inherent advantages [13]. Many PM machine designs have been presented [14,15] with one IM being presented [16] and SRM technology having this winding type as a fundamental aspect of their conventional topology [17]. The winding number of slots per pole per phase is defined as a fractional number less than unity;

$$q = \frac{Q_s}{2mp} \in \mathbb{Q} < 1 \quad (2.5)$$

Both single and double layer fractional slot concentrated windings can be constructed. Figure 2.4 shows the winding topology of the *Fractional Slot-Concentrated Winding*.

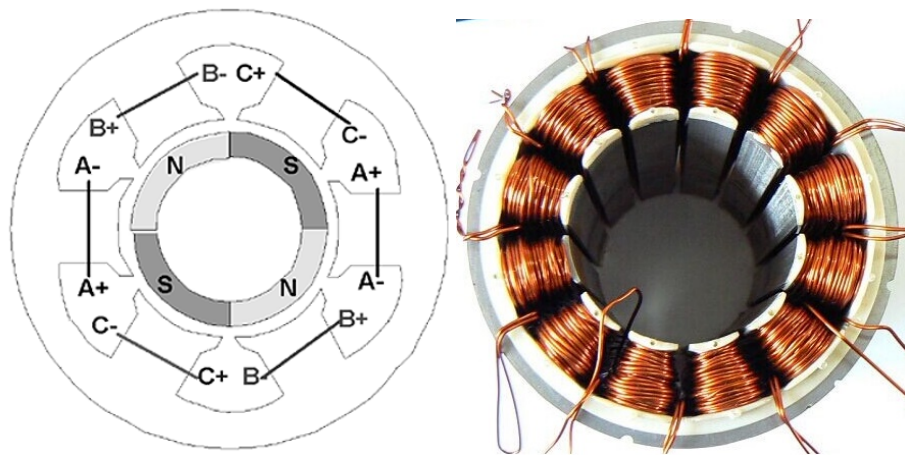


Figure 2.4: Four pole double layer fractional slot-concentrated winding [13] and short end windings [30]

From the geometry of this type of winding, there are a number of observations –

- End winding length is linked to the tooth width and radius of the coil from the shaft centreline
- The coils are non-overlapping
- The coils are simple in geometry and therefore are easier to manufacture compared to distributed windings
- Conductors are discretely placed around the airgap periphery and non-sinusoidally distributed

With a fractional slot concentrated winding, the shape of the airgap MMF is far from sinusoidal and it is possible that even harmonics exist [13]. In addition to the even harmonics, higher magnitude odd harmonics can exist in some windings, increasing the level of parasitic effects with this winding type. Despite the disadvantage of increased harmonic content, the achievable fill factor is typically above 55%, as opposed to the conventional fill factor of distributed, fractional conductor and toroidal windings between 30-35%. This could decrease the copper loss in the machine, improving efficiency and torque density. Manufacturing is simpler than with distributed windings, and therefore less laborious and, costly and the coils are non-overlapping. Thus this winding type also has increased resilience to phase to phase shorts due to their non-overlapping coils. A synchronous reluctance motor with fractional slot-concentrated windings is termed a *cSynRM* in this thesis.

2.1.4 Comparison and Conclusion

Three windings types have been briefly explored in relation to improving the synchronous reluctance motor, these are the Fractional Conductor (FCW), Toroidal (TW) and Fractional Slot-Concentrated windings (FSCW). The fractional conductor winding requires a laborious winding process, just as the conventional distributed winding. The slot fill factor is low and gains in performance are minimal and tuning one harmonic often increases another so this winding does not offer any substantial gains. The toroidal winding is arguably simpler to wind than the conventional distributed winding as the coils are wrapped around the core-back and there is potential to reduce copper losses, and has a low MMF space harmonic content. However, complicated casing arrangements with increased difficulty in manufacturing/assembly are required, coupled with a low fill factor. This winding type requires more investigation for application to SynRM technology but is not the winding of choice in this thesis. The fractional slot concentrated winding on the other hand has short end turns leading to low copper loss, a high fill factor, simple manufacturing with the possibility of novel stator constructions and lower material & manufacturing costs. The drawback of the fractional slot concentrated winding is the increased space harmonic content in the airgap. This winding type is interesting in relation to high efficiency machines. Table. 2.2 presents a summary of the three windings

and conventional distributed windings (DW) in order to facilitate a decision for further investigation.

	DW	FCW	TW	FSCW
Fund. Winding Factor, k_{w1}	+++	+++	+++	++
Harmonics, k_{wv}	+++	++++	+++	+
Fill Factor, S_{FF}	+	+	+	+++
End Length, l_{end}	+	+	++	+++
Manufacturing	+	+	+	+++
Perceived Cost	+	+	++	++
Maturity	+++	+	+	++

Table 2.2: Comparison of selected winding types

Based on Table 2.2, the Fractional Slot-Concentrated Winding is chosen as the topic of further investigation. This is due to its perceived benefits over the other types and its continued applicability to other machine types, making it a viable alternative to the distributed winding in future synchronous reluctance motors.

2.2 General Winding Considerations

In this section, considerations as to improving the machine with respect to applying fractional slot concentrated windings are discussed briefly as a forerunner to a more detailed investigation into the application of this winding type to synchronous reluctance motors.

2.2.1 Machine Losses

The two main loss mechanisms in synchronous reluctance motors are the iron loss and the stator copper loss (neglecting friction, windage and stray losses). In a given m -phase machine;

$$P_{Cu} = mI_s^2 \left(\frac{N_s l_{av}}{\sigma_e A_s} \right) \quad (2.6)$$

Where I_s is the phase current and R_{ph} is the phase resistance, here N_s is the number of series turns, l_{av} is the average conductor length (used as all turns are not the same length due to the end windings), σ_e is the electrical conductivity of the conductor material and A_s is the solid strand area. Thus in order to reduce the loss, the phase resistance must be minimized to realize a higher efficiency machine.

2.2.2 Slot Fill Factor

The first factor governing a phase resistance decrease is the slot fill factor S_{FF} . Based on slot area and the attained fill factor, which is broadly the ratio of the amount of active

copper to the slot area A_{slot} , the strand area A_s is calculated;

$$A_s \triangleq \frac{S_{FF} A_{slot}}{N_s n_l}; \quad R_{ph} \propto \frac{1}{S_{FF}} \quad (2.7)$$

Where n_l is the number of layers and N_s is the number of series turns per phase. Here it must be noted that the fill factor, $0 < S_{FF} < 1$, with usual values between 0.3 - 0.4 for conventionally wound distributed coils. The per-phase copper loss can then be expressed as;

$$P_{Cu} \propto \frac{1}{S_{FF}} \quad (2.8)$$

Therefore the stator copper loss can be reduced significantly by achieving ever higher slot fill factors. A higher fill factor means that the conductor area can be increased and thus reduce the effective resistance of a phase. From Eq. 2.8, Figure 2.5 shows the decrease in copper loss with achieved fill factor within a achievable range.

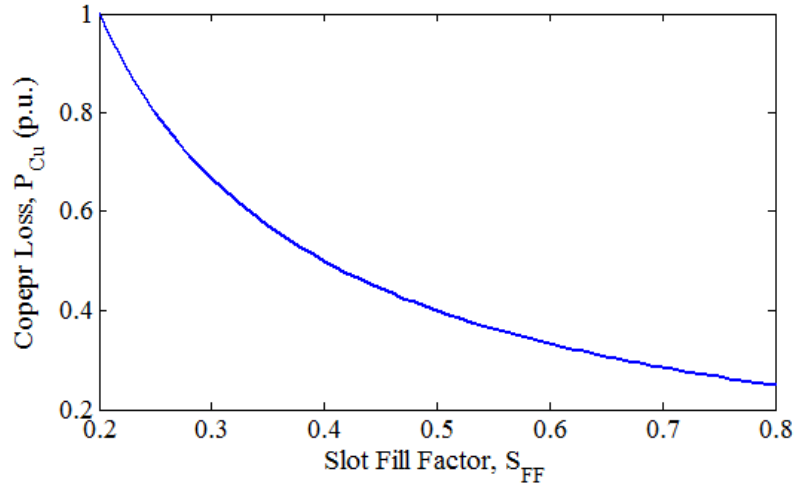


Figure 2.5: Fill factor effect on copper losses

So, by increasing the fill factor from 0.35 to 0.6, the winding loss can be theoretically reduced by 45%, which is a significant saving. With concentrated windings, is it possible, if bobbin wound, to achieve a fill of 60%, with further improvements being made by using concentrated windings with a segmented stator up to 85% fill factor [13]. A segmented stator consists of individual sections of coreback rather than the traditional continuous coreback, such that the segments can be wound and assembled afterward, facilitating a high fill factor with neat and tightly wound coils. Increased fill factors, if practically achievable in a synchronous reluctance machine topology, could provide an excellent means of increased efficiency. Seven industrial induction motors were examined in [18] and the slot fill measured, it was concluded that a reasonable value for the slot fill for an industrial induction motor from between 4 to 55kW is in the region of 0.35 to 0.45.

2.2.3 End Windings

End windings are an important consideration: they are copper masses with a resistance that contributes to loss. However, these are not active parts of the winding, *i.e.* they do not contribute to torque production but rather provide a channel for the torque producing current around the exterior portion of the machine. Coil windings have an axial length and also an average end turn length:

1. *Axial length* - conductor length in slot used in torque production.
2. *Average End Length* - current return path with unwanted heat losses that are difficult to dissipate, leading to end winding hot-spots.

Distributed windings, whether fully pitched or chorded, inherently have long end windings due to the geometry of the machine and coil placements. The end winding of a distributed winding machine generally spans one rotor pole pitch τ_p :

$$\tau_p = \frac{\pi D_\delta}{2p} \quad (2.9)$$

Where D_δ is the airgap diameter. These types of windings usually require a large number of slots and coils, distributed around the periphery of the stator so that a sinusoidal MMF distribution can be realized. It is possible to utilize single tooth windings, *i.e.* those that a single coil spans only one stator tooth pitch τ_u ;

$$\tau_u = \frac{\pi D_\delta}{Q_s} \quad (2.10)$$

Where Q_s is the number of stator slots. Typically, the end winding length in single tooth coiled machines is less than that of the equivalent distributed winding. Therefore, if the mean end winding length can be reduced, this provides a mechanism to decrease loss further. To do this, the synchronous reluctance motor could migrate from distributed windings to single tooth concentrated windings (defined in this theses as non-overlapping fractional slot concentrated windings), where the shorter end windings can be obtained. For a given number of series turns in a coil N_{sc} , the average winding length of that coil is can be written as follows;

$$L_{coil} = 2N_{sc}(l_{axial} + l_{end}) \quad (2.11)$$

The lengths l_{axial} and l_{end} are the stator stack length and mean end turn length respectively. For an m phase machine with n -series coils/phase, the winding loss can be expressed;

$$P_{Cu} = 2mnI_s^2 \left(\frac{1}{\sigma_e S_{FFA_{slot}}} \right) N_{sc}^2 (l_{axial} + l_{end}) \quad (2.12)$$

So reducing the end winding length linearly reduces the machine copper loss further, increasing machine efficiency if identical mechanical output can be achieved.

2.2.4 Winding Mass / Conductor Material

The two loss reduction methods described in Sections 2.2.2 and 2.2.3 have the effect of increasing and decreasing the machine mass respectively. For the mass of stator winding copper in the machine m_{Cu} :

$$m_{Cu} = N_c \rho_{Cu} V_{Cu} = N_c \rho_{Cu} A_s L_{coil} S_{FF} \quad (2.13)$$

Where N_c is the number of coils, ρ_{Cu} is the mass density of copper (or any other winding material) and V_{Cu} the volume of a coil. So if the fill factor is increased, the winding mass is increased due to the increased copper in the machine. In some applications this may be undesirable, and the fill factor would be required to be limited based on the maximum allowable mass of the machine. This said, if shorter end windings are achieved, the L_{coil} length is reduced, linearly reducing the mass of the copper, thus depending on the types of coils, the attainable fill factor, geometry and winding processes, the winding mass can increase or can be made to remain constant, and in some cases could possibly be decreased, even with an increased fill factor. If low mass with increased fill is desired, another option is to use an alternative conductor material. The product of resistivity and mass density of materials are important in this conductor materials consideration. Resistivity-mass density products of common metals are presented in Table 2.3.

Material	Resistivity	Mass Density	Resistivity-density product
	$\text{n}\Omega \cdot \text{m}$	$\text{kg} \cdot \text{m}^{-3}$	$\text{n}\Omega \cdot \text{kg} \cdot \text{m}^{-2} \times 10^{-3}$
Aluminum	28.24	2700	76.24
Magnesium	43.90	1740	76.38
Copper	16.78	8960	150.34
Iron	96.1	7874	757

Table 2.3: Resistivity-density products

From the table, Aluminum is likely the metal of choice when the mass a major consideration for a given application. Aluminum is more plastic than copper, it has a lower cost and a lower mass density, but lacks electrical conductivity when compared to copper. The electrical conductivity for aluminum based wire is $\sigma_{Al} \approx 36 \times 10^6 \text{S} \cdot \text{m}^{-1}$, compared to copper wire of $\sigma_{Cu} \approx 59 \times 10^6 \text{S} \cdot \text{m}^{-1}$. Now, if the fill factor is incorporated in comparison of copper and aluminum materials for windings, the ratio of a resistance of a winding is (the length and slot area will remain the same, and using typical conductivity values);

$$\frac{R_{Al}}{R_{Cu}} = \frac{\sigma_{Cu} S_{FF(Cu)}}{\sigma_{Al} S_{FF(Al)}} = 1.638 \frac{S_{FF(Cu)}}{S_{FF(Al)}} \quad (2.14)$$

And doing the same for the mass density;

$$\frac{m_{Al}}{m_{Cu}} = \frac{\rho_{Al} S_{FF(Al)}}{\rho_{Cu} S_{FF(Cu)}} = 0.302 \frac{S_{FF(Al)}}{S_{FF(Cu)}} \quad (2.15)$$

Therefore, for a reference copper fill, increasing the aluminum fill factor by possibly using compressed windings [19], the resistance values converge but with a decreased mass in the aluminum coil. A trade off for fill factor and mass can be determined, within the geometrical and winding process bounds of the machine, in order to design a lower mass machine or a reduced loss machine. This principle was used in a paper by the author in relation to low mass, high efficiency permanent magnet motors for solar powered aircraft [19], however does not form part of this thesis.

2.2.5 Thermal Aspect

From this point forward the conductor material is considered to be copper only. As a direct consequence of a higher fill factor, the amount of air in the slot is reduced and replaced by copper. With the thermal conductivity of air at $\lambda_{Air} \approx 0.03 \text{ Wm}^{-1} \text{ K}^{-1}$ and the relatively high thermal conductivity $\lambda_{Cu} \approx 390 \text{ Wm}^{-1} \text{ K}^{-1}$ for copper and increasing the fill factor, the effective slot thermal conductivity can increase significantly. As a first order approximation (neglecting wire insulation and slot liner), the equivalent slot thermal conductivity λ_{eff} can be written [20];

$$\lambda_{eff} = \lambda_{Air} \frac{(1 + S_{FF}) \lambda_{Cu} + (1 - S_{FF}) \lambda_{Air}}{(1 - S_{FF}) \lambda_{Cu} + (1 + S_{FF}) \lambda_{Air}} \quad (2.16)$$

Where, λ_{Cu} and λ_{Air} are the conductor material and air thermal conductivity respectively. This was validated using thermal FEA studies in the same paper [20]. Staton [18] presented a linear fit based on measured results on seven induction motors, which is also presented as a comparison in Fig. 2.6. The fit is represented as;

$$\lambda_{eff} \approx 0.1076 S_{FF} + 0.03 \quad (2.17)$$

This compares well to the slot homogenization equation, Eq. 2.20 in the region of $0.2 \leq S_{FF} \leq 0.5$, discrepancies are down to the conductor insulation and any impregnation in the actual machine winding acting to increase the equivalent slot thermal conductivity. With the thermal conductivity of air at $\lambda_{Air} \approx 0.03 \text{ Wm}^{-1} \text{ K}^{-1}$. It is evident in Fig. 2.6, which shows a comparison of the Staton linear fit and the slot homogenization approach, if the slot fill factor is increased from 35% to 60%, the slot thermal conductivity doubles, significantly reducing the winding temperature (assuming equal slot width).

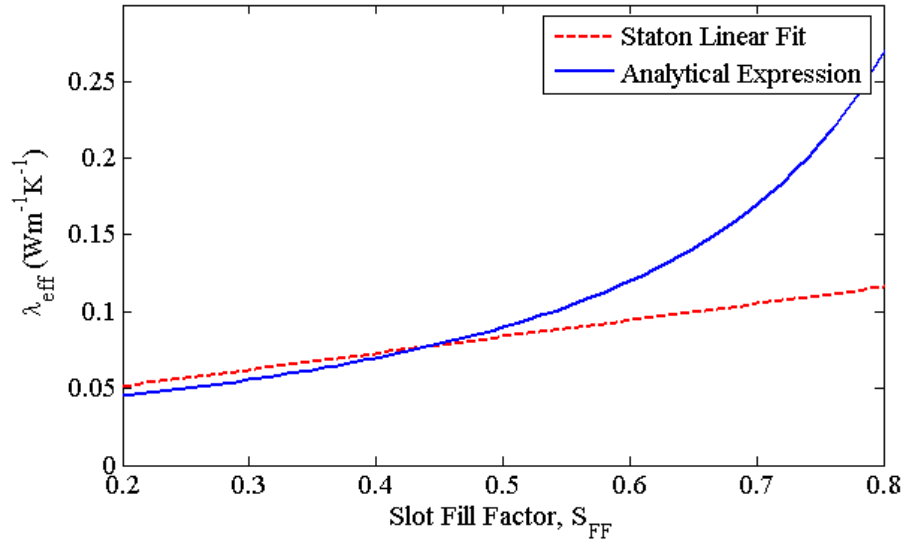


Figure 2.6: Fill factor effect on slot thermal conductivity (air cavity and copper winding)

The cSynRM can be perceived to have a potential thermal advantage over the conventional SynRM and IM if high fill factors can be achieved. However, if different slot numbers and identical stator bore are compared, the different slot widths are expected to have an effect on the slot thermal conductance. Typical thermal conductivities are presented in Table 2.4.

Material	Thermal Conductivity [$\text{W} \cdot \text{m}^{-1} \cdot \text{K}^{-1}$]	Application
<i>Air</i>	0.03	Slot filler
<i>Copper</i>	390	Conductor
<i>Aluminum</i>	237	Conductor
<i>Polyimide</i>	0.52	Strand insulation
<i>Typical Resin</i>	10	Slot filler

Table 2.4: Typical thermal conductivities of common engineering materials

The table shows that if the thermal conductivity of the wire insulation is neglected and assume air in its place, the result will be the worst case scenario effective thermal conductivity. Increasing the effective thermal conductivity by improved fill factor could allow the machine to run at higher current densities, be designed to run with lower cooling requirements or have higher overload capability.

2.2.6 Summary

In synchronous reluctance machines, increased efficiency and potentially torque density can be achieved by reducing the copper losses and operating temperature. To achieve this an increase in fill factor is desirable and lowering of the phase resistance. A fill factor increase can be fulfilled if concentrated windings are used and simultaneously the coils end turn circumferential length will reduce as well as their axial length. This winding

also allows other design options such as a longer active stack length in the frame. The increase in fill factor aids performance by reducing loss but the extra copper mass and its importance in the specific design application must be considered. If weight is a design constraint, aluminum windings can potentially be used if high fill factors can be achieved through segmented stators and compressed coils. An increased fill factor also provides a better thermal path, aiding machine cooling, and therefore reliability and operational lifetime. Lower loss and better thermal properties potentially allow increased phase currents leading to higher torque density. These benefits would be an advantageous addition to the synchronous reluctance machine applied to either industrial applications or other specialist applications where high efficiency and torque dense motors are required.

2.3 Application of FSCW to the SynRM

In this section a qualitative exploration into the adoption of fractional slot concentrated winding is presented. This focuses upon the available topologies, the advantages and disadvantages and draws conclusions as to the route forward for designing a prototype synchronous reluctance motor with fractional slot concentrated windings.

2.3.1 Fundamental Topology

As mentioned earlier, fractional slot concentrated windings have a coil span of a single stator tooth, rather than spanning a whole rotor pole in a fully pitched distributed machine. Figure 2.7 shows the distributed and fractional slot concentrated winding topologies.

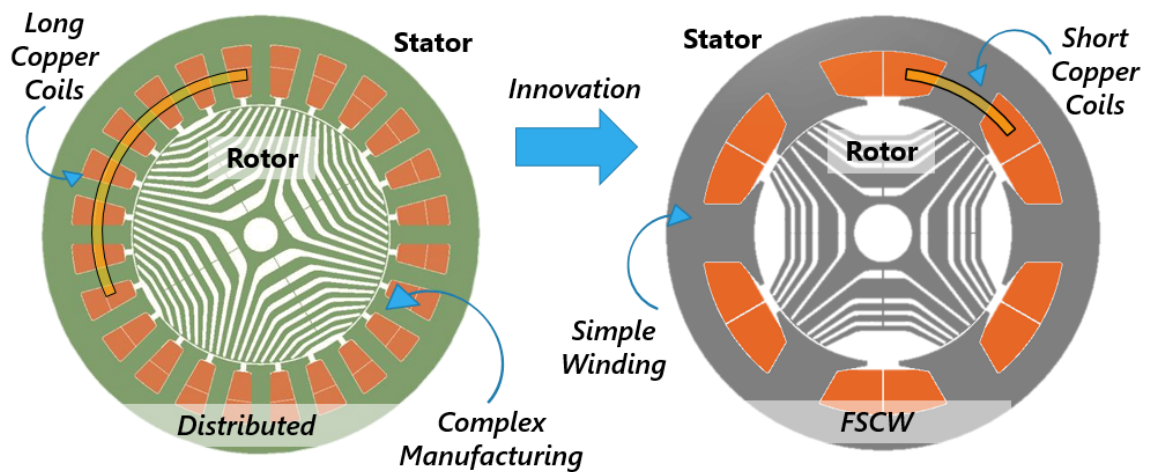


Figure 2.7: Distributed and FSCW winding topologies

Conventional SynRMs utilize polyphase distributed windings because they are traditionally associated with the induction machine; this SynRM technology possesses advantages over the induction machine under certain conditions, but they both have some undesirable characteristics which can be partially eliminated by fractional slot concen-

trated windings. A comparison of the windings, based on the detailed argument in [13], follows in Table 2.5;

	FSCW	Distributed
<i>Fill Factor</i>	55%-85%	35%-45%
<i>Stator Structure</i>	Continuous/Segmented	Continuous
<i>Overlapping Phases</i>	No	Yes
<i>End Winding Average Length</i>	Short	Long
<i>Winding Complexity</i>	Lower	Higher
<i>Spatial MMF Harmonics</i>	High	Low
<i>Winding Factors</i>	Lower	Higher

Table 2.5: FSCW vs. Distributed Winding

The long end windings in the distributed winding, caused by large coil spans, lead to extra copper that is inactive in torque production but contributes to machine mass, cost and copper loss. This is coupled with the low fill factor achieved with this winding type, lowering torque density and efficiency, as well as providing a low quality thermal path for the dissipation of heat. If a fractional slot concentrated winding machine of the same size could achieve identical electromagnetic performance, the machine would inherently have higher efficiency and lower mass due to very short coil spans reducing the end windings whilst facilitating increased copper fill factors. Such a machine could then potentially be designed to have a higher torque density, coupled with easier manufacturing and potentially lower cost. It appears that a synchronous reluctance machine equipped with fractional slot concentrated windings is an attractive proposition.

2.3.2 Single vs. Double Layer

FSCW can be of either single or double layer type. The topological difference is that in a single layer winding, only one coil side is in one slot at any one location and the double layer winding has two coil sides per slot. A comparison of FSCW in single and double layer configurations [13] is presented in Table. 2.6.

	Single Layer	Double Layer
<i>Coil Sides / Slot</i>	1	2
<i>End Turns</i>	Longer	Shorter
<i>Slot/Pole Combinations</i>	Limited	Many
<i>Ease of Manufacture</i>	V. Good	Good
<i>MMF Harmonic Content</i>	More	Less

Table 2.6: Single Layer vs. Double Layer

Therefore, a double layer FSCW has the greatest potential to realize the maximum

benefit from the transition to fractional slot concentrated windings. Single layer windings would generally be considered in a fault tolerant machine design as the coils remain non-overlapping and phase-to-phase shorts are eliminated with one coil side per slot.

2.3.3 Winding End Region Lengths

2.3.3.1 Average End Turn Length

As the coil span of fractional slot concentrated windings is typically shorter than in distributed windings, the average end turn can be expected to be shorter also. In [21] equations based on empirical observations relating to the end winding lengths l_{end} were presented for distributed and double layer fractional slot concentrated windings. These are approximated;

$$l_{end} = \begin{cases} 1.6 \left(\frac{2\pi r_w}{2p} \right) & \text{--Distributed} \\ 0.93 \left(\frac{2\pi r_w}{Q_s} \right) & \text{--FSCW} \end{cases} \quad (2.18)$$

Where r_w is the mean coil radius of the winding. The numerical constants are derived from the empirical investigations of a number of manufactured distributed and fractional slot concentrated windings. In distributed winding machines, the average end turn length is a reciprocal function of the pole-pairs p , however in the single tooth wound machine it is a reciprocal function of the number of stator teeth Q_s . Therefore, with the rotor pole span larger than the tooth span, the average end turn length is lower in the double layer fractional slot concentrated winding, reducing loss, mass and cost.

2.3.3.2 End Winding Axial Extent

Single tooth windings do not have the same end winding geometry as distributed windings and thus may allow a greater active stack length for the same frame size. To accomplish this the end winding axial extent¹ must be lower than in the distributed winding machine, as illustrated in Figure 2.8. The figure shows two machines with identical outer diameters, one with distributed windings with overlapping coils and one with fractional slot concentrated windings. If increased active length can be fitted into the same frame size, this linearly increases the torque capability of the machine. For fractional slot concentrated windings, if the end winding is assumed to be semi-circular, the axial extent of the end winding can be estimated by;

$$l_{axial,end} \approx \frac{l_{end}}{\pi} \quad (2.19)$$

The mean end turn length (mean turn circumference) of a single stator coil. Therefore, based on the short coil spans of this type of winding, based on experience it is reasonable

¹Length of the end winding perpendicular to and from the edge of the lamination stack

to say that the $l_{axial,end}$ for the double layer fractional slot winding is shorter than that of the distributed winding.

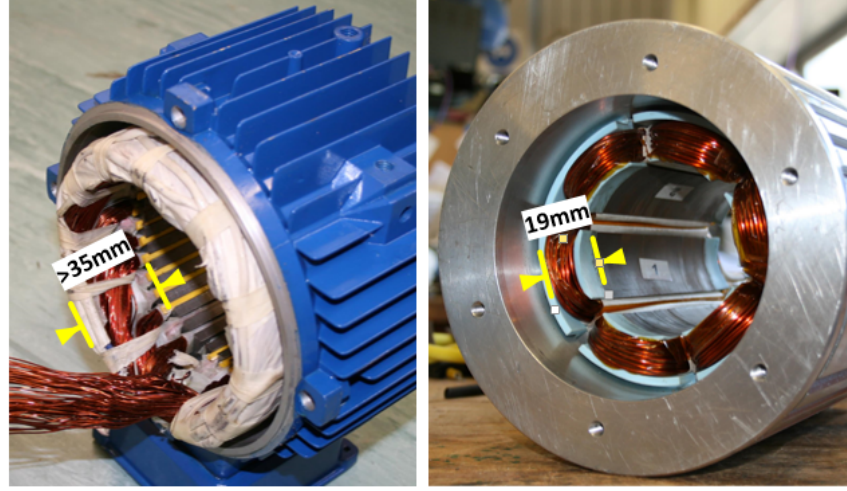


Figure 2.8: Comparison of end winding axial extents between distributed and FSCW

2.3.4 Winding Factors and MMF Harmonics

With the associated benefits of FSCW, challenges also arise when applying fractional slot concentrated windings to synchronous reluctance machines. The root cause of these is the high space harmonic content due to the discrete placement of coils around the airgap periphery, which are no longer sinusoidally distributed. Fractional slot concentrated (FSCW), fractional slot distributed (FSDW) and integer slot distributed (ISDW) can be categorised by the number of slots/pole/phase, q , (considering a three phase machine);

$$q = \frac{Q_s}{6p} = \frac{z}{n} = \begin{cases} \in \mathbb{Q} < 1 & \text{—Fractional Slot Concentrated} \\ \in \mathbb{Q} \geq 1 & \text{—Fractional Slot Distributed} \\ \in \mathbb{Z} & \text{—Integer Slot Distributed} \end{cases} \quad (2.20)$$

FSCW's are defined here as windings that span a single tooth, they are also known as tooth-coil windings. This type of winding can be split into Grade I and Grade II windings, based upon whether the denominator n , in Eq. 2.20 is even or odd [22]. The grade determines the harmonic ordinates of the winding, dictating the winding factors and MMF harmonic spectra, which can be calculated analytically. The applicable harmonics v generated by the winding are defined as [23];

$$v = \begin{cases} \pm \frac{1}{n} (2mg + 2) & -n \in \text{odd} \\ \pm \frac{1}{n} (2mg + 1) & -n \in \text{even} \end{cases} \quad g = \pm 0, \pm 1, \pm 2 \dots \quad (2.21)$$

In machines that have a slot/pole/phase of 0.5 or lower, the main flux path in the air gap region over one rotor pole pitch may consist of one slot and one tooth or less. Thus, the flux distribution can be asymmetrical, manifesting significant space harmonic content

which can be even or odd, causing parasitic effects in the machine. Sub-harmonics exist in certain slot-pole combinations (if the numerator, $z \neq 1$), contributing heavily to the iron losses in the machine. Reduction of these MMF space harmonics may be possible by using an 4+ layer winding with tooth-wound coils [24], but this is not considered further in this thesis.

2.3.4.1 Winding Factor Comparison

The corresponding winding factor equations for the winding grades for harmonic v are calculated [22];

$$\xi_v = \begin{cases} \sin\left(\frac{\pi p}{Q_s}\right) \cdot \frac{\sin\left(\frac{v\pi}{2m}\right)}{nq \sin\left(\frac{v\pi}{2mnq}\right)} & \text{—Grade I} \\ \sin\left(\frac{\pi v}{2}\right) \cdot \sin\left(\frac{v\pi}{2m}\right) \cdot \frac{\cos\left(\frac{v\pi}{Q_s}\right)}{nq \sin\left(\frac{v\pi}{2mnq}\right)} & \text{—Grade II} \end{cases} \quad (2.22)$$

Usually, all windings that have a fundamental winding factor of 0.866 and above are considered for use. The winding factors are also readily calculated for integer slot and fractional slot windings. As the conventional synchronous reluctance motor is typically of the 4 pole type, here a winding consisting of 36 stator slots, $Q_s = 36$, is considered, both fully pitched and short pitched by one & two slots, the harmonic winding factors are presented in Figure 2.9. Figure 2.10 shows the winding factors for an equivalent 4-pole fractional slot concentrated winding, consisting of 6 stator slots, $Q_s = 6$.

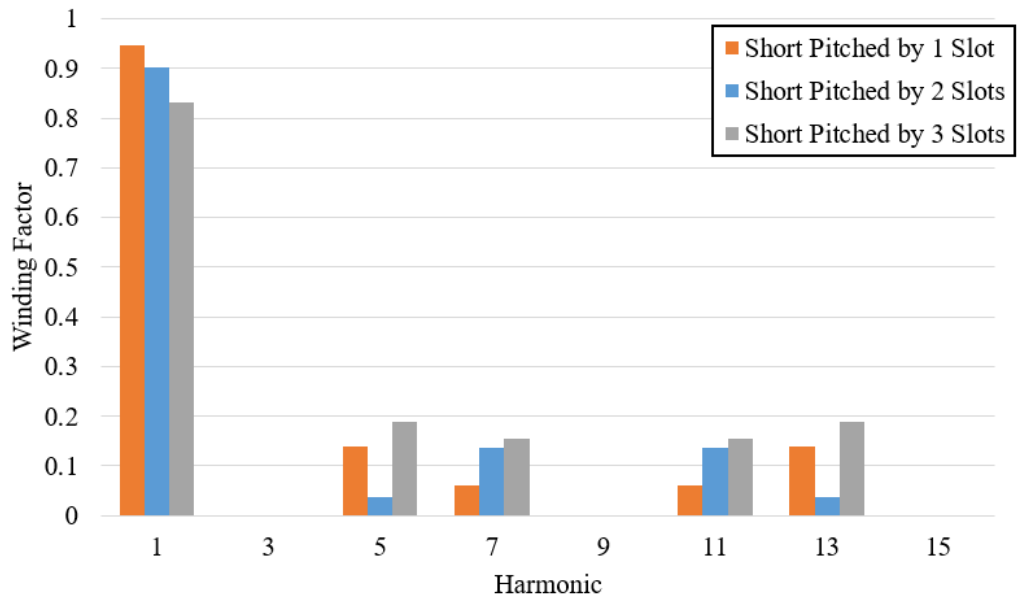


Figure 2.9: Winding factors of double layer distributed winding, $Q_s = 36$ & $p = 4$

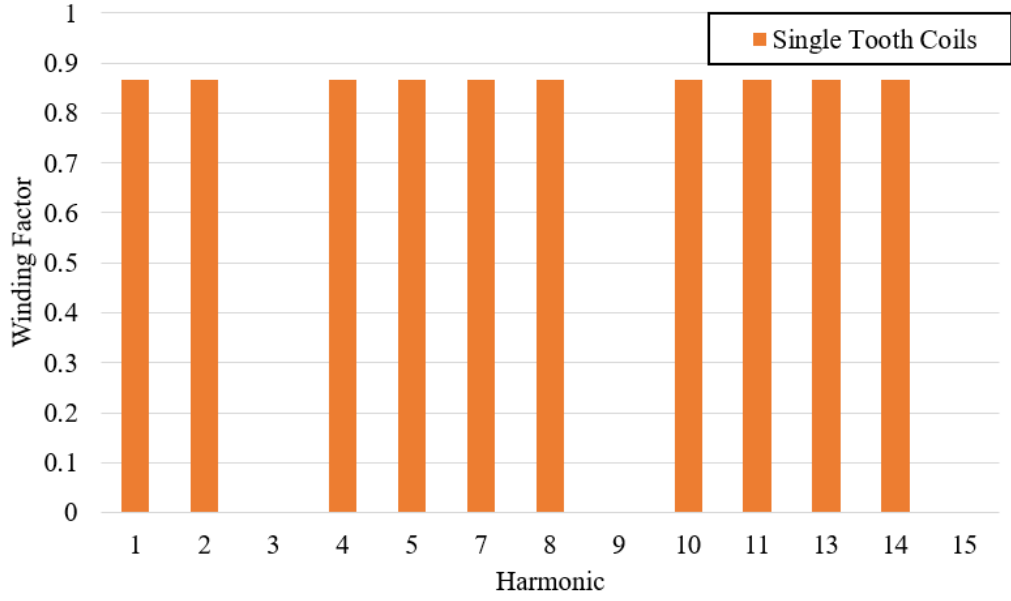


Figure 2.10: Winding factors of double layer FSCW, $Q_s = 6$ & $p = 4$

In the concentrated winding the winding factors are constant with harmonic ordinate - leading to high space harmonic content, which is presented in a subsequent section.

2.3.4.2 Applicable Slot-Pole Combinations

The dq inductances are of great importance in the synchronous reluctance machine: it is important that L_d is maximized and L_q is minimized. There is however another consideration required, most synchronous reluctance machines in the literature have a number of pole pairs ≤ 2 . This is due to a detail in the expressions for the dq magnetizing inductances $L_{md,q}$ [23], here the number of pole pairs p is considered (ignoring magnetic saturation);

$$L_{md,q} = \frac{mD\delta}{\pi p^2 \delta_{eff(d,q)}} \mu_0 l' (\xi_{w1} N_s)^2 \quad (2.23)$$

Here $\delta_{eff(d,q)}$ is the effective airgap for the axis, $l' = L_{stack} + 2g$ which is the effective core length (g is the airgap length) and ξ_{w1} is the fundamental winding factor. In the literature, the vast majority of machines considered are of the four pole type. The four pole type is suggested as the best balance between performance and manufacturability. For concentrated windings $q < 1$, the available slot pole combinations are presented in Table 2.7. For low pole numbers, the number of slot pole-combinations that allow fractional slot concentrated windings is small. These have fundamental winding factors of maximum 0.866 which is usually considered to be the minimum requirement for consideration of the application of a winding. The lower winding factor will limit the torque capability of the machine, when compared to a machine with a higher fundamental winding factor. It is evident in Table 2.7 that there are more pole-slot combinations for 8 and 10 pole machines.

	Number of Poles				
Number of Slots	2	4	6	8	10
3	0.866				
6		0.866			
9			0.866	0.945	0.945
12				0.866	0.933
15					0.866

Table 2.7: Fundamental winding factors of applicable double layer FSCW slot-pole combinations

2.3.4.3 Magnetomotive Force Waves

The MMF around the air gap periphery can be formulated as follows [21];

$$F_m(\alpha, t) = \sum_{v=1}^{\infty} \frac{4N_s}{vp\pi} \xi_v [F_{mv}^+(\alpha, t) + F_{mv}^-(\alpha, t)] \quad (2.24)$$

where the backwards and forwards rotating components are $F_{mv}^+(\alpha, t)$ and $F_{mv}^-(\alpha, t)$ which are square wave functions of both space α and time t . These MMF waves, along with the air gap permanence function determine the air gap magnetic flux density, which by decomposing the fields into radial and tangential components determine the radial forces and torque respectively. In terms of 3-phase MMF spectra, the winding factor results in Figs. 2.9 and 2.10 are carried through to their per-unit MMF spectra in Figs 2.11 and 2.12 respectively.

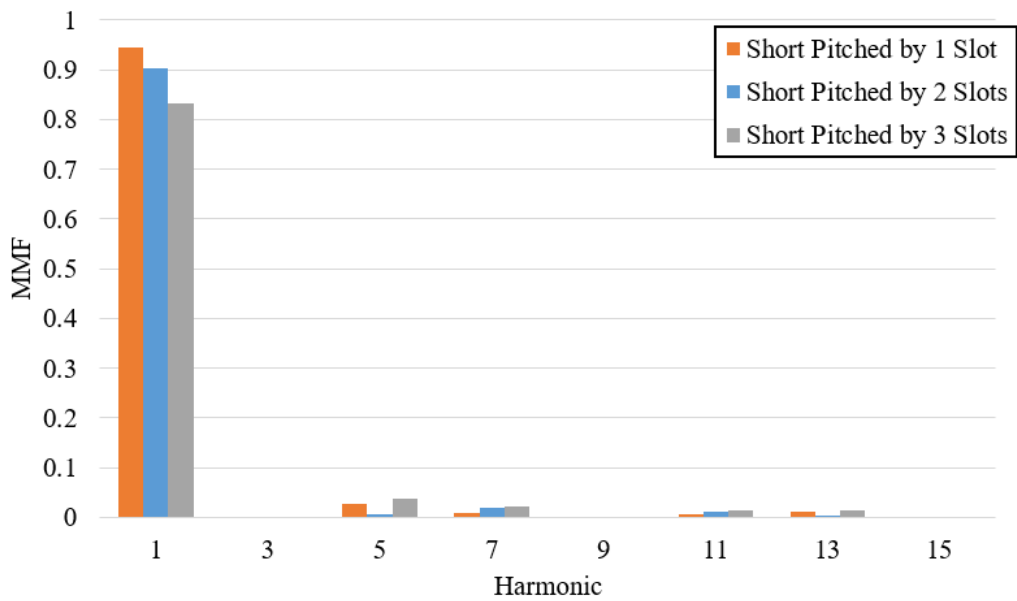


Figure 2.11: MMF of Distributed winding, $Q_s = 36$ & $p = 2$

The short pitching (chording) reduces the harmonic content at the expense of reduction of the fundamental. The MMF spectrum for the 6 slot four pole double layer FSCW is

presented in Figure. 2.12;

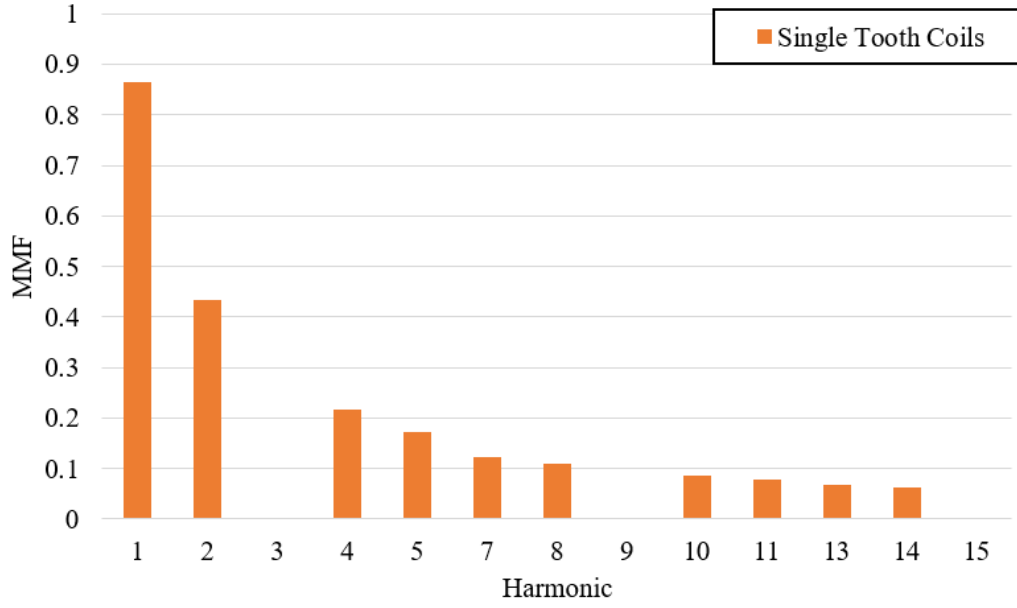


Figure 2.12: MMF of double layer FSCW, $Q_s = 6$ & $p = 2$

Note that the concentrated windings have higher harmonic amplitudes when compared to the distributed winding. Also, the concentrated winding MMF spectra contain both odd and even harmonics due to asymmetrical waveforms, which is explored further in Chapters 6 and 7.

2.3.5 Iron Loss

Due to the increased MMF harmonics in the cSynRM, the harmonic spectrum of the air-gap field will be richer. The additional MMF components will create additional harmonic fluxes in the air gap leading to higher iron losses in the cSynRM when compared to an equivalent SynRM. This iron loss will be mainly located in the rotor surface and the tooth surface due to the pulsating fluxes caused by the rapid changes in air gap reluctance when the rotor poles pass the teeth. The iron loss of the machine is calculated from a modified Steinmetz equation, taking into account the harmonics, which comprises of both eddy and hysteresis losses [23] (Bertotti separation method);

$$P_{Fe,t} = P_{Fe,Eddy} + P_{Fe,Hys} \quad (2.25)$$

$$P_{Fe,t} = \underbrace{\frac{\pi^2}{6} \left(\frac{\sigma_{Fe}}{\rho_{Fe}} \right) f^2 d^2 m_{Fe} \sum_{v=1}^{\infty} v^2 (B_{\theta,v}^2 + B_{r,v}^2)}_{Eddy Loss} + \underbrace{c_{Hys} \frac{f}{100} m_{Fe} \sum_{v=1}^{\infty} v^2 (B_{\theta,v}^2 + B_{r,v}^2)}_{Hysteresis Loss} \quad (2.26)$$

Where σ_{Fe} is the lamination material conductivity, ρ_{Fe} is its mass density, m_{Fe} is the mass of the lamination stack, d is the lamination thickness, f the electrical frequency of

the field, ν the harmonic order, c_{Hys} the material hysteresis constant and $B_{\theta,\nu}$ and $B_{r,\nu}$ are the harmonic tangential and radial fields respectively. Although only transversely laminated rotors are considered in this thesis, axially laminated (ALA) type rotors would suffer greater iron loss due to significant eddy currents. These eddy currents decrease efficiency and increase rotor heating, however the authors in [25] have gone a long way towards solving this problem, though manufacturability remains the major hindrance to the ALA type motor. To minimize iron losses, careful consideration of the lamination material and thickness is required, but the degradation in stacking factor where thinner laminations are used must also be taken into account so as to not significantly reduce flux carrying capability.

2.3.6 Torque Ripple

The asynchronous field harmonics caused by the MMF harmonics which link the rotor cause an oscillating torque, if they experience a changing permeance as the rotor rotates, leading to a degradation in torque quality. Electromagnetic torque is the result of tangential stresses in the airgap of the machine acting upon the rotor. The tangential and radial airgap fields contain harmonics derived from the machine MMF and permeance function space harmonics. These harmonics create parasitic perturbations in the airgap magnetic stress, leading to high torque ripple in the cSynRM when compared to a sinusoidally distributed machine. Excessive torque ripple leads to increased acoustic noise and vibration, which is undesirable in many applications, for example military and vehicular applications where low noise and vibration are desirable; this is explored in detail in Chapter 6 and the reader is referred there for a full treatment.

2.3.7 Inductances

The two most important parameters to design for in synchronous reluctance motors are the orthogonal axis inductances. A full consideration of both these inductances and their component parts must be considered in a design. The design must maximize the direct axis inductance and minimize the quadrature axis inductance. The orthogonal axis inductances are expressed;

$$L_d = L_{md} + L_{s\sigma} \quad (2.27)$$

$$L_q = L_{mq} + L_{s\sigma} \quad (2.28)$$

Each axis inductance incorporates a magnetizing component L_m and the stator leakage component $L_{s\sigma}$. Implications for the machine design of both of these components must be considered and are now explored.

2.3.7.1 Magnetizing Inductance

The magnetising inductances are largely due to the design of the rotor magnetic circuit where a large d -axis inductance and low q -axis inductance are desired. The change in stator winding from sinusoidally distributed to fractional slot concentrated does not impact upon the rotor design, however, it does impact the inductance. The magnetising inductance is expressed as Eq. 2.23 in Section 2.3.4.2. Clearly the inductance obeys an inverse square law with the number of pole-pairs as with the induction machine [23]. Therefore, increasing the pole number effectively decreases the torque capability (with respect to the torque index, and consequently machine efficiency). The decrease in L_{md} is more pronounced than L_{mq} due to the difference in the effective airgap δ_{eff} between the d and q axes. This change also has a negative effect on the machine power factor by reducing the saliency ratio. As the number of poles increase, the magnetising inductances decrease and the machine draws more reactive power and hence the power factor is lower. However, the power factor of all pole number machines increases with machine power rating and the low power factor is more pronounced in lower output machines. The decrease in torque capability (efficiency) and power factor decrease the inverter utilization and therefore the size of the required inverter increases proportionally. Larger outer diameter machines are therefore required if performance is to be maintained when higher pole numbers are selected.

2.3.7.2 Leakage Inductance

The stator leakage inductance component of the orthogonal axis inductances, $L_{s\sigma}$, includes both geometric and harmonic leakage terms [23, 26, 27]. These are the airgap harmonic leakage [23] (or differential leakage [26]), end-winding leakage, tooth-tip leakage and the slot leakage components. These are dealt with in greater detail and calculated for the designed machine in Chapter 3, however here, the airgap harmonic leakage is briefly considered. From Faraday's law, the propagating fundamental flux density in the airgap induces an EMF, as represented by the machine's main magnetizing inductance. As the stator of electrical machines is generally slotted, permeance harmonics induce EMFs in the winding. The airgap harmonic leakage inductance accounts for this and represents the only leakage flux that crosses the airgap [23]. As the MMF spatial harmonic content is expected to increase in a synchronous reluctance machine with fractional slot concentrated windings (Section 2.3.4.4), it is expected that the airgap harmonic leakage increases [23,26,27]. Careful consideration of the airgap leakage and its dominance over the airgap crossing magnetising inductance is required. In conventional synchronous reluctance motors with distributed windings, the so called harmonic leakage factor, which is a measure of the airgap harmonic leakage content in the machine will usually be between $0.005 < \sigma_h < 0.0275$ for windings with a number of slots per pole per phase q between 5 and 2 respectively [23, 26] - corresponding to highly distributed windings. In [27], it was calculated that the airgap leakage factor for fractional slot concentrated winding machines

can be large. The airgap harmonic leakage factors for differing slot-pole combinations are presented in Table 2.8.

	Number of Poles				
Number of Slots	2	4	6	8	10
3	0.462				
6		0.462			
9			0.462	2.15	3.29
12				0.462	1.95
15					0.462

Table 2.8: Airgap harmonic leakage factors - adapted from [27]

The calculated harmonic leakage factors are much larger than that of distributed windings due to the increased space harmonic content accompanying the adoption of fractional slot concentrated windings. Higher pole numbers appear to suffer increasing higher leakage factors, using a slot-pole combination that has a lower leakage factor is desirable.

2.3.7.3 Leakage Inductance Effects on Saliency Ratio and Power Factor

There are two definitions of saliency ratio, the *magnetising* saliency ratio ξ_{mag} and the *true* saliency ratio ξ_{true} . The former is the ratio of the direct and quadrature axis magnetising inductances, disregarding stator leakage components. The true saliency ratio, represented in Eq. 1.17 contains the stator leakage terms, including the airgap leakage inductance. The true saliency ratio as a function of stator leakage inductance is presented in Figure. 2.13. It is chosen that $L_{md} = 1$ p.u. and $L_{mq} = 0.06$ p.u. giving a magnetizing saliency ratio, $\xi_{mag} = 16$.

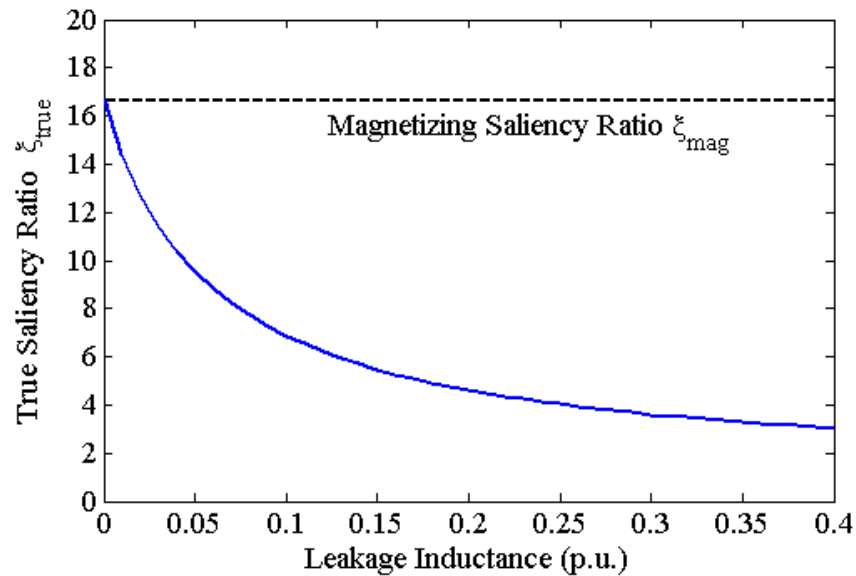


Figure 2.13: True saliency ratio as a function of leakage inductance

From the figure, it is clear that the true saliency ratio is significantly affected by increases in stator leakage inductance. For modern synchronous reluctance machines with an axially laminated rotor, true saliency ratios greater than 10 are common; this figure is lower for transversely laminated multiple flux barrier rotors. As mentioned in Chapter 1, the true saliency ratio ξ_{true} of the machine effectively determines the maximum power factor of the machine, it can be shown by development of equations derived from the machine phasor diagram that the maximum power factor capability of a machine with a given true saliency can be expressed [25];

$$\cos(\phi)|_{max} = \frac{\xi_{true} - 1}{1 + \xi_{true}} \quad (2.29)$$

Thus the power factor is directly related to the true saliency ratio of the machine and hence the stator leakage inductance. Figure 2.14 shows the change in maximum achievable power factor with increasing stator leakage inductance for $\xi_{mag} = 16$.

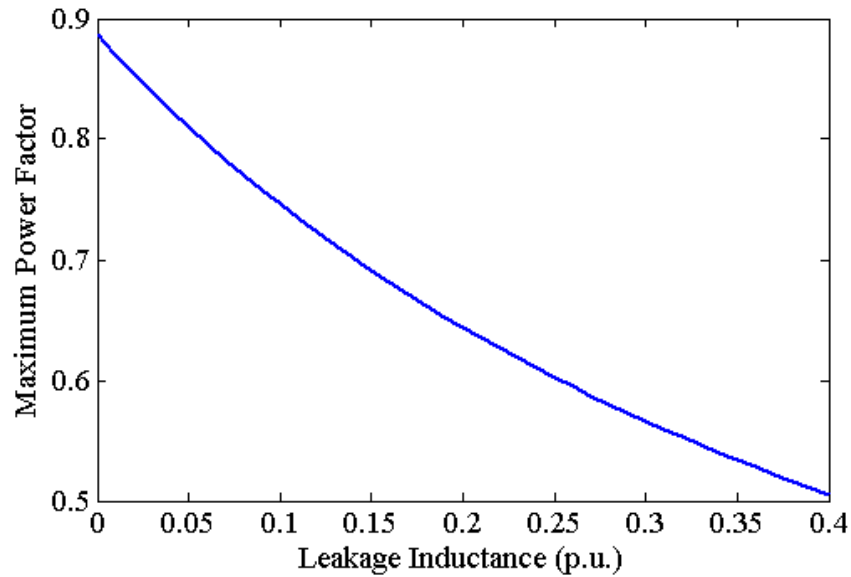


Figure 2.14: Maximum power factor as a function of leakage inductance; $\xi_{mag} = 16$

A distributed winding synchronous reluctance machine has a power factor between 0.5 and 0.6 under maximum torque per Ampere: the higher the saliency ratio, the higher the power factor. The power factor suffers due to a reduction in the true saliency ratio by increasing stator leakage inductance. The true saliency ratio and power factor degradation depend upon the relative magnitudes of the $d - q$ axis magnetising inductances and magnitude of the stator leakage inductance. In the cSynRM, the extra leakage flux increases the stator leakage inductance, effectively reducing the saliency ratio, having a negative impact on the performance of the machine. The limiting value of ξ_{true} is in fact $L_{s\sigma}$, so with a smaller q -axis magnetizing component the higher leakage has a more pronounced effect. Higher pole numbers are not advantageous in terms of magnetising or leakage inductance, but are generally worse for the same dimensions as indicated by their increased harmonic leakage factors in Table 2.8. Therefore, a low pole number machine with the

lowest possible airgap leakage factor is required for maximum performance - leading to higher efficiency and a good power factor and inverter utilization.

2.3.8 Manufacturing

If a complete or continuous stator core back is used, as is the conventional method for manufacturing a single piece stator, it is difficult to wind around a single tooth and produce a neat and compact coil with a high fill factor. The single tooth span coils of FSCW allow stator segmentation rather than utilizing a continuous stator core back. This segmentation allows coils to be pre-wound on the tooth before final stator assembly [13] (or even off the tooth and assembled onto the tooth after winding [13,19]). Thus the manufacturing of the coils is arguably simpler than a large distributed winding system and the stamping process is identical; the effective use of the raw lamination sheet may increase if the stator segments can be stamped in an optimal pattern on the sheet. Utilizing this technique can effectively reduce manufacture time and costs of the SynRM, as the stator segments can be arranged to minimize material waste with respect to lamination blanks. However, assembly of the segments to form the stator core and the mechanical integrity are aspects of using the segmented core structure reduce its desirability. Pre-compressed coils can also be manufactured to increase the efficiency and torque density even further [19]. Mecrow *et al* has previously suggested a simple segmental stator for the ease of winding single tooth coils [28], as shown in Figure 2.15.

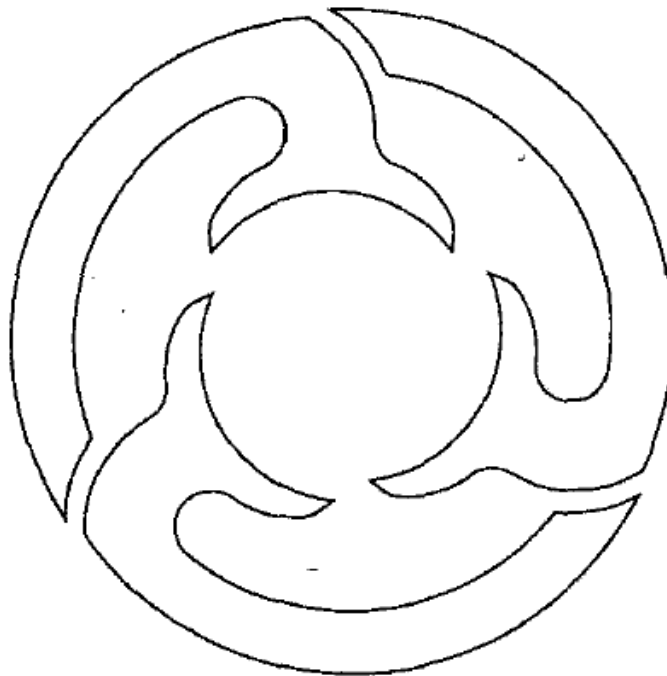


Figure 2.15: Mecrow *et al* “Segmental Stator” arrangement [28]

2.3.8.1 Mechanical Arrangement of Higher Pole SynRMs

As the number of poles increases, for a given rotor outer diameter, the available space in which to shape the flux barriers diminishes. The flux barrier design becomes very difficult at higher pole numbers due to the requirement of effectively shaping of the barriers to maximise performance - correct design of orthogonal axis flux paths is difficult. Thus, to adequately shape the flux barriers at higher pole numbers requires an increase in rotor outer diameter, which is advantageous in both torque capability and power factor, however may not be suitable in some applications with space restrictions.

In higher pole number machines, the radial and tangential ribs (Fig. 2.16) must remain at the smallest width possible. Rib width should reduce with increased pole number as the flux per pole reduces. Therefore, to ensure saturation and minimization of the q -axis inductance, the ribs have to be diminishingly small. However, punching limits and issues with mechanical integrity enforce a minimum rib width, affecting performance. Smaller ribs are possible with other forms of manufacturing such as electro-discharge-machining (EDM) and pulsed laser cutting, but in general for mass production, punching is the only viable option, however the small features potentially increase tool wear. The mechanical performance is greatly affected by the rib thicknesses and lower maximum speeds will be required with higher pole number machines to maintain structural integrity.

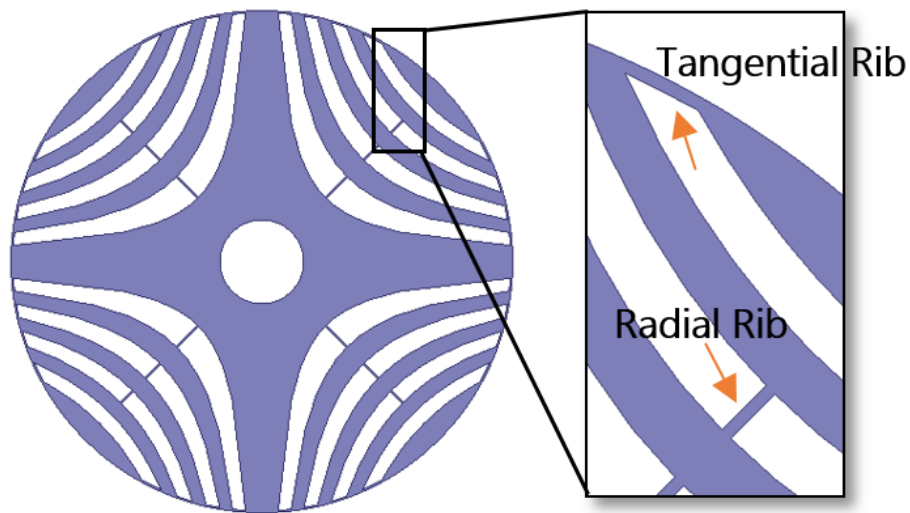


Figure 2.16: Radial and Tangential Ribs of the Rotor

As the number of poles increases, the number of barriers required for good performance does not decrease. As a consequence the number of stamped sections increases linearly with the number of poles, increasing stamping tool complexity, cost and maintenance.

2.4 Conclusion

Based on a brief comparison of three winding types, the application of fractional slot concentrated windings appears to be worthy of investigation for higher performance machines accompanied by potential manufacturing improvements of the synchronous reluctance motor. To reduce the copper loss in the machine, hence improving efficiency, two methods associated with the windings are identified; an increase in slot fill factor and a reduction in end winding length. The phase resistance is proportional to the reciprocal of the fill factor and directly proportional to the end winding length. With regard to the fill factor, an increase from typical fill factors for distributed windings of 0.35 to 0.6 provides a 45% decrease in copper loss. A decrease in end winding length also adds to reducing this loss, however an increase in fill factor is associated with an increase in copper mass and the end winding reduction is associated with a decrease in copper mass - as such other materials could be used for winding and aluminum was identified as it has the lowest resistivity-mass density product. An increase in fill factor aids the slot thermal conductivity by reducing the air in the slot - providing an improved thermal path. Migration from distributed to fractional slot concentrated windings in a synchronous reluctance motor has a number of benefits, but also some associated disadvantages. These are summarized as;

ADVANTAGES OF ADOPTION:

1. More effective use of active materials (copper)
2. Increased fill factor; $0.6 \leq S_{FF} \leq 0.85$, lower winding losses (though larger mass)
3. Increased thermal conductivity, hence an improved thermal path with reduced hot spot temperatures in end windings
4. Physical and electric isolation of phases at end windings
5. Allow segmented stators / removable teeth
6. Simplistic winding / ease of manufacture

DISADVANTAGES OF ADOPTION:

1. MMF Space harmonics
 - (a) Torque ripple
 - (b) Higher iron loss
 - (c) Unwanted noise and vibration
 - (d) Increased leakage inductance (airgap harmonic leakage higher, but lower end winding leakage)

2. Difficult to take advantage of higher pole number machines (as with other machine types, including the IM)

Therefore, in designing a fractional slot concentrated winding synchronous reluctance machine, the cSynRM, the following rules should be adhered to;

1. Use a double layer winding (lower MMF content and shorter end turns)
2. Select a winding with the highest fundamental winding factor (highest torque producing capability)
3. Use a low pole number (best performance) - higher pole number advantages are outweighed by disadvantages
4. Select a winding with a low harmonic leakage factor (higher power factor)
5. Use segmented stator technology (ease of manufacture and compactness of coils related to fill factor)

Based on the arguments in this Chapter, a novel machine topology that encompasses the advantages of the synchronous reluctance machine, but shifts from the conventionally sinusoidal distributed winding to the advantageous single tooth windings can be realized. Synthesis of such a machine has not been presented in the literature. In the design single tooth windings are utilized in order to reduce copper loss, reduce end winding size and length, increase machine manufacturability and allow performance improvements which are not possible with distributed windings. The cSynRM is proposed in this thesis to work around the undesirable characteristics of the conventional SynRM in order to address the research challenges identified in Chapter 1. The remainder of this thesis presents the design, analysis and validation of a synchronous reluctance machine with a fractional slot concentrated winding arrangement.

2.5 References

1. Grop, H.; Soulard, J.; Persson, H., "Theoretical investigation of fractional conductor windings for AC-machines - definition, air-gap m.m.f. and winding factors," *Electrical Machines*, 2008. ICEM 2008. 18th International Conference on , vol., no., pp.1,6, 6-9 Sept. 2008
2. Grop, H.; Soulard, J.; Persson, H., "Stator slot leakage in AC-machines equipped with fractional conductor windings," *Electrical Machines and Systems*, 2009. ICEMS 2009. International Conference on , vol., no., pp.1,6, 15-18 Nov. 2009
3. Cipin, R.; Patocka, M., "AC fractional winding design by the new method," *Power Electronics, Electrical Drives, Automation and Motion (SPEEDAM)*, 2012 International Symposium on , vol., no., pp.609,613, 20-22 June 2012
4. Jensen, B.B.; Jack, A.G., "Toroidally wound induction machines," *Electrical Machines (ICEM)*, 2010 XIX International Conference on , vol., no., pp.1,5, 6-8 Sept. 2010
5. G. Cafici, "Asynchronous Motor," T. P. Office, Ed. United Kingdom, 1968
6. Jensen, B.B.; Jack, A.G.; Atkinson, G.J.; Mecrow, B.C., "Performance of a Folded-Strip Toroidally Wound Induction Machine," *Industrial Electronics, IEEE Transactions on* , vol.59, no.5, pp.2217,2226, May 2012
7. Yu-Han Yeh; Min-Fu Hsieh; Dorrell, D.G., "Different Arrangements for Dual-Rotor Dual-Output Radial-Flux Motors," *Industry Applications, IEEE Transactions on* , vol.48, no.2, pp.612,622, March-April 2012
8. Ji-Young Lee; Byoung-Kuk Lee; Tao Sun; Jung-Pyo Hong; Woo-Taik Lee, "Dynamic analysis of toroidal winding switched reluctance motor driven by 6-switch converter," *Magnetics, IEEE Transactions on* , vol.42, no.4, pp.1275,1278, April 2006
9. Bumby, J.R.; Martin, R.; Mueller, M.A.; Spooner, E.; Brown, N.L.; Chalmers, B.J., "Electromagnetic design of axial-flux permanent magnet machines," *Electric Power Applications, IEE Proceedings -* , vol.151, no.2, pp.151,160, Mar 2004
10. Matsuo, T.; Lipo, T.A.; , "Rotor design optimization of synchronous reluctance machine," *Energy Conversion, IEEE Transactions on* , vol.9, no.2, pp.359-365, Jun 1994
11. Moghaddam, Reza R.; Magnussen, F.; Sadarangani, C.; , "Novel rotor design optimization of synchronous reluctance machine for high torque density," *Power Electronics, Machines and Drives (PEMD 2012)*, 6th IET International Conference on , vol., no., pp.1-4, 27-29 March 2012
12. Brown, Geoff; , "Developing synchronous reluctance motors for variable speed operation," *Power Electronics, Machines and Drives (PEMD 2012)*, 6th IET International Conference on , vol., no., pp.1-6, 27-29 March 2012
13. L-Refaie, A.M.; , "Fractional-Slot Concentrated-Windings Synchronous Permanent Magnet Machines: Opportunities and Challenges," *Industrial Electronics, IEEE Transactions on* , vol.57, no.1, pp.107-121, Jan. 2010
14. El-Refaie, A.M.; Jahns, T.M.; Novotny, D.W.; , "Analysis of surface permanent magnet machines with fractional-slot concentrated windings," *Energy Conversion, IEEE Transactions on* , vol.21, no.1, pp. 34- 43, March 2006

15. Reddy, P.B.; El-Refaie, A.M.; Kum-Kang Huh; Tangudu, J.K.; Jahns, T.M.; , "Comparison of Interior and Surface PM Machines Equipped With Fractional-Slot Concentrated Windings for Hybrid Traction Applications," *Energy Conversion, IEEE Transactions on* , vol.27, no.3, pp.593-602, Sept. 2012
16. Abdel-Khalik, A.S.; Ahmed, S.; , "Performance Evaluation of a Five-Phase Modular Winding Induction Machine," *Industrial Electronics, IEEE Transactions on* , vol.59, no.6, June 2012
17. Mecrow, B.C.; , "New winding configurations for doubly salient reluctance machines ," *Industry Applications, IEEE Transactions on* , vol.32, no.6, pp.1348-1356, Nov/Dec 1996
18. Staton, D.; Boglietti, A; Cavagnino, A, "Solving the More Difficult Aspects of Electric Motor Thermal Analysis in Small and Medium Size Industrial Induction Motors," *Energy Conversion, IEEE Transactions on* , vol.20, no.3, pp.620,628, Sept. 2005
19. Widmer, J.D.; Spargo, C.M.; Atkinson, G.J.; Mecrow, B.C., "Solar Plane Propulsion Motors With Precompressed Aluminum Stator Windings," *Energy Conversion, IEEE Transactions on*, no.99
20. Idoughi, L.; Mininger, X.; Bouillault, F.; Bernard, L.; Hoang, E., "Thermal Model With Winding Homogenization and FIT Discretization for Stator Slot," *Magnetics, IEEE Transactions on* , vol.47, no.12, pp.4822,4826, Dec. 2011
21. Magnussen, F.; Sadarangani, C., "Winding factors and Joule losses of permanent magnet machines with concentrated windings," *Electric Machines and Drives Conference, 2003. IEMDC'03. IEEE International* , vol.1, no., pp.333,339 vol.1, 1-4 June 2003
22. Salminen, P.; Niemela, M.; Pyhonen, J.; Mantere, J., "Performance analysis of fractional slot wound PM-motors for low speed applications," *Industry Applications Conference, 2004. 39th IAS Annual Meeting. Conference Record of the 2004 IEEE* , vol.2, no., pp. 1032- 1037 vol.2, 3-7 Oct. 2004
23. "Design of Rotating Electrical Machines", Juha Pyrhonen, Tapani Jokinen, Valeria Hrabovcova, John Wiley & Sons, 24 Feb 2009
24. Fornasiero, E.; Alberti, L.; Bianchi, N.; Bolognani, S., "Considerations on Selecting Fractional-Slot Nonoverlapped Coil Windings," *Industry Applications, IEEE Transactions on* , vol.49, no.3, pp.1316,1324, May-June 2013
25. Boldea, I.; Fu, Z. X.; Nasar, S.A., "Performance evaluation of axially-laminated anisotropic (ALA) rotor reluctance synchronous motors," *Industry Applications Society Annual Meeting, 1992., Conference Record of the 1992 IEEE* , vol., no., pp.212,218 vol.1, 4-9 Oct 1992
26. Gieras, Jacek F. Permanent magnet motor technology: design and applications. CRC press, 2002.
27. Ponomarev, P.; Lindh, P.; Pyrhonen, J., "Effect of Slot-and-Pole Combination on the Leakage Inductance and the Performance of Tooth-Coil Permanent-Magnet Synchronous Machines," *Industrial Electronics, IEEE Transactions on* , vol.60, no.10, pp.4310,4317, Oct. 2013
28. Mecrow, B.C.; Jack, AG.; Haylock, J.A; Hoefer, U.; Dickinson, P.G., "Simplifying the manufacturing process for electrical machines," *Power Electronics, Machines and Drives, 2004. (PEMD 2004). Second International Conference on (Conf. Publ. No. 498)* , vol.1, no., pp.169,174 Vol.1, 31 March-2 April 2004
29. http://www.easa.com/sites/files/winding_failures/goodfull.jpg; Accessed: 28/03/2016 11:17am
30. <http://www.motor-machinery.com/product/BLDC-stator-winder.html>; Accessed: 28/03/2016 11:25am

Chapter 3

Prototype: Design and Performance

This chapter presents the design of a synchronous reluctance machine with fractional slot concentrated windings (cSynRM). It brings the cSynRM concept to the pre-prototype stage so that the technology can be compared to existing technology through FEA studies. The manufacture and construction of a prototype machine based on the design and its experimental verification are presented in subsequent chapters. Firstly, the design of the motor is presented and then performance of the optimized geometry through FEA is reported. The machine magnetizing and various leakage inductances are calculated analytically so that the dominant leakage components can be identified, key figures of merit are then determined and analysed and machine performance predicted with the assistance of finite element studies. The analytical calculations in this chapter are based on a theory developed in Pyhronen [1], Gieras [2] and Lipo [3]. The mechanical aspects of rotor design and rotordynamic analysis is also presented, the effects of rotor skewing and inclusion of semi-magnetic slot wedges being explored. An FEA performance comparison of the designed motor with an equivalent size induction motor and a conventionally wound synchronous reluctance motor is also presented in this chapter.

3.1 Machine Sizing and Stator Electromagnetic Design

A research group standard frame size of 150mm by 150mm is used, giving the machine an active material aspect ratio of unity. In many respects, the machine specification is similar to that of a standard industrial 3 phase machine with a base speed of 1500rpm operating from a standard VSD supply with rectified DC link voltage level of 560V based on a 415V AC 3ph supply. The machine is chosen as a totally enclosed non-ventilated type. High efficiency targets for the machine size are chosen: this reflects the requirement of a high fill factor of approximately 60%, which is achievable in practical machine construction, as will be verified in Chapter 4. The motor specification for the design is outlined in Table 3.1.

Parameter	Value
Stator Outer Diameter, D_{os} [mm]	150
Active Stack Length, L_s [mm]	150
Base Speed, ω_{base} [rpm]	1500
Number of Phases, m	3
DC Link Voltage, V_{DC} [V]	560
Cooling	TENV
Winding	FSCW
Efficiency, η [%]	>90
Winding Fill Factor, S_{FF}	≈ 0.6

Table 3.1: Fixed Machine Specifications

3.1.1 Key Dimensions

The sizing of the machine stator electromagnetic dimensions made using a parametric geometry in a 2D finite element model: the following dimensions are sought;

- Stator tooth width, t_t
- Stator core-back depth, t_{cb}
- Rotor outer diameter, D_{ro}
- Tooth tip depth
- Tooth span angle

By varying these parameters around reasonable starting values, the final values can be selected based on maximizing the torque per unit total loss. The total loss includes the stator copper loss and both the stator and rotor hysteresis and eddy current loss calculated from FEA and includes a factor of 1.6 to account for increased losses due to manufacturing processes. The FEA optimization includes both iron loss and assumes a fixed slot fill factor for calculation of the winding losses; the stator line current and DC link voltage are fixed at its rated speed of 1500rpm. The optimal rotor outer diameter for the maximum torque per unit loss is determined to be $D_{ro} = 88\text{mm}$, the stator core-back depth $t_{cb} = 12\text{mm}$, the tooth width $t_t = 20\text{mm}$, with the tooth span and tooth tip depth set to 46 degrees and 1.6mm respectively. The machine power factor increases linearly with D_{ro} [3], however the torque per unit loss decreases slightly as the slot area decreases, thus the selected rotor outer diameter maintains the highest power factor whilst maintaining the specified machine efficiency of >90%. The stator is chosen to be segmented in order to facilitate a high slot fill factor and ease of coil winding, Figure 3.1 depicts the finalized dimensions of the final stator segment and shows the interlocking aspect of the segment design in the core-back. The radius of the interlock is chosen as 2mm.

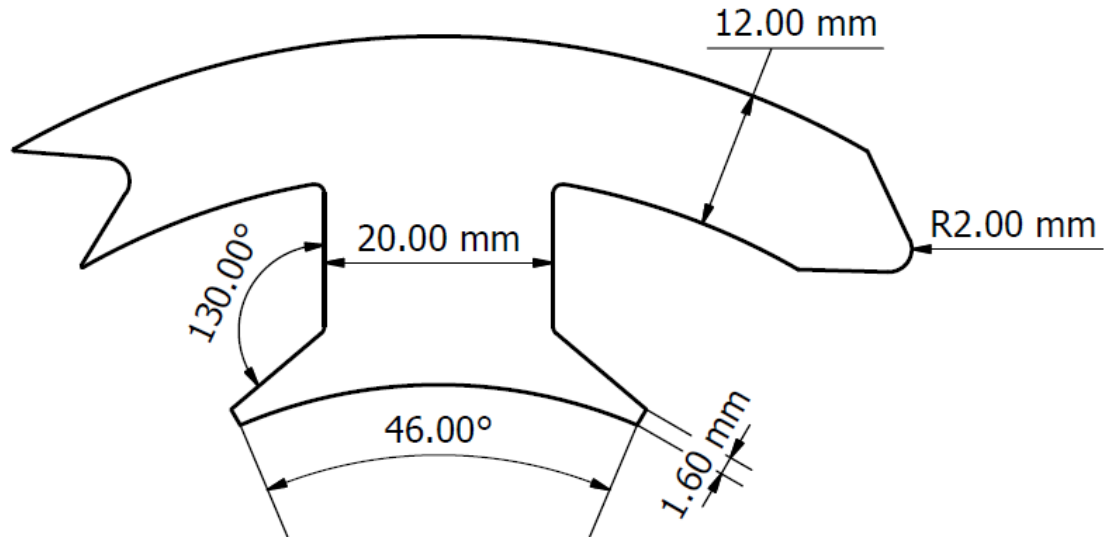


Figure 3.1: Complete stator segment dimensions

3.1.2 Stator Segmentation

In order to fulfill the high fill factor requirement, the stator is segmented as in Fig. 3.1. Segmentation of the stator yoke allows the tooth to be wound before assembly, resulting in high fill factors but introduces inter-segment air gaps which degrades the performance of the machine. The interface gap is unknown, but assuming it is of the same magnitude as the yoke to housing interface gap, which according to Staton [9] has a maximum value of 0.1mm and an average value of 0.037mm, the degradation of the torque and power factor must be assessed. A finite element model is setup such that the inter-segment gap could be varied between 0 and 0.1mm in steps of 0.01mm. Figure 3.2 shows the relations between the machine torque and power factor with inter-segment gap length normalized to zero inter-segment air gap length.

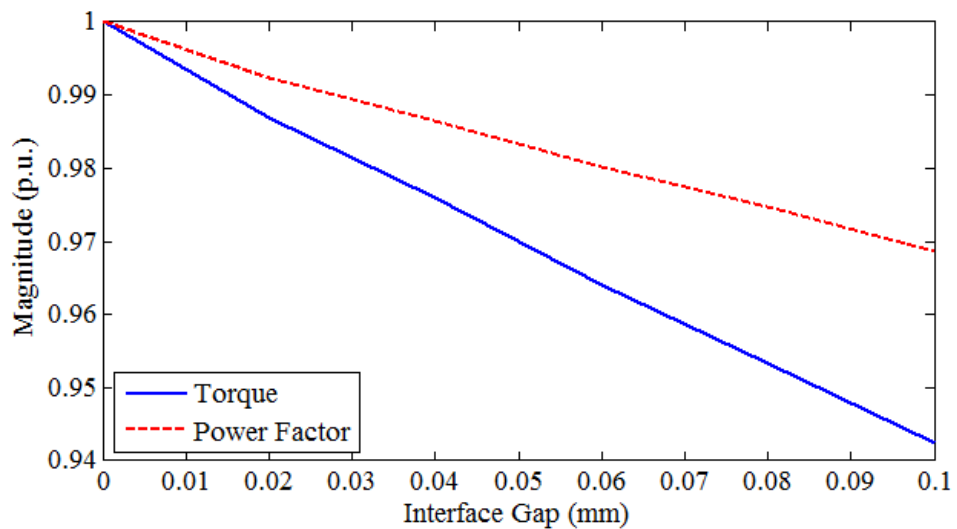


Figure 3.2: Effect of interface gaps

With the stator current fixed at the rated current, at rated speed under maximum torque per Ampere current angle, both the torque and power factor decrease linearly with an increase in airgap width. The torque reduces to 94% and the power factor to 97% for the maximum interface gap of 0.1mm corresponding to 20% of the main radial airgap length $\delta = 0.5\text{mm}$. As the stator segment assembly is shrink fitted into the case, the air gaps are expected to be small, if the average value given by Staton is used the machine torque will be at 98% and the power factor at 99% of a machine with a continuous core-back, showing that the inter-segment air gaps have a negligible impact on the performance of the prototype machine. Figure 3.3 shows the flux plots for three inter-segment gaps lengths, 0mm, 0.03mm and 0.05mm from top to bottom. In each case, the peak core-back and tooth flux densities are stated over an electrical period. The flux density and magnetic vector potential ranges in all plots are identical, at an identical operating point and time step. Although the flux density changes in the core-back the flux densities in the teeth appear to be only marginally affected, with the leakage paths also changing to reflect this. As indicated in the machine torque and power factor results in Fig. 3.2, machine performance is only marginally impaired at the likely levels of inter-segment interface air-gap lengths.

3.1.3 Winding Design and Configuration

With the main stator dimensions calculated the winding must be selected. The machine is three phase $m = 3$ with $Q_s = 6$ and $p = 2$, therefore the number of slots per pole;

$$q = \frac{Q_s}{2pm} = \frac{z}{n} = \frac{1}{2} < 1 \quad (3.1)$$

A double layer fractional slot concentrated winding (all teeth wound) is selected to minimize harmonic content when compared to the single layer variant. This winding has applicable harmonic ordinates [5];

$$v = \pm \left(\frac{1}{n} \right) (6g + 2); g = 1, 2, 3, 4, 5... \quad (3.2)$$

Thus, the harmonics take on the values 1, -2, 4, -5, 7... etc. The negative indicates a backwards counter-rotating asynchronous harmonic with respect to the fundamental. Odd and even ordinates exist due to the airgap flux asymmetry over a rotor pole pair when $q = 0.5$. The winding factors for this double layer winding can be analytically determined;

$$k_{wv} = \sin \left(\frac{\pi p}{Q_s} \right) \frac{\sin \left(\frac{v\pi}{2m} \right)}{nq \sin \left(\frac{v\pi}{2mnq} \right)} = \frac{\sqrt{3}}{2} \approx 0.866 = \text{constant} \quad (3.3)$$

The harmonic winding factors are equal to that of the fundamental, resulting in high levels of space harmonic content in the MMF. The winding factors of the selected winding and the respective MMF harmonics are presented in Figure. 3.4. The winding layout is

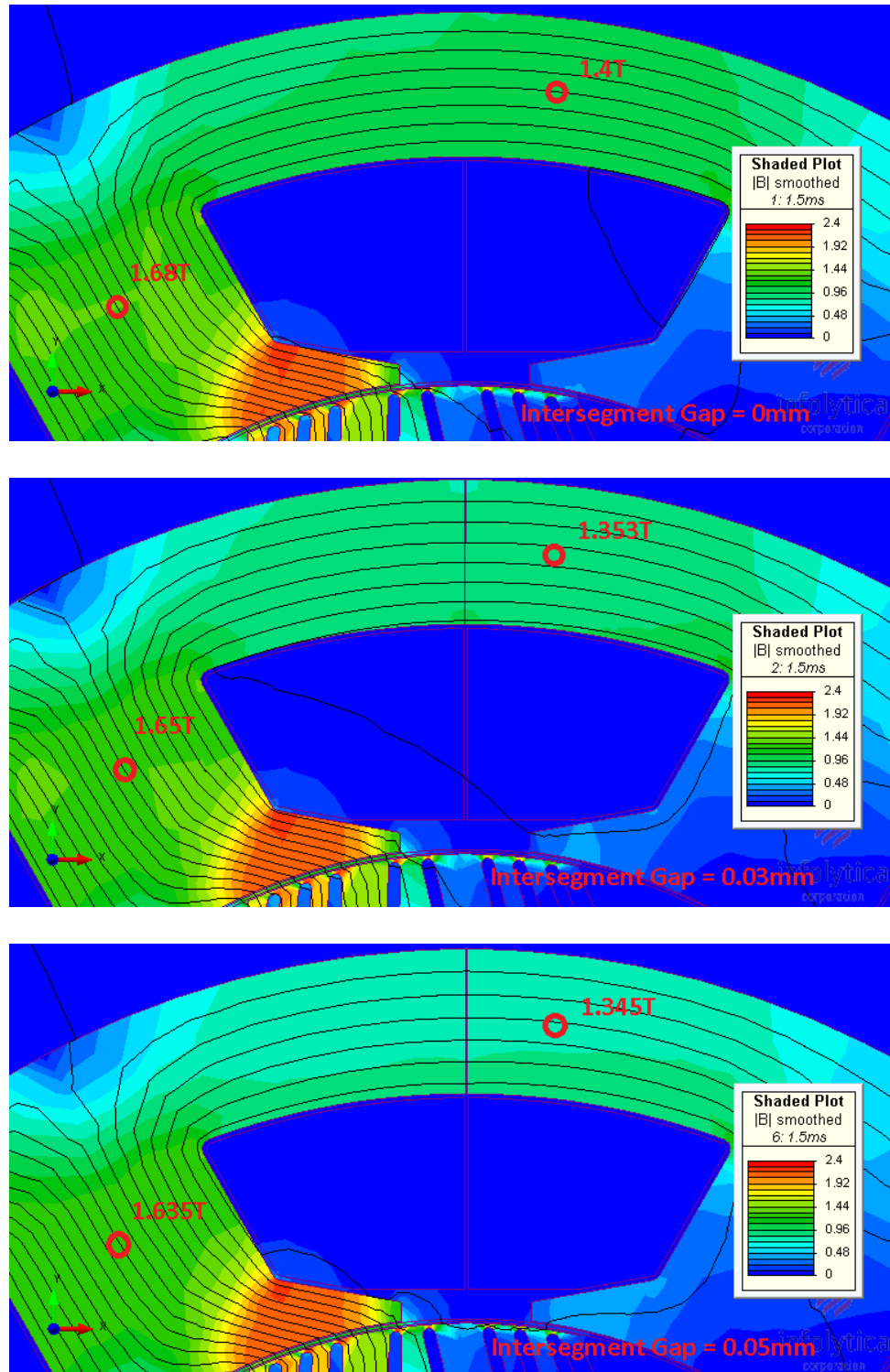


Figure 3.3: Inter-segment airgap flux plots with inter-segments gaps of 0mm, 0.03mm and 0.05mm (top to bottom)

presented in Figure. 3.5 and the airgap periphery MMF distribution is presented in Figure. 3.6 for three different three instantaneous current values.

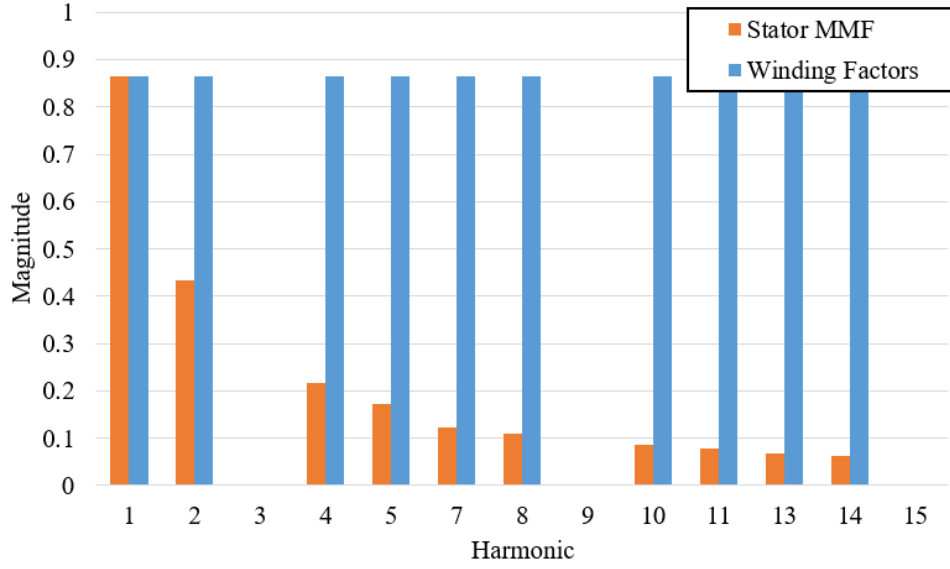


Figure 3.4: Winding factors and 3ph MMF harmonic spectrum

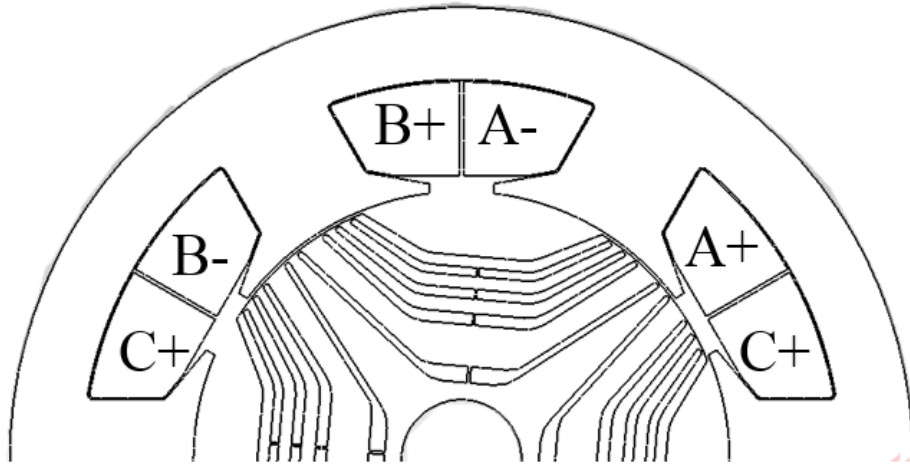


Figure 3.5: Winding layout showing each phase coil sides

The number of turns per phase (star connected) must then be calculated for a given maximum terminal voltage at rated speed. From a sinusoidal voltage source inverter, without going into over modulation, the maximum line voltage $U_{L-L}|_{\max}$ for a given DC link voltage U_{DC} is written [6];

$$U_{L-L}|_{\max} = \frac{\sqrt{3}U_{DC}}{2\sqrt{2}} \quad (3.4)$$

therefore the maximum RMS phase voltage for the cSynRM on a DC link voltage of

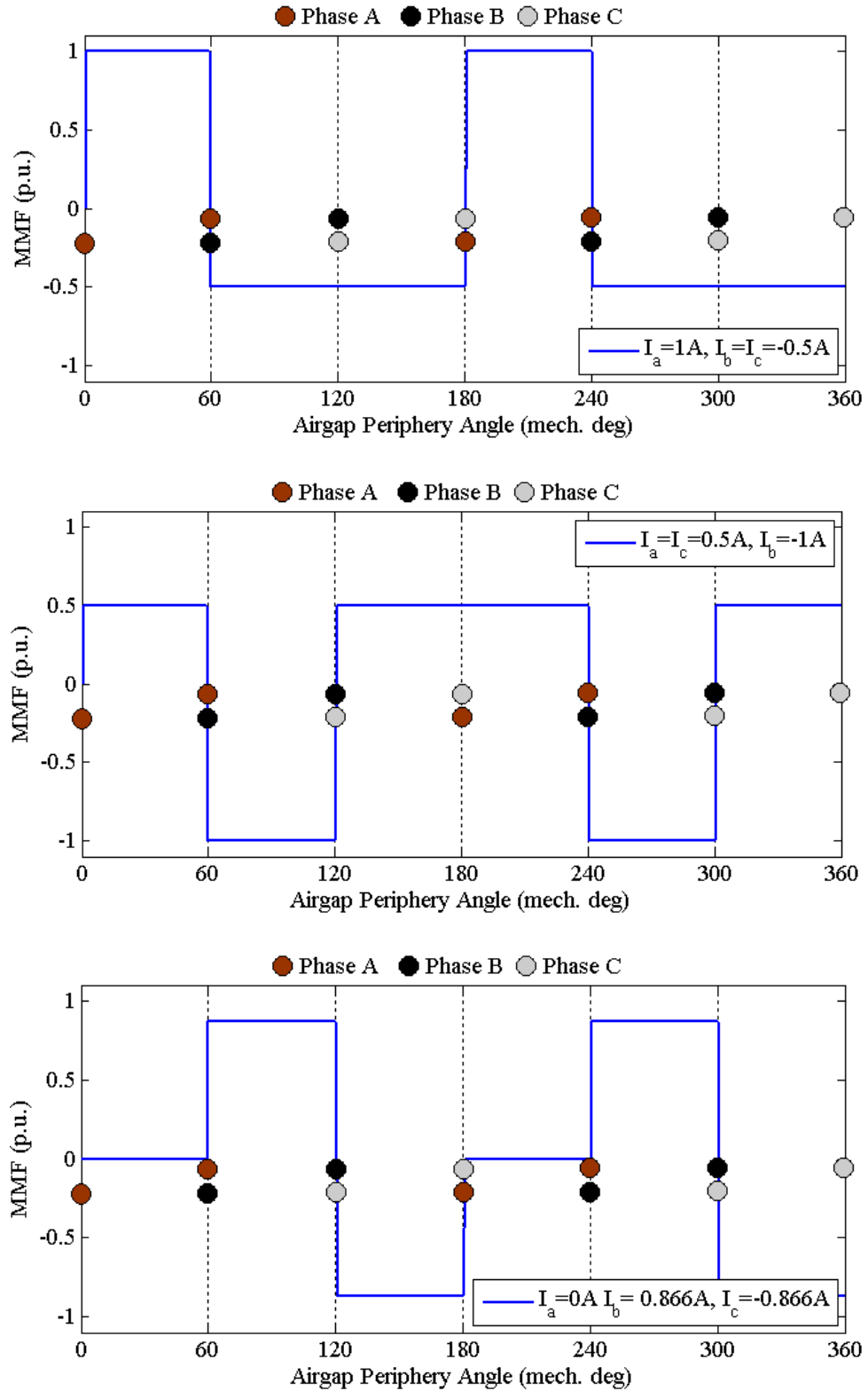


Figure 3.6: Three phase MMF distribution for various three phase current instants

560V¹;

$$U_{ph}|_{\max} = \frac{\gamma U_{DC}}{2\sqrt{2}} \approx 200V \quad (3.5)$$

The utilisation factor $\gamma = 0.95$ is used as a voltage limit as a percentage of the full DC link voltage level. The number of turns per phase N_{ph} can be calculated based on the following analysis with the assumption that the winding flux is almost sinusoidal as a function of time, which is valid when the calculations are based upon the fundamental flux density wave in the airgap and $\hat{B}_{\delta 1}$ is the peak value of that wave. The flux function can be written;

$$\phi(t) = \hat{\phi} \sin(\omega t) \quad (3.6)$$

where $\hat{\phi}$ is the peak value of the airgap flux penetrating a fully pitched winding. Now, according to Faraday's law of induction, the winding phase induced emf due to the time varying flux is expressed;

$$e(t) = -N\zeta_{w1} \frac{d\phi(t)}{dt} = -N\zeta_{w1} \omega \hat{\phi} \cos(\omega t) \quad (3.7)$$

where ζ_{w1} is the fundamental winding factor, N is the number of turns and ω is the angular velocity of the time varying flux wave, constituting the peak induced emf $\hat{e} = N\zeta_{w1} \omega \hat{\phi}$. Assuming a sinusoidal induced EMF, the RMS value is written;

$$U = \frac{\hat{e}}{\sqrt{2}} = \frac{N\zeta_{w1} \omega \hat{\phi}}{\sqrt{2}} \quad (3.8)$$

The peak flux must then be determined from the integral over the rotor pole pitch τ_p of the fundamental flux density wave $B_{\delta 1}$;

$$\hat{\phi} = r \int_0^{l'} \int_0^{\tau_p} \hat{B}_{\delta 1}(\theta) d\theta dz \quad (3.9)$$

Solving the integral, the peak flux is readily determined to be able to be expressed as;

$$\hat{\phi} = \alpha \hat{B}_{\delta 1} \tau_p l' \quad (3.10)$$

Where α is a waveform shape constant and for a sinusoidal wave is equal to $\pi/2$ and l' is the effective axial length of the machine. Using the above equations to solve for the number of series turns per phase results in the expression;

$$N_{ph} = \frac{\gamma \sqrt{2} U_{ph}|_{\max}}{\alpha \omega_e \zeta_{w1} \hat{B}_{\delta 1} \tau_p l'} \quad (3.11)$$

Which for an assumed sinusoidal wave, of $\hat{B}_{\delta 1} = 0.8T$, gives a value of $N_{ph} = 105.3$

¹The DC link voltage of a input rectifier of a three phase VSI is commonly calculated as $U_{DC} = 1.35U_{(L-L)in}$; $U_{(L-L)in} = 415V$ in the UK.

turns, which must then be conditioned to an integer value;

$$z_{Q_s} = \text{round} \left\lceil \left\lfloor \frac{2mN_{ph}}{Q_s} \right\rfloor \right\rceil \in \mathbb{Z}_{\text{even}} \quad (3.12)$$

Thus the lowest even integer of Eq. 3.11 is 104 turns. In a double layer winding with two coils per phase, the number of coil turns $N_{coil} = 52$. The phase resistance and end winding characteristics can then be calculated. The slot area is calculated as $A_{slot} = 560\text{mm}^2$ and the desired slot fill factor $S_{FF} = 0.6$, thus the wire diameter is calculated to be 2mm without insulation, corresponding to 2.19mm. The chosen wire has Grade II insulation (thicker insulation than standard wire) with a temperature grade of Class F (155 deg C).

3.1.4 End Length and AC Losses

An important consideration in a machine of this type is the end winding length, as the short end windings of the single tooth coils facilitate the machines superior performance over a conventional synchronous reluctance motor. The average end length for a double layer fractional slot concentrated winding is estimated (adapted from [7]), as presented in Chapter 2;

$$l_{end} \approx \frac{2.92 \left[\frac{D_{sso} - D_{ssi}}{4} + \frac{D_{ssi}}{2} \right]}{Q_s} \quad (3.13)$$

Thus the average end turn length for the prototype machine is calculated to be $l_{end} \approx 50\text{mm}$. If the end winding is assumed to be semi-circular, the axial extent of the end winding can be estimated by in the range of the following equality;

$$l_{axial(end)} \approx \frac{l_{end}}{\pi} \quad (3.14)$$

Where an end winding axial extent is predicted to be approximately 17mm. The per phase resistance R_{ph} is then calculated by;

$$R_{ph} = \frac{N_s l_m}{\sigma_{Cu} A_c} = \frac{2N_s}{\sigma_{Cu} A_c} (l_{axial} + l_{end}) \quad (3.15)$$

Thus the phase resistance is calculated to be $R_{ph} = 0.228\Omega$ for standard copper conductors, two coils in series per phase with 52 turns each. The calculated phase resistance is the DC resistance of the coil, the any AC skin effect must also be considered. The skin depth is calculated;

$$\delta = \frac{1}{\sqrt{0.5\omega_s \sigma_c \mu_0}} \quad (3.16)$$

Then, computed at a maximum rotor speed of 5000 rpm ($f_s = 166\text{Hz}$), in the conductor is 5mm, thus having no AC effect on the stator winding resistance due to the

conductors used in the design being 2mm in diameter. The proximity effect also exists, however, the slot average flux density will be very low as the slot width is considerable and due to the low pole number and low fundamental frequency, the proximity effect in this case is ignored.

3.2 Rotor Electromagnetic Design

With SynRM technology, in order to obtain good machine performance, the saliency ratio ξ and the torque index Θ must be maximized through good electromagnetic design of the rotor. The saliency ratio of the machine is mainly dictated by the electromagnetic design of the rotor, in particular the design of the *flux guides* with the aim of maximizing the q -axis reluctance and minimizing the d -axis reluctance. The stator leakage inductance does have an effect on the saliency ratio and must be taken into account. A recent and comprehensive study for conventionally wound synchronous reluctance motors by Moghaddam [10], as well as the vast archive of literature suggests there are a number of key criteria when selecting the rotor dimensions;

- Number of barriers (flux guides)
- Radial and tangential rib width
- Barrier insulation ratio

The barrier insulation ratio is the ratio of iron to air in the rotor, a 50-60% ratio generally provides best performance. The design of a synchronous reluctance machine rotor is therefore a multifaceted design process. Electromagnetic design must be traded off with mechanical strength and therefore maximum speed, as well as lamination manufacturability, in line with what can be achieved with the available manufacturing options for the required production volumes. Here, a single one off prototype is considered in the context of this thesis.

3.2.1 Number of Flux Barriers (Flux Guides)

In the majority of literature, two terms are often used for the shaped segments of a transversely laminated synchronous reluctance machine rotor. These are;

- *Flux barriers* - which are the air segments designed to minimize the q -axis flux
- *Flux guides* - which are the iron segments design to carry the d -axis flux

The number of flux barriers N_b , or flux guides N_g directly affects the torque capability, power factor and torque ripple of the machine through modifying the d - q inductances of the machine. Minimization of the q -axis inductance and maximization of the d -axis inductances are a key objective in the design of a synchronous reluctance rotor. A third

term, the number of layers N_l in relation to the number of barriers is $N_l = 2N_b + 1$ or $N_l = 2N_b$ if a cut-out is included, is essentially the sum of the segments in the design. The number of barriers is also a function of the number of poles, here only 4 pole designs are considered. The so called insulation ratio is the ratio of the width of the flux guides to the flux barriers. Rotor designs are analysed through finite element studies, the key performance indicators are charted with increasing barrier number whilst the insulation ratio is maintained constant at 0.5. The rotors are presented in Fig 3.7 and the results presented in Fig. 3.8. In the analysis the insulation ratio and the rib thicknesses (radial and tangential) remain constant. The radial ribs are included for mechanical strength.

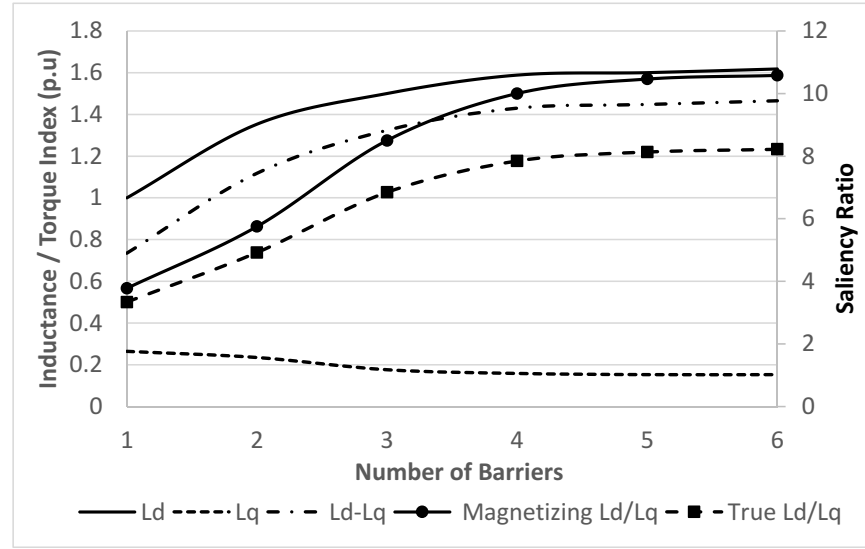


Figure 3.8: Key performance criteria variation with N_b

Figure 3.8 shows the general trend of machine d - q axis inductances with increasing barrier number alongside the saliency ratio (both true and magnetizing) and the torque index: the results are computed through non-linear FE analysis. It shows that rotors with $N_b = 1$ to $N_b = 5$ and $N_b = 5$ with cutout (number 6 on x -axis), equating to $N_l = 3$ to $N_l = 12$ provide increasing performance, though there is a clear plateau effect after 5 barriers. By increasing the number of layers the q -axis inductance is minimized whilst the d -axis inductance is maximized. The q -axis flux path reluctance is increased due to the increased distribution of air in the rotor, whilst the flux guiding capability in the d -axis is simultaneously increased, increasing the d -axis inductance. Thus, with increasing barrier number the saliency ratios and torque index are maximized, indicating a machine with maximum performance characteristics. Torque capability and power factor are increased with increasing barrier number and maximum of 12 layers is generally sufficient for maximum performance. The cutout provides a marginal performance boost due to an increased q -axis reluctance. These findings are in line with the literature [10] who report similar characteristics.

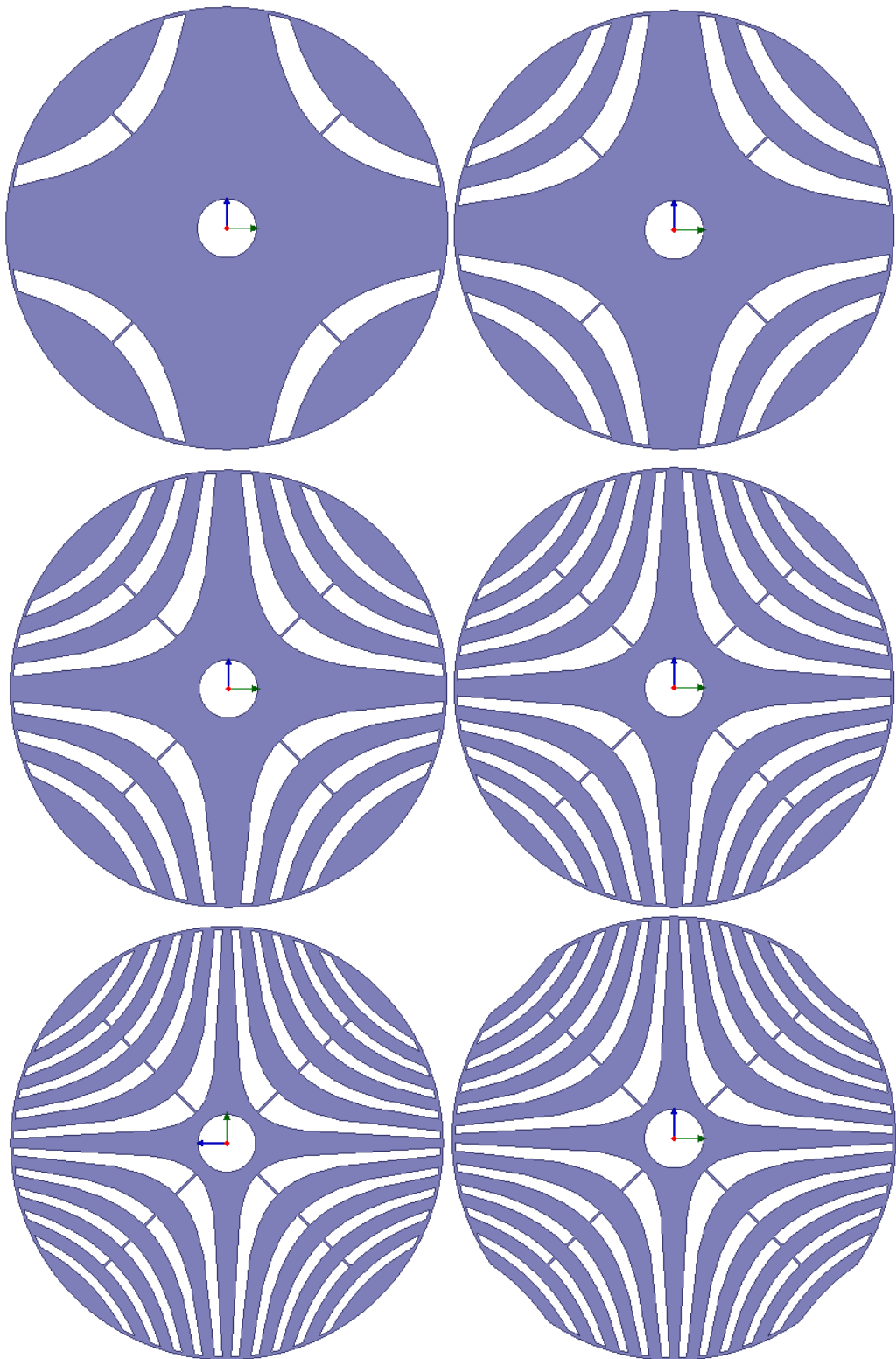


Figure 3.7: Barrier Number Visualisation, 1 to 5 barriers and 5 barriers with cut-out, equivalent to 3 to 12 layers

3.2.2 Tangential and Radial Rib Width

The tangential and radial ribs, shown in Figure 3.9, are important both electromagnetically and mechanically. These ribs must be saturated under normal operation as to inhibit any q -axis flux leakage that would otherwise reduce machine performance. This suggests that the width of t_t and t_r , the tangential and radial ribs, must be small in practical machine designs: widths equal to the lamination thickness are achievable in practice when using stamping techniques. However, small ribs impact upon the mechanical strength of the rotor and therefore affects not only the magnetic performance, but also the maximum operating speed relating to the maximum tensile stress of the rotor lamination material.

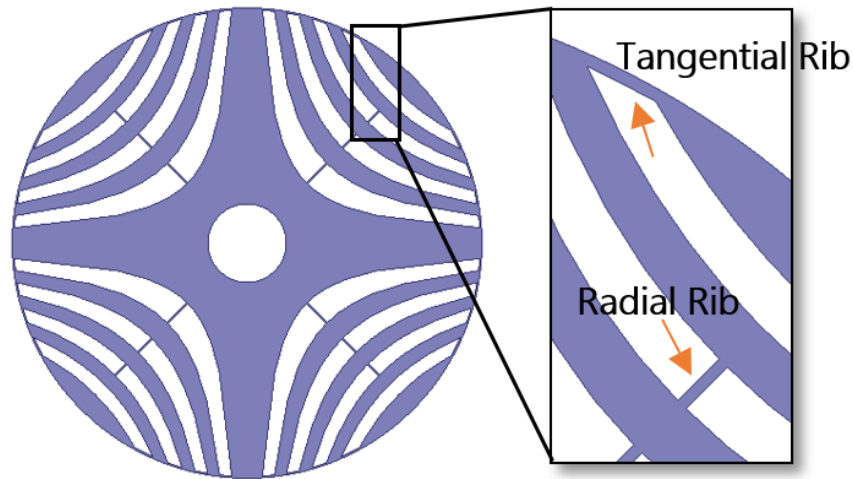


Figure 3.9: Depiction of the rotor tangential and radial ribs

Figure 3.10 shows the orthogonal axis inductances as a function of current whilst varying rib thicknesses between 0.01 and 3mm, derived from FEA studies. It is clear that any increase in the tangential or radial rib thicknesses significantly increases the q -axis inductance in the unsaturated region, thus small thickness ribs maximize the electromagnetic performance of the machine, maximizing the power factor (reduce converter size) and also to maximize the mean torque capability (torque/power density). The effect on the q -axis inductance with tangential rib thickness is slightly more pronounced as q -axis flux can now circulate around the tips of the flux barriers in a low reluctance path, lowering the power factor and torque capability in the unsaturated region. The d -axis inductance is relatively unchanged with radial rib thickness as would be expected, but as the tangential rib thickness is increased from effectively zero to 0.1mm, the flux capturing capability of the rotor increases the d -axis inductance. In summary, the radial and tangential ribs should be small enough to provide maximum electromagnetic performance but still function to hold the rotor segments together under mechanical stress. Again, these FEA results are in good agreement with findings in the literature [10].

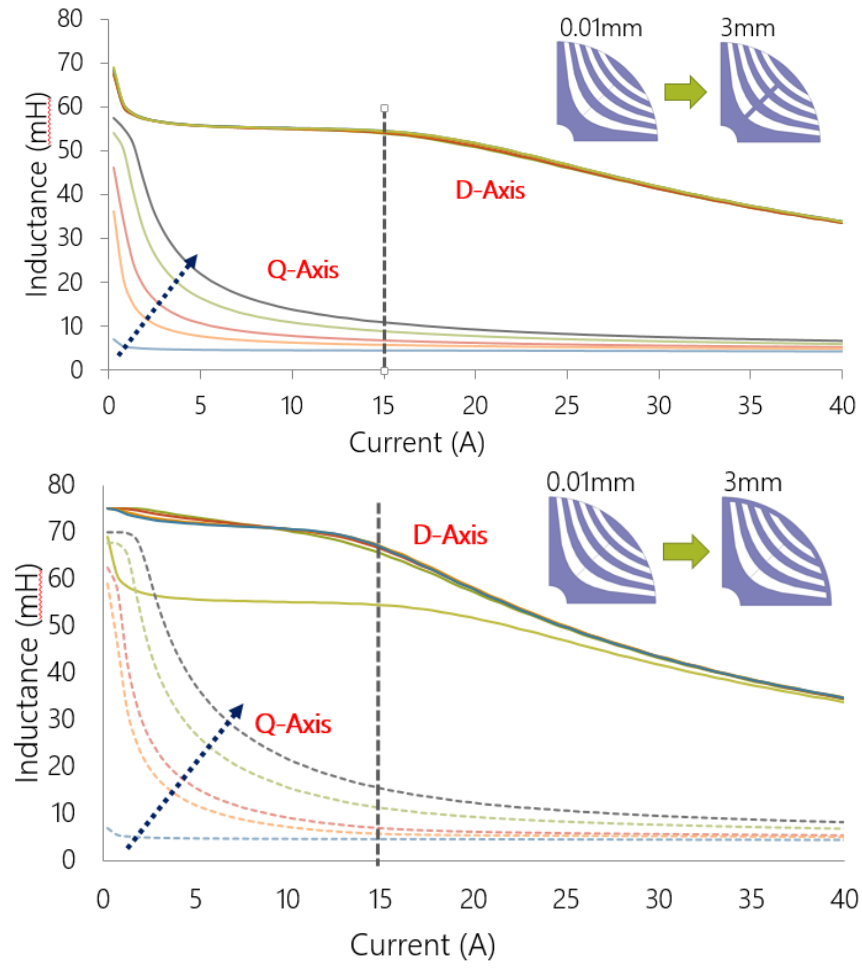


Figure 3.10: $L_{d,q} = f(i)$ for radial (top) and tangential (bottom) rib thickness variation

3.2.3 cSynRM Rotor Design

The design and optimization of the rotor lamination profile is presented in-depth in Chapter 6, which deals with a developed novel post-processing tool, the rotor design and optimization leading to the final rotor lamination profile. As the specific details are left until Chapter 6, here only a short summary of the rotor design is presented. The rotor design for the cSynRM prototype machine must have as high a saliency ratio as possible, whilst maintaining mechanical strength. In this thesis, fractional slot concentrated windings have been applied to synchronous reluctance machines, and it was suggested in Chapter 2 that they could potentially manifest large torque ripple. Here a 6 slot, 4 pole machine with a transversely laminated multiple flux barrier synchronous reluctance rotor is presented, the design is typical of that of a conventional synchronous reluctance motor with high saliency and low torque ripple when magnetized by a distributed winding stator with a large number of slots. The rotor is not optimised for use with fractional slot concentrated windings. A 2D cross-section as used in the FEA model is presented in Figure 3.11.

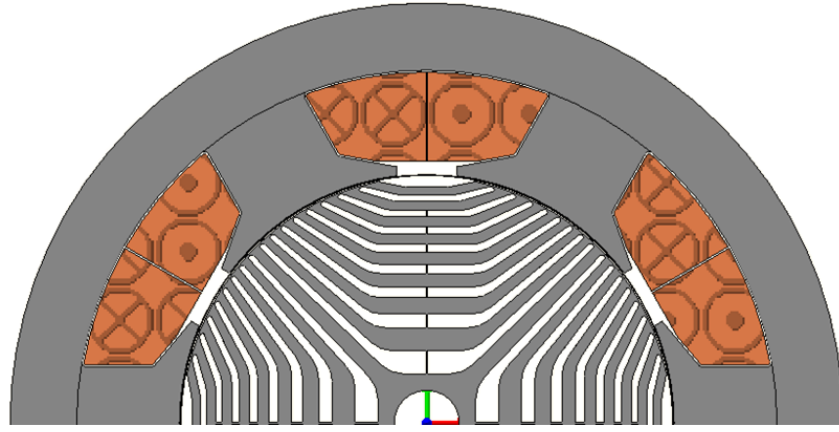


Figure 3.11: 6-slot 4-pole cSynRM 2D cross-section

If the same rotor as in Fig. 3.11 was inserted into a 36 slot distributed wound stator, the torque ripple is low, this however is not the case with the equivalent 4-pole fractional slot concentrated winding. Figure 3.12 shows the FEA computed torque waveforms for the rotor with the distributed winding (SynRM) and the chosen fractional slot concentrated winding (cSynRM). Both machines have identical sinusoidal current source excitation and are simulated at 1500rpm, the base speed of the cSynRM and are simulated using a 2D time stepping finite element model in Infolytica MagNet.

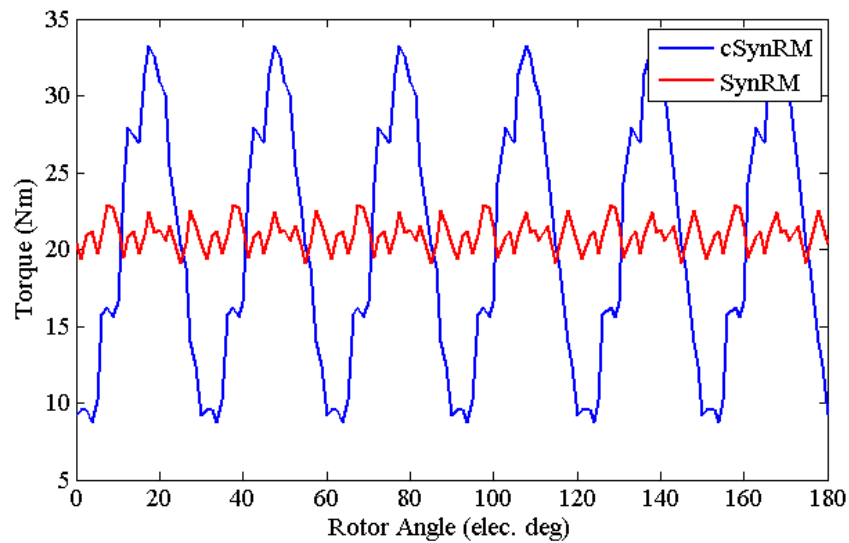


Figure 3.12: Comparison of torque waveforms (SynRM and cSynRM)

From Fig. 3.12, it is clear that there is considerable torque ripple with the fractional slot concentrated winding and not with the distributed winding. The excitation pattern and rotor design are identical, only the stator and coil distribution has changed. The torque ripple as a percentage of the mean torque is 106% in the cSynRM and is less than 10% in the SynRM, whilst the magnitude of the mean torque is approximately 22Nm in both machines. The high level of torque ripple is unacceptable in many applications and is usually found in switched reluctance machines (SRM), but not synchronous reluctance machine

technology as they usually have distributed windings. Analysis must be performed and the issues mitigated through improved electromagnetic design in order to realize a practically viable machine, with improvements in the torque quality. For now, it is sufficient to say that the high torque ripple derives from the discrete placement of coils around the airgap periphery and follows from the high levels of space harmonic content in the MMF distribution for the cSynRM machine. A full analysis can be found in Chapter 6, for now a qualitative discussion of the optimised rotor lamination profile is presented.

3.2.4 Final Rotor Lamination Profile

The final rotor design, achieved through simple optimization as detailed in Chapter 6, shows a good mean torque capability with significantly lower torque ripple than described in Section 3.2.3. The improved electromagnetic design allowed maintenance of the mean torque level but a reduced torque ripple to approximately 40%. The cross section of the final motor geometry is presented in Figure 3.13.

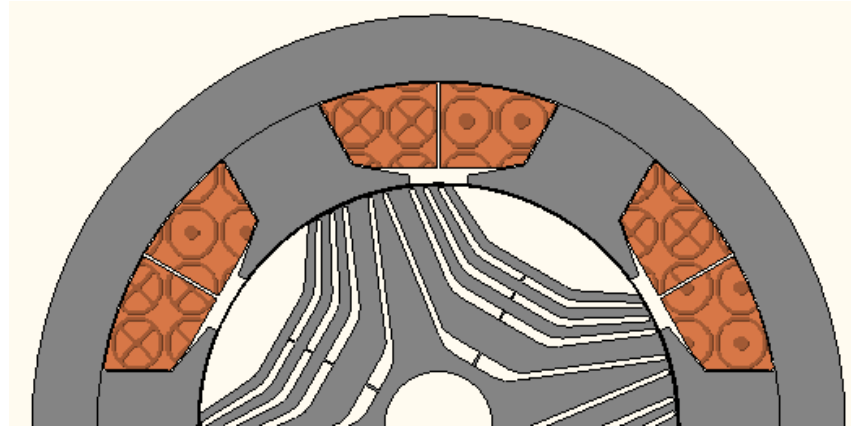


Figure 3.13: Initial rotor design

With regard to the rotor features, a four flux barrier (5 flux guides) design results from the electromagnetic optimization; a q -axis cut out is also incorporated into the rotor lamination profile with two functions. Firstly the q -axis cut out helps to reduce the machines torque ripple and it also acts to reduce the machines q -axis inductance, increasing the magnetizing saliency ratio of the machine. The radial and tangential rib widths are small, 0.3mm width for both the tangential and radial ribs, with the exception that the innermost radial rib is increased to a thickness of 0.5mm for the mechanical integrity of the rotor. Mechanical stress analysis of the rotor design using FEA studies is presented in Section 3.7. The small rib widths provide maximum electromagnetic performance (by easily saturating with a low applied MMF, acting to limit the q -axis magnetizing inductance) but do act to reduce the maximum operating speed of the motor at these small dimensions. Rotordynamic analysis, including bending modes and torsional modes of the final rotor design is presented in Section 3.7. The prototype rotor design minimizes parasitic effects

through improved electromagnetic design, as described in Chapter 6. A tab is included in the lamination profile for location of the lamination stack on the shaft key way.

3.3 Analytical Inductances

The inductances of the cSynRM are very important with regard to machine performance, dictating the saliency ratio and the torque index. This section details analytical inductance calculations for the cSynRM prototype geometry: it is assumed that the iron is infinitely permeable and that saturation can be taken into account by a suitable saturation factor k_s . Firstly, the orthogonal axis magnetizing inductances are calculated and then the various leakage inductances are calculated, assuming that they do not vary with saturation or rotor angle. Under these assumptions, standard calculation methods apply and it must be noted that the direct axis inductance is more susceptible to saturation effects than the quadrature axis inductance. The main purpose of this section is to identify the dominant stator leakage component of inductance in a machine of this design and to approximate its unsaturated saliency ratio.

3.3.1 Airgap Length

The selection of the airgap length is important as a smaller airgap means a lower magnetizing current is required leading to a higher power factor, however iron losses may increase reducing the efficiency. Mechanical limitations also play an important role and thus the airgap length is chosen based on experience of constructing demonstrator machines at Newcastle University. The airgap length is selected as 0.5mm and matches closely with that suggested by Lipo [1] and the second by Say [11];

$$\delta = 3\tau_p\sqrt{2p} \quad (3.17)$$

$$\delta = 0.2 + 2\sqrt{D_\delta L_s} \quad (3.18)$$

Where τ_p is the rotor pole pitch, p the number of rotor pole pairs, D_δ the airgap diameter and L_s the stack length. These are based on mechanical limitations and experience in the design of both synchronous and asynchronous machines as in [1,2].

3.3.2 Magnetizing Inductances

Both the d and q axis magnetizing inductances can be calculated by the same equation, which is a general expression for the magnetizing inductance of a synchronous machine described in [1], the d and q axis only differ due to the effective airgap δ_{eff} respective to

its own axis. The magnetizing inductance can be expressed [1];

$$L_m = \frac{mD_\delta\mu_0l'}{\pi p^2\delta_{eff}}(k_{w1}N_s)^2 \quad (3.19)$$

where, m is the number of phases, D_δ is the airgap diameter, l' is the effective core length, k_{w1} the fundamental winding factor, N_s the number of series turn per phase and the effective airgap δ_{eff} is given by [13];

$$\delta_{eff} = gk_C(1 + k_S) \quad (3.20)$$

Here g is the minimum airgap, k_S a saturation factor and k_C is Carter's factor given as [2];

$$k_C = k_{Cs}k_{Cr} = \left(\frac{\tau_{us}}{\tau_{us} + k_S b_{s1}}\right) \left(\frac{\tau_{ur}}{\tau_{ur} + k_r b_{r1}}\right) \quad (3.21)$$

where k_{Cs} and k_{Cr} are the Carter factors relating to the stator and rotor. The τ terms relate to the stator and rotor slot pitches and the b terms the actual/equivalent slot opening widths. In general, the slot opening correction factor is given as [3];

$$k = \frac{2}{\pi} \left[\arctan\left(\frac{b_1}{2g}\right) - \frac{2g}{b_1} \ln \sqrt{1 + \left(\frac{b_1}{2g}\right)^2} \right] \quad (3.22)$$

This analytical formula is derived from conformal mapping solutions of the field pattern at the slot opening and it beyond this scope to explore this further. With the stator geometry for the cSynRM prototype, the stator, rotor and total Carter factors are 1.24, 1.13 and 1.4 respectively. The magnetizing inductance calculations, based on this theory, are expected to differ from actual values due to saturation conditions in the rotor radial and tangential ribs which are neglected in the analysis.

3.3.2.1 Direct-Axis Inductance

In the direct axis, the effective airgap is the mechanical airgap of 0.5mm corrected by Carter's factor. The magnetizing inductance with d -axis effective airgap assuming a saturation factor of $k_S = 0.3$ (as suggested by the authors in [1, 3 and 11]), is given as;

$$\delta_{eff(q)} = gk_C(1 + k_S) = 0.91\text{mm} \quad (3.23)$$

$$L_{md} = \frac{3D_\delta\mu_0l'}{\pi p^2\delta_{eff(d)}}(k_{w1}N_s)^2 = 35.29\text{mH} \quad (3.24)$$

3.3.2.2 Quadrature-Axis Inductance

In the quadrature axis, the q -axis effective airgap is larger due to the rotor cut out and the rotor flux barriers which contain air. Here it is assumed that the q -axis flux crosses the

majority of the flux barriers. The largest contributor to the airgap length is the q-axis cut out and again assuming a saturation factor $k_S = 0.3$, the q-axis inductance is given as;

$$\delta_{eff(q)} = (g + l_{cutout} + \sum w_{air}) k_C (1 + k_S) = 21.6\text{mm}$$

where l_{cutout} is the cutout depth and $\sum w_{air}$ is the sum of the widths of the air barriers in the rotor, then the magnetizing inductance is calculated as;

$$L_{mq} = \frac{3D\delta\mu_0 l'}{\pi p^2 \delta_{eff(q)}} (k_{w1} N_s)^2 = 1.6\text{mH} \quad (3.25)$$

3.3.3 Stator Leakage Inductances

Also contributing to the axis inductances is the stator leakage inductance, the total direct and quadrature axis inductances of the cSynRM prototype are written as Eq. 2.27 & Eq. 2.28. This stator leakage inductance $L_{s\sigma}$ comprises of a number of components [2];

$$L_{s\sigma} = \left(\frac{2\mu_0 N_s^2 l'}{pq} \right) \left(\lambda_s + \frac{l_e}{l'} \lambda_e + \lambda_{tt} + \lambda_h \right) \quad (3.26)$$

Where λ_s , λ_e , λ_{tt} and λ_h are the slot leakage, end winding, tooth tip and differential (airgap harmonic) permanence coefficients respectively. The permanence coefficients and associated inductances are calculated in this subsection and all calculations follow those described by Gieras [2]. The slot leakage, end winding and tooth tip leakage inductance arise solely due to the geometry of the machine and do not cross the airgap. The differential leakage inductance, otherwise known as the harmonic leakage component is partly due to the geometry of the machine but is mainly due to space harmonic content in the airgap and is the only leakage flux to cross the airgap. The expressions used here are based on conformal mapping techniques.

3.3.3.1 Stator Slot Leakage

The flux mostly crosses the airgap and links the rotor, however some of it crosses the slot from tooth to tooth, which is a slot flux leakage. The *slot leakage inductance* relating to this slot leakage flux is given as;

$$L_s = \left(\frac{2\mu_0 N_s^2 l'}{pq} \right) \lambda_s \quad (3.27)$$

Where the slot leakage permanence coefficient λ_s is dependent upon the slot geometry. The dimensions of interest for analytical calculation of the slot leakage and the tooth tip leakage are presented in Fig. 3.14;

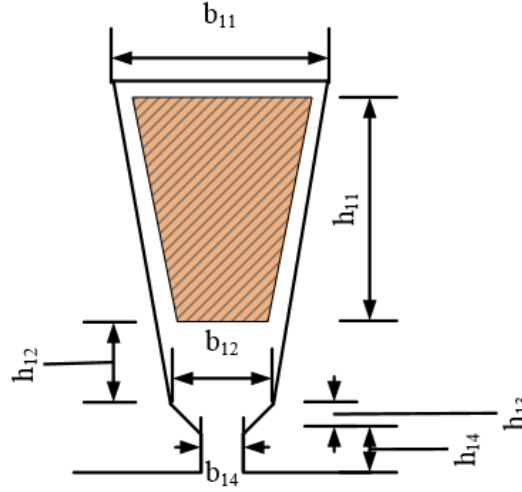


Figure 3.14: Slot dimensions in relation to the slot leakage permanence

The dimension h_{11} is the height of the coil, b_{11} is the width of the top of the slot, b_{12} is the length of the narrowest part of the slot, height h_{12} is the distance between the bottom of the coil and slope of the tooth tip. The width b_{14} is the slot opening, h_{14} is the height of the tooth tip and h_{13} is the height of the tooth tip slope. For the prototype slot geometry, using conformal mapping techniques, the slot permanence coefficient λ_s for double layer horizontal divided windings is given by [2];

$$\lambda_s = \frac{h_{11}}{3b_{12}}k_t + \frac{h_{12}}{b_{12}} + \frac{2h_{13}}{b_{12} + b_{14}} + \frac{h_{14}}{b_{14}} \quad (3.28)$$

where the factor [2];

$$k_t = 3 \left(\frac{4t^2 - t^4(3 - 4\ln t) - 1}{4(t^2 - 1)^2(t - 1)} \right) \quad \& \quad t = \frac{b_{11}}{b_{12}} \quad (3.29)$$

Working through based on geometrical dimensions, the slot leakage inductance is determined to be $L_s = 1.67\text{mH}$. The calculation assumes that the flux crosses the slot in a straight and horizontal fashion and does not include the leakage close to the airgap where this assumption becomes invalid: this is modeled as the tooth tip leakage inductance separately (conformal field maps). This calculation method is based on the methods in [1,3,6].

3.3.3.2 Tooth Tip Leakage

Some flux also crosses from tooth tip to tooth tip in the machine, the *tooth tip leakage inductance* accounts for slot leakage close to the airgap not included in the slot leakage inductance calculation. It can be approximated by [2];

$$L_{tt} = \left(\frac{2\mu_0 N_s^2 l'}{pq} \right) \lambda_{tt} \quad (3.30)$$

the tooth tip permanence coefficient λ_{tt} is given by [2];

$$\lambda_{tt} = \left(\frac{5g}{b_{14}} \right) \cdot \left(5 + \frac{4g}{b_{14}} \right)^{-1} \quad (3.31)$$

Where g is the airgap minimum length. Again, working though the calculation based on the prototype machine geometry, the tooth tip leakage inductance $L_{tt} = 182\mu\text{H}$.

3.3.3.3 End Winding Leakage

The end turns at the extremity of the stack length also have an associated leakage flux that does not link the main magnetic circuit. This *end winding leakage* inductance can be expressed analytically, where here the end winding leakage inductance can be approximated by [2];

$$L_{ew} = \left(\frac{2\mu_0 N_s^2 l'}{pq} \right) \lambda_{ew} \quad (3.32)$$

the end winding permanence coefficient λ_{ew} is given by;

$$\lambda_{ew} = 0.34q \left(1 - \frac{2}{\pi} \frac{w_c}{l_{ew}} \right) \quad (3.33)$$

The end winding leakage inductance $L_{ew} = 138\mu\text{H}$. As the stator coils are wrapped around a single tooth, mutual end winding coupling is very low and not taken into account in the calculation. This approach is similar to that described in [3] which has good correlation with the methods described in [13,14]. The tighter the stator coil end turns are to the iron stack, the shorter the mean end winding length l_{ew} . This maximizes the ratio $\frac{2}{\pi} \frac{w_c}{l_{ew}}$ and hence minimizes the end winding permeance coefficient. These tight coils, as expected in the cSynRM prototype, act to maintain a lower end winding leakage inductance.

3.3.3.4 Airgap Harmonic Leakage

The *differential leakage* or *airgap harmonic leakage inductance* is the only leakage to cross the airgap. Spatial harmonics create fluxes that cross the airgap and link the rotor: this is leakage as it is asynchronous to the rotor synchronous speed. The harmonic leakage can be approximated as [2];

$$L_h = \left(\frac{2\mu_0 N_s^2 l'}{pq} \right) \lambda_h \quad (3.34)$$

where the airgap harmonic leakage permanence coefficient λ_h is approximated by [2];

$$\lambda_h \approx \left(\frac{mq\tau_p k_{w1}^2}{\pi^2 \delta_{eff}} \right) \left(\frac{\pi^2 (10q^2 + 2)}{27} \sin^2 \left(\frac{30}{q} \right) - 1 \right) = \left(\frac{mq\tau_p k_{w1}^2}{\pi^2 \delta_{eff}} \right) \sigma_h \quad (3.35)$$

Here σ_h is a factor describing the magnitude of the harmonic leakage, m is the number of phases, τ_p is the rotor pole pitch and q the number of slots per pole per phase. The air-gap harmonic leakage inductance is approximated by $L_h = 7.04\text{mH}$. Notice that this leakage depends upon the effective airgap length, this will be important in the measurement of the stator leakage inductance in Chapter 5. A relatively large value of the air gap harmonic leakage is not a surprising result for this machine as the rich MMF harmonic content as a result of the chosen slot-pole combination is well known.

3.3.4 Summary and Saliency Ratio Calculations

From the analytical calculations, it is clear that the dominant leakage component is the airgap harmonic leakage inductance L_h . This is due to the high levels of space harmonic content in the small airgap, which acts to degrade the saliency ratio of the machine. The slot leakage is the second largest component, followed by the tooth tip and end winding leakage components. This appears to show that the end effects are low with regard to flux leakage and the major leakage is actually airgap crossing. The sum of the calculated leakage inductances giving a calculated total leakage inductance is $L_{s\sigma} = 9.02\text{mH}$, negating the airgap harmonic leakage the *geometric* (or *constructional*) leakage inductance is calculated $L_c = 1.99\text{mH}$. Table 3.2 summaries the analytically calculated prototype magnetizing and leakage inductances as well as the true and magnetizing saliency ratios of the prototype machine. The calculated inductances are compared with FEA in this chapter, Section 3.4 and are also compared with measurements in Chapter 5.

Inductance Component	Symbol	Value
d-Axis Magnetizing Inductance	L_{md}	35.3mH
q-Axis Magnetizing Inductance	L_{mq}	1.60mH
Slot Leakage Leakage	L_s	1.67mH
Tooth-Tip Leakage	L_{tt}	0.181mH
End Winding Leakage	L_{ew}	0.138mH
Airgap Harmonic Leakage	L_h	7.04mH
Total Stator Leakage	$L_{s\sigma}$	9.02mH
Constructional Stator Leakage	$L_c = L_{s\sigma} - L_h$	1.99mH
Direct Axis Inductance	L_d	44.29mH
Quadrature Axis Inductance	L_q	10.60mH
Magnetizing Saliency Ratio	ξ_{mag}	22.06
True Saliency Ratio	ξ_{true}	4.17

Table 3.2: Summary of prototype inductances and calculated rotor saliency

The magnetizing saliency ratio, which ignores any leakage, is very large. A high saliency ratio is desirable for multiple flux barrier rotors. The true saliency ratio taking

into account the leakage inductance is significantly lower, based on the analytical approximations of the various leakage inductances, this lower saliency ratio is the result of the impact of the airgap harmonic leakage caused by the space harmonic content in the airgap. It is interesting to note that if the airgap harmonic leakage was of the magnitude compared to that of distributed windings ($\sigma_h < 0.0275$ [1,2]), the true unsaturated saliency ratio would be closer to 9, rather than 4, leading to a higher power factor and efficiency. This section therefore shows the detrimental effect on the machines saliency by the space harmonic content of the airgap due to the adoption of fractional slot concentrated windings.

3.3.5 Note On Analytical Inductance Calculation

Although some leakage fluxes with their corresponding inductances will somewhat vary with rotor position and localized saturation etc., the calculated inductances represent an estimate of the average values based on the respective permeance coefficients. The inductance calculations presented do not take into account all saturation effects and only the lumped saturation factor modulates the magnetizing inductances where as the leakage inductances are calculated neglecting saturation altogether. Saturation is mainly an issue with the d -axis magnetizing inductance due to the small airgap, however in the q -axis the effective airgap is large and any saturation effects are minimal. The finite element method is much more accurate in calculating the saturated orthogonal axis inductances, however, the analytical results are still very useful for a first-order approximation of the unsaturated d -axis inductance, the q -axis inductance and the leakage inductances, especially in determining the dominant stator leakage component.

3.4 Final Design Performance Analysis

For accurate performance calculation at load and calculation of the saturated orthogonal axis inductances, finite element analysis is best employed. The following section uses finite element analysis performed in Infolytica MagNet and Motorsolve to calculate the machine performance.

3.4.1 Rated Load Performance

The performance of the designed Fractional Slot-Concentrated Winding Synchronous Reluctance Motor (cSynRM) is now calculated through finite element studies. The 2D finite element studies include the calculated lumped element end winding leakage in order to partially account for end effects, the calculation is found in Section 3.3. At the rated operating point of 1500rpm, it is chosen that the total permissible loss (copper + factored

iron loss) is 340W ². Based on this loss figure, the rated current found to be $I_s = 21.2\text{A}$. The simulation uses pure sinusoidal excitation, no time harmonics are included and the chosen current angle in the constant torque region (including the rated operating point) is set at 45 degrees, corresponding to maximum torque per Ampere. The rotor speed is held at base speed $n_{base} = 1500\text{rpm}$ ($f_s = 50\text{Hz}$). Two-dimensional finite element analysis is performed for the final design: a flux contour plot and shaded magnetic flux density plot is presented at the rated load point in Fig. 3.16, for an arbitrary rotor angle. Table 3.3 shows the FEA calculated performance of the final design at the operating point ($I_s = 21.2\text{A}$, $n = 1500\text{rpm}$, $P_{loss} = 340\text{W}$).

Performance Criteria	FEA Result
Electromagnetic Torque, T_{em} (Nm)	21.98
Efficiency, η (%)	91.1
Torque Ripple, ΔT (% of mean)	44%
RMS Current Density, J (A/mm ²)	6.75
RMS Line Current, I_{line} (A)	21.2
Total Loss, P_{loss} (W)	341
Winding Loss, P_{Cu} (W)	301
Iron Loss, P_{Fe} (W)	37.7
Power Factor, $\cos\{\varphi\}$	0.48
Inverter Utilisation ($0.01 \cdot \eta \cdot \cos\{\varphi\}$)	0.44

Table 3.3: cSynRM Performance at 1500rpm with $I_s = 21.2\text{A}$ (340W loss)

The table shows that the final design has a good energy conversion efficiency, facilitated by a reduction in copper loss with high fill factor and short end windings due to the single tooth coils and the segmented stator. The lower copper loss and corresponding current density have benefits in regard to the machines thermal performance. The machine produces 21.98Nm of torque at 1500rpm , equating to approximately 3.5kW for 341W of losses. The iron loss is calculated in the software using the modified Steinmetz equation and Bertotti separation method. As predicted, the machine power factor is low, this has been explained in both Chapter 2 and in this chapter - this then leads to poor inverter utilization, even at high energy conversion efficiency. The efficiency meets the required efficiency specification of $>90\%$ as outlined in Table. 3.1. These results are verified in Chapter 5 though experimental measurements of a prototype machine on both static and dynamic test rigs.

²The loss figure of 340W is typically used at with the Electrical Power Group at Newcastle University as a figure for research grade electrical machine comparison.

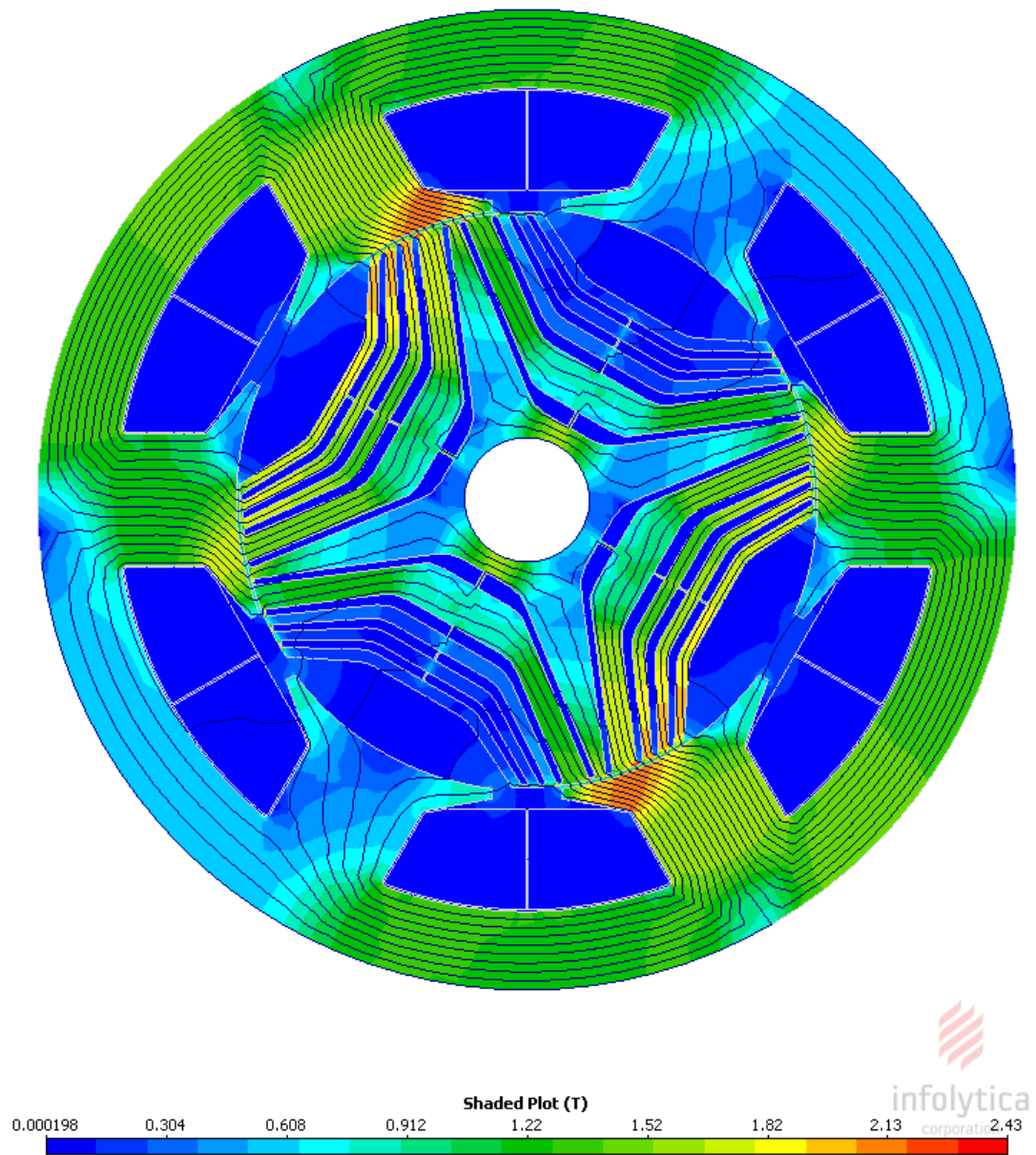
Prototype Design 1**Flux function (Wb/mm)
Flux density (T)**

Figure 3.15: 2D FEA plot of the designed machine at rated operating point

3.4.2 FEA Torque vs Speed Curve

The torque-speed envelope is calculated using finite element studies by applying rated current and setting a maximum voltage level with respect to the DC Link voltage. A current angle of 45 degrees is initially applied and then the simulation increases the speed of the machine until the voltage limit is hit, which is at the knee point of the end of the constant torque region. At this point the current angle is increased with speed such that the operating point is within the DC link voltage limit. This process continues across the speed range until no torque can be produced by the machine. This simulation was performed in the software Infolytica Motorsolve, which gives near identical results to the FEA software Infolytica MagNet but simplifies efforts by automating the torque-speed curve generation. Figure. 3.16 shows the torque-speed and power-speed curves of the designed machine at rated current.

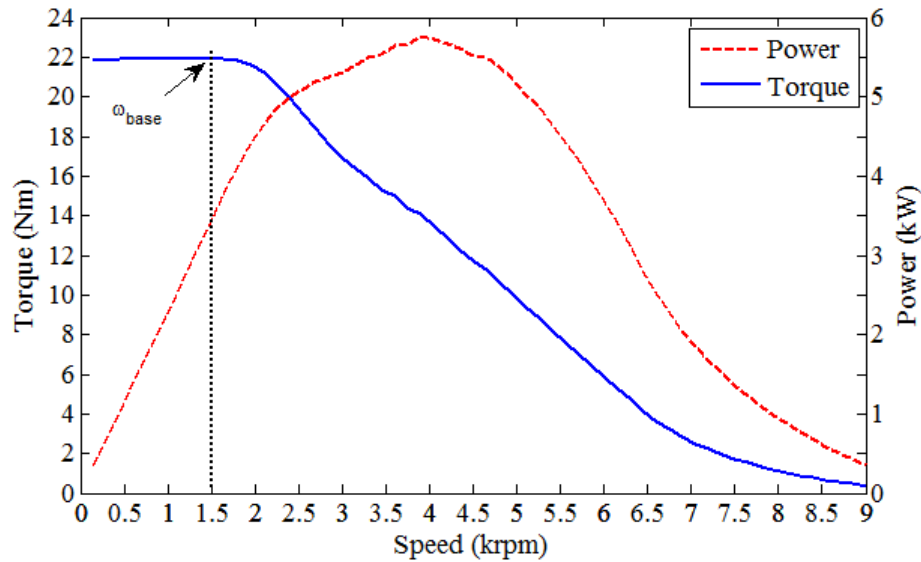


Figure 3.16: Torque and power vs speed curves for rated current limit

From Fig 3.16, the constant torque region has a slight voltage headroom on the base speed operating position at rated current compared with the design point of 1500rpm, this is due to the rounding down of the number of turns and also the inclusion of the utilisation factor in the number of turns calculation. It is clear that by adjusting the current angle from 45 degrees (maximum torque per Ampere) through to 85 degrees, a maximum speed of 9000 rpm can be achieved by the machine. The machine power rises linearly in the constant torque region and has a constant power region from 2500 rpm to 5000 rpm giving a constant power speed range (CPSR) of 3.33 and a maximum speed range of 6. These results are compared with experimental results in Chapter 5.

3.4.3 FEA Calculated Inductances

In Section 3.3, the final machine design orthogonal axis inductances were calculated analytically: these are the *unsaturated inductances* that are compensated for constant sat-

uration by a crude lumped element saturation factor. The machine inductances can also be calculated through the finite element method and a detailed analysis and comparison of their characteristics with the conventionally wound SynRM is presented in Chapter 7. Here, the stator MMF is aligned with phase-A and the rotor is rotated into the d - and q -axis positions for a range of currents between 0 and 40A. This allows calculation of the machines orthogonal axis inductances as a function of current and shows the saturation characteristic. Figure. 3.17 shows the FEA evaluated d - and q - axis inductances, L_d and L_q .

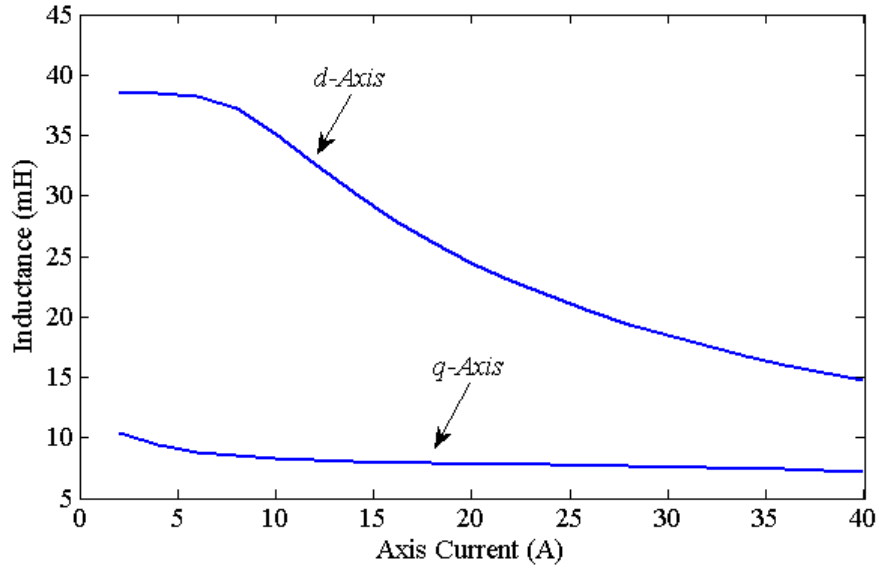


Figure 3.17: FEA calculated d - and q -axis inductances

The figure shows the inductances calculated from the d - q -axis flux linkages. The q -axis inductance saturates quickly, in the region of axis current 0 to 5A the radial and tangential ribs are saturating, once this material is saturated the q -axis inductance remains relatively constant at approximately 8mH across the current range. This d -axis inductance shows a strong saturation characteristic with increasing axis current as would be expected. In the unsaturated region (between 0 and 5A axis current) the FEA calculated unsaturated d - and q -axis inductances are $L_d^{FEA} = 38.5\text{mH}$ and $L_q^{FEA} = 10.4\text{mH}$. These values are very close to the analytically calculated axis inductances from Section 3.3, where the analytically calculated q -axis inductance is 10.60mH and the d -axis inductance is 44.29mH. These inductances are compared with measured values in Chapter 5. Chapter 5 also attempts to split the inductances into magnetizing and leakage components and measurement of the stator leakage inductance is also attempted. Figure. 3.18 shows the magnetic vector potential contour plots of the rotor in the d -axis and q -axis positions.

From the FEA calculated inductances, the saliency ratios can be calculated. The analytical value from Section 3.3 is $\xi_{true} = 4.17$, the FEA results give $\xi_{true} = 3.70$. The true saliency ratio in the cSynRM machine is greatly reduced due to the high stator leakage inductance. The saturated saliency ratio is calculated as 3.11.

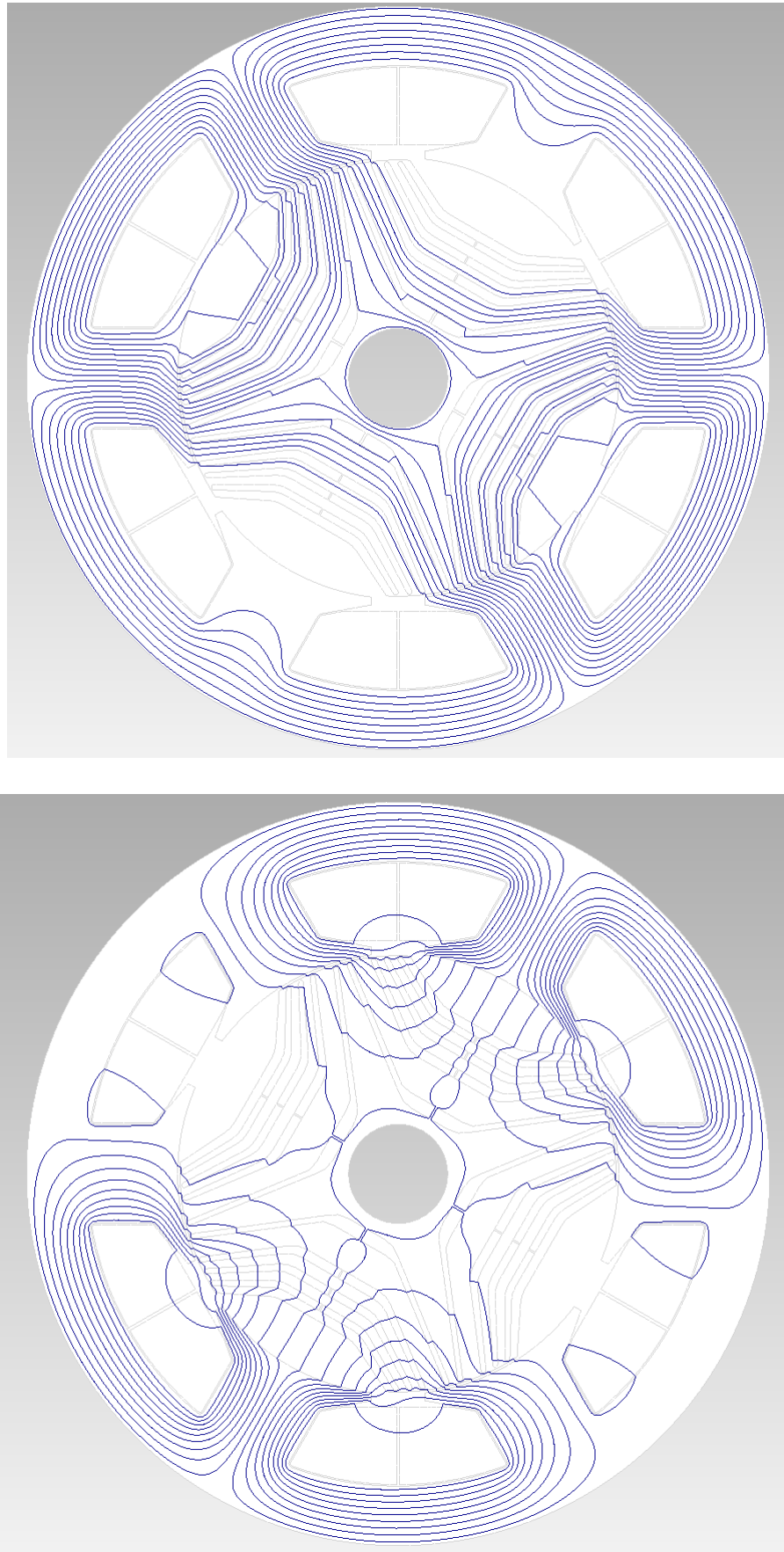


Figure 3.18: Flux plots in the d - and q -axis rotor positions

3.4.4 Note on cSynRM Inductances

The inductances as presented are for a single rotor angles with respect to the MMF being aligned with phase-A and the rotor being aligned with that axis in the d - and q -axis positions. It must be noted here that if the MMF axis is rotated around the machine and the orthogonal axis inductances computed with respect to this, the inductances in the dq frame oscillate about a mean value. This is further investigated in Chapter 7.

3.5 Influence of Slot Wedges and Rotor Skew

3.5.1 Semi-Magnetic Slot Wedges

Usually, electrical machines use a non-magnetic slot wedge made from either a high temperature plastic or glass fibre that have a relative permeability of $\mu_r = 1$. The function of the slot wedge is solely to hold the windings into the stator slot and prevent them from bulging out into the airgap. It has been shown in the literature [15] that switching to a semi-magnetic slot wedge with a low, but >1 relative permeability in the range $2 \leq \mu_r \leq 10$ can act to reduce the harmonic content in the airgap by modulating the flux paths. This leads to an improved (more sinusoidal) flux distribution, but does lead to increased tooth tip leakage flux due to the increase in permeability. In this simple study, two commercially available semi-magnetic slot wedge materials are compared through FE analysis to ascertain whether such wedges are advantageous in reducing the torque ripple without compromising machine performance. Figure 3.19 shows the position and shape of the slot wedges used in the FE model.

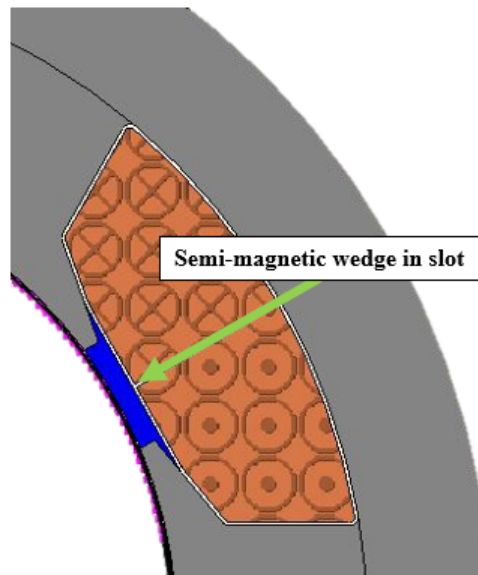


Figure 3.19: Semi-magnetic wedge model

The chosen semi-magnetic wedge materials are commercially available and found in varying applications. The two materials are the Camawi and SPU-H HP wedge materials,

Table 3.4 outlines their mechanical properties.

	Camawi	SPU-H HP
Thickness [mm]	2	2
Electrical Conductivity [S/m]	0.22	0.95
Specific Weight [$\text{g} \cdot \text{cm}^{-3}$]	3.4	3.5
μ_r	3-6	2-3
Compressive Strength [MPa]	160	200
Temperature Class	F (155)	H (180)

Table 3.4: Semi-magnetic wedge mechanical properties

The two modeled semi-magnetic wedges have $\mathbf{B} - \mathbf{H}$ curves given by the manufacturers, these are presented in Figure. 3.20 along with the calculated relative permeability curves.

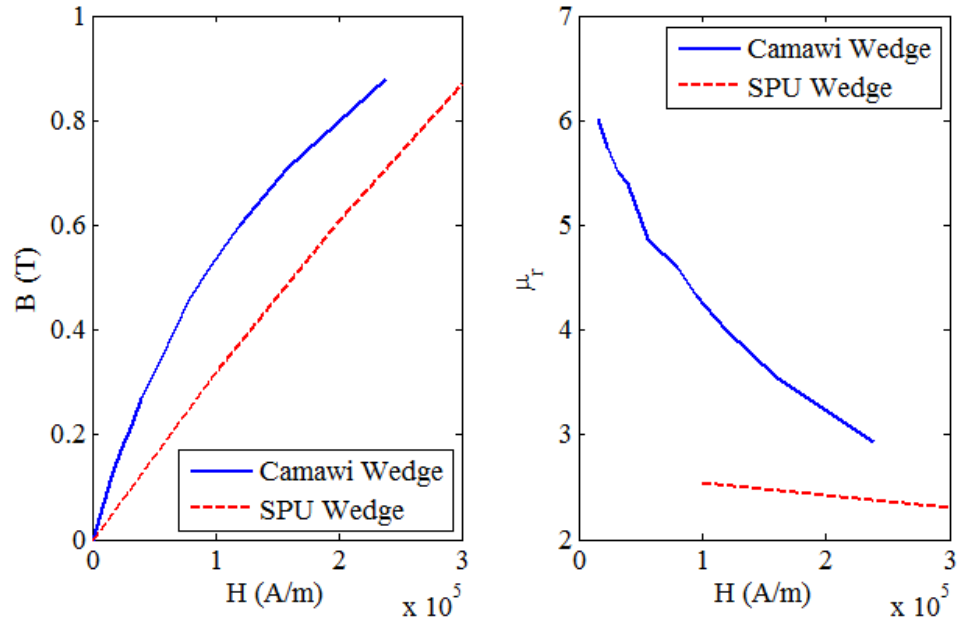


Figure 3.20: Semi-magnetic wedge B-H and relative permeability curves

In the finite element study, 2D models are solved over an electrical cycle at rated current and rated speed of the prototype machine. The results suggest that the inclusion of the semi-magnetic slot wedges affects the iron loss, the torque capability and the power factor of the machine. Figure 3.21 shows the relative magnitudes of these performance criteria considered in the study.

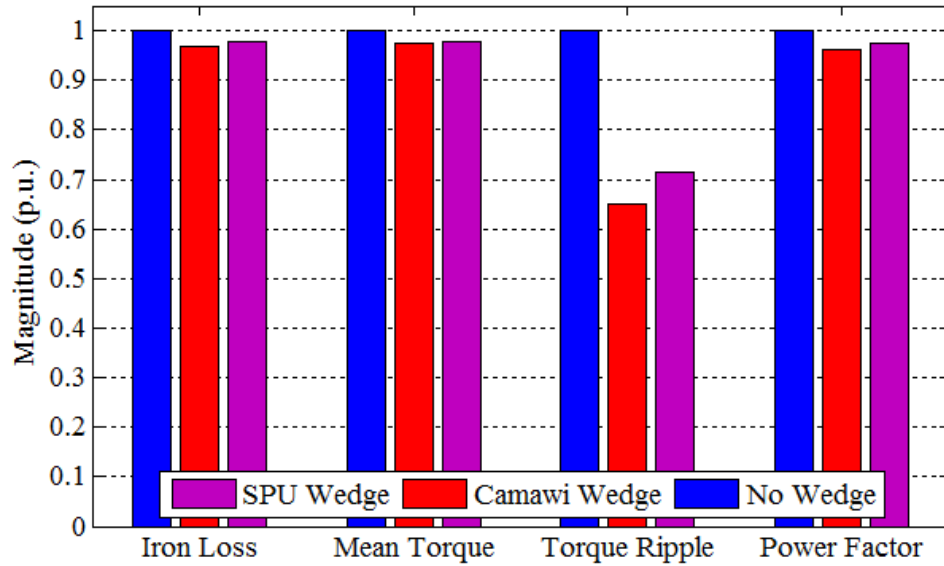


Figure 3.21: Machine performance criteria variation for different slot wedge materials

The inclusion of the semi-magnetic slot wedge can significantly reduce torque ripple at a little cost of mean torque. However, the tooth tip leakage flux will increase as a result of the semi-permeable bridge across the tooth tips, acting to decrease the power factor of the machine. A simultaneous benefit is the slight reduction of the iron losses, due to the improved harmonic content in the airgap, potentially increasing the efficiency of the machine if wedge loss is minimal. The higher permeability Camawi semi-magnetic slot wedge reduces the mean torque to approximately the same level as the lower permeability SPU wedge, but it does reduce the torque ripple by a greater extent. Quantitatively, by utilizing the Camawi wedge the torque ripple can be reduced by 34.8% to approximately 28% of the mean torque opposed to 44% in a non-magnetic wedged machine, for a mean torque reduction of only 2.6%. The iron loss in the rotor is affected by the introduction of semi-magnetic slot wedges, with up to a 20% reduction in rotor iron loss equating to a 3% overall iron loss reduction. The reduction of the torque ripple, and rotor iron losses confirms that the inclusion of the semi-magnetic slot wedges affects mainly the asynchronous harmonic content in the airgap as the mean torque produced by the fundamental flux wave is only slightly affected. However, with these advantages, a reduction in power factor of the machine by up to 4% is observed. The high permeability Camawi wedge has the greatest benefit in terms of torque quality and iron loss reduction, but also delivers the lowest mean torque and lowest power factor. Semi-magnetic slot wedges are not implemented in the prototype machine due to sourcing and cost issues, but is an area for further research.

3.5.2 Skewing Effects

Another method of torque ripple reduction is to skew the machine's laminations. This acts to average out some of the harmonics to diminish their effect and can be performed

in two ways, either rotor or stator lamination skewing. Skewing is difficult to implement during prototyping, stator skewing in particular has an effect on the stator coil placement and also the assembly of the segmented stator core approach: rotor skewing is the easier option due to the lack of conductors or magnets present in the synchronous reluctance rotor design. With either rotor or stator skewing, or a combination of both, there is an associated skew factor [1,2,3,13];

$$k_{sv} = \frac{360}{vp\pi\theta_m^{deg}} \sin\left(\frac{vp\pi\theta_m^{deg}}{360}\right) \equiv \text{sinc}\left(\frac{vs\pi}{2\tau_p}\right) \quad (3.36)$$

Where θ_m^{deg} is the rotor skew angle in mechanical degrees and s is the arc length of the skew in meters. Figure 3.22 shows the skew factors for low order harmonics as a function of rotor skew angle in mechanical degrees.

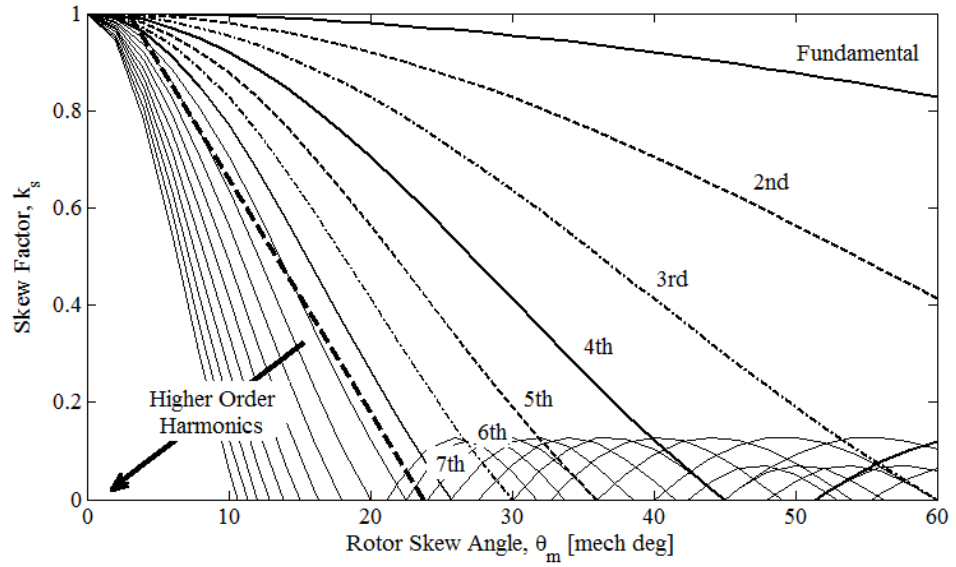


Figure 3.22: Skew factors with skew angle

Now, in order for the cancellation of the v th harmonic, the following condition must be met;

$$\frac{vs\pi}{2\tau_p} = k\pi \Rightarrow \sin\left(\frac{vs\pi}{2\tau_p}\right) = k_{sv} = 0 \quad (3.37)$$

implying when the following condition is met;

$$\frac{vs}{2\tau_p} = k \in \mathbb{Z} \quad (3.38)$$

Therefore, re-arranging for the skew to effect a harmonic cancellation, setting the integer value $k = 1$ and utilizing the relationship between the rotor and stator pitches to give the skew as a function of machine parameters (number of stator slots Q_s and number

of rotor pole pairs p), the harmonic v to be canceled and the stator slot pitch τ_u ;

$$s = \frac{2\tau_p}{v} = \frac{\tau_u Q_s}{pv} \quad (3.39)$$

Thus for complete cancellation of the 2nd order harmonic, the stator (or rotor) must be skewed by an amount equal to $\frac{3}{2}\tau_u$. In terms of reducing the torque ripple in the machine, a full treatment is given in Chapter 6, however it is sufficient to say here that the reduction in mean torque due to the modulation of the fundamental skew factor is significant when trying to reduce the second order harmonic and thus skew is not warranted. For this slot-pole combination the second order harmonic drops off slowly and in order to half its contribution the fundamental falls to around 0.85, seriously diminishing an already low fundamental winding factor. This a specific issue to this slot-pole combination (and other FSCW combinations) with single tooth coils, as such, skew is not considered further for the prototype machine.

3.6 3D Effects

In the designed machine, there are 3D leakage effects not accounted for in 2D FEA. These are the end winding leakage and also fringing fields near to the core edges around air gaps. The end winding leakage inductance is calculated analytically in Section 3.3 to be $L_{ew} = 138\mu\text{H}$ and can be incorporated into the 2D FEA as a lumped inductance. As the machine is long and the end winding leakage inductance is small, the end effects associated with the end winding leakage is small, however the axial fringing fields will have more a prominent role. A 3D FEA model including the end windings is solved at the rated operating point to ascertain the level of performance degradation 3D effects have in the designed machine: Figure 3.23 shows the 3D model. Figure 3.24 shows the torque wave forms of the 2D and 3D FEA solutions. The difference in mean torque between the 2D and 3D FEA solutions is 8.3%, giving a 3D FEA mean torque of 20.05Nm compared to the 2D FEA mean torque of 21.98Nm. The torque ripple between sees a larger change with the 2D FEA at 44.8% and the 3D FEA torque ripple slightly reduced at 39.5%, approximately a 12% decrease in the torque ripple, however, this could be due to the coarser discretization used in the 3D model to reduce the computation time. The 3D FEA also has a slight impact on the iron loss of the machine, Table. 3.5 presents a separated view of the iron loss between the two FEA solutions. The iron loss is again calculated using the Bertotti separation method.

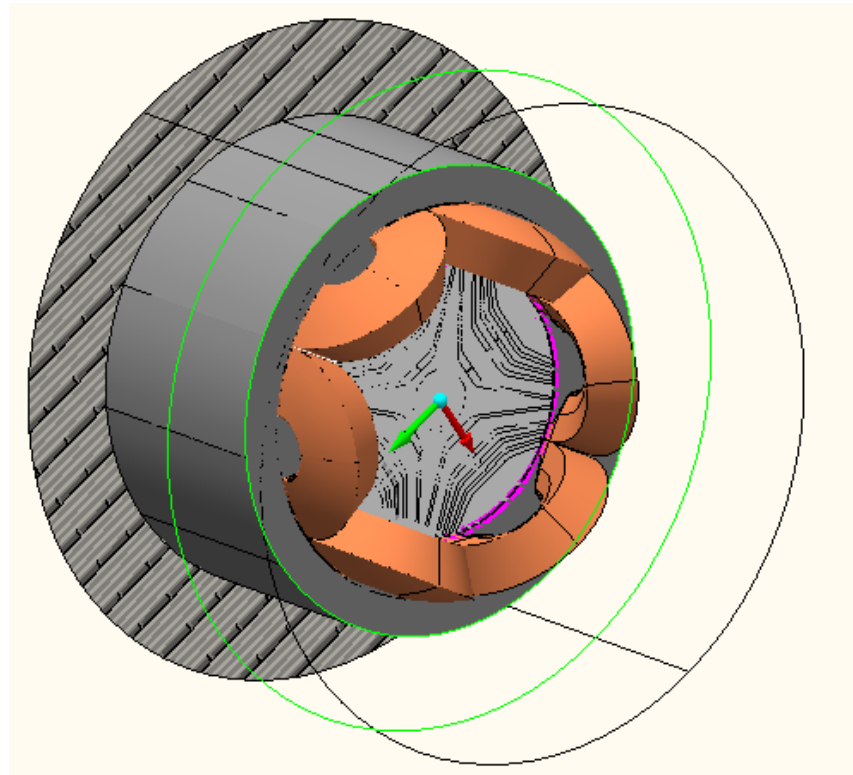


Figure 3.23: 3D model of the prototype machine end windings

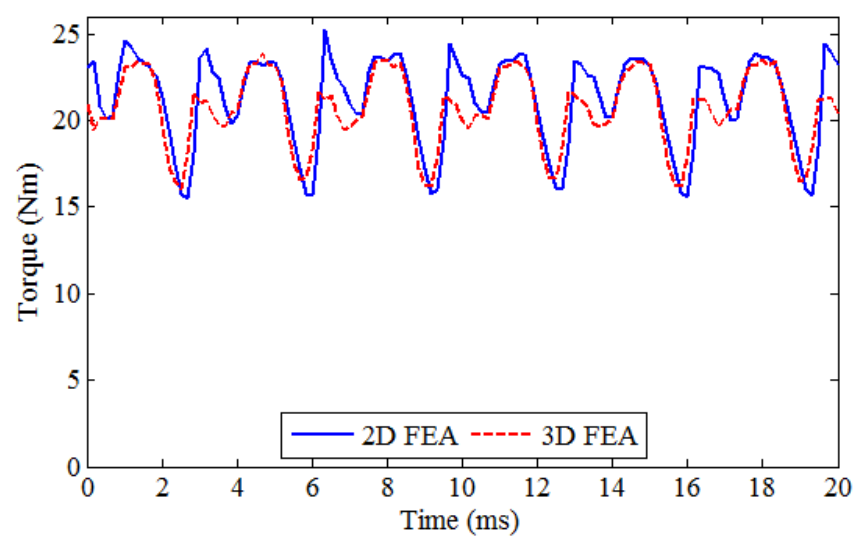


Figure 3.24: 3D vs 2D FEA Torque Waveforms

	2D FEA	3D FEA
Stator Eddy Current Loss (W)	2.85	3.24
Stator Hysteresis Loss (W)	24.00	26.22
Rotor Eddy Current Loss (W)	2.45	3.02
Rotor Hysteresis Loss (W)	8.37	10.04
Total Stator Iron Loss (W)	26.85	29.46
Total Rotor Iron Loss (W)	10.82	13.06
Total Iron Loss (W)	37.68	42.53

Table 3.5: 3D vs 2D FEA Iron Losses

The 3D FEA predicts a 12.8% higher iron loss (both eddy current and hysteresis losses) than the 2D FEA model, an increase of total machine loss of only 1.4%; the copper loss is dominant in low speed low pole number machines. The increase in iron loss can be attributed to the change in magnetic conditions within the machine due to the associated leakage permeance components and coarser discretization. The 3D FEA also predicts a marginally lower power factor of 0.475 compared to that of the 2D FEA model of 0.480, this is accounted for by the 3D leakage paths not factored into the 2D FEA solution. Thus, the 3D modeling shows that while the machine performance is slightly reduced in terms of mean torque, power factor and increased iron loss, the end effects have a minimal impact on performance. The 3D FEA takes considerable computation time (3.5 hours) with respect to computation time of the 2D FEA (4 minutes) on a high performance desktop PC.

3.7 Rotordynamic Calculations

This section presents a brief mechanical analysis of the prototype rotor, more specifically the mechanical stresses both at maximum speed and over-speed conditions (twice maximum speed) to confirm the structural integrity of the rotor design within the design speed range. The first bending mode is calculated analytically and the rotor torsional modes are analysed through finite element methods. Using a mechanical finite element model, the rotor stress, deformation and safety factor are calculated. The commercial finite element package ANSYS Mechanical is used to model and solve the rotordynamic analysis. Based on the methods by Gieras [2] analytical analysis is used to calculate the first critical speed of the rotor assembly, corresponding to the first bending mode of the rotor shaft and stack structure. In the analysis the material M250-35A [16] is used with the mechanical properties as in Table 3.6.

	Data-Sheet Value
Yield Strength (MPa)	455
Tensile Strength (MPa)	575
Young's Modulus (GPa)	195
Mass Density ($\text{kg} \cdot \text{m}^{-3}$)	7600

Table 3.6: Mechanical properties of M250-35A

3.7.1 Rotor Stress, Deformation and Safety Factor

Analysis of the mechanical loading of the rotor is important, especially as there are very small features such as the radial and tangential ribs that link the long and relatively thin flux guides. The 4-pole 50Hz rotor nominal design speed is $\omega_m = 1500\text{rpm}$ with a maximum speed of 5000rpm. At speed, the centripetal forces acting on the rotor cause stress throughout the rotor lamination stack, leading to deformation of the rotor structure. If these stresses are high enough, the material could yield. The von-Mises equivalent stress is calculated through finite element models in ANSYS, the finite element stress analysis at 5000rpm (maximum speed) and 10,000rpm (twice maximum speed) is performed to analyze the stress distribution and the deformation of the prototype rotor and to confirm the mechanical integrity of the design.

3.7.1.1 5000 rpm (Maximum Speed)

Stress Distribution Figure 3.25 shows the result of the von-Mises (equivalent) stress distribution at 5000rpm with exaggerated deformation (x1000). The maximum calculated von-Mises equivalent stress at the base speed of 5000 rpm is 54 MPa, which is located at the inner radial ribs. Other points of high stress are throughout the radial and tangential ribs in the rotor where the material is of a small width. As the ultimate tensile strength of the lamination material is 575 MPa, the stress distribution in the rotor at maximum speed is well within safe limits and it would be expected that rotor deformation at this speed will be minimal as is shown next.

Rotor Deformation Figure 3.26 shows the local deformation (exaggerated x1000) at 5000 rpm due to the centripetal forces. The maximum calculated deformation at the base speed of 5000 rpm is $5.2\mu\text{m}$, which as a percentage of the air gap is approximately 1%. The maximum deformation occurs at positions not at the air gap periphery, so its effects regarding airgap closure are minimized. At the relevant points, the airgap closure at 5000 rpm is approximately $2\mu\text{m}$ (<0.5% of airgap width), therefore, at this speed the deformation is negligible and will have no effect on the mechanical or electromagnetic operation of the machine. The minimum deformation is calculated to be located around the shaft area and the main magnetic spider component of the rotor, as would be expected.

D: LATEST DESIGN 20mm SHAFT 0.5mm RIB
 Equivalent Stress
 Type: Equivalent (von-Mises) Stress
 Unit: Pa
 Time: 1
 10/09/2012 13:01

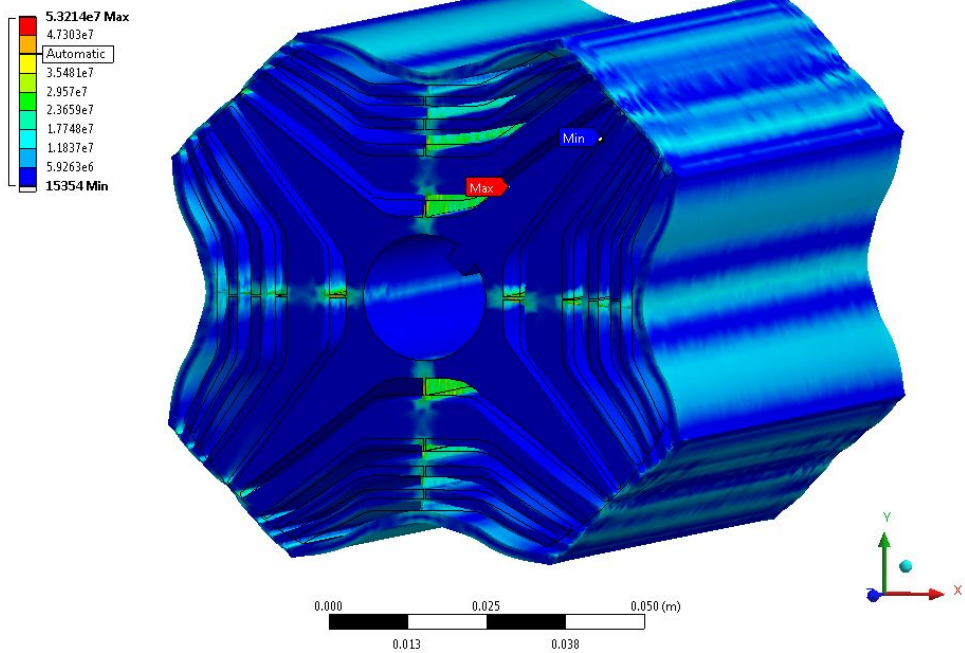


Figure 3.25: von-Mises stress distribution at 5000rpm (exaggerated deformation)

D: LATEST DESIGN 20mm SHAFT 0.5mm RIB
 Total Deformation
 Type: Total Deformation
 Unit: m
 Time: 1
 10/09/2012 13:01

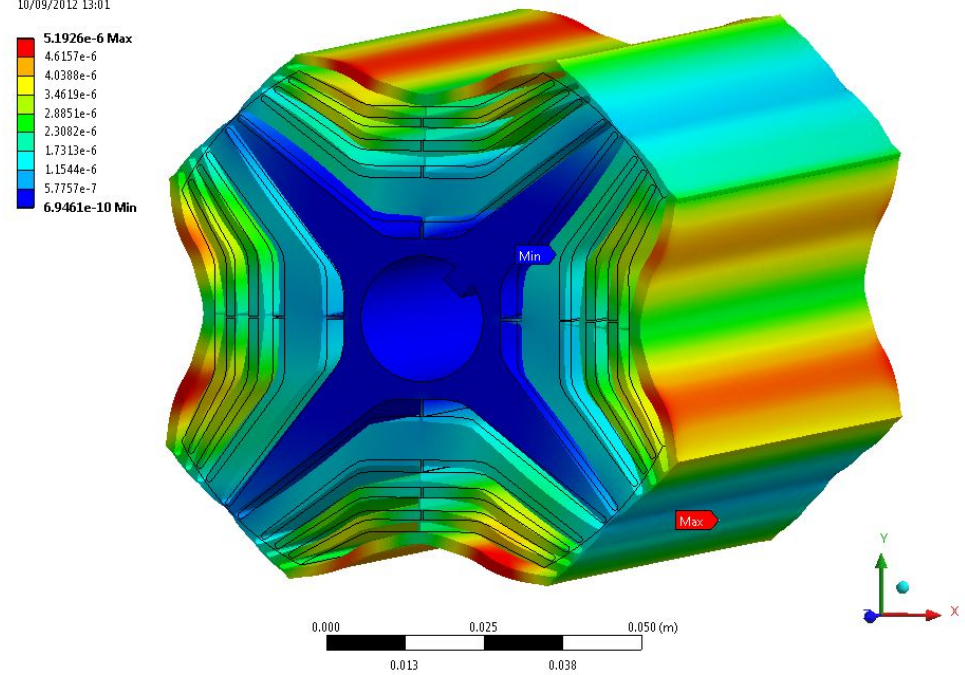


Figure 3.26: Deformation distribution at 5000rpm (exaggerated)

Safety Factor Based on the calculated von-Mises (equivalent) stress and the ultimate tensile strength of the lamination material, the minimum safety factor with M250-35A silicon steel at the rated base speed of 5000 rpm is 8.5, which is well within allowable limits as a minimum safety factor between 1.8 and 2.2 is usually used in design calculations.

3.7.1.2 10,000 rpm (2x Maximum Speed)

Stress Distribution Figure 3.27 shows the result of the von-Mises (equivalent) stress distribution at 10,000rpm with exaggerated deformation (x1000). The maximum calculated von-Mises equivalent stress at the base speed of 10,000 rpm is 213 MPa, which is again located at the inner radial ribs. Other points of high stress are throughout the radial and tangential ribs in the rotor where the material is of a small width, as before. As the ultimate tensile strength of the lamination material is 575 MPa, the stress distribution in the rotor at maximum speed is still under half of the maximum, which is within safe limits and it would be expected that rotor deformation, even at this speed, will be minimal.

Rotor Deformation Figure 3.28 shows the local deformation (exaggerated x1000) at 10,000 rpm due to the centripetal forces. The maximum calculated deformation at 10,000 rpm is $20.77\mu\text{m}$, which as a percentage of the air gap is approximately 4%, this deformation again occurs at positions not at the air gap periphery. The maximum airgap closure at relevant locations on the rotor surface and at 10,000 rpm is approximately $10\mu\text{m}$ or 0.01mm (approx 2% of airgap length). At this speed the deformation is more pronounced but still rather low and will have no effect on the mechanical or electromagnetic operation of the machine.

Safety Factor Again, based on the calculated von-Mises (equivalent) stress and the ultimate tensile strength of the lamination material, the minimum safety factor with M250-35A silicon steel at twice the rated base speed, 10,000 rpm is 2.1, which is within generally allowable limits of minimum safety factor between 1.8 and 2.2. If a safety factor limit of 2 is enforced, the designed rotor has a maximum permissible mechanical speed at twice the prototype maximum speed.

3.7.2 Rotor Resonant Modes

With the previous section suggesting that in the steady state, the rotor stress distribution and mechanical strain are minimal and that the rotor maximum safe speed is twice the rated maximum speed, other mechanical considerations must also be investigated, the resonant modes. There are two main types of resonant phenomena in electrical machine rotors [16];

- *Bending modes* - which is the bending of shaft and lamination stack along the shaft length

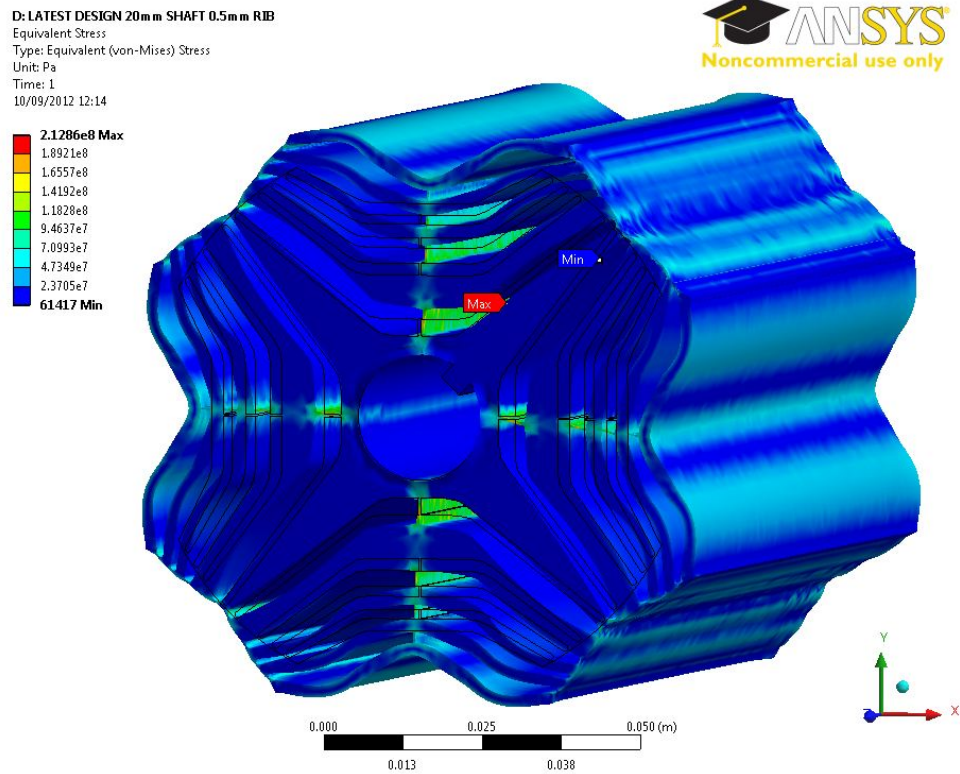


Figure 3.27: von-Mises stress distribution at 10,000rpm (exaggerated deformation)

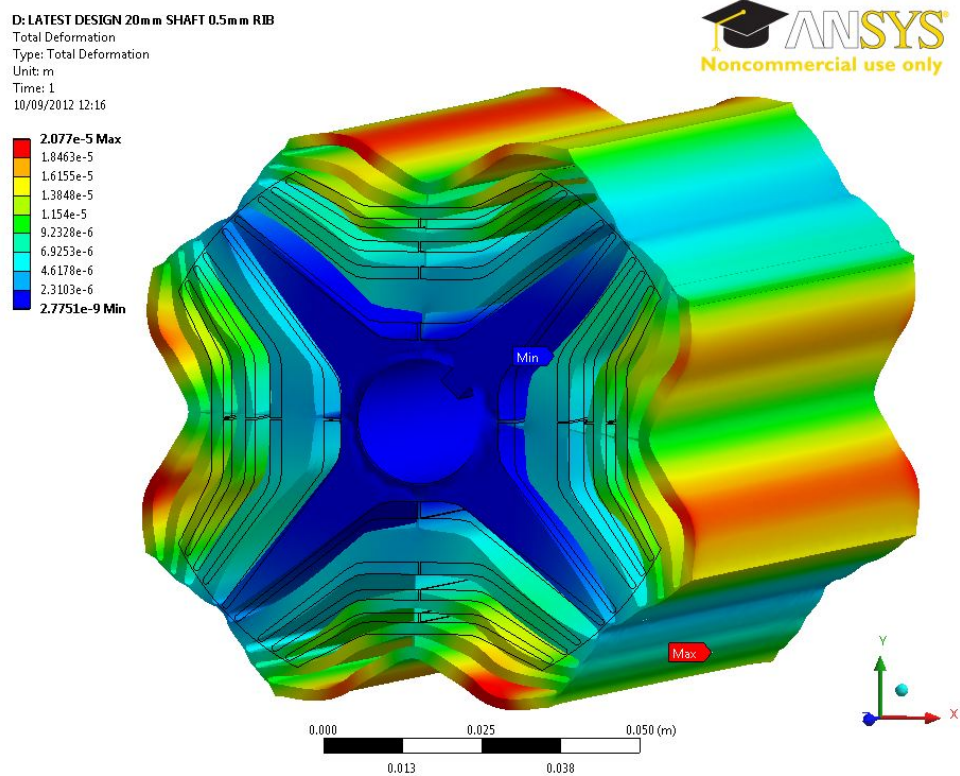


Figure 3.28: Deformation distribution at 10,000rpm (exaggerated)

- *Torsional modes* - which is the twisting of the shaft and lamination material about the shaft axis

The bending modes can be calculated analytically with a good degree of accuracy as in [16,17] and the torsional modes are best calculated with the ANSYS mechanical finite element package. Here, the first bending mode, or *first critical speed* is calculated, which is the first mechanical resonance linked with the first bending mode of the rotor-lamination stack. It is key that the machine operation is not close to this critical speed in order to avoid mechanical complications.

3.7.2.1 First Bending Mode - The First Critical Speed

The first critical speed can be calculated analytically, using relatively simple formula if the assumption is made that the composite structure of the shaft and the lamination stack cannot slide against one another, i.e. there is infinite friction between components and that the lamination stack is considered to be a solid mass of lamination material, without lamination and viscous bonding material in between any laminated sections. These assumptions result in a lumped composite stiffness of the shaft-rotor structure, K . In this case, the first critical speed n_{c1} of the structure can be calculated by [2];

$$n_{c1} = \frac{1}{2\pi} \sqrt{\frac{K}{m_{stack} + m_{shaft}}} \quad (3.40)$$

where m_{stack} and m_{shaft} are the masses of the lamination stack and the shaft respectively and the lumped composite shaft-lamination stiffness, K is calculated by [2];

$$K = 48 \left(\frac{E_{stack} I_{stack}}{l_{stack}^3} + \frac{E_{shaft} I_{shaft}}{l_{shaft}^3} \right) \quad (3.41)$$

where I is the second moment of inertia of the respective component (stack or shaft) E is the Young's modulus of the components material (stack or shaft) and l is either the length of the lamination stack or the length between the bearings on the shaft. The second moments of inertia for the rotor stack and the shaft are calculated from;

$$I_{stack} = \frac{\pi}{64} (D_{stack}^4 - D_{shaft}^4) = 2.93 \times 10^{-6} \text{m}^4 \quad (3.42)$$

$$I_{shaft} = \frac{\pi D_{shaft}^4}{64} = 7.85 \times 10^{-9} \text{m}^4 \quad (3.43)$$

The masses are calculated in Infolytica Motorsolve based on lamination material M250-35A and the shaft material 316 stainless steel as in the prototype machine, the results of the masses are $m_{stack} = 3.39\text{kg}$ and $m_{shaft} = 0.48\text{kg}$. The lamination stack length is 150mm and the distance between the bearings in the prototype machine is 200mm. The two materials have have same Young's modulus of approximately 190GPa giving a composite stiffness coefficient from Eq. 3.54 as $K = 8.02 \times 10^9$. The first critical speed

is then calculated using Eq. 3.53 as $n_{c1} = 7230\text{rpm}$ - thus, the rotor assembly is well sized mechanically as the base operating speed is 1500rpm , with a maximum speed of 5000rpm . The first critical speed is between the maximum design speed of the rotor and the safe mechanical limit.

3.7.2.2 Rotordynamic Torsional Modes

As well as the bending mode, the torsional modes are calculated using ANSYS Mechanical FEA modal analysis to predict the torsional resonant frequencies of the rotor. This numerical procedure calculates the natural frequencies and mode shapes of the rotor relating to the torsional vibration of the rotor. From the each n -th modal frequencies f_n identified, the rotor critical speeds (rpm) are identified [17];

$$n_n = \frac{60f_n}{v} \quad (3.44)$$

where v is the mode order. Table 3.7 shows the first three FEA calculated resonant frequencies and the corresponding rotor speeds;

MODE	FREQUENCY	CRITICAL SPEED
	(Hz)	(krpm)
1	2218	133
2	4692	140
3	4985	149

Table 3.7: Rotor critical speeds

It is seen that the torsional critical speeds are well above the rotor speed for this rotor design and they do not pose any difficulty to operation. The different resonant modes have different deformation characteristics, the first torsional harmonic mode deformation (exaggerated x1000) are shown in Fig. 3.29, the maximum deflection is approximately 0.83mm at the rotor periphery, which would close the airgap of 0.5mm , however the rotation speeds required to excite this torsional mode are well outside the capability of the machine.

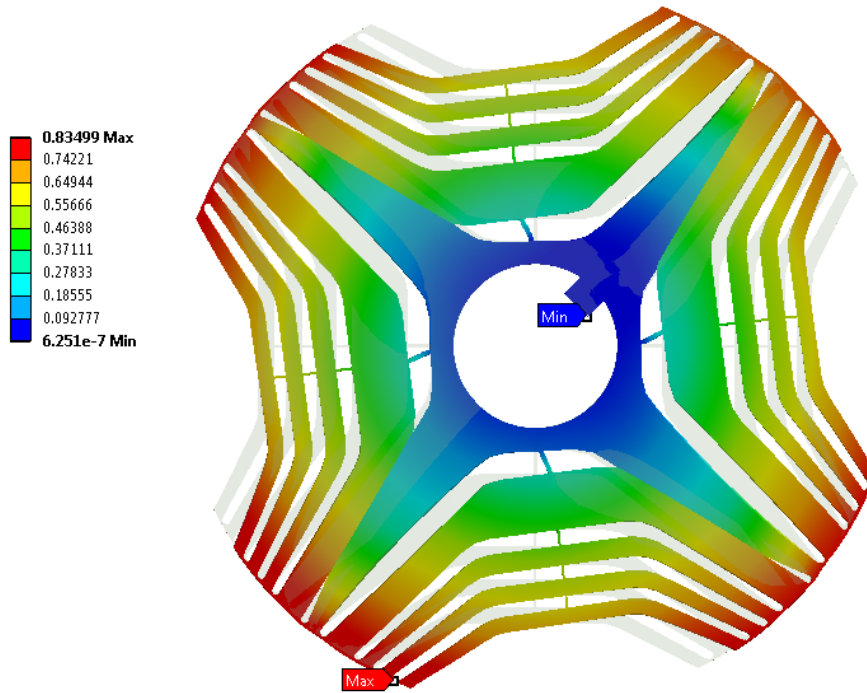


Figure 3.29: Exaggerated deformation characteristic for mode $\nu = 1$

Rotordynamic analysis shows that the designed rotor is mechanically safe within the designed operating range. The mechanical integrity in terms of stress distribution and permissible deformation is acceptable upto a rotor speed of 10krpm. The first bending mode of the rotor is well above the machines maximum operating speed, the rotor therefore always runs sub-critical and any torsional modes are not excited until well above the machines operating speeds.

3.8 FEA Machine Comparisons

Finite element analysis simulation tools are widely used and trusted in the performance evaluation of electrical machines. The software used in this particular study is Infolytica MotorSolve IM and BLDC as well as the general electromagnetic software Infolytica MagNet. Finite element analysis is used to compare the performance of three models, a commercial induction machine, a corresponding synchronous reluctance machine from Newcastle University and the novel concentrated winding synchronous reluctance machine, which is the focus of this thesis.

3.8.1 Commercial Induction Motor

The FEA induction machine model is derived from an commercially available industrial induction motor. A motor was purchased, dismantled and its dimensions recorded and then translated into a mechanical model used in the finite element analysis. This machine gives a good basis for comparison as it has almost identical principal dimensions with

the prototype cSynRM machine. The induction motor used in this study, before its dismantling, is presented in Figure 3.30 with the nameplate specifications presented in Table 3.8.

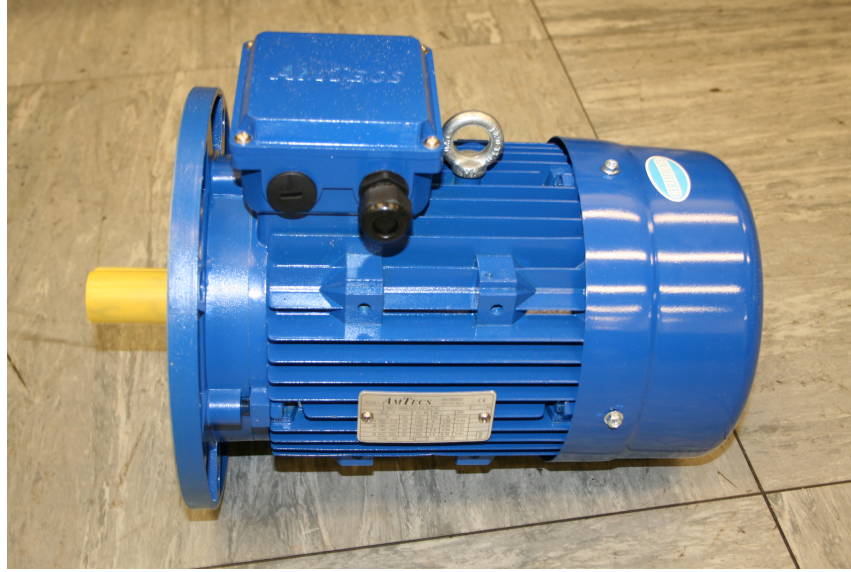


Figure 3.30: Induction motor before teardown

NAMEPLATE PARAMETER	VALUE
Peak Output Power (kW)	4.0
Rated Voltage (V)	415
Rated Current (A)	8.38
Rated Power Factor	0.80
Rated slip (%)	5.33
Number of Phases, m	3
Total Mass (Active mass + casing)	29 kg

Table 3.8: Induction machine specification

After the dismantling, the induction motor was cut into two halves in the plane perpendicular to the shaft axis in order to obtain the lamination dimensions by examining the lamination profiles of the stator and rotor. This allows modeling in the FEA software. The induction motor has a cast aluminum cage with cast aluminum end rings and is of typical construction for small frame size industrial motors.

3.8.2 Equivalent Synchronous Reluctance Motor

The FEA SynRM machine model is derived from a SynRM designed for another Newcastle University research project, which is based upon the commercially available industrial induction motor as it uses the same stator, a SynRM rotor was designed to fit into the

existing IM stator constraints. The rotor is of the transversely laminated type and is optimised with hyperbolic flux barriers with a saliency ratio $\xi_{true} = 8$ and is designed to match the mechanical output of the induction motor. It is beyond the scope of this thesis to provide extensive design information on the SynRM and only its performance is reported for comparison. Figure 3.31 shows the induction machine lamination profiles used for obtaining critical magnetic and electric parameters for the finite element model, which is also shown.

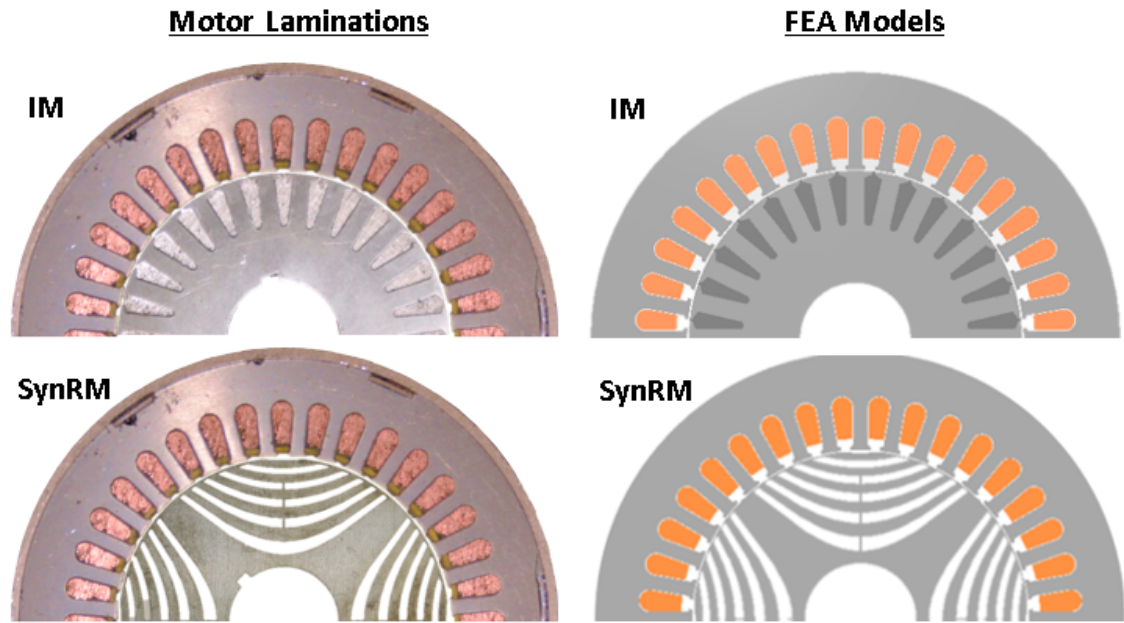


Figure 3.31: Induction and SynRM lamination profiles with FEA realisation

These two machines are compared with the designed synchronous reluctance motor with fractional slot concentrated windings, the cSynRM prototype machine, as in Figure 3.13. Table 3.9 shows the difference in geometrical parameters for the compared machines.

MACHINE VOLUMES AND MASSES			
Parameter	<i>IM</i>	<i>SynRM</i>	<i>cSynRM</i>
Stator OD [mm]	155		150
Stack length [mm]	155		150
Electromagnetic Volume [mm ²]	2.92×10^6		2.65×10^6
Rotor core mass (kg)	6.04	4.73	3.39
Rotor bar mass (kg)	0.64	-	-
Rotor end ring mass (kg)	0.12	-	-
Stator core mass (kg)	9.86	9.86	8.88
Stator winding mass (kg)	2.48	2.48	2.05
Total Mass (kg)	19.14	17.07	14.32

Table 3.9: IM, SynRM and cSynRM machine volumes and masses

From Table 3.9, the mass of the cSynRM is reduced compared to both the IM and

SynRM due to a lack of rotor conductors, the rotor design with large cutouts and shorter end windings (the mass is also marginally reduced due to the 5mm shorter outer diameter and stack length with the cSynRM). The cSynRM has an advantage in not only mass over the two base machines, but raw material cost also, based on a reduced copper mass as the lower rotor mass only contributes to scrap lamination material with no value. There is a difference in electromagnetic volume of 9% between the distributed wound machines with the SynRM, the distributed winding machines having a slightly larger OD and stack length. The total slot areas per phase are 950 and 1050 sq. mm for the distributed winding and the fractional slot concentrated winding stators respectively. The increase in slot area is attributed to differences in slot geometry. The active mass of the induction machine is higher than that of both the reluctance machines due to the loss of rotor cage and some rotor iron in those machines. In industrial terms, weight reduction is not of high importance, but in mobile applications such as road and rail vehicles, weight is of major concern. This could mean that applications such as hybrid electric heavy trucks and ships, where there are some VSD controlled ancillaries, may be attracted to this technology. For the same mechanical power output the reluctance machines are required to produce less torque as there is no slip and the rotor rotates synchronously at 1500rpm with the 50Hz 4-pole stator field. Manufacture of the reluctance machines is arguably easier due to the lower number of engineering/manufacturing operations required, as is apparent when looking at the construction of the dismantled induction machine compared to that of the SynRM or cSynRM, the segmental nature of the cSynRM stator must be taken in to account.

The three specifications for the machines are presented in Table 3.10 and assumes a slot fill factor of $S_{FF} = 0.34$, as calculated from examining the induction motor stator windings. The IM and SynRM have an identical stator, winding and connections. The cSynRM has fractional slot concentrated windings and the design is to the specification as presented in this chapter.




MACHINE SPECIFICATIONS			
Parameter	<i>IM</i>	<i>SynRM</i>	<i>cSynRM</i>
DC Link Voltage [V]	590	590	590
Winding Factor	0.96	0.96	0.86
Stator Coil Turns	94	94	52
Winding Connection			
Phase Resistance [Ω]	5.1	5.1	0.38
Measured End Winding Axial Extent [mm]	38	38	18.5
Rotor Inertia [$\text{kg} \cdot \text{m}^2$]	0.00865	0.00616	0.00308

Table 3.10: IM, SynRM and cSynRM machine specifications

All machines are operated from the same DC link voltage, the windings of the IM and SynRM have the same parameters and are designed for delta connection and the winding is of the single layer type. The cSynRM winding was designed as star connected, has much shorter end windings and is of the double layer winding type (each tooth wound). Based on practical measurements on the industrial induction motor and the prototype cSYnRM, the distributed windings on the IM and SynRM stators have a much longer axial extent of the end winding than the cSynRM. This means the IM and SynRM have an increased package size. Based on calculations for the rotor geometries and materials, the induction motor has the highest rotor inertia, followed by the SynRM, where the cSynRM has a significantly lower rotor inertia than the IM and the SynRM which leads potentially to faster speed dynamics.

3.8.3 Constant Loss Operation

As a comparison, the machines were simulated in FEA under a constant loss condition in order to compare the performance per loss of the IM, SynRM and the cSynRM. All machines are operated at an identical synchronous speed of 1500rpm, excited with three phase balanced and sinusoidal currents. The motors are now considered at a constant loss condition of 340W, again driven at their rated speed (or slip). The synchronous speed for all three machines is 1500rpm at 50Hz (4-pole motors), a slot fill factor of 33.8% is used in this study for all machines, as determined by examining the industrial induction motor. Table 3.11 shows the motor performances at the rated operating point. End winding losses based on measured conductor lengths of prototype machines are taken into account and the IM model matches closely with that of the performance data on its nameplate.

MACHINE COMPARISON (CONSTANT LOSS OF 340W)			
Parameter	<i>IM</i>	<i>SynRM</i>	<i>cSynRM</i>
Loss - Stator Winding (W)	199	287	294
Loss - Rotor cage (W)	128	-	-
Loss - Iron (W)	16.9	56	47
Total Loss (W)	345	343	341
Speed (rpm)	1420	1500	1500
Slip (%)	5.3	-	-
Line Current (A rms)	6.25	7.5	16
Torque (Nm)	15.4	20.1	16.1
Power (kW)	2.29	3.23	2.53
Power Factor	0.80	0.62	0.483
Efficiency	86.8	90.4	88.4
Slot Fill Factor (%)	33.8	33.8	33.8
Current Density (A/mm ²)	6.38	7.66	8.26

Table 3.11: Constant loss performance of the IM, SynRM and the cSynRM

The induction machine produces a mean torque of 15.4Nm for 345W of loss, where as the SynRM produces a mean torque of 20.1Nm for a loss of 343W. This means that for the same losses, the SynRM produces approximately 1.3x the torque of the induction motor. This figure is close to that in [5], however the FEA figure is slightly lower due to increased iron loss at higher currents in the SynRM that are neglected in that analytical analysis. This figure also means that for the same loss, the SynRM can produce around 1.38x the mechanical output power due to increased torque output and rotor synchronicity. The mean torque of the cSynRM is 16.1Nm, it is reduced by a factor of 0.8 when compared to the SynRM which is very close to the ratio of the square of the fundamental winding factors of the machines, equal to 0.81, which would predict a cSynRM mean torque of 16.4Nm. The SynRM has a peak to peak torque ripple of 4Nm whereas the cSynRM machine has a torque ripple of 9Nm. The induction machine runs at the highest power factor, at 0.8, the SynRM runs at a respectable power factor of 0.62 due to its high saliency ratio, however the cSynRM runs with a power factor of 0.48 due to the increased leakage inductance as explained previously and is aligned with predictions in Chapter 2. This low power factor impacts the electric drive sizing and also its cost. Both reluctance machines have higher energy conversion efficiency compared to the induction machine. The rotor cage loss being non-existent in the reluctance machines, and as such, the copper loss in the reluctance machines is confined to the stator. The rotor, and therefore the bearing temperatures, are expected to reduce compared to that of the induction motor. This is advantageous as the rotor is usually difficult to cool, increasing the robustness of the motor, its reliability and potentially its operational life. The induction motor exhibits the lowest efficiency, of 86.8%, the SynRM has an efficiency of 90.4% and the cSynRM in between with an efficiency of 88.4% however it must be noted that this motor is slightly smaller than the other motors. However, as the fill factor of the machines is low and the fact that the cSynRM advantages come from its higher achievable fill factors, the result is not surprising. The cSynRM machine performance is comparable to that of similar sized switched reluctance motors [6] but is driven from a conventional three-leg inverter. A comparison with a cSynRM with higher fill factors is now made and discussed.

3.8.4 cSynRM with Increased Fill Factor

As the advantage of the cSynRM motor topology increases with fill factor, Table 3.12 shows the consequences of increasing the fill factor to levels that are practicable. The change in per unit slot thermal conductivity as described in Chapter 2, λ_{eff} is also presented. Again, these calculations allow a total machine loss of 340W.

Fill Factor	Parameter				
	Torque (Nm)	P.F.	η (%)	Mass (kg)	λ_{eff} (p.u.)
34% (IM)	16.1	0.482	88.4	15.77	1.11
50%	19.5	0.480	90.7	16.94	1.6
58% (cSynRM)	21.9	0.477	91.2	17.44	2.09
70% (Compressed)	23.9	0.474	92.3	18.17	3.05

Table 3.12: cSynRM increased fill factor performance (340W loss)

For a constant total (consisting of both copper and iron loss) loss of 340W, it is evident from Table 3.12 that the torque density of the cSynRM can be significantly increased by increasing the fill factor: this fill factor must be in the bounds of a practical winding. An increase in fill factor from 34% to 58% (the increase in fill factor from the industrial motor to the fill achieved in the prototyped cSynRM motor) provides approximately a 37% increase in torque density and over a 2.8% increase in efficiency. The slot thermal conductivity increases almost four-fold, so the machine with higher fill factor will run at lower temperatures than a low fill factor machine. These performance benefits are accompanied by a small 1.66% reduction in power factor and a 15.22% increase in machine weight, which are undesirable. The winding mass increases by 1.67kg in going from 0.34 to 0.58 fill factor which the copper has a market value of only £6.79 as of June 2015. The corresponding power increase is 920W, leading to an 135W/£ increase in power density by increasing the fill factor. Despite this significant increase in copper, the active weight of the cSynRM is still less than the original induction motor.

The power factor decreases due to the increase in stator MMF, creating higher magnitude harmonic fluxes, contributing to an increase in stator leakage inductance. It is unlikely that unless compressed coils are used, a fill factor of 70% will be achieved in practice and a more reasonable value, as achieved in the prototype machine, is around 55-60%. When increasing the fill factor in order to increase the torque density of the cSynRM, it is important to note that the increase in stator current has an upper limit, even for constant winding copper loss. The increased stator MMF will also increase the magnetic operating point, leading to higher iron loss and saturation. This saturation affects the magnetizing inductance and fundamentally limits the useful torque capability of a given geometry. The converter needs to be taken into account also, with device selection and cooling becoming an issue at higher current levels.

In [7] it is suggested that higher fill factors improve the slot-liner to lamination interface, which acts to decrease the overall thermal resistance of the copper to ambient thermal path. This reference also shows that the slot thermal resistance depends upon the slot areas, surfaces and perimeters. Based on both slot geometries, the equivalent slot thermal conductivities and the stator slot surface areas suggest that the cSynRM has a

higher slot thermal resistance if identical fill factors are used, however the improved fill factor reduces the thermal resistance to below that of the induction motor, which coupled with the lower losses, acts to effect a temperature improvement in the cSynRM over the IM and SynRM.

3.8.5 Axial Extents

All machines are the same frame size and have near identical principal dimensions. As in Table 3.10, the measured axial extent of the end windings in the distributed machine is 38mm at each end, suggesting a total active length of 231mm including the 155mm stack length. The cSynRM has axial extents of the concentrated winding of 18.5mm, such that the total active length is only 188mm. This gives a total end-end length difference of 43mm. If the coil to end cap clearances are maintained, the outer casing length could be reduced, saving weight and space, or, the active stack length could be increased by up to 43mm to achieve a higher power rating in the same frame size. If the full extent is used, as the torque is proportional to the stack length, the mechanical torque could be increased, potentially enabling a motor power rating in the frame size smaller from what would usually be required.

3.8.6 Machine Mass and Cost

The masses of the active materials are calculated from the CAD model and the assigned material. The cost of those materials is based on market prices (as of calculation in June 2015), with respect to copper is £4.07/kg and a suggested £/kg of lamination material by a major manufacturer of £2.00/kg. The rotor cage is Aluminum, the costing for this is based upon the market price of £1.16/kg. No attempt has been made to estimate the manufacturing cost as this is very complicated, depending on manual or automatic operations and is beyond the scope of this thesis. Table 3.13 shows the motor component masses at their practical slot fill factors and their associated costs, lamination scrap is not included in the costing.

	IM Mass (kg)	SynRM Mass (kg)	cSynRM Mass (kg)
Rotor Core	7.00 [£12.18]	4.73 [£9.46]	3.39 [£6.78]
Stator Core	9.86 [£19.97]	9.86 [£19.72]	8.88 [£17.76]
Stator Winding	2.48 [£8.47]	2.48 [£8.75]	3.51 [£14.29]
Total Mass	19.14 kg	17.07 kg	15.78 kg
Total Cost	£40.65	£ 37.93	£ 38.83

Table 3.13: Comparison of mass and costs of motor components

From the market prices, the SynRM is the lowest cost machine in terms of raw materials, the cSynRM follows slightly behind due to the increased copper in the machine

(significantly increased fill factor) which is the most expensive metal in the constructions. The IM has the highest cost due to the increased rotor mass over the SynRM. The perceived manufacturing costing is as follows; the IM will likely require the most manufacturing operations and the cSynRM requiring the least. The SynRM will come somewhere in between as it still has complicated distributed windings but has no rotor cage casting. Therefore, it can be argued that the cSynRM is a lower cost option with a simpler manufacturing process to accompany its efficiency and low mass advantages. The segmental nature of the stator core must be taken into account as additional manufacturing processes and stages are required in order to fabricate the end winding supports and assemble the stator segments into a complete core.

3.9 Conclusion

This chapter has presented the design, performance calculations and a performance comparison with current technology. The concluding points of this chapter are;

- Optimal stator and winding design can be achieved for maximum torque per total loss through finite element analysis
- The skin and proximity AC losses are minimal in the designed machine due to low frequency operation and wide slot widths
- Inter-segment air-gaps on segmented stators do not significantly adversely affect machine performance
- The machine inductances were calculated analytically and the air gap harmonic leakage was found to be the dominant leakage component, significantly reducing the true saliency ratio and therefore the machine power factor
- The inclusion of semi-magnetic slot wedges can significantly reduce the torque ripple and also the iron loss at the expense of slightly decreased mean torque and power factor
- Rotor skewing is not a valid torque ripple reduction mechanism with $q = 0.5$ due to the rate of change of the skew factors with rotor skew angle
- 3D effects are minimal in this machine due to its long length and the dominant leakage component being 2D in nature
- Rotor mechanical strength is safe for twice the rotor maximum operating speed and both the bending and torsional vibration mode critical speeds are above that of the maximum operating speed
- Torque ripple and low power factor are two challenges with the developed topology

It is found through finite element studies that for identical fill factor the cSynRM machine exhibits higher performance in many respects compared that of the induction machine, but slightly lower performance when compared to the conventional synchronous reluctance motor. When the fill factor is increased to practically achievable values, i.e. 58%, the cSynRM outperforms both base machines types in terms of energy conversion efficiency, torque density, slot thermal conductivity. Coupled with its simple and robust construction, no rotor conductors and having a mass identical to that of the conventional synchronous reluctance motor and lower than that of the induction motor, the cSynRM is an attractive prospect. The cSynRM is presented as a low cost, easy to manufacture option to induction machine and conventionally wound synchronous reluctance technologies. Finite element studies have confirmed the Chapter 2 theoretical suggestions that torque ripple, low power factor and increased iron loss deserve special consideration when designing a synchronous reluctance machine with fractional slot concentrated windings. A significant increase in torque density can be achieved, along with efficiency and thermal improvements, provided a high fill factor can be achieved, despite the larger slot widths. High torque ripple and low power factors are characteristics of the cSynRM and must be subject to further research in order to improve the prospect of practical adoption when competing with alternative technologies.

3.10 References

1. Pyrhonen, J., T. Jokinen, and V. Hrabovcová. "Design of Rotating Machines." (2008)
2. Gieras, Jacek F. Permanent magnet motor technology: design and applications. CRC press, 2002
3. Lipo, Thomas A. Introduction to AC machine design. Wisconsin Power Electronics Research Center, University of Wisconsin, 2004.
4. Soong, W. L. "Sizing of electrical machines." Power Engineering Briefing Notes (2008): 17-18.
5. Salminen, Pia, Markku Niemela, J. Pyhonen, and Juhani Mantere. "Performance analysis of fractional slot wound PM-motors for low speed applications." In Industry Applications Conference, 2004. 39th IAS Annual Meeting. Conference Record of the 2004 IEEE, vol. 2, pp. 1032-1037. IEEE, 2004.
6. Mohan, Ned, and Tore M. Undeland. Power electronics: converters, applications, and design. John Wiley & Sons, 2007
7. Magnussen, Freddy, and Chandur Sadarangani. "Winding factors and Joule losses of permanent magnet machines with concentrated windings." In Electric Machines and Drives Conference, 2003. IEMDC'03. IEEE International, vol. 1, pp. 333-339. IEEE, 2003.
8. Iwasaki, S.; Deodhar, R.P.; Yong Liu; Pride, A.; Zhu, Z.Q.; Bremner, J.J., "Influence of PWM on the Proximity Loss in Permanent-Magnet Brushless AC Machines," Industry Applications, IEEE Transactions on , vol.45, no.4, pp.1359,1367, July-aug. 2009
9. Staton, Dave, Aldo Boglietti, and Andrea Cavagnino. "Solving the more difficult aspects of electric motor thermal analysis in small and medium size industrial induction motors." Energy Conversion, IEEE Transactions on 20, no. 3 (2005): 620-628.
10. Moghaddam. R, "Synchronous Reluctance (SynRM) in Variable Speed Drive (VSD) Applications", PhD Thesis, KTH, Stockholm, Sweden, 2011
11. Say, M. G. Performance and design of AC machines. English LB S., 1995.
12. I. Boldea, 'Reluctance Synchronous Machines and Drives', Clarendon Press, 1994
13. A. I. Voldek, 'Electrical Machines', Leningrad, Russia: Energy, 1974
14. Potgieter, J. H J; Kamper, M.J., "Evaluation of calculation methods and the effect of end-winding inductance on the performance of non overlap winding PM machines," Electrical Machines (ICEM), 2012 XXth International Conference on , vol., no., pp.243,249, 2-5 Sept. 2012
15. Anazawa, Y.; Kaga, A.; Akagami, H.; Watabe, S.; Makino, M., "Prevention of harmonic torques in squirrel cage induction motors by means of soft ferrite magnetic wedges," Magnetics, IEEE Transactions on , vol.18, no.6, pp.1550,1552, Nov 1982
16. Dabrowski M., 'Construction of Electrical Machines', Warsaw: WNT, 1977
17. Harris, Cyril M. 'Harris' Shock and Vibration Handbook'. Chapter 38, 'Torsional Vibration In Reciprocating And Rotating Machines', New York: McGraw-Hill, 2002.
18. T. A. Lipo, 'Synchronous Reluctance Machines-A Viable Alternative for AC Drives?', Electric Machines & Power Systems, Vol. 19, Iss. 6, 1991

19. Widmer, J.D.; Mecrow, B.C., "Optimized Segmental Rotor Switched Reluctance Machines With a Greater Number of Rotor Segments Than Stator Slots," *Industry Applications, IEEE Transactions on* , vol.49, no.4, pp.1491,1498, July-Aug. 2013
20. Staton, D.; Boglietti, A.; Cavagnino, A., "Solving the More Difficult Aspects of Electric Motor Thermal Analysis in Small and Medium Size Industrial Induction Motors," *Energy Conversion, IEEE Transactions on* , vol.20, no.3, pp.620,628, Sept. 2005
21. Behn-Eschenburg, H., "On the magnetic dispersion in induction motors, and its influence on the design of these machines," *Electrical Engineers, Journal of the Institution of* , vol.33, no.165, pp.239,278, April 1904
22. Moghaddam. R, "Synchronous Reluctance (SynRM) in Variable Speed Drive (VSD) Applications", PhD Thesis, KTH, Stockholm, Sweden, 2011

Chapter 4

Prototype: Fabrication and Assembly

This chapter details the fabrication and assembly of the prototype cSynRM machine based on the design presented in the previous chapter. A working prototype acts as a *proof of concept*, permitting experimental validation of the motor electromagnetic and mechanical design through static and dynamic testing, which is the focus of the next chapter. The fabrication of the final prototype motor was performed in-house at Newcastle University. The prototype stator and rotor components are first discussed with regard to the chosen fabrication techniques and special consideration given to the fabrication difficulties faced due to the fine rotor features (thin flux barriers) in the design. The winding of the stator coils and assembly of the associated insulation system is then discussed in detail. All relevant mechanical drawings relating to the prototype machine can be found in Appendix A. Figure 4.1 shows a 3D CAD model of the prototype machine.

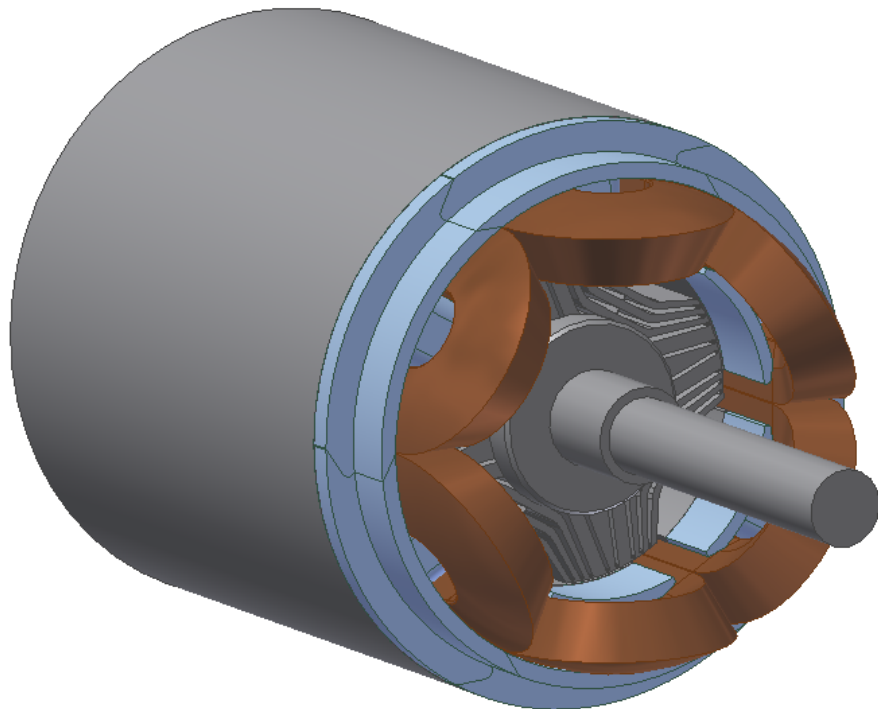


Figure 4.1: 3D CAD model of prototype cSynRM

4.1 Stator Stack Manufacture

The first stage in the fabrication of the prototype machine is to produce the stator core lamination stack. This stator stack consists of segments (segmented core back between each tooth) to facilitate high fill factors and ease of winding the single tooth coils. Before cutting of the lamination profile by wire EDM, a stack of $422 \times \text{M250-35A}$ laminations of dimensions $200\text{mm} \times 200\text{mm}$ are glued together using a specialist electrical machine epoxy and clamped using two thick steel end plates, held together in a 'sandwich' by four threaded bars, one in each corner. The compression of the stack when the steel end plates tightened together allows the glue to distribute uniformly in between the laminations and force excess glue to the edges of the stack. The stacking factor k_s of the lamination stack describes the reduction of flux carrying capability in the core due to the lamination surface coating and the bonding material between the individual laminations. This reduces the amount of active lamination material in a given stack length and for the prototype machine, which has an stack length of $l = 150\text{mm}$, a total of 422 laminations of 0.35mm thickness were used. This corresponds to an active core length of approximately 147mm and a core stacking factor of 0.98. The compressed stacks are then set to cure in an industrial oven at 180°C for 3.5 hours, and are then brought out of the oven to cool prior to cutting.

4.2 Electro-Discharge-Machining Technique

The stator and rotor core lamination sets were cut using wire Electro-Discharge-Machining (EDM) technology to remove material. This cutting technique is suitable only for one-off prototypes and very low volumes due to its slow cutting speed, the typical achieved cutting speed during stator and rotor core cutting was 1mm/min . This cutting time depends not only upon the length of the cutting path in the part but also its complexity and its material. As the cutting edge does not excessively heat the material like laser cutting or mechanically deform it like punching, minimal magnetic damage occurs, resulting in high precision and magnetically superior parts and tolerances as good as $\pm 0.001\text{mm}$ can be achieved by the use of wire EDM techniques. In order for the wire EDM machine to cut the desired lamination profiles for the stator and the rotor cores, small starting holes must be located into the lamination stacks. There are two methods of performing this manufacturing operation. Conventional drilling, whereby a drill press and conventional drill bit are used to cut through the lamination material, or by using an EDM technique. Due to the small features in the rotor design (thin flux barriers), start holes of diameter 1mm are required to be sunk into the stack length.; a conventional titanium drill bit of this diameter could not easily or with great accuracy cut through the desired stack length of 150mm or even if the stack length is segmented into separate stacks of approx 40mm - leading to tip wandering and possible shearing of the drill bit. Therefore, a 'Sinker EDM' is used to 'drill' the start holes. In this technique, a 30cm long cylindrical electrode of

1mm diameter is used, both this electrode and the work-piece are covered by a dielectric fluid during lamination cutting when the material is removed.

4.3 Coil Manufacture and Stator Assembly

4.3.1 Slot Fill Factor

The stator was chosen as a six slot stator ($Q_s = 6$) with a double layer single tooth winding arrangement, requiring six stator coils, two per phase. As a high slot fill factor ($\approx 60\%$) is specified for the machine, a computer model of the slot and the placement of the coil turns in the slot was created in MotorCAD, and is presented in Figure. 4.2. Coil trials were also performed on a mock stator in order to confirm the achievable slot fill factor. With the segmented nature of the stator, the desired fill factor was expected to be achieved. In the prototype design, the available slot area is approximately 560mm^2 , the chosen slot liner is a NOMEX paper of 0.3mm thickness. As well as insulating the stator core from the coil, the slot liner is wrapped around each coil in the centre of the slot to form a vertical coil divider of 0.6mm width. The number of series turns per phase was calculated previously to be $N_s = 104$, thus the required number of turns per coil is therefore $N_c = 52$. The calculated copper diameter to achieve the specified fill factor is approximately 2mm which is a standard wire size in available wire gauges. The slot cross section and conductor placement for the number of conductors and correct fill factor is shown in Fig. 4.2, with conductor insulation. The chosen copper diameter and number of turns then corresponds to a gross slot fill factor of 58.6% including insulation and a coil (net) fill factor of 60.63%. The conductors have Grade II, temperature Class F (155 degC) insulation. The specification of Grade II means that the wires Polyimide insulation is of double thickness compared to standard 'Grade I' insulated wire. Grade II wire helps to increase insulation integrity and has higher mechanical strength.

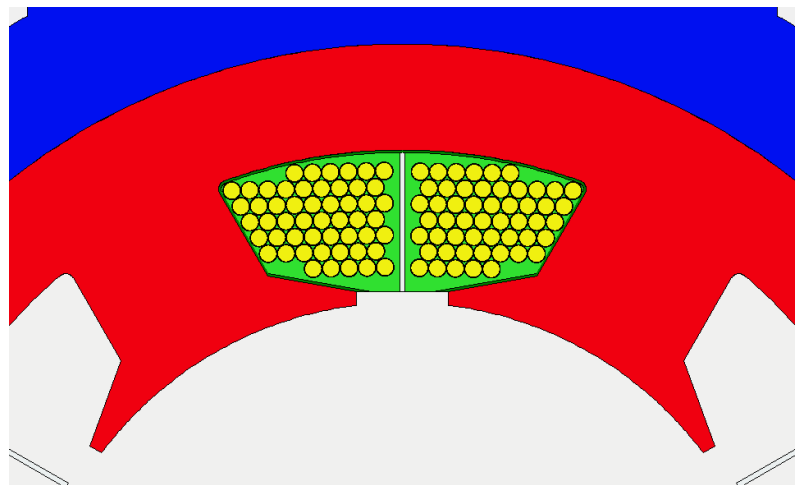


Figure 4.2: Conductor placements in the slot

4.3.2 Stator Segment Coil Winding

As the stator is segmented into six individual segments, each with its own coil, the stator winding process is relatively simple when compared to distributed winding systems. In the case of the single tooth winding, the coil can be wound directly on to the toothed segment and then the stator core assembled when all segments are wound. Each fabricated stator segment was prepared with its slot liner, end winding supports and numbered, ready for the winding process. In order to assist coil winding, a jig was designed and fabricated to hold the stator segment in position on the winding machine. The stator segment is held in a fixture and clamped with four retaining clips, the whole jig is then slotted into the winding machine on a spigot ready for winding on a programmable coil winding machine. The wire is held at a constant tension during the winding procedure: this allows neat coils to be wound, resulting in a high fill factor and short end turns. Figure. 4.3 shows the winding jig and a unwound stator segment and Figure. 4.4 shows a stator segment being wound on the winding machine: note the neat and uniform nature of the wound turns. For assessing the practicality of assembling wound stator segments, a semicircular mock stator of full stack length, consisting of two stator segments and a retaining frame manufactured from aluminum to allow trials to take place. The two completed stator segments and coils can then be fitted into the mock stator - the required slot fill factor was achieved if the two segments fit together as expected and the inter-segment airgap is small, as expected. All combinations of stator segments fitted into the mock stator, therefore, full stator stack assembly would be possible with the coils at their desired fill factor. In Figure 4.5, the mock stator and the two completed two test coils on stator segments is shown.

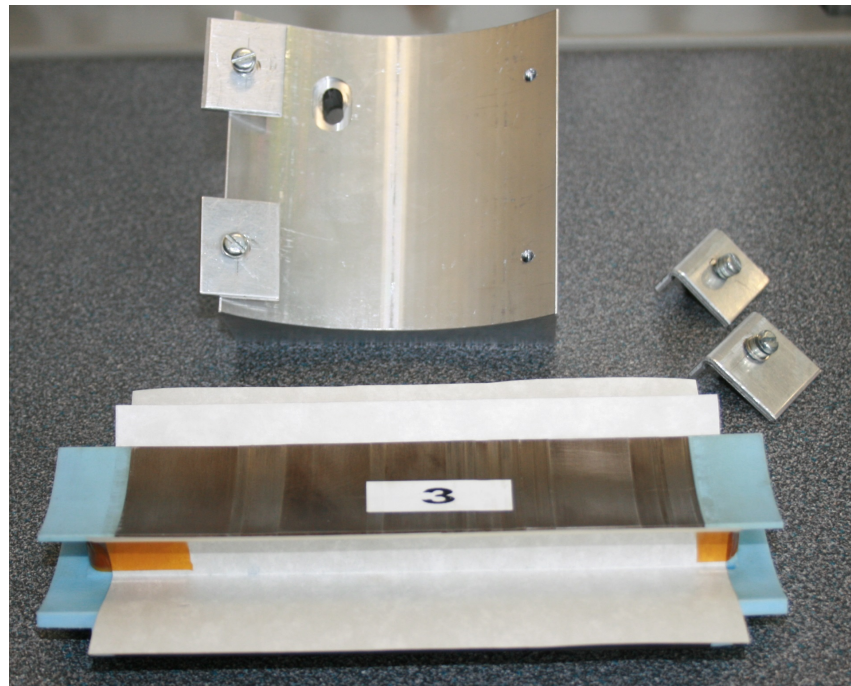


Figure 4.3: Stator segment with end pieces and winding jig

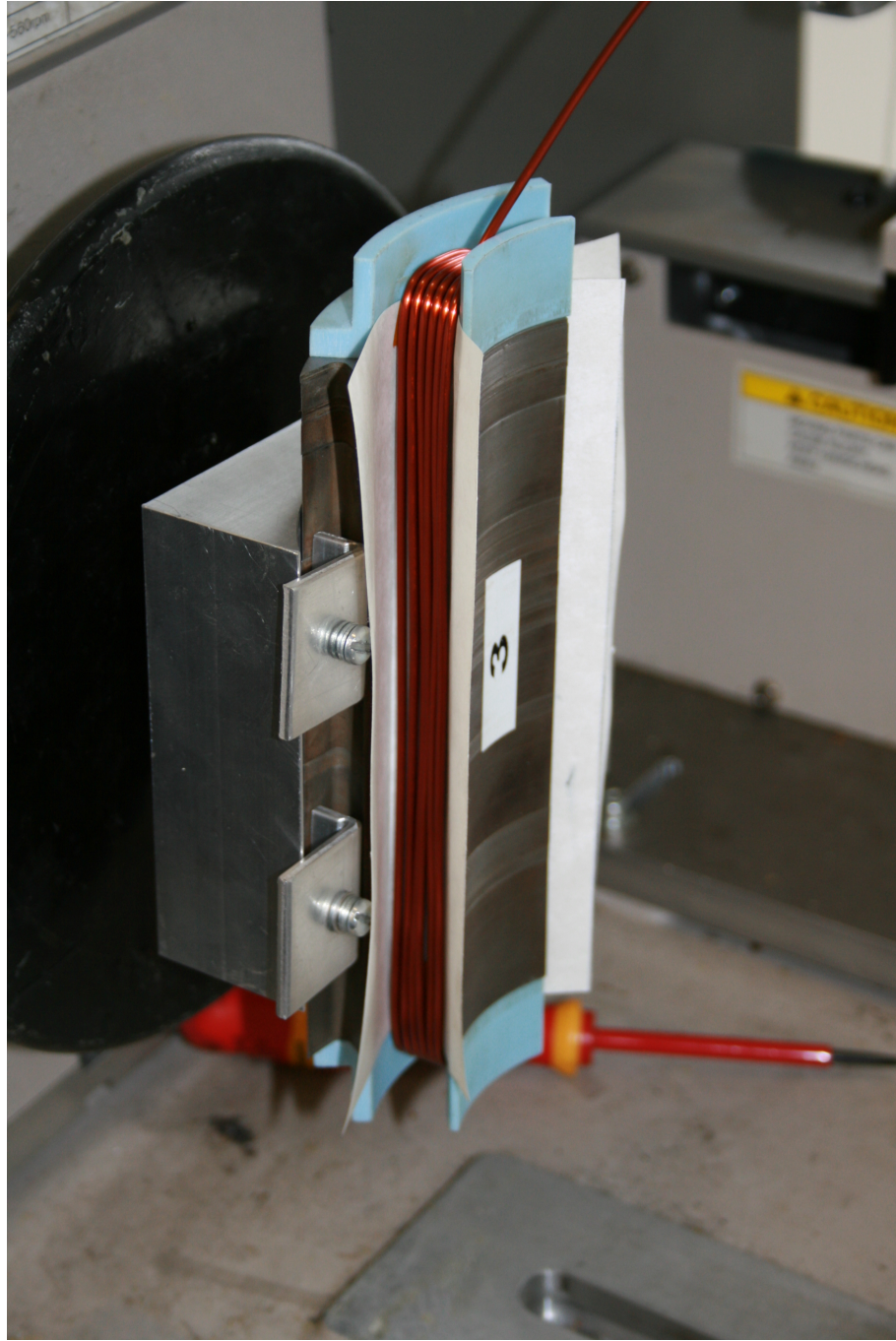


Figure 4.4: Close-up of a stator coil being wound

It is evident from Fig. 4.5 and the segment assembly trials that stator coil end windings had a very short axial length and that the conductor circumferential length were also small by achieving a neat and tight end winding. Table 4.1 shows the calculated and measured phase resistance and end winding axial length.

Parameter	Calculated	Measured
R_{ph} [Ω]	0.23	0.23
l_{axial} [mm]	21	19

Table 4.1: Calculated and measured coil parameters

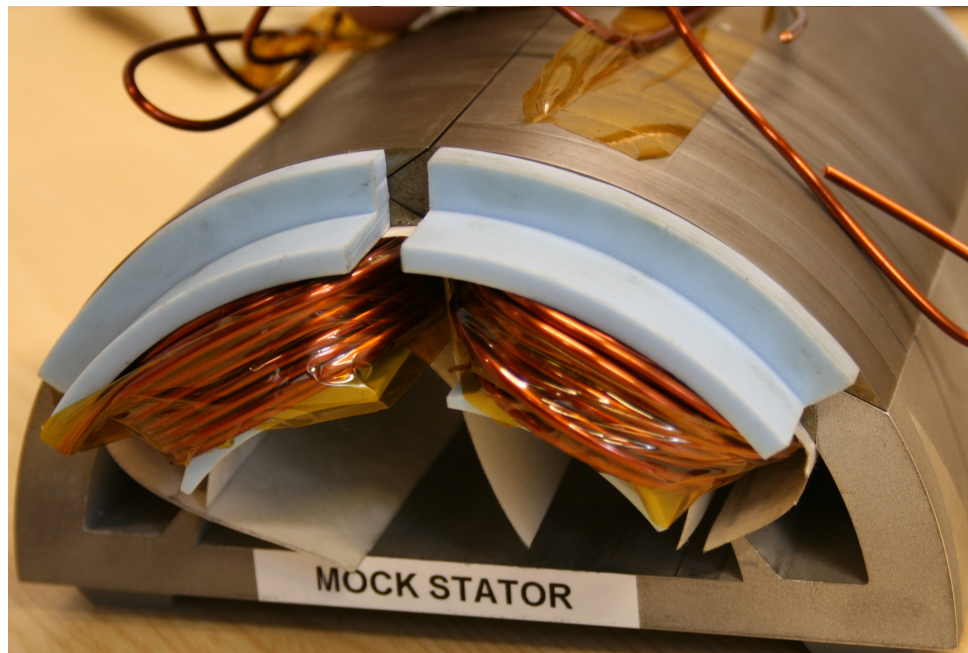


Figure 4.5: Two trial coils in the mock stator

4.3.3 End Winding Supports

In order to facilitate neat and tight stator coils to maximise the slot fill factor, minimise the axial length of the end winding and help prevent end winding short circuits, end winding supports were CNC milled from high temperature plastic. These end winding mechanical supports help to maximize the potential of concentrated single tooth windings by providing mechanical support to the end winding and to increase the effectiveness of the slot insulation. If a conductor is bent smaller than a certain bend radius, insulation damage can occur on the inner and outer faces of the bend: this is usually at a sharp edge of a lamination stack. To avoid this, end winding supports are designed with a 5mm minimum bend radius to lower the risk of insulation damage and coil to ground shorts on the edge of the stator stack. The slot insulation extends out of the slot by 5mm each side of the lamination stack; the end winding supports have a 5mm face parallel to the slot side: this prevents the conductor pushing the slot liner onto the sharp corner of the lamination, increasing the slot liner effectiveness. Mechanical support is provided by the upper and lower faces that extend over the majority of the end winding. The end winding experiences forces during machine operation, leading to vibration and mechanical wear, and potentially could eventually produce a short circuit. With the end winding supported, the natural frequency of the end winding increases making it less susceptible to end winding forces and vibration. A photograph of the completed end cap, fabricated from high temperature plastic, is shown in Figure 4.6. The fabricated end winding supports are segmented to fit with the stator segments and are held in place during winding with the Polyimide electrical insulation tape, Kapton®.

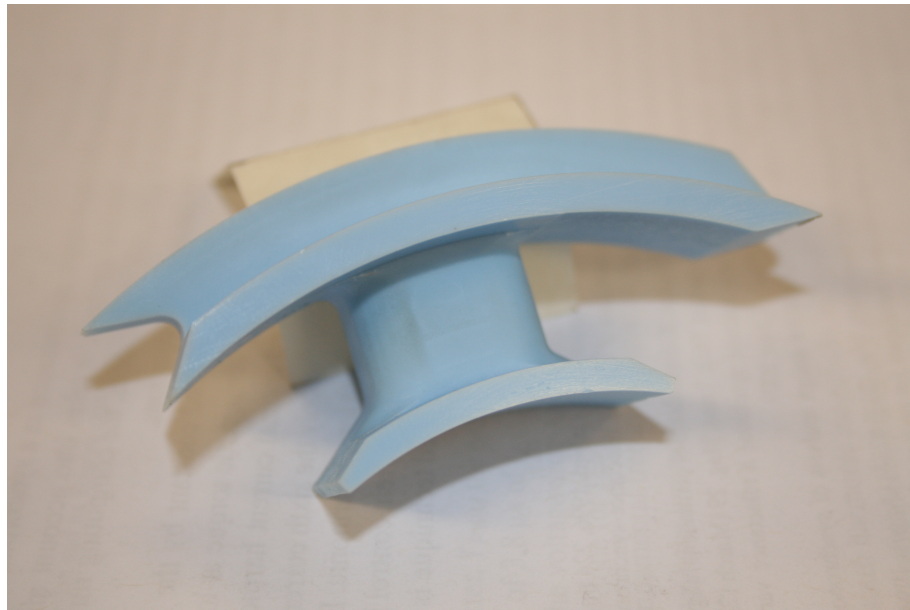


Figure 4.6: Segmental end winding support

4.3.4 Stator Stack Assembly

The final stator assembly procedure is to fit the six assembled stator segments into the stator casing. As the stator core is fabricated and assembled in segments, once the coils have been wound, all of the segments are brought together in their interlocking configuration and large 'jubilee' clips placed around the assembly. These are then tightened, pulling the stator lamination segments closer together and closing the inter-segment air gaps. The manufactured aluminum stator housing is then heated in the oven to allow thermal expansion at 180 degC. Whilst the case is heated, one end of the compressed stator lamination stack is lowered into the housing and then using a soft hammer is slowly slid into the case until it hits the stop (the compression clips are removed, as required, as the laminations progress further into the housing) - effectively aligning the stator lamination stack with the case in the correct position. The housing is left to cool and the lamination segment assembly is effectively shrink fitted against the housing with fit of approximately 0.05mm. The stator coil leads are then ready for termination and the final assembly stages of the motor. Figure 4.7 shows the stator segment assembly after shrink fitting into the outer casing.

4.3.5 Stator Coil Terminations

The final stage in prototype assembly for the stator is to bring out the stator coil connections and terminate them to the stator termination ring. The termination ring is designed so that the machine could potentially be rapidly reconfigured in either a star or delta winding arrangement. The sockets in the termination ring take standard high voltage banana plugs (sheathed): this allows easy and safe connection of the stator coils with external leads. Inside the stator, the 12 flying leads from the 6 stator coils were sheathed with a

temperature Class H high voltage fiberglass insulator, terminated with crimped ring terminals and the join covered with heat shrink tubing. Figure 4.8 shows the 12 flying leads of the 6 stator coils with their insulation and ring terminals. These 12 ring terminals are then connected to 12 insulated banana plug sockets on the terminal ring to allow external connections to each coil in any configuration. Figure 4.8 clearly shows the termination ring with the colour coded receptacles and coil labels. The figure also shows the five leads of K type thermocouples used to measure the stator coil end-winding , coreback, case and stator slot temperatures during testing.

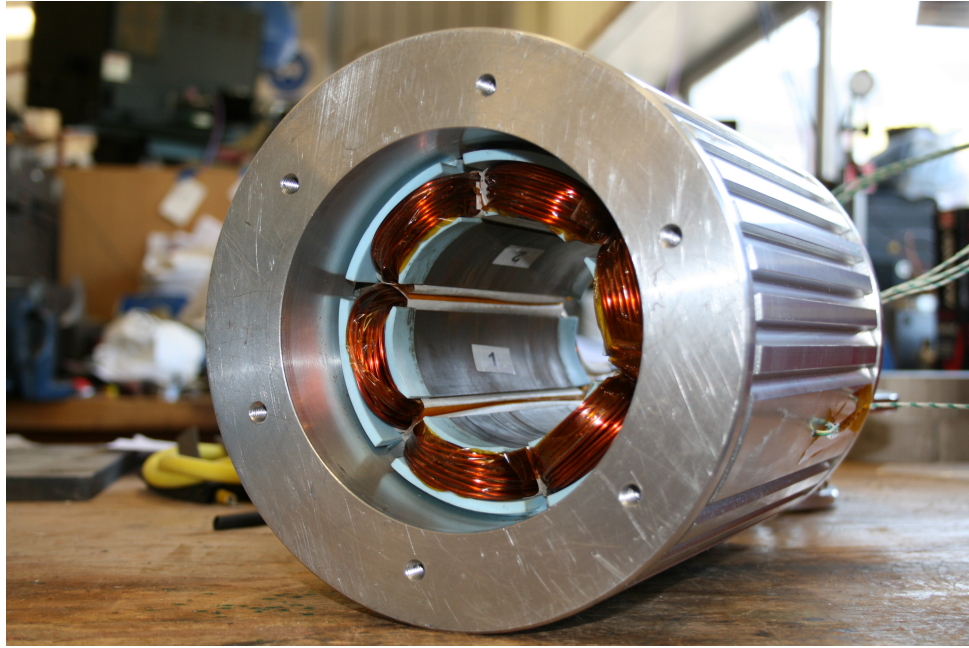


Figure 4.7: End turns and winding supports on completed stator

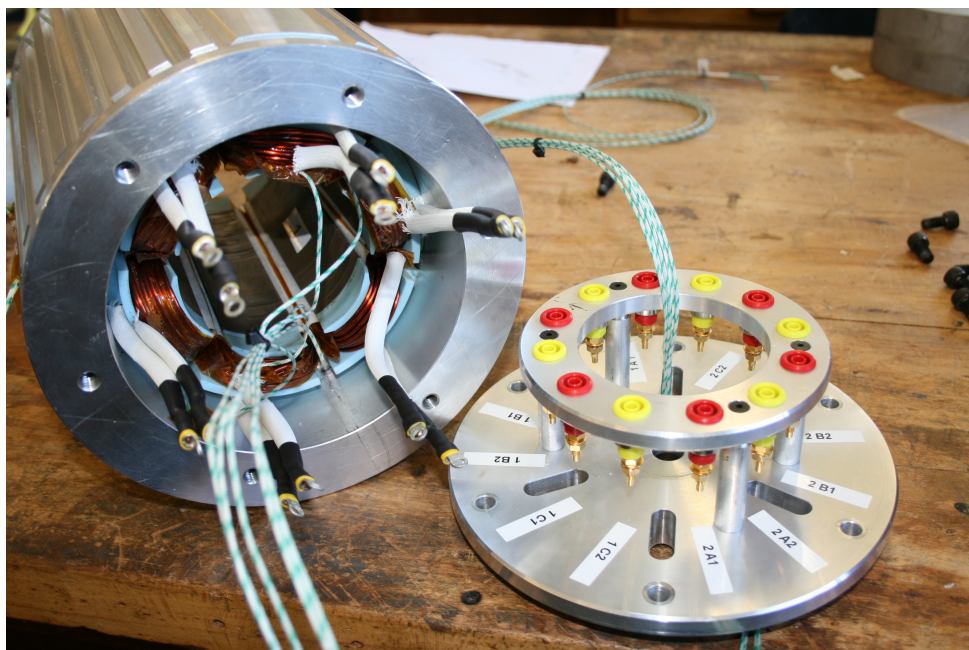


Figure 4.8: Stator terminal ring and stator coil terminations of the prototype machine

4.4 Rotor Stack Manufacture and Assembly

The rotor lamination stack was challenging to fabricate, the intricate rotor design with its multiple fine features proved to be demanding in terms of manufacturability and manufacturing time. The first attempt at fabricate the rotor stack resulted in failure, however the lessons learned during this stage of the manufacturing process carried through to successful fabrication of the final rotor stack used in the prototype cSynRM machine.

4.4.1 First Rotor Stack

As with the stator core lamination stack, a complete stack length of 150mm with 422 M250-35A laminations of size 200mm x 200mm x 0.35mm, glued. This size of lamination allows adequate clamping of the stack in the EDM wire machine during cutting. This particular stack was cut by an external contractor, a precision engineering firm with specialism in injection molding tools. The full lamination stack was supplied to the contractor after being stacked, glued and clamped in-house by mechanical workshop technicians. Figure 4.9 shows the complete 150mm long rotor lamination stack with the rotor design partially cut and some test start holes visible in the upper left corner of the stack.



Figure 4.9: The complete first rotor lamination stack (partial cut) at the contractor

As mentioned, this fabrication attempt was not successful. There were a number of reasons for this and are outlined as follows;

- The stack length was too long at 150mm to accurately sink 1mm start holes for the wire EDM machine - this resulted in wandering of the hole trajectory down the stack length, even with EDM sinking

- The stack length was too long at 150mm for the thin 0.25mm EDM wire - this caused the wire to repeatedly snap and extend cutting time and cost
- The fine features caused the wire EDM machine to stop with an alarm / wire snap - this was due to the small shards of lamination material from the flux barriers released after a complete barrier cut
- The manufacture was not carried out in one run - this caused a number of clocking (cutting alignment) errors when reloading the stack into the EDM machine and the slots were cut in the wrong positions

This stack was discarded. Figure 4.10 shows the wire EDM partially cut lamination profile, this was the result of three months manufacturing time where approximately 50% of the cutting was complete.

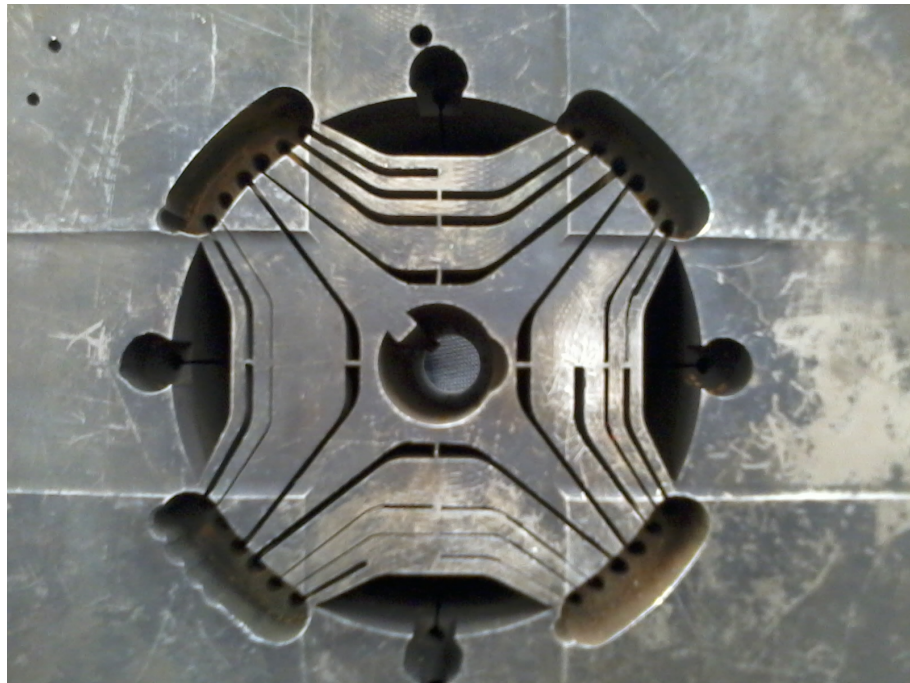


Figure 4.10: The first rotor lamination stack - partial cut of failed manufacture

4.4.2 Final Rotor Stack

The final rotor lamination stack was manufactured at Newcastle University using in-house sinker and wire EDM machines as described in Section 4.1. To overcome the manufacturing difficulties experienced by the external contractor, multiple shorter stacks of lamination material were assembled to effect the following;

- Eliminate start hole divergence along the axial length of the stack - giving accurate starting positions for each stack along the entire 150mm lamination stack
- Reduce the tension on the EDM wire to prevent snapped wire alarms

- To minimize the risk of the small lamination segments from the cut flux barriers causing difficulty and enable easier and quicker clearance of any stoppage that did occur

For the manufacture of the final rotor lamination stack, four square stacks of M250-35A laminations of dimensions 200mm x 200mm x 40mm were used. The laminations were unglued but clamped as with the stator core lamination stack manufacture. As with the stator stack, the depth for the prototype rotor active stack length was $l = 150\text{mm}$, with a total of 422 laminations of 0.35mm thickness were used, corresponding to an actual core length of approximately 147mm and a core stacking factor of 0.98. A completed lamination stack and rotor is presented in Fig. 4.11.



Figure 4.11: Completed prototype rotor stack and shaft assembly

4.5 Mass Manufacturability

The electro-discharge-machining techniques used in prototype fabrication could not be used for mass manufacture as the cutting rate is typically 1mm per minute. The overall peripheral cutting distance for the rotor is approximately 7 metres, giving a cutting time per 40mm depth stack segment of just under two hours. For the given stack length of 150mm and the use of four 40mm stacks to make up the full stack, the total cutting time for the rotor only is only just under 8 hours. This time does not account for any preparation of the stacks (raw lamination cutting, gluing, clamping, baking and start hole drilling), which adds significant time to the manufacture process. The stator follows a similar timescale and process but with the added complexity of stator segment winding

and assembly. Therefore, EDM can only be used for prototyping purposes and other manufacturing methods would be required for any larger volumes. Traditional lamination stamping is one option for mass production or the use of pulsed laser cutting for smaller volumes - in both techniques magnetic damage to the thin magnetic flux guides on the rotor would need to be investigated and the small features could potentially cause increased tool wear if stamped. It is beyond the scope of this thesis to consider any mass manufacturing further as this thesis explores a '*proof of concept*' prototype motor only.

4.6 Conclusion

This chapter has presented the manufacture and assembly of the prototype synchronous reluctance motor with fractional slot concentrated windings (cSynRM). Both rotor and stator core lamination stack manufacture was performed using EDM techniques which is only suitable for prototyping or low volume production due to excessive manufacturing times. Small rotor features in small synchronous reluctance motors, such as the thin flux barriers, add to the manufacturing complexity. The engineer must take into account the inter-dependencies relating the electromagnetic performance, mechanical integrity and the manufacturing processes, especially when designing for mass production. When producing prototypes using EDM machining, shorter 'biscuits' of laminations are significantly easier to cut than long stacks. Segmenting the stator core-back facilitates ease of coil winding, attaining high slot fill factors (at least upto 60% can be obtained) and neat single tooth coils. Using specially designed end winding supports complements the segmental nature of the stator and produces a tight and neat end winding with high natural frequency and short axial extent. Assembly of stator segments is straightforward and can be easily shrink fitted into casings, closing the inter-segment airgap. Final assembly included termination to a special termination ring with direct access to each coil for rapid configuration of the stator winding and mounting to a knee plate, ready for experimental testing.

Chapter 5

Prototype: Testing and Verification

This chapter documents the experimental testing of the constructed prototype machine. Firstly, the insulation system is comprehensively tested for short circuit faults. The test method and the results are presented for locked rotor DC testing, performed on the prototype machine and compared with finite element studies to verify the d - q axis flux linkages and inductances as well as the machine torque capability. Additionally, the test method and results of locked rotor AC testing are also presented and compared with the DC test results. As the stator leakage inductance has been identified as a key contributor to the low power factor of this machine, the test method and results of an AC removed rotor test are presented in an attempt to measure the stator leakage inductance and verify the analytical estimation. Finite element studies also supplement the analysis and measurement of the stator leakage inductance. Thermal tests are also reported at rated current and finally, the test method and results of full running tests at rated load and speed are presented to confirm machine torque, power factor and efficiency predictions.

5.1 Insulation System

Before measurement of the machine parameters and performance, the insulation integrity of the prototype machine was assessed using a high-voltage motor test instrument. Standard MegOhm, HiPot and surge tests were carried out on the prototype, in particular coil to ground and inter-turn shorts were assessed according to the IEEE 95-2002 [1] and IEC 60034 [2] standards. With single tooth coils, insulation damage due to packing the turns into the slot and short end turn lengths with small radii can arise. The prototype was designed with end winding supports as described in Chapter 4 with the aim of minimizing any potential shorts to ground. All six individual stator coils were measured to have an average insulation resistance of $> 100\text{G}\Omega$ and a typical leakage current around $I_l = 0.02\mu\text{A}$, indicating good insulation system [3]. These DC tests cannot accurately detect inter-turn insulation degradation in a stator coil. AC impulse testing [4,5] involves applying multiple AC test wave forms to the coil under test governed by IEEE 522-2004 and IEC 60034-15 standards. These impulse waves have very fast rise times (μs) and a

high voltage is generated across the coil, any weak turn-turn insulation will breakdown and begin to arc if the inter-turn induced voltage is high enough. Puncture or breakdown of weak insulation is detected by a change in the response waveform as a change in amplitude, frequency or phase. This is attributed to the change in coil inductance which modifies the coil's resonant frequency [6,7]. All six stator coils were tested for inter-turn shorts and no inter-turn shorts were detected. The machines insulation is therefore intact and capable of withstanding the inverter DC link voltages of approximately 590V.

5.2 Locked Rotor DC Testing

Locked rotor DC testing is an off-line test method that allows the magnetic characterization of electrical machines to be compared to finite element studies for verification of the magnetic model. Direct current tests are used in this thesis to verify the rotor electromagnetic torque capability, the orthogonal axis flux linkages and their corresponding orthogonal axis inductances. These are then compared to the FEA derived results under the same locked rotor DC conditions. The FEA model used in the comparison of the results is a 2D model which is compensated for 3D leakage effects by analytical methods - a lumped end winding leakage inductance. According to the literature, direct current test methods are less susceptible to iron loss and skin effect errors during measurement than rotating AC methods and thus can provide a higher degree of accuracy in measurements regarding magnetic characterization of electrical machines [8].

5.2.1 Equipment and Setup

The locked rotor DC test method is often used in the magnetic characterization of switched reluctance motors (SRM) [9,10] in which one phase is connected at any one time during a test. This is valid in the SRM as it represents an instant in 3ph sinusoidal excitation operation, however in the prototype cSynRM this procedure is modified to include the two other phases as it is a three phase machine, identical to that when testing permanent magnet motors using locked rotor DC conditions [11,12]. A DC current flows at 1p.u. in Phase A and -0.5p.u. in the other two phases as this represents a genuine operating condition of the cSynRM. The rotor can be locked at various angles using a machinist's dividing head. The dividing head used during the DC locked rotor testing had a resolution of one mechanical degree; this corresponds to two electrical degrees. Figure 5.1 shows the winding configuration of the machine when connected to a programmable DC power supply, as presented in Fig. 5.2 which shows the full DC locked rotor test rig.

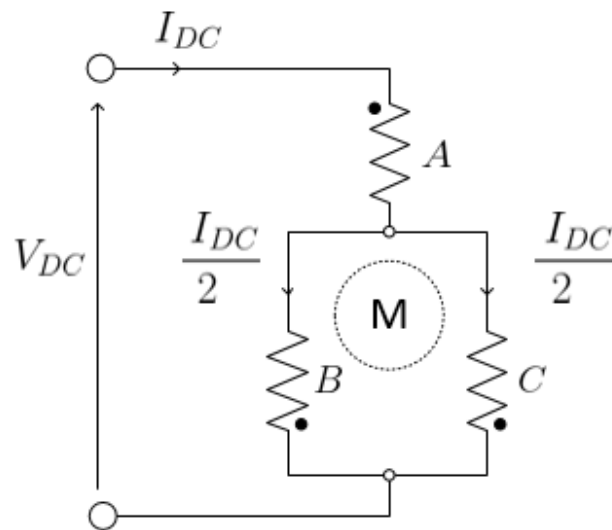


Figure 5.1: DC Testing Winding Configuration

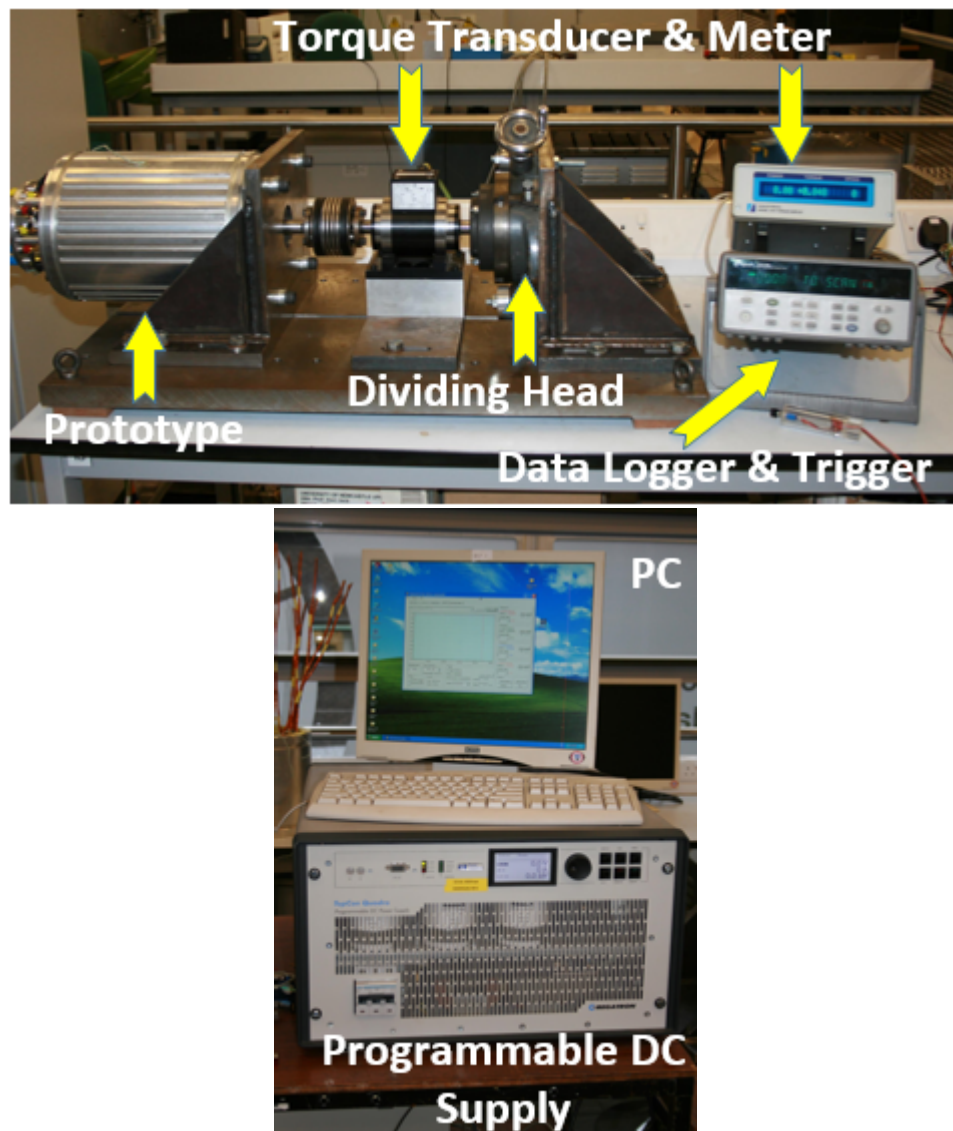


Figure 5.2: Locked rotor DC test rig

5.2.2 Static (DC) Torque Tests

Locked rotor DC testing allows static torque testing to be performed, otherwise known as the DC torque or locked rotor torque. This test allows measurement of the motor electromagnetic torque as a function of rotor angle. This is a common test in the switched reluctance motor but it can also be applied to the SynRM [13]. A DC terminal current I_{DC} is fed into Phase A, the current is shared in the other two coils according to Fig. 5.1. The current is supplied by a 52V 400A programmable DC power supply and the torque is measured using a Magtrol TM210 Torque Transducer in-line with the rotor shaft and the dividing head. Torque measurements are made with the rotor locked at various rotor angles, the test procedure is as follows;

1. Lock the rotor at 0 degrees with the dividing head
2. Supply a continuous current I_{DC}
3. Measure torque and record value
4. Increment rotor angle until 180 degrees mechanical
5. Increment current and repeat step 4 until complete

In these measurements, the rotor angle was advanced by one mechanical degree as to give provide a high resolution measurement of the torque waveform over the rotation. The DC currents supplied correspond to the peak value of the RMS AC currents of 5A, 10A, 15A and 20A, giving 724 torque samples which can then be compared to finite element studies. The coupled torque transducer provides a DC voltage level representative of the developed electromagnetic torque which is captured by an Agilent Data-logger connected to a PC. The data-logger is manually triggered by hand for each rotor angle and current magnitude. The measured data requires post-processing to obtain the torque wave forms. Firstly, any DC offset is taken out and then the DC voltage level is scaled using the manufacturer provided scaling factor for the TM210 torque transducer of 50mV/Nm to acquire the electromagnetic torque.

5.2.2.1 Measurement and FEA Comparison

Static 2D finite element solutions in Infolytica MagNet are used in this comparison, with 3D effects compensated for by the inclusion of the per phase lumped end winding leakage inductances as calculated later in this chapter. The finite element studies are performed with identical currents to the empirical test for a direct comparison. Figures 5.3 to 5.6 present the measured vs. finite element torque wave forms for a rotor positions between 0 and 180 mechanical degrees (This represents two whole electrical cycles) in steps of one mechanical degree.

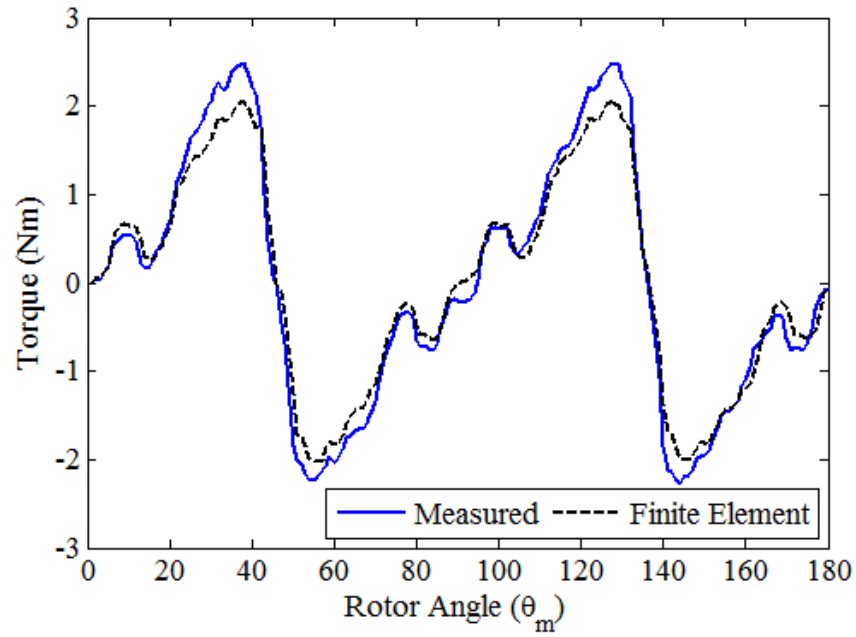


Figure 5.3: Static Torque - 5A

It is evident from the 5A data that the measured result is greater than the FEA result. One contributing factor to this may be the test equipment accuracy as the rated torque of the torque transducer is 50Nm and sensitivity and accuracy may well be affecting the result at very low torque levels below its rated. The device datasheet indicates a $\pm 0.1\%$ error at rated torque ($50\text{Nm} \pm 0.05\text{Nm}$), though it is unclear what the effects are low down the measurement scale. Other factors to contribute would be a shorter airgap, longer stack length, increased airgap diameter or deviation from the modeled material data. The airgap was verified with feeler gauges at 0.5mm and the rotor diameter and stack length confirmed to their design values.

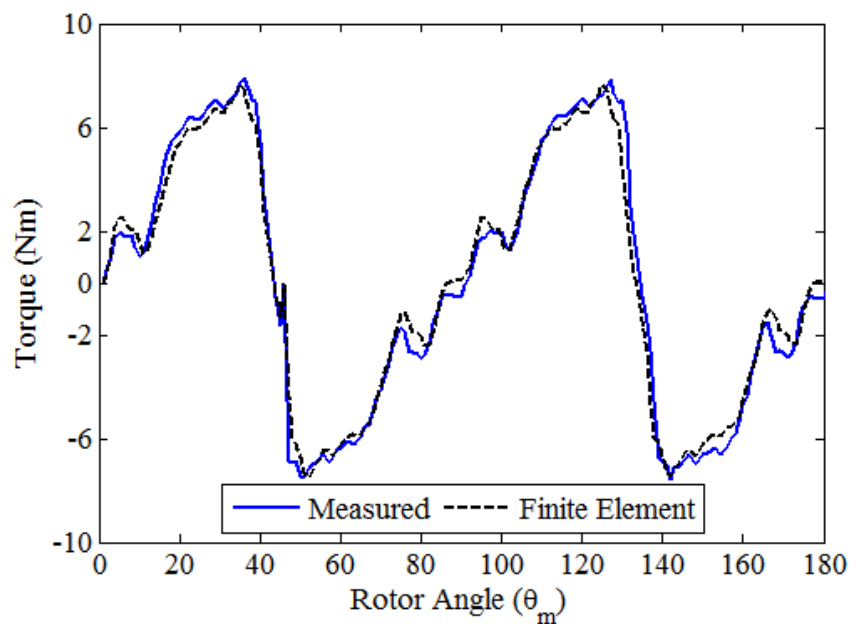


Figure 5.4: Static Torque - 10A

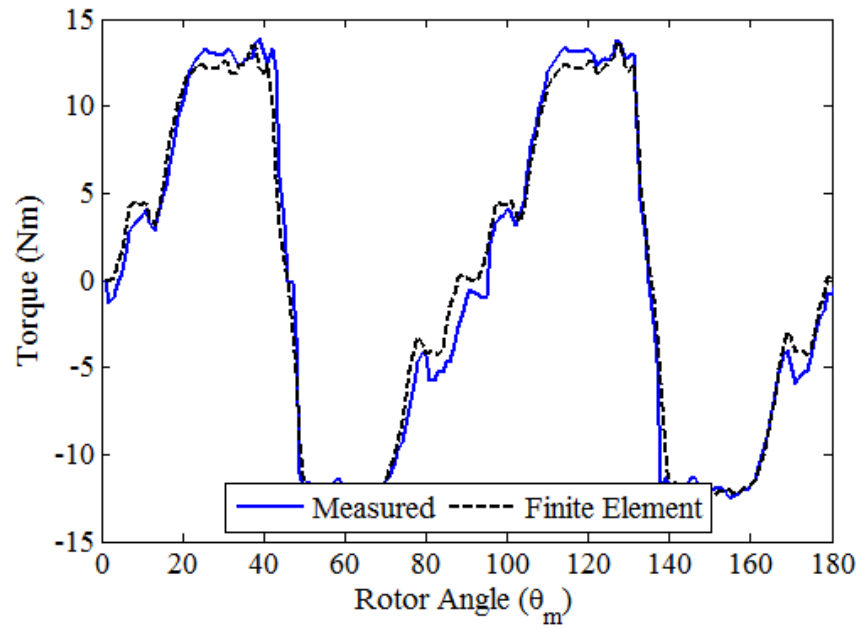


Figure 5.5: Static Torque - 15A

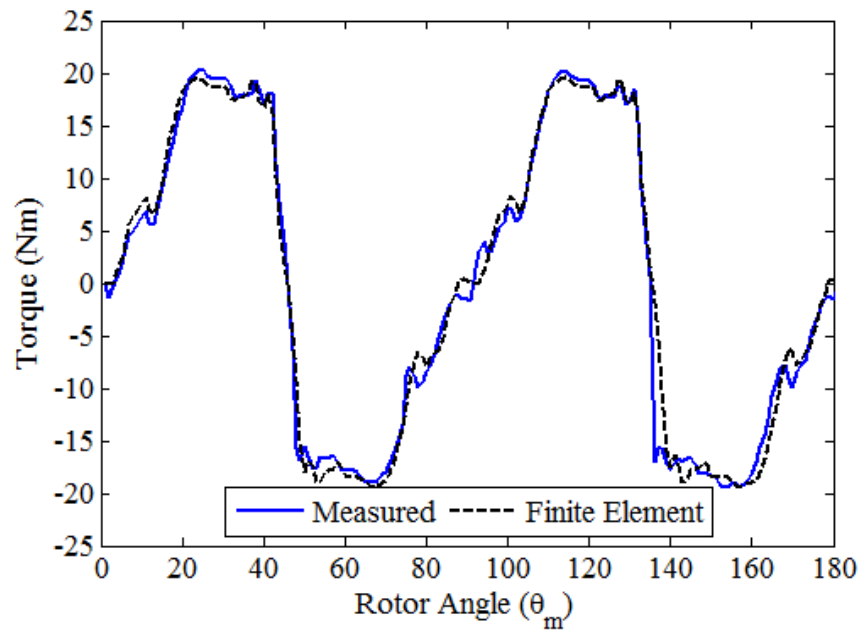


Figure 5.6: Static Torque - 20A

It is clear through Figs. 5.3 to 5.6 that the measured torque closely follows the FEA predicted torque wave forms, the harmonic content is well replicated in the measured results. The measurement error appears to decrease with increasing torque, this is as the measured torque increases toward the rated torque of the transducer and the DC level output signal becomes more appreciable in magnitude. The mean error between the measured and FEA torque waveforms is 3%. The torque cycle is repeated over the 180 mechanical degrees as expected as the current angle goes through 180 degrees in electrical terms in 90 degrees mechanical for a two pole-pair machine¹. There was no variation in the result

¹Mechanical degrees are related to the electrical angle through $p\theta_m = \theta_e$ where $p = 2$.

between phases.

5.2.2.2 Fundamental Component of Torque

It must be noted that rotor angle corresponds to the current angle of the motor as the stator MMF is aligned with the magnetic axis of Phase A. This allows computation of the static maximum torque current angle and subsequent calculation of the motor's torque index. In the experimental data it would be expected that the torque would follow the function of $\sin(2\theta_e)$ perfectly if there were no parasitic effects and the machine was perfectly sinusoidal in nature. However, the curves are not perfectly sinusoidal, which is due to slotting effects of both the rotor and the stator, localized saturation and space harmonics set up by the machine's spatial MMF profile. Figure 5.7 shows the 20A torque data superimposed with its fundamental component over 180 electrical degrees with the associated normalized harmonic spectrum (computed using an FFT). The maximum torque can be found to be at 45 electrical degrees as one would expect, with a torque magnitude of 19Nm.

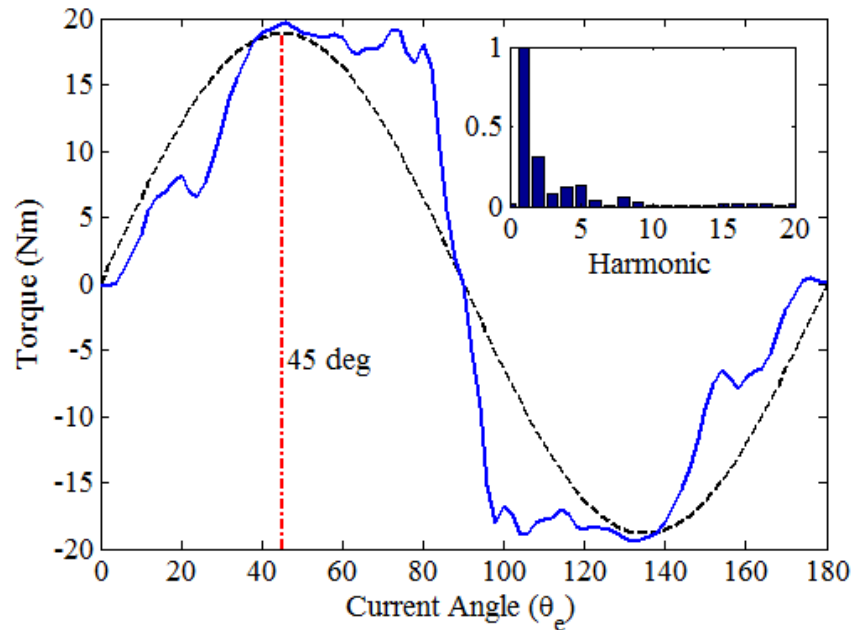


Figure 5.7: Static Torque - 20A with Fundamental and Harmonic Spectrum

5.2.2.3 Mean Cyclic Torque

The *mean cyclic torque* can be calculated if the torque is averaged over the positive half cycle;

$$T_{AV} = \frac{1}{\Delta\theta_m} \int_0^{\theta_m=45^\circ} T(\theta_m) d\theta_m \quad (5.1)$$

Here θ_m is the mechanical angle of the rotor. This then allows comparison of the measured and FEA torque waveforms that include all harmonic contributions into a single numerical figure. Figure 5.8 shows the measured and FEA averaged torque per DC

current level over 90 electrical degrees (45 mechanical degrees) vs. applied current. This shows that the developed torque in the prototype machine accurately follows the predicted torque, that saturation is modelled with a good level of accuracy in the finite element studies and that the harmonic content is accurately modeled.

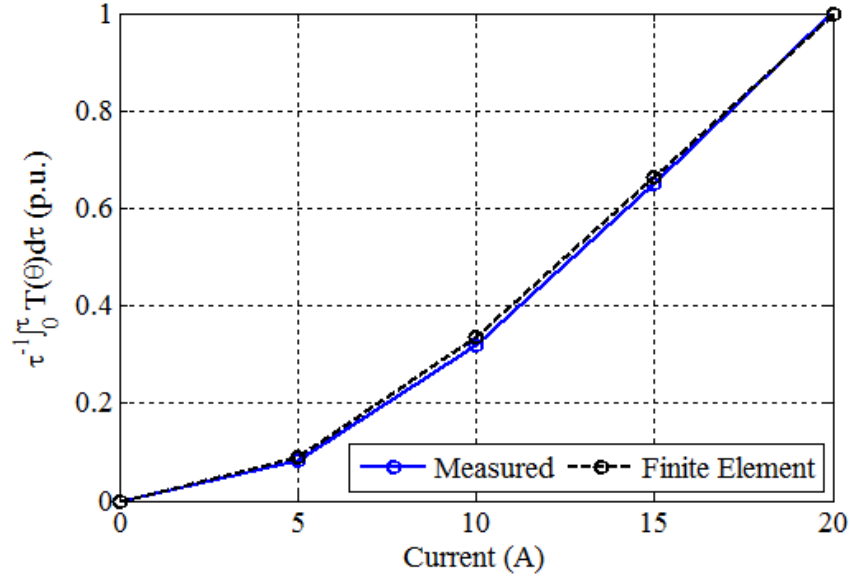


Figure 5.8: Averaged Torque vs Current

5.2.2.4 Torque Index Estimation

From the fundamental torque data, the conventional equation in the dq frame can be used to estimate the torque index, which is a typical figure of merit of the torque capability of synchronous reluctance machines [8,13];

$$\Theta = |L_d - L_q| = \left(\frac{2}{3}\right) \left(\frac{T}{pI^2 \sin(2\theta_e)}\right) \times 1000 \quad (5.2)$$

Where T is the measured torque, p is the number of rotor pole pairs, I^2 is the square of the applied current and $\sin(2\theta_e)$ relates to the current angle of the machine based upon the mechanical rotor angle. From the DC torque results at rated operating current, the fundamental torque is calculated as 20.98Nm, and the torque index is estimated to be 15.87.

5.2.3 Flux Linkages

The orthogonal axis flux linkages are an important machine parameter and the axis saturation curves determine machine performance. A widely applied DC test method is known as the '*Direct Method*' or '*Instantaneous Flux Linkage*' test [8-13], commonly used for characterization of switched reluctance motors. The coil arrangement used during the static torque tests is maintained (Fig. 5.1) when using this method to validate the cSynRM magnetic model. In this test, multiple pulses of DC voltage, with a low duty

cycle and DC level just enough to obtain the required peak current, are applied across the machine terminals. The low voltage ensures low eddy current losses associated with the steel magnetization and thus provides an accurate measurement of the flux linkages - taking into account any winding resistance drops to ensure accurate calculation. The voltage and current at the machine terminals are measured and the flux linkage calculated for different rotor angles. The low duty cycle ensures that between pulses the current (and the flux linkage) falls to zero before the next rising edge. The flux linkage $\Psi[t]$ is calculated by;

$$\Psi[t] = \int_0^t V_{DC}[t] - RI_{DC}[t] dt = \int_0^t \mathcal{F}[t] dt \quad (5.3)$$

Here $V_{DC}[t]$ is the applied voltage waveform and $I_{DC}[t]$ is the measured current waveform. The flux linkage depends on the correct identification of the effective resistance R , the correct value of which ensures that the flux linkage falls to zero between pulses. As the test is performed over a short period ($\approx 3s$) temperature effects on R are minimal and can be neglected. Eq. 5.3 is approximated numerically using trapezoidal integration [14];

$$\Psi[t_n] \approx \frac{t_{n+1} - t_n}{2} \sum_{n=1}^N (\mathcal{F}[t_{n+1}] - \mathcal{F}[t_n]) \quad (5.4)$$

During testing, $V_{DC} = 19V$ to allow a current rise to $I_{DC} > 40A$ with 1024 sample points over four pulses with 30% duty cycle. Figure 5.9 shows an example of the measured current and voltage waveforms and the calculated flux linkage with time for a single rotor angle.

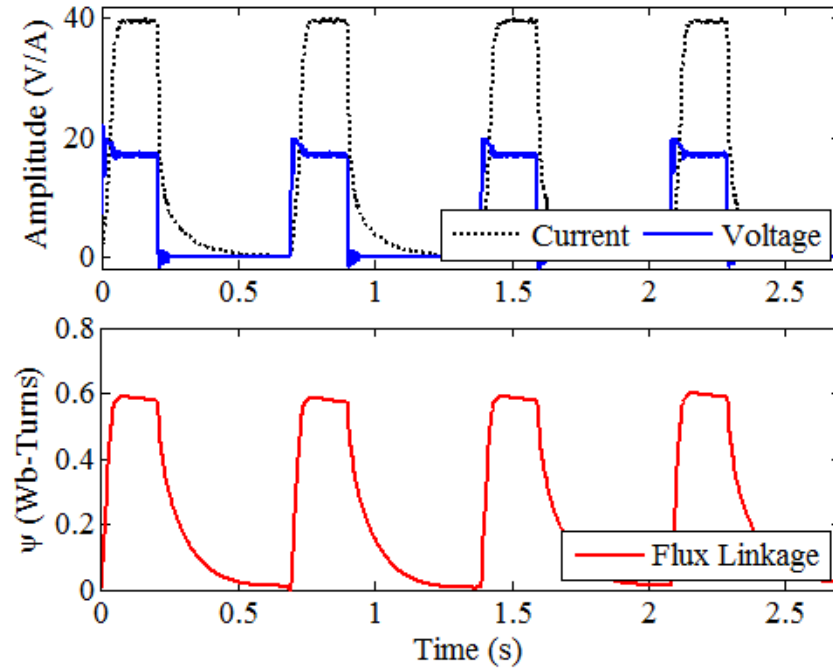


Figure 5.9: Measured Voltage and Current Data with Calculated Flux Linkage Waveform

The required orthogonal axis flux linkages are calculated as follows;

$$\Psi_d[t] = \int_0^t V_{DC}[t] - RI_{DC}[t] dt \Big|_{\theta_m=\theta_d} \quad (5.5)$$

$$\Psi_q[t] = \int_0^t V_{DC}[t] - RI_{DC}[t] dt \Big|_{\theta_m=\theta_q} \quad (5.6)$$

The pulse train is supplied by a 52V 400A TopCon programmable DC power supply and the voltage and current measured by differential and current probes connected to an oscilloscope. The rotor is locked with a dividing head, which is used to control the rotor angle. Voltage and current pulse trains are measured and recorded for post-processing in MATLAB®. The test procedure for obtaining the flux linkages is described in Fig. 5.10.

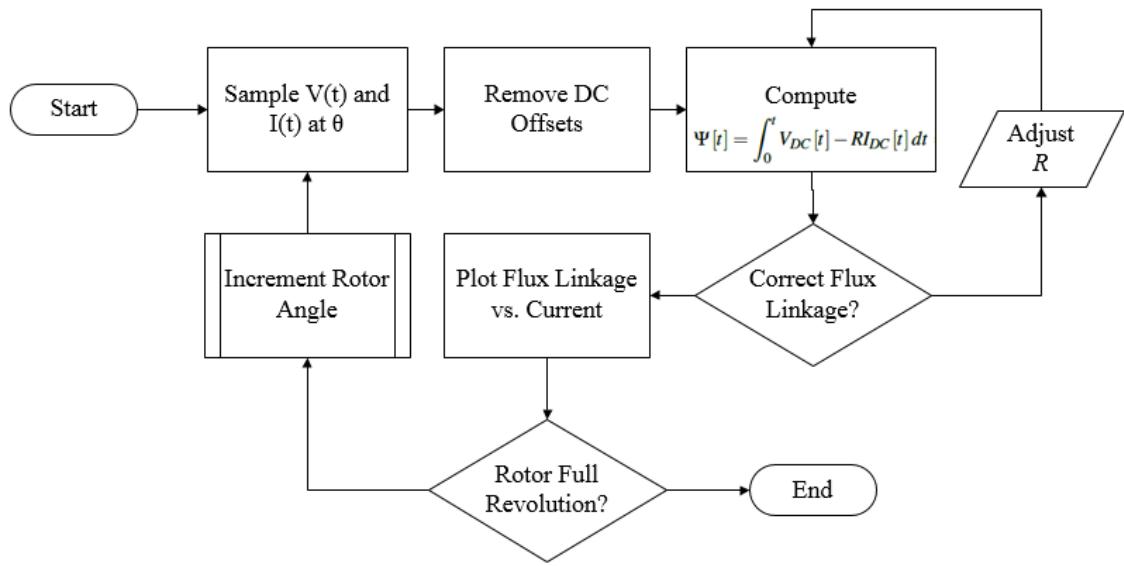


Figure 5.10: Algorithm for Flux Linkage Calculation from DC Testing

By following the procedure the orthogonal axis flux linkages can be calculated and compared with finite element solutions. Figure 5.11 shows the measured d - q axis flux linkages, $\Psi(i)$ in the d and q axis positions, with the finite element computed flux linkages. The direct axis flux linkage follows the 2D FE model with additional lumped element end winding inductances closely, which again validates the magnetic model and suggests the software models saturation correctly based on the material data for M250-35A as the flux linkages in the saturation region show minimal deviation between measured and simulated. The q -axis flux linkage is lower in the FEA study than the measured data, this is due to rotor and end leakage effects not considered in the lumped leakage inductance included in the 2D FEA, the maximum error is however only around 7%.

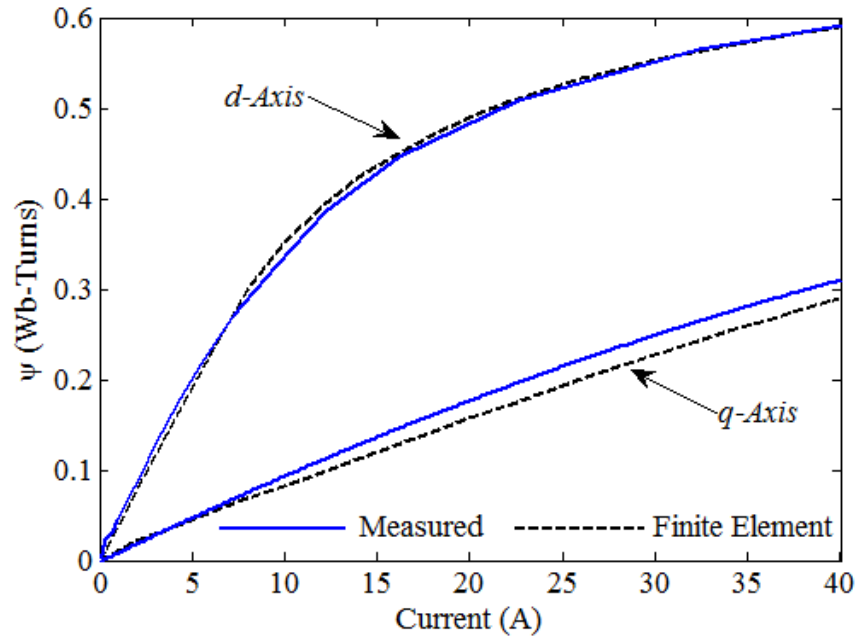


Figure 5.11: Orthogonal Axis Flux Linkages (Direct Current Method)

Figure 5.12 shows a surface plot for visualization of the measured and FEA flux linkages for each rotor position. The measured d -axis flux linkages follow the FEA derived curve closely, however it is evident that around the q -axis, the flux linkages differ as in Fig. 5.11. The peak of the wave corresponds to the d -axis and the trough corresponds to the q -axis.

5.2.4 3D Effects of Q-Axis Inductance

The 2D FEA accurately models the d -axis flux linkage due to the simplicity of the flux paths in this rotor position, any 3D effects are compensated by a lumped element end winding leakage inductance. The q -axis flux linkage is less well modeled by the 2D FEA studies due to the complexity of the flux paths when magnetizing the q -axis rotor position, leading to more pronounced 3D effects. In Figure 5.11, the measured q -axis flux curve is higher than that of the 2D FEA calculated curve, indicating a higher q -axis inductance. This effect is similar to that of the magnetization characterization of the switched reluctance motor in the unaligned position. In this position, due to the complexity of the flux path and air gap in this position the flux tends to 'fringe' in the axial direction. The associated increase in magnetic permeance with this fringing causes an increase in the unaligned inductance, or in the case of the synchronous reluctance machine the q -axis inductance. As with the switched reluctance motor, in the case of SynRM technology, the q -axis inductance can be expressed;

$$L_q = f_q L_{mq} + L_{s\sigma}$$

The L_{mq} term is the magnetizing inductance and the stator leakage inductance is given

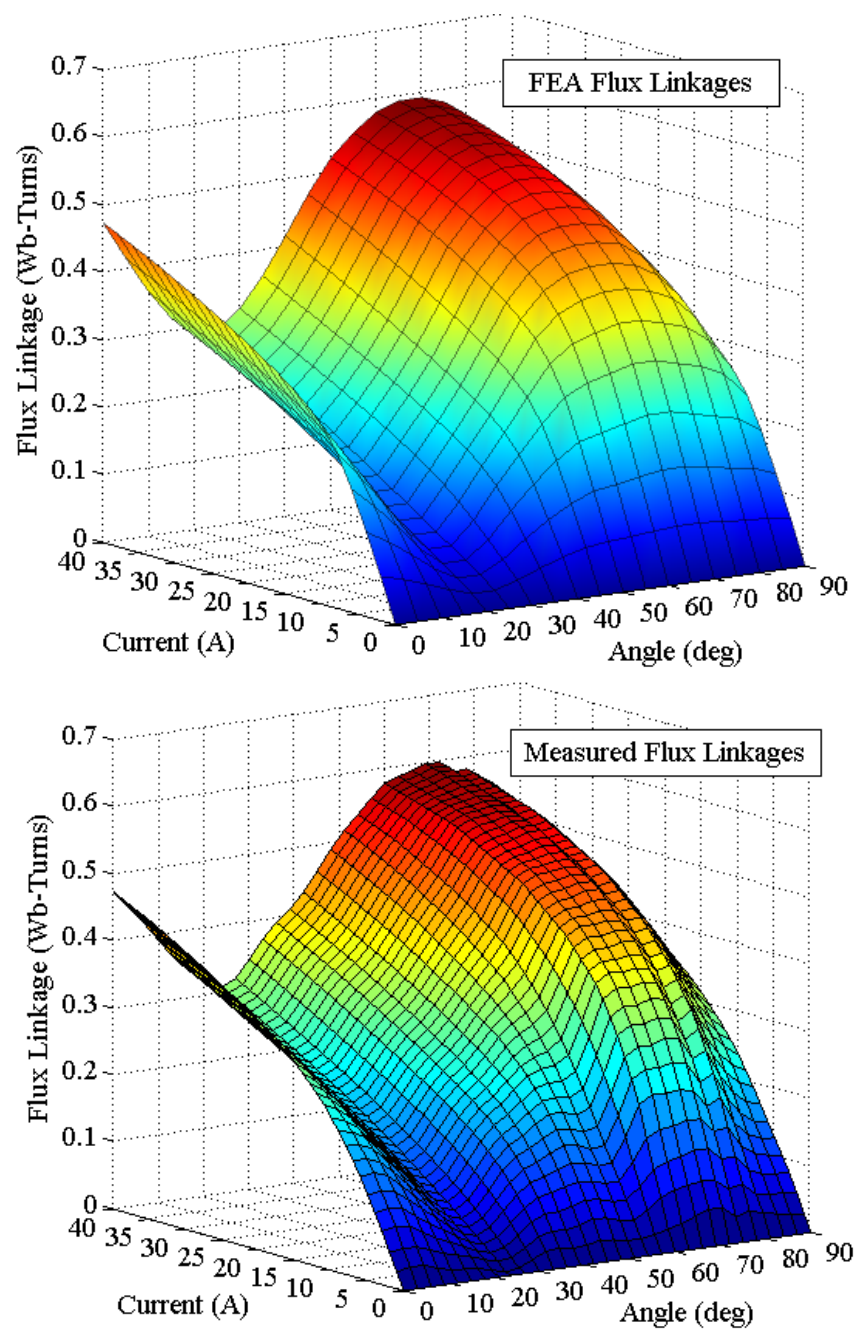


Figure 5.12: Measured and FEA flux linkages with rotor angle and current (surfaces)

as $L_{s\sigma}$. The end winding effects are included in the stator leakage inductance by the lumped element end winding inductance L_{ew} in the modeling which is calculated later in this chapter. The factor f_q can be considered as an axial fringing factor, describing the increase in permeance due to 3D fringing effects in the q -axis rotor position. The factor f_d also exists, which is a factor describing the permeance increase when the rotor is in the d -axis rotor position, it will however be negligible due to the small airgap and fringing effects are low. This is a possible explanation why the d -axis magnetization curve is accurately modeled and the q -axis magnetization is more susceptible to 3D effects.

5.2.5 Inductances

With the orthogonal flux linkages obtained via the instantaneous flux linkage test, it is then possible to compute the corresponding apparent axis inductances, $L_d(i_d)$ and $L_q(i_q)$ by the following relations;

$$L_d(i_d) = \frac{\Psi_d(i_d)}{i_d} \quad (5.7)$$

$$L_q(i_q) = \frac{\Psi_q(i_q)}{i_q} \quad (5.8)$$

Where $\Psi_d(i_d)$ and $\Psi_q(i_q)$ are the measured flux linkages i_d and i_q are the associated currents. The experimental curves are computed in MATLAB®, compared with the finite element studies and presented in Fig. 5.13.

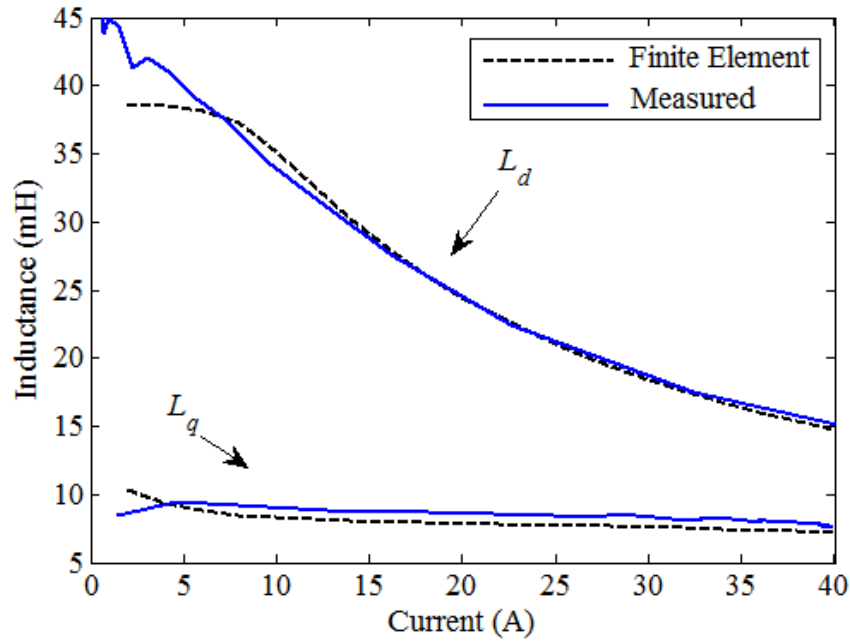


Figure 5.13: d - q axis Inductances (Measured and FEA)

The d -axis inductance determined by DC testing is larger than that of the FEA study in the early unsaturated region, this is due to sensitivity of the method for low current

levels [8,13]. The measured q -axis inductance is larger throughout the full current range, this is due to the inadequacy of the analytical lumped end winding leakage inductance representing the 3D leakage effects in the FEA study as described in Section 5.2.4. It is known that the inductance varies with rotor position in this machine (Chapter 7 deals with this aspect of machine characteristic), however, with the equipment available, it was not possible to experimentally determine this characteristic.

5.2.6 Saliency Ratio

Based on the inductance measurements in the d - q axes, the unsaturated saliency ratio ξ_{unsat} and also the rated saliency ratio ξ_{sat} (saliency ratio at rated current, otherwise known as the saturated saliency ratio) can be calculated. Thus with the saliency ratios defined;

$$\xi_{\text{unsat}} = \left. \frac{L_d}{L_q} \right|_{i < 5\text{A}} \quad \& \quad \xi_{\text{sat}} = \left. \frac{L_d}{L_q} \right|_{i=i_{\text{rated}}} \quad (5.9)$$

they can be readily calculated from both experimental and FEA data. Table 5.1 shows the results of the measured and FEA saliency ratios and orthogonal axes inductances with the percentage error. An estimate of the torque index for both experimental and FEA data is also presented.

	Measured	FEA	FEA Error
$L_d(\text{unsaturated})$ [mH]	~41.56	38.51	-7.34%
$L_d(\text{saturated})$ [mH]	23.48	23.99	2.17%
$L_q(\text{unsaturated})$ [mH]	9.44	10.39	10.06%
$L_q(\text{saturated})$ [mH]	8.33	7.69	-7.68%
ξ (unsaturated)	~4.40	~3.70	-15.91%
ξ (saturated)	~2.89	~3.11	10.28%
Torque Index, Θ	15.5	16.3	5.16%

Table 5.1: Saliency Ratio (DC Flux Linkage Tests)

The saliency ratio is very sensitive to the q -axis inductance - errors in the FEA q -axis flux linkages are amplified when calculating the saliency ratios.

5.3 Locked Rotor AC Testing

Another applicable test regime is the standstill AC test. This can also be used in the magnetic characterization of synchronous motors [8,11-13]. Standstill or AC locked rotor testing is equivalent to the locked rotor DC testing, however an appropriate AC waveform is injected into the windings rather than DC. It is sufficient here to use a single phase supply, 50Hz and with variable voltage control. The test is performed at 50Hz which is the frequency of the motor at rated speed, and a variable voltage V_{AC} is applied to the

winding terminals, this is selected such that the maximum achievable current with the supply I_{AC} is reached within the bounds of the machines rated and overload currents. Sinusoidal AC waveforms are supplied to the machine windings by a programmable AC power supply and the terminal voltage and current measured by differential and current probes connected to an oscilloscope. The rotor is again locked with the dividing head, which is used to control the rotor locked angle. Voltage and current waveforms are measured and recorded for post-processing in MATLAB®. The test procedure for obtaining the inductances by the AC test regime is presented in Fig. 5.14.

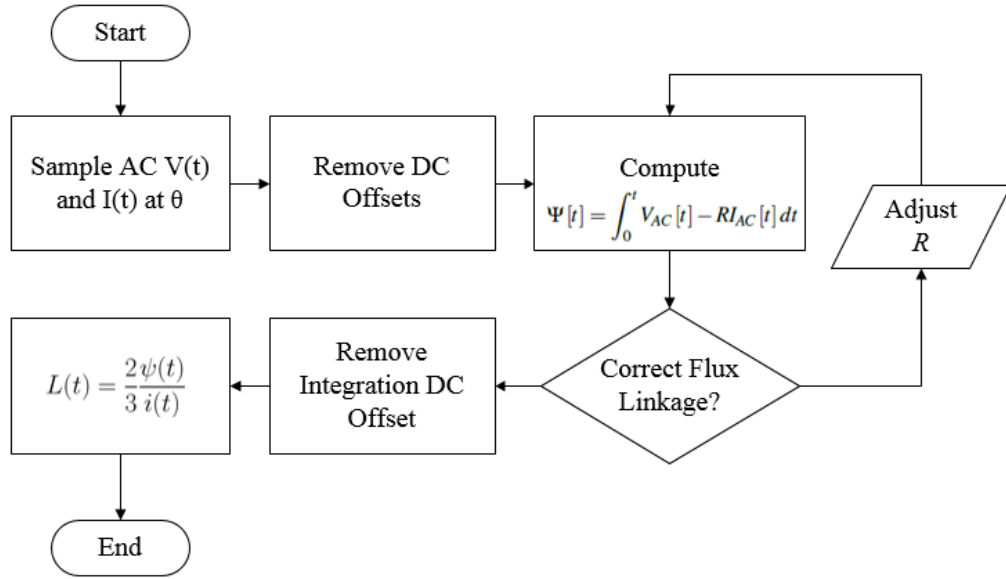


Figure 5.14: Algorithm for Inductance Calculation from AC Testing

5.3.1 Equipment and Setup

The AC signals are supplied by the programmable AC power supply at 50Hz. The programmable AC supply used for AC testing has a voltage limit of 160V. Figure 5.15 shows the winding configuration of the machine as connected to the programmable AC power supply. Figure 5.16 shows the locked rotor AC test rig - the AC power supply and the test bed. Figure. 5.17 shows the test voltage and current waveforms in both the d - and q -axis rotor positions. Due to the voltage limit on the power supply, in the d -axis position, the current was unable to reach the rated current of the machine, resulting in limited d -axis data. As a consequence full characterization of the d -axis is not possible from this AC standstill testing. However, q -axis data was obtained up to the rated current point, giving data into the saturation region of the machine.

It is evident in Fig. 5.17 that the d -axis voltage waveform reaches a higher peak value than the q -axis waveform due to the difference in reactance. The AC voltage waveform for the d -axis hits the voltage limit of the power supply of 160V, as such there is distortion in peak region of the sinusoidal waveform.

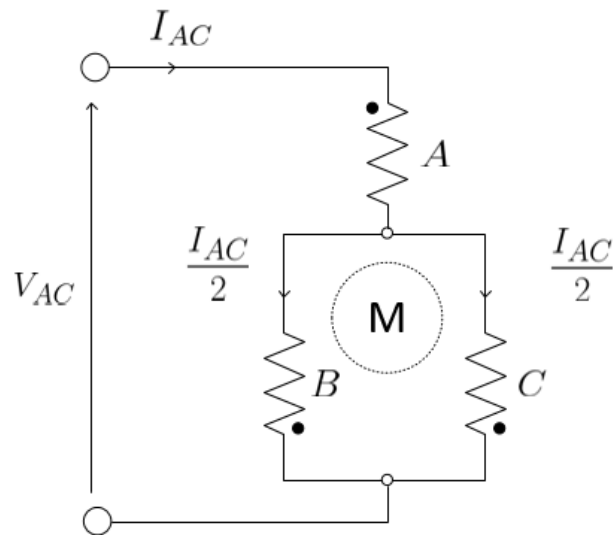


Figure 5.15: AC Testing Winding Configuration

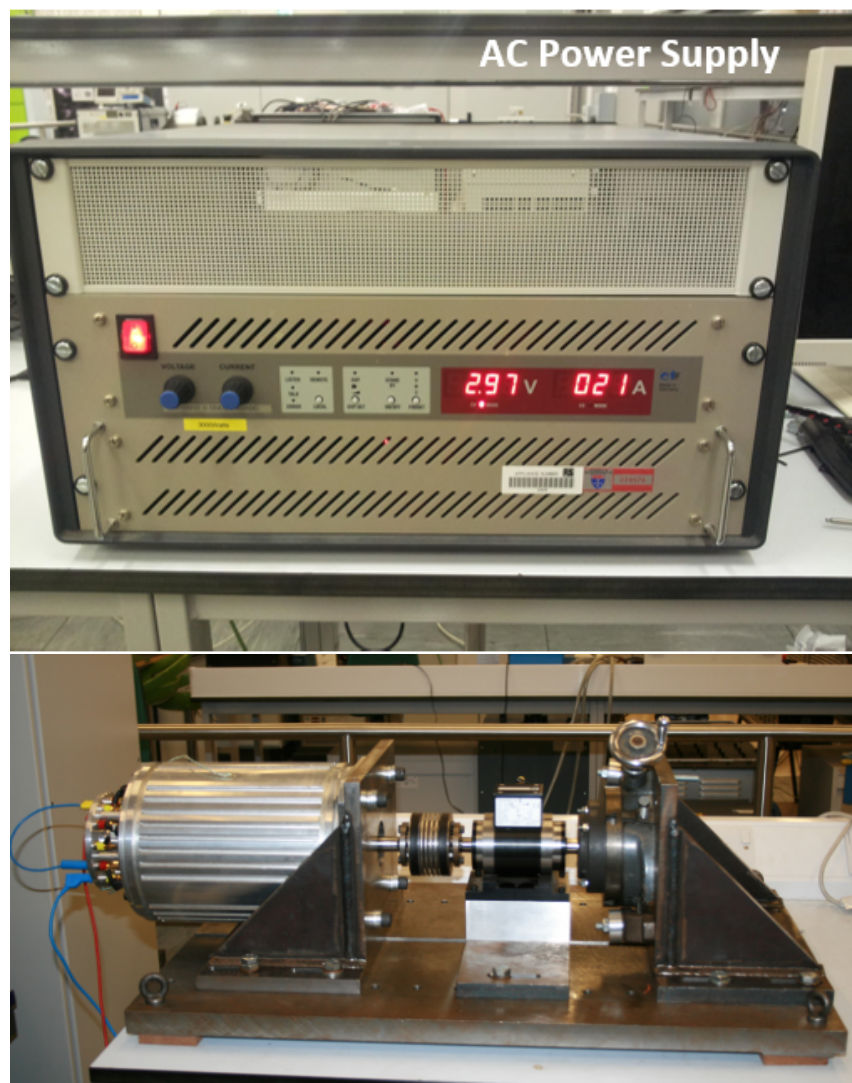


Figure 5.16: Locked rotor AC test rig

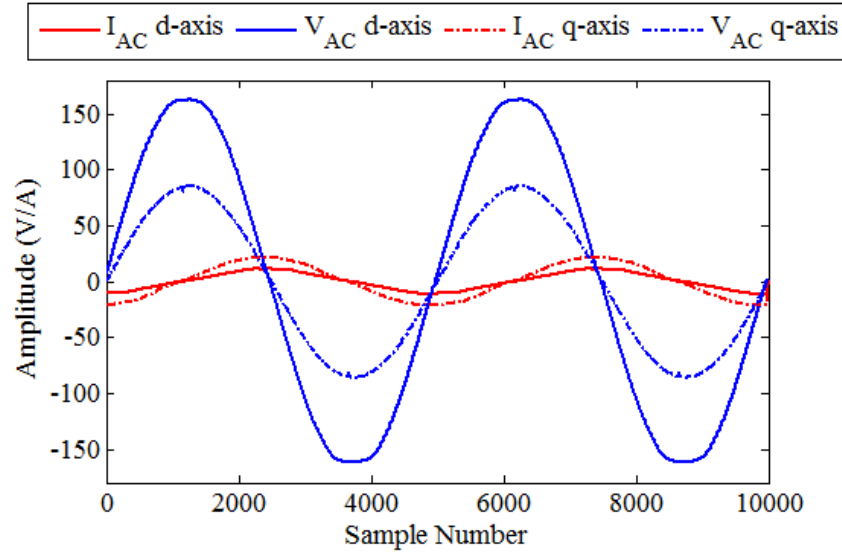


Figure 5.17: AC Test Waveforms

5.3.2 AC Magnetization

With AC current excitation, the machine magnetic circuit is magnetized during the positive half cycle and also over the negative half cycle. This AC magnetization gives rise to a hysteresis loss during the measurements, much greater than that under DC excitation. Using the measured waveforms for the d - q axes, the flux linkages $\Psi[t]$ are calculated by;

$$\Psi[t] = \int_0^t V_{AC}[t] - RI_{AC}[t] dt = \int_0^t \mathcal{F}[t] dt \quad (5.10)$$

Where $V_{AC}[t]$ is the applied AC voltage waveform and $I_{AC}[t]$ is the measured current waveform. Figure. 5.18 shows the direct and quadrature axis AC magnetization curves (showing the hysteresis loops) at a frequency of 50Hz. The magnetization sequence starts from zero and follows the green arrow up and returns on the upper black arrow, follows into negative magnetization by the lower right hand arrow and back up on the left hand upwards arrow to zero.

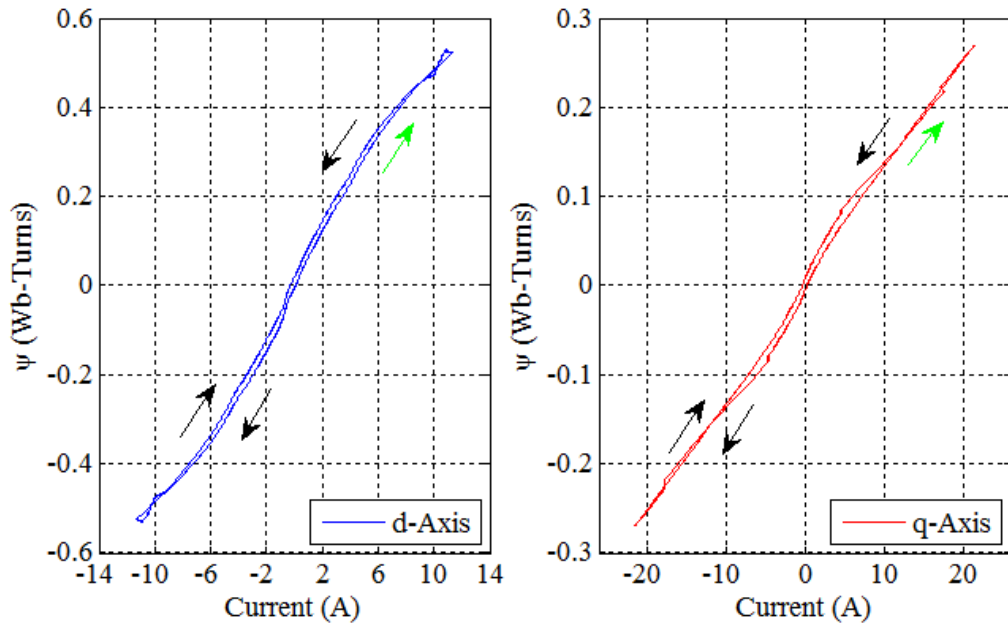
5.3.3 Inductances

With the measured orthogonal axis magnetization curves in both the forward direction from zero to the maximum positive flux linkage at the $d-q$ axis rotor positions, the d - q axis inductances can be calculated using the following expressions;

$$L_d[t] = \frac{2}{3} \frac{\Psi_d[t]}{I_{AC,d}[t]} \quad (5.11)$$

$$L_q[t] = \frac{2}{3} \frac{\Psi_q[t]}{I_{AC,q}[t]} \quad (5.12)$$

Where the factor $\left(\frac{2}{3}\right)$ comes from the winding configuration [8,11], $\Psi_d[t]$ and $\Psi_q[t]$

Figure 5.18: d -axis (left) and q -axis (right) AC magnetization curves

are the measured magnetization curves and the currents $I_{AC,d}[t]$ and $I_{AC,q}[t]$ are the measured current wave forms for the d - and q -axes respectively. Thus, the machine axis inductances based on the AC standstill test can be plotted against the results of the FE simulations and DC current testing, this is presented in Fig. 5.21.

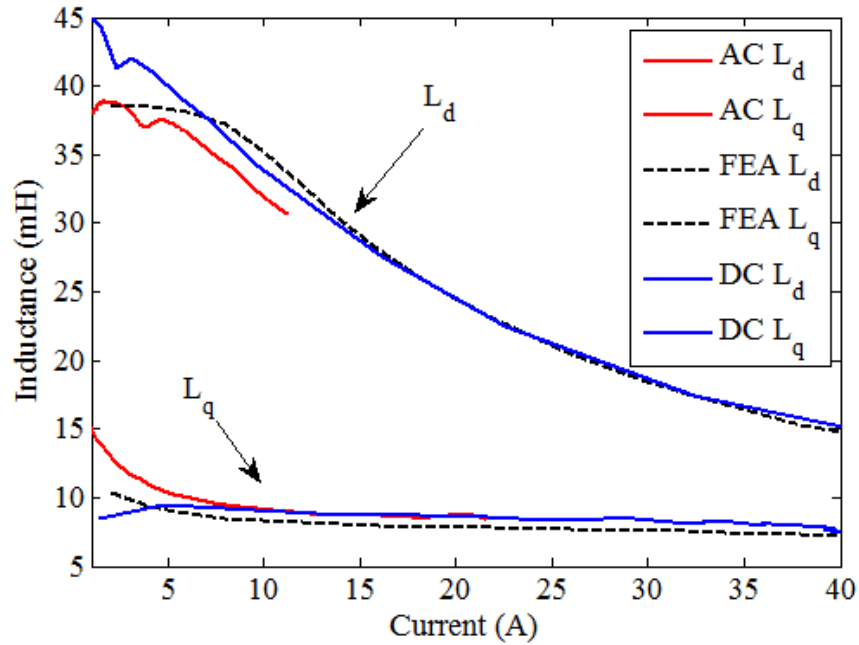


Figure 5.19: Inductance Comparison (AC, DC and FEA data)

From Fig. 5.19 the calculation of L_d based on the AC test is slightly lower than that of the DC. Theoretically, lower frequency AC measurements would give a greater accuracy and provide data close to that of the DC tests as any AC effects are minimized. In the q -axis position, the computed L_q matches closely the DC current test result.

5.4 Stator Leakage Inductance

The stator leakage inductance in the synchronous reluctance machine is important in determining the performance of the machine, as detailed in Chapter 2. The stator leakage inductance has a greater effect on the q -axis inductance as the magnetizing component is significantly lower than the d -axis magnetizing component, consequently the saliency ratio is very sensitive to the q -axis inductance and therefore the stator leakage inductance. In fact, the limiting value of the q -axis inductance is the stator leakage inductance. Thus, the stator leakage inductance plays a large role in determining the performance of the machine. In the cSynRM this leakage inductance is higher than a conventional SynRM with distributed windings as explained in Chapter 2. The leakage inductance can be determined through FEA studies and through empirical measurement. The stator leakage inductance was attempted to be measured in [13] with an Agilent LCR meter - this is not strictly valid as the LCR meter uses low current and high frequency to determine inductance, the skin effect may be significant, severely limiting accuracy. This section attempts to measure and calculate through FEA studies the stator leakage inductance for the prototype motor and compare the results to analytical calculations.

5.4.1 Removed Rotor Test

In order to measure the stator leakage inductance, the standard test according to IEEE 115-2009 and IEC 60034-4:2008 [15,16] is the so called '*Removed Rotor Test*' or 'R.R.' test. This test is applicable for synchronous machines [13, 17-19]. Measurement involves removing the rotor from the stator and performing a three phase AC test and an impedance Z measured. Two components of the measured reactance X_a are included. The stator leakage reactance $X_{s\sigma}$ component is included in the measurement, which includes flux not crossing the air gap boundary and the stray reactance crossing the airgap boundary X_b . The stator leakage reactance is calculated:

$$X_{s\sigma} = X_a - X_b \quad (5.13)$$

Where X_a is the measured leakage reactance from the applied stator voltage and current with the rotor removed, calculated by;

$$X_a = \sqrt{Z^2 - R^2} \quad (5.14)$$

$$Z = \frac{U}{\sqrt{3}I} \quad \& \quad R = \frac{P}{3I^2} \quad (5.15)$$

The reactance due to the flux crossing the airgap boundary created by the stator winding, which is in the space usually occupied by the rotor is typically measured by introducing a search coil of N_b turns into the void. The search coil is placed in the rotor void at a diameter slightly less than bore diameter to ensure no inter-slot leakages are included.

The coil length is equal to the full stack length and the width of the coil is equal to one rotor pole pitch. The search coil ends must be stretched and positioned away from the end regions as not to link any end winding leakage fluxes that are already included in X_a . Figure 5.20 shows the typical design and placement of the search coil as indicated by IEC 60034-4:2008 [16].

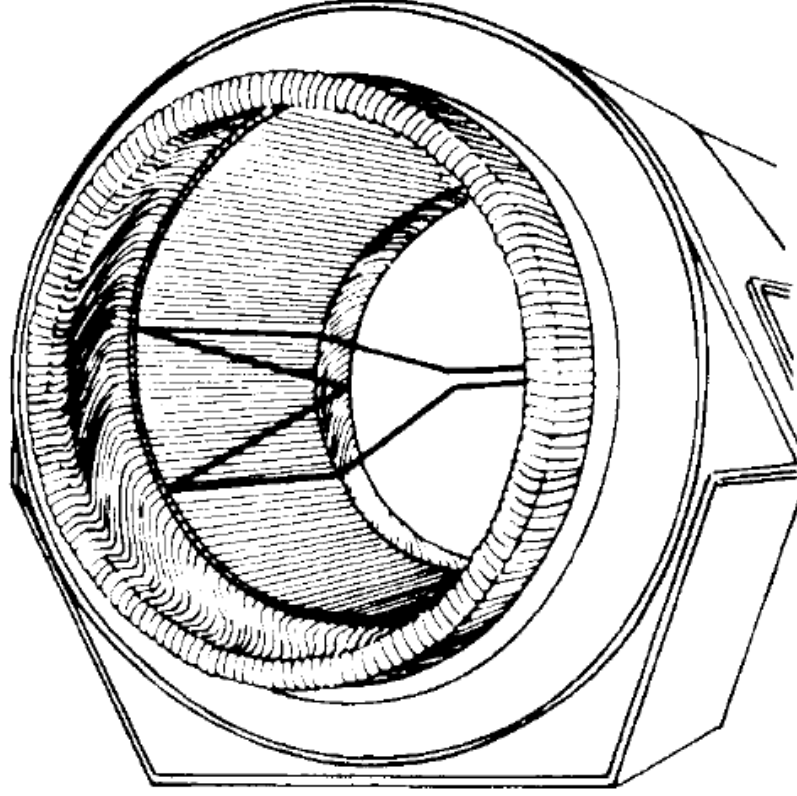


Figure 5.20: Ideal search coil design and placement [16]

From the measured induced voltage in the search coil U_c , the airgap boundary crossing reactance is approximated by [16];

$$X_b \approx \frac{U_c}{I} \frac{N \zeta_{w1}}{N_b \sin\left(\frac{q' \pi}{3q2}\right)} \quad (5.16)$$

Where N is the number of series turns per phase of the motor, ζ_{w1} is the fundamental winding factor, q is the number of slots per pole per phase and q' is the number of whole slots per rotor pole pitch. Then the stator leakage inductance is given [11];

$$L_{s\sigma} = \frac{X_{s\sigma}}{2\pi f} \quad (5.17)$$

During testing, the voltage drop across the stator resistance cannot be neglected and must be accounted for in the reactance calculations. Fig. 5.21 shows the prototype machine and search coil in the rotor void.

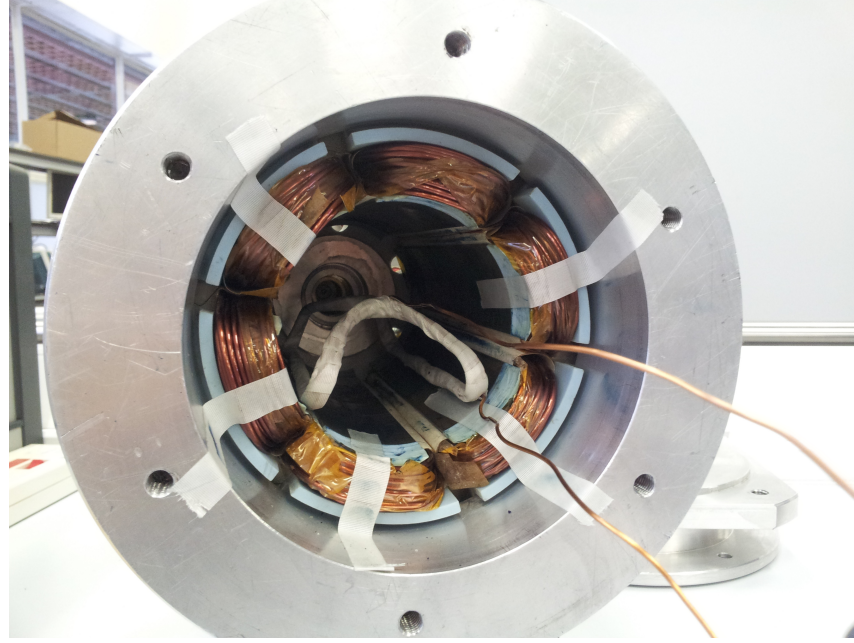


Figure 5.21: Removed rotor testing of the prototype machine showing search coil

5.4.2 Leakage Inductance

The stator leakage inductance can also be determined through finite element studies by replicating the removed rotor test by modeling a search coil in the rotor void, where $\mu_{r,void} = 1$. The FE results can then be compared with measurements on the prototype motor. The 2D FEA studies here are compensated for by introducing an estimated lumped element end winding leakage inductance into the FEA model for direct comparability with the measured values.

5.4.2.1 Lumped End Winding Inductance

The lumped end winding leakage inductance L_{ew} for single coil of a three phase machine can be approximated for a stator number of slots Q_s , number of coil turns, N_{coil} in coil area, A , and coil pitch, τ_p [20];

$$L_{ew} = 2\mu_0 \left(\frac{N_s^2 l'}{pq} \right) \lambda_{ew} = 0.68\mu_0 \left(\frac{N_s^2 l'}{p} \right) \left(1 - \frac{2w_c}{\pi l_e} \right) \quad (5.18)$$

Where l_e is the mean end turn length and w_c the width of the coil. The analytically calculated lumped end winding inductance is $138\mu\text{H}$, this is in agreement with the inductance calculation using Infolytica Motorsolve which uses a finite element method with a 3D end winding model to calculate this inductance and suggests an end winding leakage inductance of $L_{ew} = 139\mu\text{H}$, suggesting that the analytical calculation can be considered reasonably accurate. The end winding leakage inductance is very small due to the tightly wound, neat coils close to the stator core, reducing the flux leakage in the end winding region. Figure 5.22 shows the 3D FEA end winding model representative of the prototype.

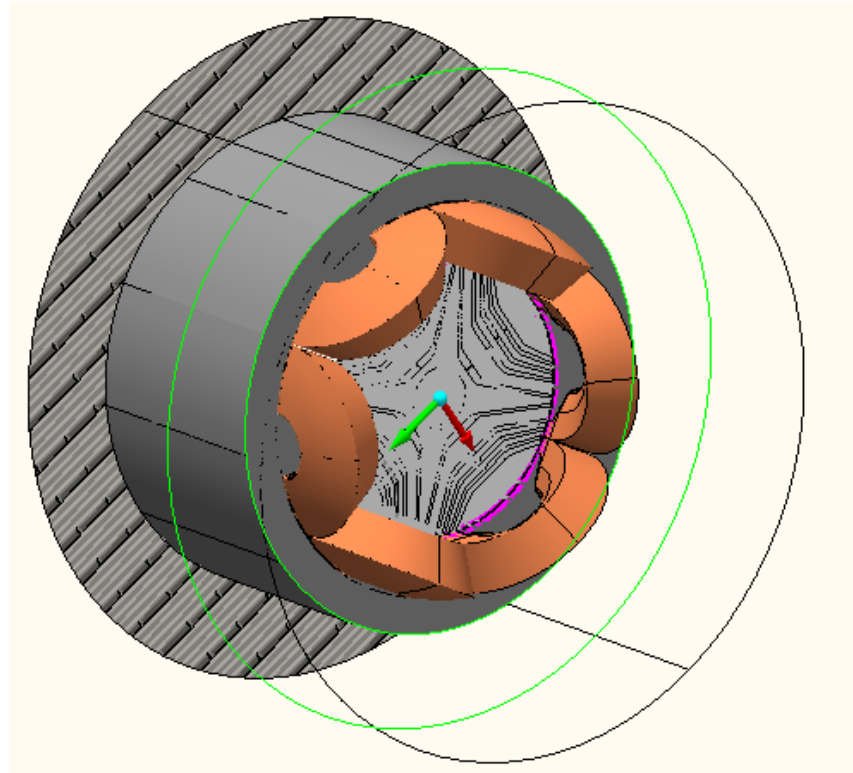


Figure 5.22: Representative 3D FEA End Winding Model

5.4.2.2 Finite Element Modeling

The prototype machine model is modeled in Infolytica MagNet and the rated current is fed into the stator windings. An electrical transient study is performed and the induced voltages are computed for both the stator and search coils. The FEA results of both methods are then passed to MATLAB® for post-processing and calculation of the stator leakage inductance. Figure 5.23 shows the solved finite element models with the search coil (shown in red) - at the same time instant.

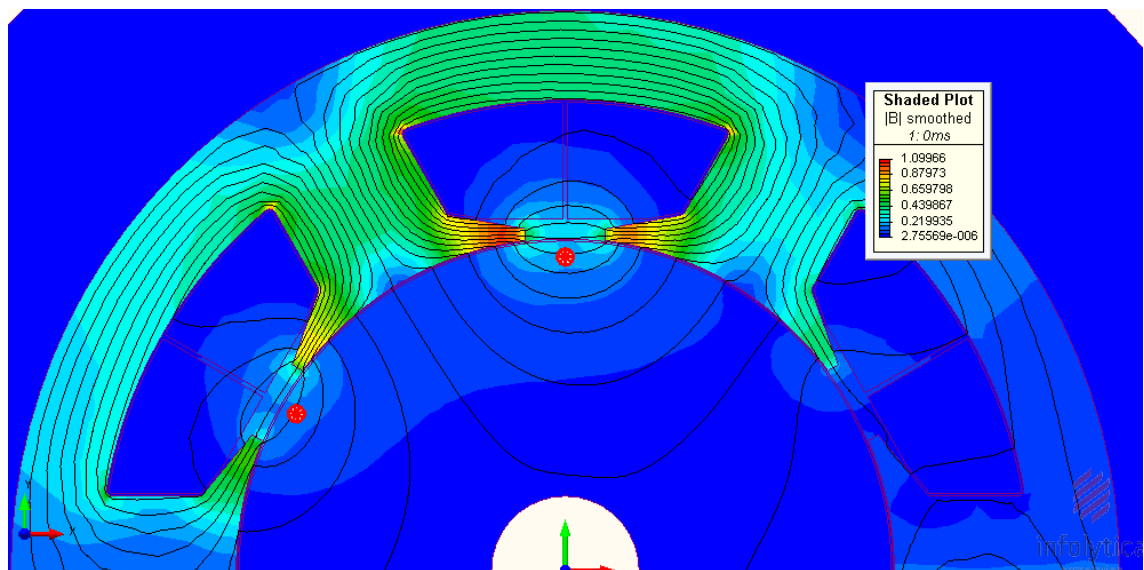


Figure 5.23: Removed Rotor FEA showing search coil

5.4.2.3 Measurements

The removed rotor test is performed on the prototype machine with the rotor removed and an insulated search coil of 10 turns placed inside the void. During testing, the machine's terminals were connected through a three phase variac and balanced three phase sinusoidal currents allowed to flow at the magnitude of the rated current, controlled by the 50Hz variac output voltages. The terminal and search coil voltages were measured using differential voltage probes and the stator current with a high precision current clamp. The three phase machine terminal voltage was set at 31.29V, allowing the line current of 21.5A to flow. The induced voltage in the search coil was measured at 0.81V. The test was run for a short amount of time to prevent any significant temperature rise in the machine introducing error into the reactance calculation due to increased stator winding resistance. The stator leakage reactance and inductance are calculated using the measured results in Eq. 5.13 to 5.17 and they are found to be $X_{s\sigma} = 1.04\Omega$ and $L_{s\sigma} = 3.32$ mH respectively.

5.4.2.4 Results Comparison

The stator leakage inductance results are compiled here. The FEA studies and the experiments on the prototype machine are compared with analytical calculations presented in Chapter 3. Table. 5.2 summarizes the results.

	FEA	Measured	% Difference	Analytical
	$\mu_{r,void} = 1$			
$X_a (\Omega)$	1.403	1.432	2.05%	-
$X_b (\Omega)$	0.388	0.390	0.51%	-
$X_{s\sigma} (\Omega)$	1.015	1.041	2.52%	0.625
$L_{s\sigma} - L_h$ (mH)	3.220	3.316	2.93%	1.99

Table 5.2: Summary of the Stator Leakage Inductance Results

Table 5.2 shows very good agreement between the FEA study where $\mu_{r,void} = 1$ and the measured results, with the difference within 3%. The measured results are slightly higher than the FEA results as might be expected as the FEA geometrical model does not account for any stray leakage. With regard to the analytical calculation of the stator leakage inductance, the calculated constructional leakage inductance $L_{s\sigma}^c = L_{s\sigma} - L_h = 1.99$ mH is a small component of the total stator leakage inductance which includes the airgap harmonic leakage component; this component is not measured in the removed rotor test. The airgap harmonic leakage component is the dominant leakage component in the prototype machine as detailed in Chapter 3 and is analytically calculated as $L_h = 7.04$ mH.. The constructional leakage inductance is summed with an unknown stray component in the FEA and measured values. A possible explanation is that the removed rotor test does actually measure a proportion of the high level of airgap harmonic leakage that is not negated by the search coil, which is its key function. The standardized test method of the

removed rotor may not account for, or remove entirely, the airgap harmonic leakage component leading to inaccurate predictions of the stator leakage inductance with this airgap crossing component dominates the leakage inductance. The method of the removed rotor is usually utilized in testing (a)synchronous machines with distributed windings which have very low airgap harmonic leakage - these machines do not have the same issue as the cSynRM and the removed rotor test is therefore a standard test and considered to give a reasonably accurate measurement of the stator leakage inductance. It is concluded here that care must be taken in using the removed rotor test when dealing with windings having a large airgap harmonic leakage factor as results may be significantly different. Of course, 3D effects, stray losses and experimental error can also account for any discrepancies.

5.5 Summary of Results

This section presents a summary of the static testing of the prototype machine. Static test results and any relevant and corresponding finite element and analytical results which are calculated in Chapter 3 are presented along side those measured results.

5.5.1 Result Comparison

The DC torque, DC and AC flux linkage testing results are used for calculation of the torque index, the orthogonal axis inductances and the machines saliency ratio under both unsaturated & saturated conditions. The stator leakage inductance is also presented where the removed rotor measurements are under the column 'R.R' and the equivalent FEA study is compared. Table 5.3 shows the results.

	DC Torque	AC- Ψ (50Hz)	DC- Ψ	FEA	R.R.	Analytical
Torque Index, Θ	15.87	-	15.5	16.3	-	16.84
L_d (unsat) [mH]	-	~38.7	~41.56	38.51	-	44.29
L_q (unsat) [mH]	-	~12.1	9.44	10.39	-	10.60
L_d (sat) [mH]	-	-	23.48	23.99	-	-
L_q (sat) [mH]	-	-	8.33	7.69	-	-
ξ (unsat)	-	3.19	~4.40	~3.70	-	4.89
ξ (sat)	-	-	~2.89	~3.11	-	-
$L_{s\sigma}$ [mH]	-	-	-	3.22	3.316	9.02

Table 5.3: Summary of static test results

The measured results show excellent agreement with the FEA design study. The good correlation with the measured results (AC, DC and DC Torque) provide global FEA model verification, providing confidence in the use of the model to simulate machine performance. The analytical calculations are relatively close to the FEA and measured values

in the unsaturated region, it is very difficult to analytically predict the saturation characteristics of the inductances.

5.5.2 Machine Performance

The steady state performance of the machine can be determined by conventional d - q theory. This theory estimates machine performance through known machine parameters which have been determined by 2D FEA studies and empirical measurements. The two key performance indicators of the synchronous reluctance motor are the mean torque and power factor. Under maximum torque per Ampere control, the mean torque and power factor are determined by;

$$T_{dq} = \left(\frac{3}{4}\right) p (L_d - L_q) i_s^2 \quad (5.19)$$

$$\cos(\phi) = \frac{\xi - 1}{\sqrt{2}} \sqrt{\frac{1}{\xi^2 + 1}} \quad (5.20)$$

Where in this case the saturated saliency ratio is 2.89 as determined by the instantaneous flux linkage test. The calculated torque capability at rated current based on the DC torque test is 21.39Nm opposed to the FEA calculation 21.9Nm. The calculated power factor of 0.443 opposed to the FEA power factor of 0.455, which is higher due to the lower leakage flux in the FEA study. Therefore the measured results used in the calculation via d - q methods accurately predict the FEA derived results.

5.6 DC Thermal Testing

Current controlled DC was provided to the stator coils connected in series to generate 300W of continuous copper loss, representative of the winding loss at rated load (assuming cold resistance at 20 deg C). During the test the current was fixed at 21A. Continuous current was used to allow the voltage to rise over time with the increasing stator resistance due to the increase in temperature. Thermocouples were located on the case, end winding, inside the slot and on the stator core back iron. The temperature rise of the various machine locations was measured over an 8 hour period. Measurements were made using an Agilent data logger with a signal multiplexer, connected to a computer. Fig. 5.24 shows the temperature measurements over this period for the various locations inside the machine: no cooling fan was used during thermal testing.

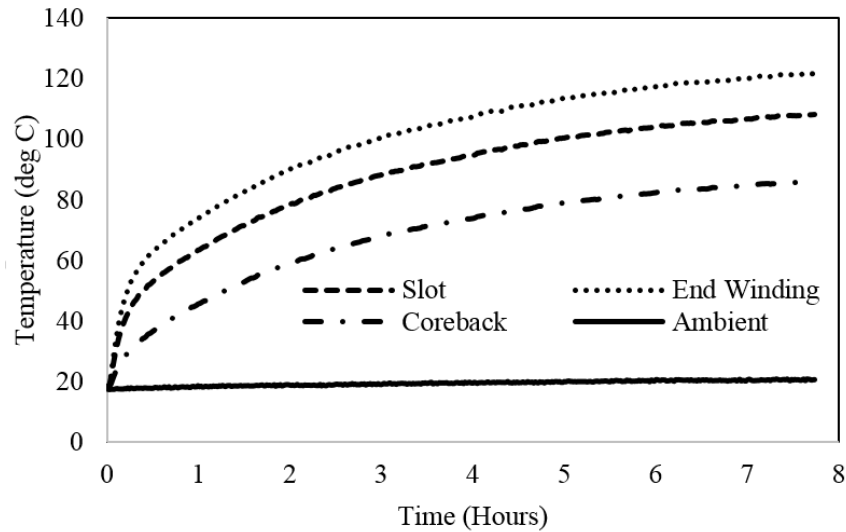


Figure 5.24: Measured temperature rise of prototype cSynRM for 300W winding loss

As indicated by the figure, the maximum temperature rise is in the end winding region where a hot spot temperature of 120 deg C was reached after an 8 hour thermal soak. This is well within the capability of the Class F insulation system, which is rated at 155 degC. After the thermal test was complete, repeat insulation integrity tests were performed and the average resistance of the coil to ground insulation was measured at $> 90\text{G}\Omega$.

5.7 Full Running Testing

In the previous sections, the results of comprehensive standstill testing to measure machine parameters and validate against the FEA and analytical calculations was presented. Here, the results of dynamometer testing, in order to further validate the design, are presented.

5.7.1 Equipment and Setup

The prototype machine is fed by a commercially available ABB ACS850 variable speed drive. The prototype is set up back to back with a 10kW computer controlled Magtrol hysteresis brake dynamometer which is used to load the machine. Comprehensive instrumentation is used during testing; the machine terminal voltages and currents are measured using Tektronix precision current clamps and differential voltage probes connected to two Tektronix 4034 digital oscilloscopes as well as a Yokogawa WT1600 digital power analyzer, which also calculates the three phase apparent, real and reactive powers and the motor power factor. Torque and speed measurements are taken from a torque sensor and shaft mounted speed encoder located within the hysteresis dynamometer which is controlled by the combination of an industrial PC and Magtrol DSP6001 dynamometer controller. The hysteresis brake is water cooled by an automatic temperature controlled

chiller and the prototype machine is coupled to the hysteresis brake by a rubber coupling. Figure 5.25 shows the complete test rig including all attached instrumentation.

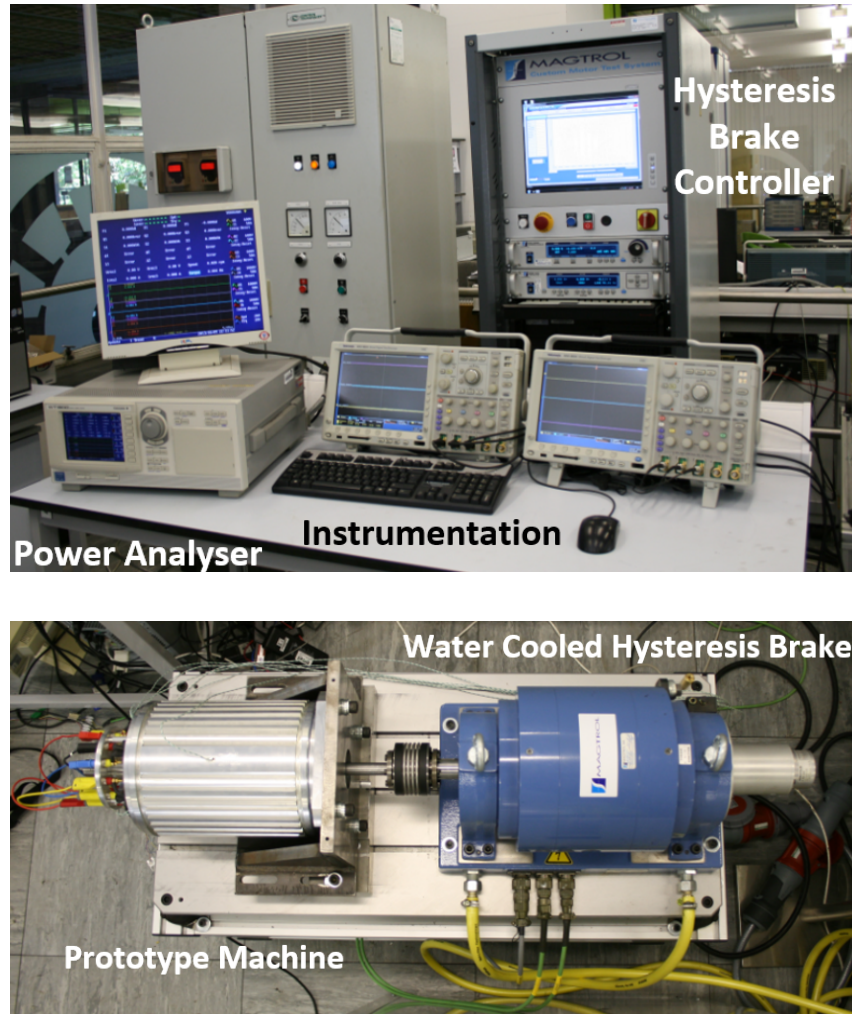


Figure 5.25: Full running rig showing instrumentation and the test bed

5.7.2 Rated Speed and Current

In this test regime, the machine was run at its rated speed of 1500rpm on the dynamometer and the machine's rated current of $I_s = 21.2A$ fed into the terminals by loading the machine with the hysteresis brake until this current limit. This current limit corresponds to 297W of copper loss, leading to a FEA calculated total loss of 341W (not including windage and friction). Table 5.4 shows the measured results of key machine parameters in comparison with FEA calculated values. It should be noted that the drive uses sensorless Direct Torque Control rather than a clearly defined current angle control as assumed in all FEA analysis. Because of this control scheme the applied phase currents are not perfectly sinusoidal. Therefore the FEA and measured results are not directly comparable but assist in the verification of the machines dynamic operation that can be achieved with the available equipment.

	FEA	Measured
Current, I_s [A]	21.2	21.2
Torque, T [Nm]	21.98	19.98
Output Power, P_{out} [kW]	3.45	3.15
Efficiency, η [%]	91.2	90.8
Power Factor, $\cos(\phi)$	0.48	0.49

Table 5.4: Rated speed and current measurement comparison with FEA

The results actually are very close to that of the 3D FEA predicted results for the machine base speed and applied phase current. The phase current at rated current level is presented in Figure. 5.26.

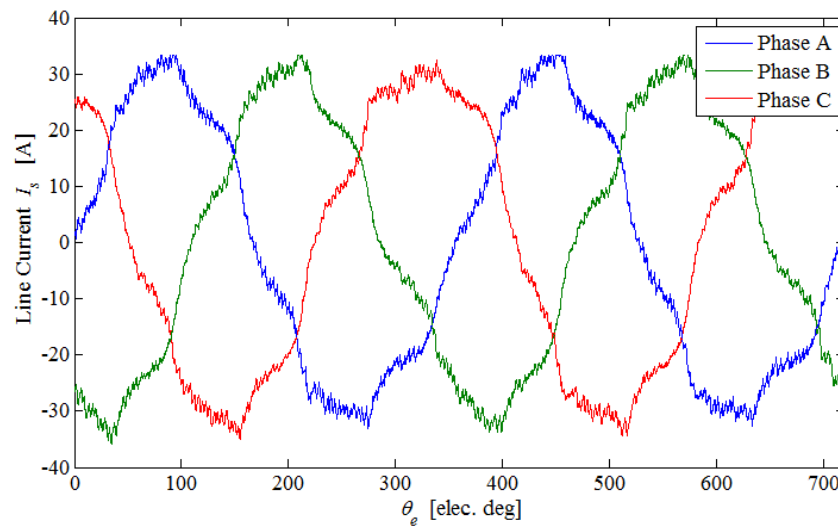


Figure 5.26: Applied current waveform at rated speed and RMS line current

5.7.3 Rated Speed and Torque

In this test regime, the machine was run at its rated speed of 1500rpm and the machine's rated torque of 22Nm achieved by loading the machine with the dynamometer brake. The current required to achieve the rated torque through 2D FEA is $I_s = 23.4\text{A}$ corresponding to 361W of copper loss. Table 5.5 shows the measured results of key machine parameters in comparison with FEA calculated values.

	FEA	Measured
Current, I_s [A]	23.4	23.4
Torque, T [Nm]	24.2	22.0
Output Power, P_{out} [kW]	3.8	3.5
Efficiency, η [%]	90.0	88.9
Power Factor, $\cos(\phi)$	0.47	0.49

Table 5.5: Results at stator line current to achieve rated torque

For rated current, the machines torque capability is down slightly though achieves a high efficiency of over 90%, to meet the design torque value the line current is increased slightly but the machines efficiency drops to under the desired >90%. This makes the machine an IE3 Premium efficiency standard machine, but verging very close to that of the IE4 Super-premium efficiency - the machine is let down by its low fundamental winding factor and harmonic issues.

5.7.4 Torque vs. Speed

The maximum safe speed of the hysteresis brake dynamometer is 3000rpm, which is twice the base speed of the prototype machine. With the machine having a maximum speed of around 9000 rpm, measurements of the torque speed envelope are extremely limited with the available equipment. Measurements are made at 500 to 3000 rpm in 500rpm increments, the measured torque-speed points with the 2D FEA calculated torque-speed curve is presented in Figure 5.27.

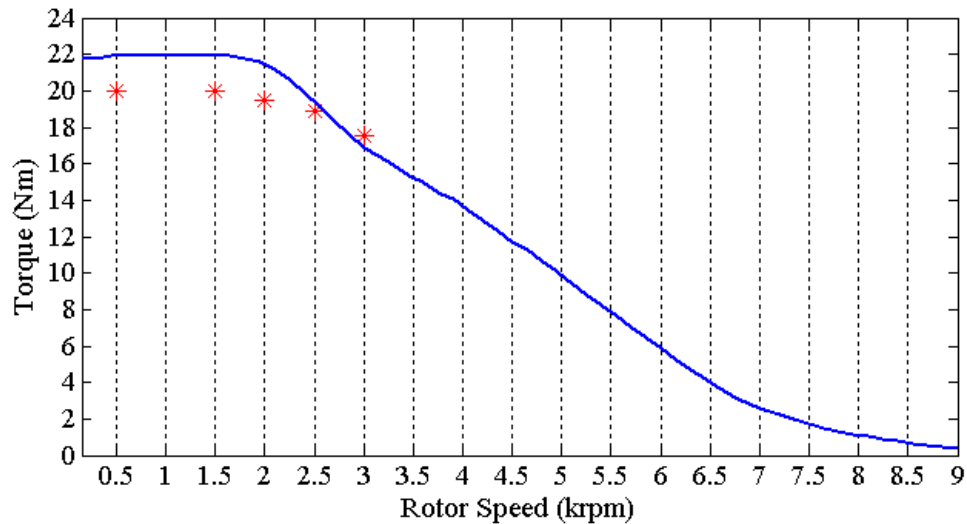


Figure 5.27: Measured and FEA torque speed curves; Blue: FEA Red: Measured

The measured curve runs to 3000rpm and in the constant torque region run 1.9Nm under the 2D FEA calculated curve, the mean torque in this region does match closely the 3D calculated torque of 19.8Nm. The torque starts to drop off around 2000rpm as predicted by the FEA as it enters the constant power region. Due to the equipment used for testing, the full torque-speed curve of the machine and any subsequent calculation of the constant power speed range are not possible as the mechanical safe limiting speed of the brake is 3500rpm. With the available equipment it was not possible to measure torque ripple of the prototype machine, but this would be a valuable extension to the work.

5.8 Conclusion

This chapter has presented the testing and verification of the FEA modeled cSynRM design through static and rotating measurements on the prototype motor. Firstly the integrity of the insulation system was verified by both DC HIPOT and surge testing. Secondly, the FEA electromagnetic model was globally verified through a combination of DC torque tests, DC and AC flux linkage testing and removed rotor testing. The DC torque test validated the torque producing capability of the machine and suggested a value of the machine's torque index close to that of the FEA. In both DC and AC test regimes, the measured flux linkages correlated very closely to the FEA results, especially in the d -axis position with a 7% error in the q -axis position due to significant axial fringing fields being the main contributor to the increase in the q -axis inductance. Good correlation between FEA and measurement was found at all rotor positions, with the FEA representing the harmonic content of the torque waveform very accurately.

The motor orthogonal axis inductances were verified through measurements and the leakage reactance determined by the removed rotor tests also correlated very closely with the FEA study. The AC test was found, in agreement with the literature, to be the least closely match the FEA curves due to its susceptibility to AC effects in the measurements. The removed rotor test with a search coil in the bore of the prototype machine verified the leakage reactance of the motor and one method recently proposed in the literature was found to be inaccurate when compared to measured results. Simple dq model calculations based on the measured data were found to provide reasonable approximations to the machine's dynamic performance, showing that the measured orthogonal axis inductances results accurately predict the steady state performance of the cSynRM. Thermal measurements were taken corresponding to 300W of copper loss via DC current injected into the windings. The thermal measurements show that the motor is within its thermal rating of Class F (155 deg C), with a hotspot temperature rise of 100 deg C (hotspot temperature of 120 deg C).

This chapter serves as FEA model and prototype verification based on standstill and dynamic testing. For rated current, the machine's torque capability is down by 10% when compared to 2D FEA, though the model 3D FEA model is <3%. The machine achieves a high efficiency of over 90% in test conditions. In order to meet the design torque value the line current is increased slightly but the machines efficiency drops to under the desired >90%. The measured dynamic torque values match closely to the 3D FEA study in Chapter 3.

5.9 References

1. IEEE Std 95-2002, IEEE Recommended Practice For Insulation Testing Of AC Electric Machinery With High Direct Voltage
2. IEC 60034-18-1, Rotating Electrical Machines - Part 18-1: Functional Evaluation Of Insulation Systems - General Guidelines
3. Juha Pyrhonen, 'Design Of Rotating Electrical Machines', Wiley-Blackwell, 2008
4. IEC 60034-15, Rotating Electrical Machines - Part 15: Impulse Voltage Withstand Levels Of Form-Wound Stator Coils For Rotating A.C. Machines
5. IEEE Std 522-2004, IEEE Guide For Testing Turn Insulation Of Form-Wound Stator Coils For Alternating-Current Electric Machines
6. John Wilson, 'Current State Of Surge Testing Induction Machines', Baker Instrument Company
7. United States Patent Number 5,111,149, "Method and Apparatus for Automatically Calculating the Integrity of an Electric Coil".
8. I. Boldea, 'Reluctance Synchronous Machines and Drives', Clarendon Press, 1994
9. T. J. E. Miller, 'Switched Reluctance Motors and Their Control', Magna Physics Publishing, 1993
10. T. J. E. Miller, 'Electronic Control of Switched Reluctance Machines', Newnes, 2001
11. W. L. Soong: "Inductance Measurements for Synchronous Machines", Power Engineering Briefing Note Series #2, 8 May 2008
12. Stulrajter, M.; Musak, M., "Unconventional methods for PM Synchronous Motor parameters investigation," ELEKTRO, 2012 , vol., no., pp.260,265, 21-22 May 2012
13. Jovanovic, M.G.; Betz, R.E., "Off-line testing of reluctance machines," Energy Conversion, IEEE Transactions on , vol.14, no.3, pp.264,269, Sep 1999
14. Riley, Hobson, Bence, 'Mathematical Methods for Physics and Engineering', Second Edition, Cambridge University Press, 2004
15. IEEE Std 115-2009 - IEEE Guide for Test Procedures for Synchronous Machines Part I - Acceptance and Performance Testing; Part II - Test Procedures and Parameter Determination
16. IEC 60034-4:2008 - Methods for determining synchronous machine quantities from tests
17. Rogers, T. A., "Test Values of Armature Leakage Reactance," American Institute of Electrical Engineers, Transactions of the , vol.54, no.7, pp.700,705, July 1935
18. Enache, M.-A.; Campeanu, A.; Enache, S.; Vlad, I., "Possibilities for reluctance synchronous machines parameters experimental determination," Applied and Theoretical Electricity (ICATE), 2012 International Conference on , vol., no., pp.1,6, 25-27 Oct. 2012
19. Chiver, O.; Micu, E.; Barz, C., "Stator winding leakage inductances determination using finite elements method," Optimization of Electrical and Electronic Equipment, 2008. OPTIM 2008. 11th International Conference on , vol., no., pp.69,74, 22-24 May 2008
20. J. Gieras, 'Permanent Magnet Motor Technology: Design and Applications', Third Edition, CRC Press, 2008

Chapter 6

Novel Harmonic Torque Analysis Technique

In previous chapters, it was concluded that in order to improve the performance of the machine topology proposed in this thesis, the torque ripple must be analysed and reduced before the cSynRM can compete with machine types with an inherently lower torque ripple. The aim of this chapter is to present a novel method of analysing the torque production in synchronous machines so that the contributions of individual field harmonics to the resultant torque waveform can be calculated. Such a tool can be applied to a cSynRM that is known to have a large torque ripple to assess the torque ripple components and aid the design engineer in determining electromagnetic design changes so that the torque quality can be improved. Firstly, the Maxwell stress concept is reviewed and applied to torque production in electrical machines. Extraction of the airgap flux density field from FE solutions and its harmonic analysis is then presented, leading to the concept of harmonic Maxwell stresses in the airgap region. The theory is then developed such that calculation of the harmonic torque contribution to the resultant waveform for a particular field harmonic is possible. Post-processing of finite element solutions is used to compute the harmonic torque components and compares the cSynRM initial design and the final prototyped design.

6.1 Introduction

In general, torque ripple is a significant concern in electrical machines, causing unwanted acoustic noise and vibration [1] as well as limiting the range of the machine to applications where torque quality is of high importance. Effective reduction in torque ripple is an important consideration and challenge for electrical machine designers. Torque ripple analysis, and therefore mitigation, is limited with finite element solutions as no information relating to the composition or cause can be explicitly found with standard modelling, only the resultant torque waveform. The mean torque and torque ripple are the only figures of merit that can be determined. These figures of merit are limited as no detailed

information on harmonic field contribution are explicitly available. Detailed information would be useful to machine designers in order to assist iterative geometry selection associated with practical machine design. There are many papers focusing on torque ripple reduction in synchronous machines, the majority of which suggest design changes [2-6], whilst others concentrate on the drive and control aspect of mitigating torque ripple [7-9]. The source affecting torque ripple in the synchronous reluctance motor is the Stator MMF and permeance interaction which is applicable in all salient synchronous machines and will be most evident in machines with a high level of MMF space harmonic content. In synchronous reluctance machines, as it was shown in Chapter 2, the stator MMF space harmonics causes many unwanted parasitic effects; their effect on the torque ripple of the machine is now explored. The study focuses on space harmonic content and time harmonics are not considered in the present study.

6.2 Airgap Maxwell Stresses

Considering a 2-dimensional model, there exists only a z -component of magnetic vector potential, this can be expressed by the quasi-Poisson equation. The finite element (FE) software used is 'Infolytica MagNet' and solves in a Cartesian coordinate system [10];

$$\frac{\partial}{\partial x} \left(\frac{1}{\mu} \frac{\partial A_z(x,y)}{\partial x} \right) + \frac{\partial}{\partial y} \left(\frac{1}{\mu} \frac{\partial A_z(x,y)}{\partial y} \right) = \begin{cases} -\mu J_z \\ 0 \end{cases} \quad (6.1)$$

Where A_z is the axial component of the magnetic vector potential due to the current density J_z . The homogeneous equation is solved in non-conducting regions and the numerical solution calculates the magnetic vector potential in the solution domain. From this, magnetic flux densities, forces and torques are computed in the software - the Cartesian solution is transformed to a cylindrical coordinate system by a transformation matrix.

6.2.1 Stator Magnetomotive Force Waves

The stator MMF in an electrical machine is important in torque production; it is especially important in reluctance machines as it also serves as a magnetizing force. The resultant MMF in the air gap is a function of space and time which can be written as rotating waves [11];

$$F_m(\theta, t) = \sum_{k=1}^{\infty} \sum_{c=1}^{n_c} \frac{4N_s \xi_{wk}}{kp\pi} (F_{mk}^+(\theta, t) + F_{mk}^-(\theta, t)) \quad (6.2)$$

Where N_s the number of series turns per phase and ξ_{wk} is the harmonic winding factor. The forwards $F_{mk}^+(\theta, t)$ and backwards $F_{mk}^-(\theta, t)$ rotating harmonic MMF components can be written as co-sinusoidal waves in space and time. The stator MMF waves interact with the machine permeance function (a function of space and time also) to form the air

gap flux. Therefore it is key, in order to reduce any parasitic or unwanted effects, that the space harmonic content in the air gap flux must be minimised. Calculation of both winding factors and MMF is readily performed analytically for applicable harmonics. Accurate calculation of airgap magnetic fields is difficult to determine analytically, due to permeance variation, saturation and other effects. Performing time stepping 2D FEA analysis at the desired operating points, the air gap field can then be extracted, defined by an arc in the centre of the air gap. As the air gap is small, the assumption is made that the variation across the air gap in the radial direction is negligible.

6.2.2 Conventional Stress Theory

The Maxwell stress is well understood and commonly applied to electrical machines [10, 12], and it can be shown that calculation of the resultant magnetic *forces* is readily achieved by computing the following surface integral of the airgap Maxwell Stress tensor \mathbb{T} ;

$$\mathbf{F} = \oint \mathbb{T} \cdot d\mathbf{S} \quad (6.3)$$

Here, the magnetic Maxwell stress tensor, can be written in matrix form;

$$\mathbb{T} = \frac{1}{\mu_0} \begin{bmatrix} \frac{B_r^2 - B_\theta^2 - B_z^2}{2} & B_r B_\theta & B_r B_z \\ B_\theta B_r & \frac{B_\theta^2 - B_r^2 - B_z^2}{2} & B_\theta B_z \\ B_z B_r & B_z B_\theta & \frac{B_z^2 - B_r^2 - B_\theta^2}{2} \end{bmatrix} \quad (6.4)$$

In the matrix B_z is any axial component of the magnetic flux density and the diagonal terms are the magnetic pressure components, normal to the the rotor surface surface \mathbf{s}_1 , and the off-diagonal terms are the airgap shear stresses. It is these shear stresses that give rise to torque production in electrical machines. Thus the total force, with radial and tangential components, based on the Maxwell stress tensor method, can be calculated by integrating over a closed surface, \mathbf{s}_1 , in the air gap according to Eq. 6.3. Figure 6.1 shows the Maxwell stresses of interest on the rotor surface.

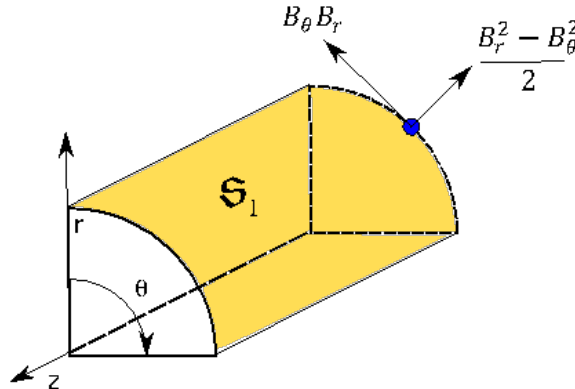


Figure 6.1: Cylindrical co-ordinate system use to evaluate the stress tensor

If it is assumed that the machine has no field variation in the z -direction ($B_z = 0$), which is an assumption of 2D analysis. The expressions simplify and the magnetic stress of interest for torque production is the tangential shear stress (tangential force density) is extracted from the matrix;

$$\sigma_\theta = \frac{B_\theta B_r}{\mu_0} \quad (6.5)$$

This can be visualised in the airgap with field lines, as in Fig. 6.2.

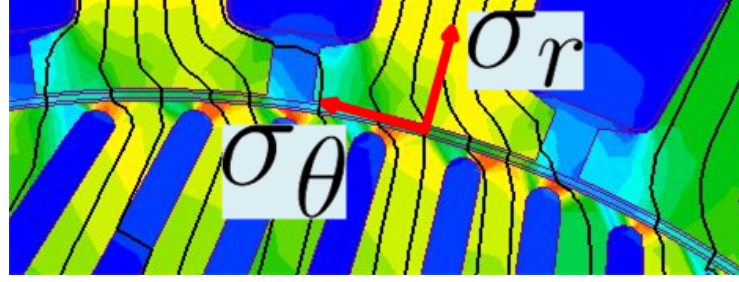


Figure 6.2: Stresses in the air gap of a loaded machine

Following on from this, the rotor electromagnetic torque can be derived and the expression of interest is the surface integral of the tangential stress σ_θ over the rotor surface [13];

$$T_z = \frac{1}{\mu_0} \iint \sigma_\theta dS = \frac{r^2}{\mu_0} \int_0^{l_a} \int_0^{2\pi} B_\theta B_r d\theta dz \quad (6.6)$$

It is important to note here that this expression allows calculation of only the *total* or *resultant* electromagnetic torque developed by the machine. This conventional calculation contains no information on harmonic torque components due to the air gap field harmonics. This calculation does however *take into account* all harmonics and non-linearities in the *resultant* torque waveform if the field values B_θ and B_r are obtained from finite element solutions, but does not give explicit information on the composition of that resultant waveform. The method developed in this chapter aims to overcome failings of the conventional method.

6.3 Field Post-Processing

Using 2D FE, the solution of magnetic fields is obtained for one electrical cycle. From the solution of the x - y field values around the airgap, a linear transformation matrix calculates the radial and tangential components, which are finally used to calculate the machine torque at a particular time instant by Eq. 6.6. The torque computation conventionally uses the resultant radial and tangential field components for calculation. It is evident that various harmonics exist and contribute to this resultant field. Thus by extending the theory, calculation of an individual field harmonic component and its effect on the resultant

torque waveform should be able to be obtained through post-processing in MATLAB®.

6.3.1 Harmonic Decomposition

The air gap field is Laplacian, the solutions of which are harmonic functions, lending themselves to linear superposition. By discretizing the field in the airgap from the sampled waveform and applying the 1-dimensional Discrete Fourier Series (DFS), the harmonic decomposition $F[k]$ of the airgap field, or any discrete function $f[n]$ of N discrete samples is obtained. Considering only spatial harmonics, a DFS transform pair is defined;

$$F[k] = \frac{1}{N} \sum_{n=0}^{N-1} f[n] e^{-ikn(\frac{2\pi}{N})} \in \mathbb{C} \quad (\text{Harmonic Decomposition}) \quad (6.7)$$

$$f[n] = \sum_{k=0}^{N-1} F[k] e^{ikn(\frac{2\pi}{N})} \in \mathbb{R} \quad (\text{Harmonic Reconstruction}) \quad (6.8)$$

Equation 6.7 performs a discrete harmonic decomposition into the complex vector $F[k]$, and Equation 6.8 reconstructs the discrete function in the spatial domain as a function of index around the airgap periphery $f[n]$. The radial and tangential components as a function of space can be expressed in DFS form by;

$$B_r[k] = \frac{1}{N} \sum_{\theta=1}^{N-1} B_r[\theta] e^{-ik\theta(\frac{2\pi}{N})} = B_r^k \quad (6.9)$$

$$B_\theta[k] = \frac{1}{N} \sum_{\theta=1}^{N-1} B_\theta[\theta] e^{-ik\theta(\frac{2\pi}{N})} = B_\theta^k \quad (6.10)$$

Where, $\theta = n(\frac{2\pi}{N})$ and $k \in \mathbb{Z}^+$ (harmonic numbers of positive integer value). These equations allow harmonic decomposition of the radial and tangential magnetic field components in the air gap of any electrical machine. The output of these equations are complex numbers relating to the magnitude and phase of the harmonic waveform. The harmonic amplitude and phase are calculated by conventional methods in complex algebra. It can be shown that reconstruction of the time series waveform can be written as a sum of harmonic cosines;

$$B[n] = 2 \sum_{k=0}^{\left(\frac{N}{2}\right)-1} B[k] \cos(k\Omega_0 n) \quad (6.11)$$

Here, the discrete angle $\Omega_0 = \frac{2\pi}{N}$. The multiplication factor '2' comes from the summation of a symmetrical double sided harmonic spectrum output given by Eq. 6.9 or 6.10 where the output magnitudes on each half spectrum are half the actual magnitude. This is only mathematically significant and does not reflect any physical interpretation. This developed form of the magnetic flux density wave can then be used in development of the harmonic stress calculations.

6.3.2 SynRM and cSynRM MMF Spectra

As an example and to illustrate the difference in MMF, airgap harmonics and shear stress distributions between a synchronous reluctance machine (SynRM) and the proposed machine with fractional slot concentrated windings (cSynRM), Figure. 6.3 shows the analytically calculated MMF spectra of a fully pitched distributed winding stator with 36 slots, and a 4 pole 6 slot synchronous reluctance rotor with a double layer winding. From the figure, it is evident that the harmonic content in the cSynRM is substantially greater than the SynRM as presented in Chapter 2.

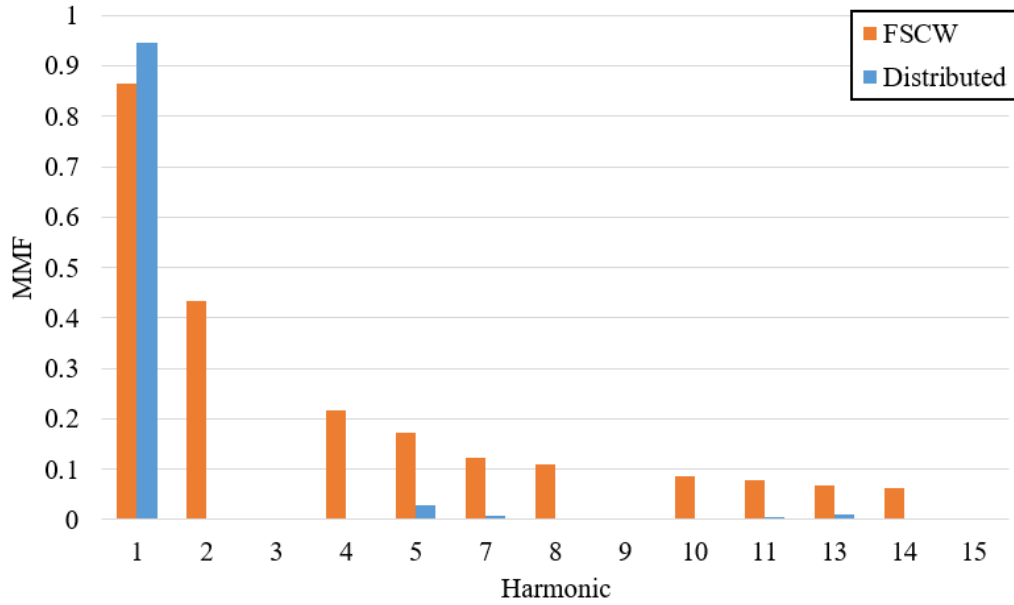


Figure 6.3: 3ph MMF Harmonic Spectra

6.3.3 SynRM and cSynRM Airgap Field Spectra

The high level of MMF harmonics interact with the airgap permeance function creating the airgap magnetic flux density distribution, these are derived here from FEA studies. The distribution is reflected in Figure 6.4 (airgap periphery angle is over 2π electrical radians) where the higher space harmonic content is observed in both the radial and tangential field waveforms, differing in magnitude from the MMF due to the effect of the permeance function. These asynchronous harmonics contribute to the magnetic shear stress on the rotor which perturb the fundamental torque producing component of the shear stress, leading to a reduction in torque quality, this will be explored in due course. The waveforms, from FEA analysis, presented in Figure. 6.4 are at a single point in time (rotor angle).

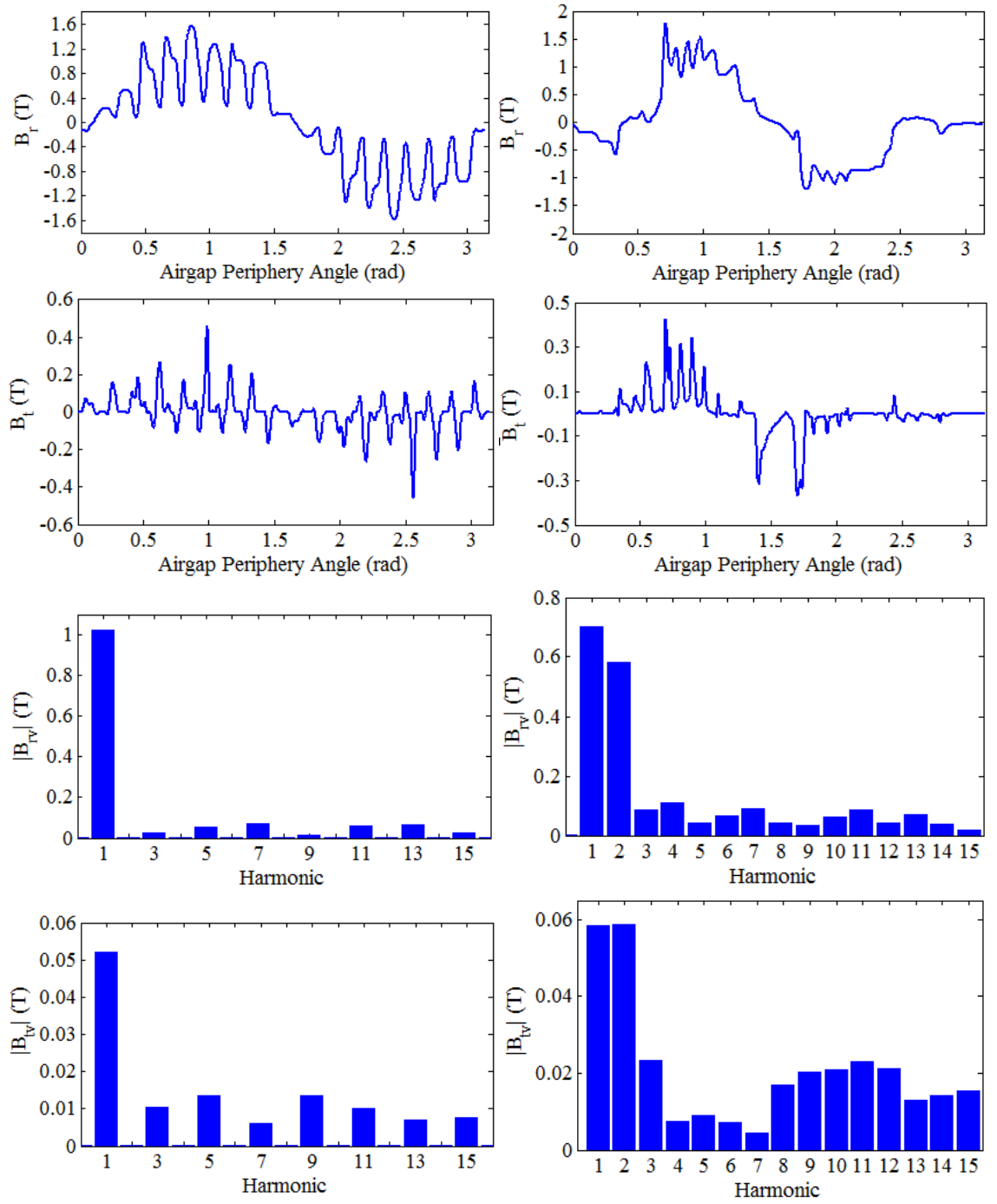


Figure 6.4: Top to bottom: Radial field, radial field harmonic spectrum, tangential field, tangential field harmonic spectrum; Left: SynRM, Right: cSynRM

6.3.3.1 3D Airgap Field Maps

The harmonic analysis of the waveforms in Fig. 6.4 is for a particular time instant. The airgap flux density wave is actually a travelling wave, a function of both space θ and time t : $B = B(\theta, t)$. Figure 6.5 and 6.6 show the wave progression across an electrical cycle for the distributed winding machine and a fractional slot concentrated winding machine (the prototyped motor).

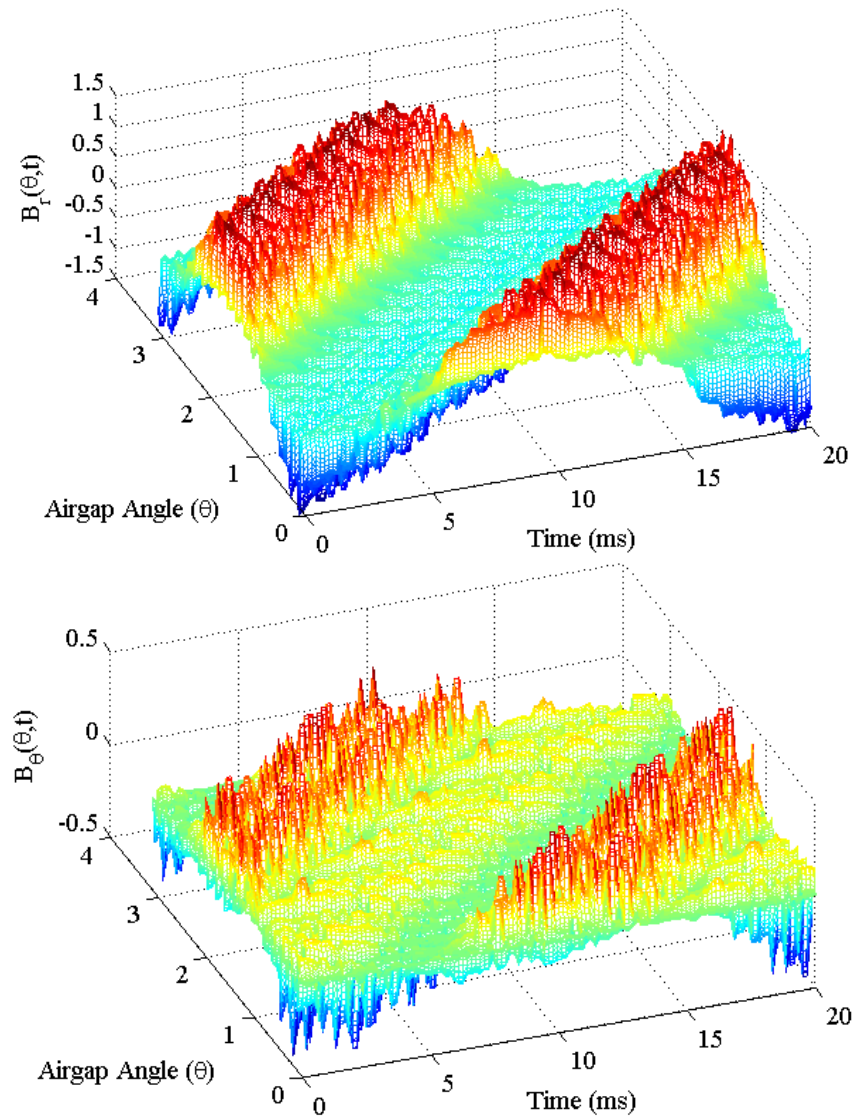


Figure 6.5: Distributed machine; Top: Radial field, Bottom: Tangential field

The distributed machine has a recognisable pattern: the airgap flux density wave is almost constant with regard to its harmonic content as it progresses in space through the electrical cycle. However, in the fractional slot concentrated winding machine, the pattern is changing across the electrical cycle, therefore its harmonic content changes with time. Thus, the following conclusions can be made;

- The distributed winding machine has almost constant space harmonic content containing only odd harmonics
- The FSCW machine has non-constant space harmonic content that can contain both odd and even harmonics, travelling forwards and backwards
- It is seen that airgap space harmonics vary with time, travelling forwards and backwards

Usually, time harmonics are induced by non-sinusoidal current waveforms, however here a time varying harmonic is derived from a space harmonic. The currents used in the

simulation are purely sinusoidal in nature with no time harmonic content. The stator MMF profile of the machine was studied at different time instants in Chapter 3, this showed that at some instants certain even space harmonics exist, but they do not exist at others: the FE calculated airgap flux density waves confirm this.

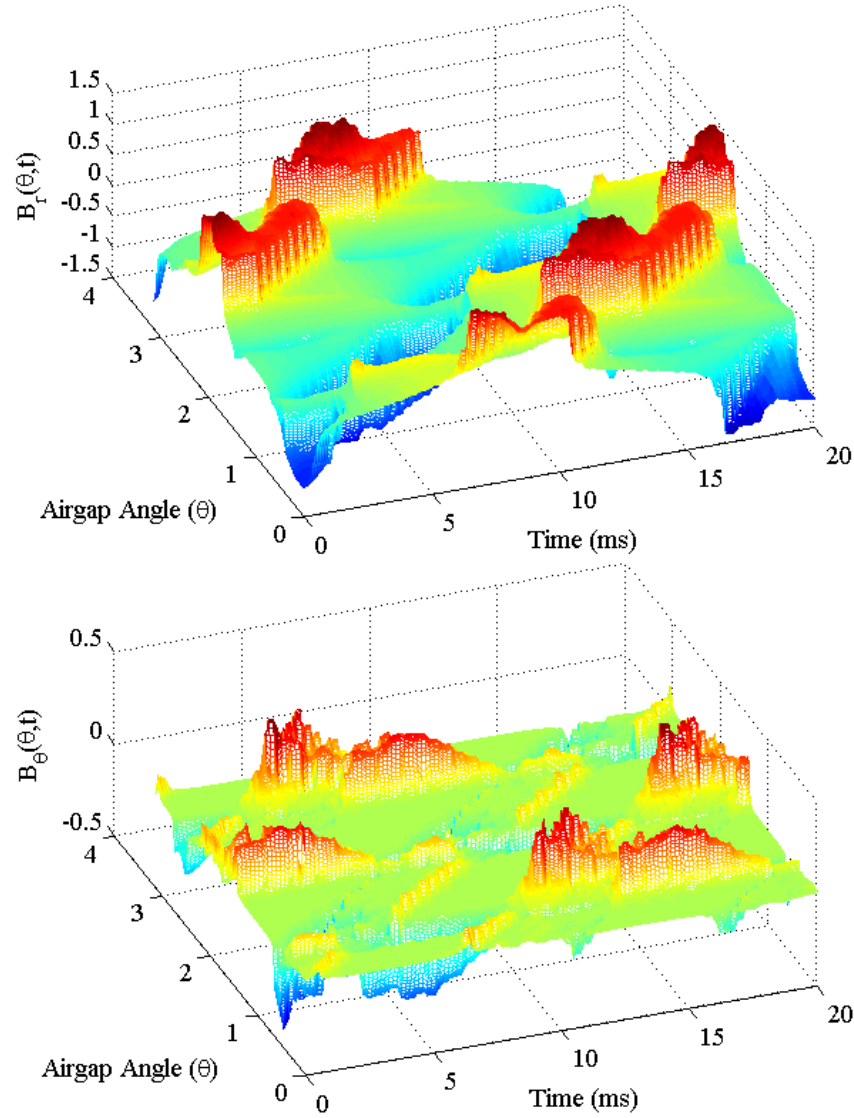


Figure 6.6: FSCW machine; Top: Radial field, Bottom: Tangential field

6.3.3.2 Even Airgap Harmonics

It is clearly evident that even harmonic numbers exist in the cSynRM airgap flux density waveform, which do not appear at all in the conventionally wound machine. This is because of the distribution of the coils for the cSynRM slot pole combination, where the resultant MMF, and therefore airgap flux density waves, lack symmetry about the x -axis. Symmetry makes the Fourier coefficients of even order harmonics go to zero. Lack of symmetry about the x -axis gives these coefficients a non-zero magnitude, hence the even harmonics present in the cSynRM machine.

6.4 Harmonic Stress Components

Now that access is available to the harmonic components of the field quantities, development of the torque equation can begin. For a singular point in time, or rather a rotor position, there is a specific magnetic field distribution in the air gap, which is decomposed with Eqns. 6.9 and 6.10, the discrete waveform can be presented as Eq. 6.11 in the continuous domain;

$$B_{r,\theta}(\theta) = 2 \sum_{k=1}^{\infty} |B_{r,\theta}^k| \cos(k\theta + \widehat{\varphi_{r,\theta}^k}) \quad (6.12)$$

where $|B_{r,\theta}^k|$ is the harmonic magnitude and $\widehat{\varphi_{r,\theta}^k}$ is the harmonic phase; the k is not an exponent, it is the harmonic ordinate. Therefore, for each harmonic field;

$$B_{r,\theta}^k(\theta) = 2|B_{r,\theta}^k| \cos(k\theta + \widehat{\varphi_{r,\theta}^k}) \quad (6.13)$$

Then, the tangential stress, as a function of space for a specific harmonic takes the form;

$$\sigma_{\theta}^l(\theta) = \frac{4}{\mu_0} \left[|B_{\theta}^m| |B_r^n| \cos(m\theta + \widehat{\varphi_{\theta}^m}) \cos(n\theta + \widehat{\varphi_r^n}) \right] \quad (6.14)$$

Where m and n are used as the harmonic ordinates for the tangential and radial fields and l is the resultant harmonic shear stress harmonic. At one point in the air gap the stress is due to all of the harmonics acting on that point and the resultant tangential magnetic stress is calculated by simply summing over the harmonic range;

$$\sigma_{\theta}(\theta) = \sum_{k=1}^{\infty} \sigma_{\theta}^l(\theta) \quad (6.15)$$

Calculation of the individual harmonic torque components is now possible. As an illustration between the force densities in the conventionally wound (distributed) synchronous reluctance machine and the novel cSynRM (fractional slot concentrated wound) and the asymmetry, the resultant shear stress distributions for the two machines for a time instant are presented in Figure. 6.7 over a rotor pole pair. The figures show that the radial stress (pressure) density is higher than the tangential shear stress in both machines. Both force densities in the SynRM are periodic over π electrical radians, however this is not the case in the cSynRM - this is the asymmetry from even harmonics in the waveform.

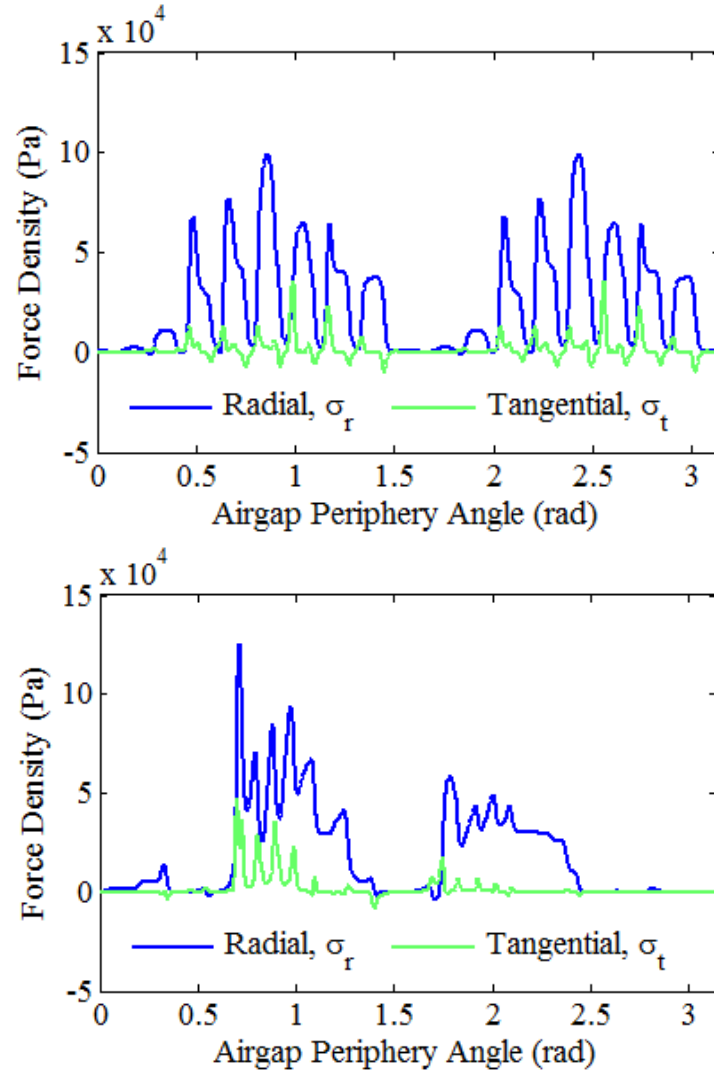


Figure 6.7: Resultant radial and tangential stresses (force densities); Top: SynRM, Bottom: cSynRM

6.5 Torque Analysis

6.5.1 Harmonic Torque Calculation

The development of the torque equation, Eq. 6.6 and the harmonic fields in Eq. 6.14 leads to an expression for harmonic torque components (for a single point in time);

$$T_z^l = \frac{4r^2}{\mu_0} \int_0^{l_a} \int_0^{2\pi} \left[|B_\theta^m| |B_r^n| \cos(m\theta + \widehat{\varphi}_\theta^m) \cos(n\theta + \widehat{\varphi}_r^n) \right] d\theta dz \Big|_{t=t_l} \quad (6.16)$$

We can evaluate the z -axis integral immediately; we can also set for convenience $\widehat{\varphi}_r^n = 0$ and then define a difference angle between the two harmonic components as $\varphi_d^k \triangleq \widehat{\varphi}_r^n - \widehat{\varphi}_\theta^m$ and noting that the integral only exists when $n = m = k$ such that the equation

becomes;

$$T_z^l = \frac{4l_a r^2}{\mu_0} \int_0^{2\pi} \left[|B_\theta^k| |B_r^k| \cos(k\theta) \cos(k\theta + \varphi_d^k) \right] d\theta \quad (6.17)$$

Solving the remaining integral, by making use of a trigonometric identity for cosines;

$$\begin{aligned} \int_0^{2\pi} \left[|B_\theta^k| |B_r^k| \cos(k\theta) \cos(k\theta + \varphi_d^k) \right] d\theta &= |B_\theta^k| |B_r^k| \left. \frac{\sin(2k\theta + \varphi_d^k) + 2k\theta \cos(\varphi_d^k)}{4k} \right|_0^{2\pi} \\ &= |B_\theta^k| |B_r^k| \left(\frac{\sin(4\pi k + \varphi_d^k)}{4k} + \pi \cos(\varphi_d^k) - \frac{\sin(\varphi_d^k)}{4k} \right) \end{aligned} \quad (6.18)$$

and by elementary analysis, $k \in \mathbb{Z}^+$ such that;

$$\frac{\sin(4\pi k + \varphi_d^k)}{4k} \rightarrow \frac{\sin(\varphi_d^k)}{4k}$$

and thus the integration is simplified and the harmonic torque expression becomes;

$$T_z^l = \frac{4\pi l_a r^2}{\mu_0} |B_\theta^k| |B_r^k| \cos(\varphi_d^k) \quad (6.19)$$

Where $|B_r^k|$ is the magnitude of the radial field k^{th} harmonic, $|B_\theta^k|$ is the k^{th} harmonic of the tangential field, which are either forwards or backwards rotating harmonic fields, and φ_d^k is the phase angle between the k^{th} harmonic of the radial and tangential fields. The factor '4' in the equation comes from Eq. 6.13 regarding the DFS decomposition of the field components from the finite element solution, it is again not physically significant. Eq. 6.19 allows harmonic torque calculation for each point in time or rotor angle. From this, the resultant torque can be calculated at a time instant and if a time stepping transient with motion study is performed, the individual airgap field harmonics contribution to torque production can be charted, providing valuable information. The resultant torque T_z at a particular time instant t , mean torque $\overline{T_z}$ over a full mechanical rotation of time interval $t = 0$ to $t = T$ with N_T time samples and percentage torque ripple are expressed in the following equations.

$$T_z = \frac{4\pi l_a r^2}{\mu_0} \sum_{k=1}^{\infty} |B_r^k| |B_\theta^k| \cos(\varphi_d^k) \quad (6.20)$$

$$\overline{T_z} = \frac{4\pi l_a r^2}{N_T \mu_0} \sum_{t=0}^T \left(\sum_{k=1}^{\infty} |B_r^k| |B_\theta^k| \cos(\varphi_d^k) \right)_t \quad (6.21)$$

$$T_z^{\%} = \frac{\max(T_z)_t - \min(T_z)_t}{\max(T_z)_t} \times 100\% \quad (6.22)$$

This set of equations provide the framework for a finite element post processing technique to provide detailed information of the torque quality of synchronous machines. The

following observations are made;

1. The rotor electromagnetic torque is proportional to the rotor electromagnetic volume, $\pi l_a r^2$ - as is known by the conventional equations.
2. The magnitude of a rotor electromagnetic torque component is proportional to the harmonic magnitudes of the field components and the cosine of the phase between the two fields at that point in time.
3. The resultant torque at a time instant is simply the summation of all of the harmonic torque components at that time instant.
4. As the integral goes to zero if $n \neq m$, this implies that only B_r and B_θ of the same harmonic order can interact in order to produce a torque in the case where there is only a stator MMF providing the airgap field.

The developed equations are applicable to synchronous machines with a single excitation source. Due to their simplicity, their solution is straightforward and quick when using a computing platform such as MATLAB.

6.5.2 Implementation

The process of determining the harmonic torque components is easily automated using interoperability between software packages through custom scripting in VBScript. MATLAB® is used as front end application to run the finite element software in the background and to extract the required data and post-process this data based on Eqns. 6.19 to 6.22. The developed method can be incorporated into the motor design cycle; a simplified flow diagram incorporating the technique is presented in Figure 6.8.

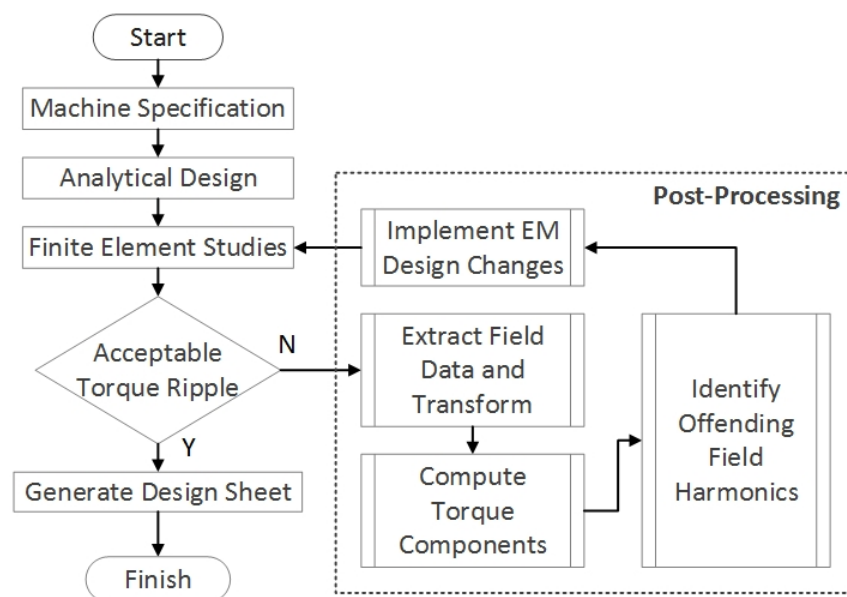


Figure 6.8: Design cycle implementation

The technique can be performed iteratively to achieve a reduction in torque ripple, but the technique alone cannot achieve results, the electromagnetic design changes are chosen by the designer, aided by the information obtained from this tool.

6.6 FSCW Synchronous Reluctance Machine

The developed technique is now applied to two machine designs, the initial machine design with the unoptimised rotor and the final prototyped design, in order to demonstrate the technique and analyse the difference between the two machines in terms of their harmonic torque components. The FEA is performed using non-linear materials in a 2D model with sinusoidal current waveforms. The solution time for a transient over an electrical cycle is 4 minutes, post processing of the extracted airgap field data is performed using MATLAB with a processing time of approximately 1 minute.

6.6.1 Initial Machine Design

Fractional slot concentrated windings can be applied to synchronous reluctance machines as detailed in previous chapters, and it was found that they exhibit a large torque ripple, meaning a poor torque quality which is undesirable. From the developed theory and its practical implementation, the airgap harmonic contributions to the torque ripple can be calculated through the developed post-processing technique. Here a 6 slot, 4 pole machine with an unoptimised, transversely laminated multiple flux barrier synchronous reluctance rotor is analysed. A 2D model used in the FEA is presented in Figure. 6.9.

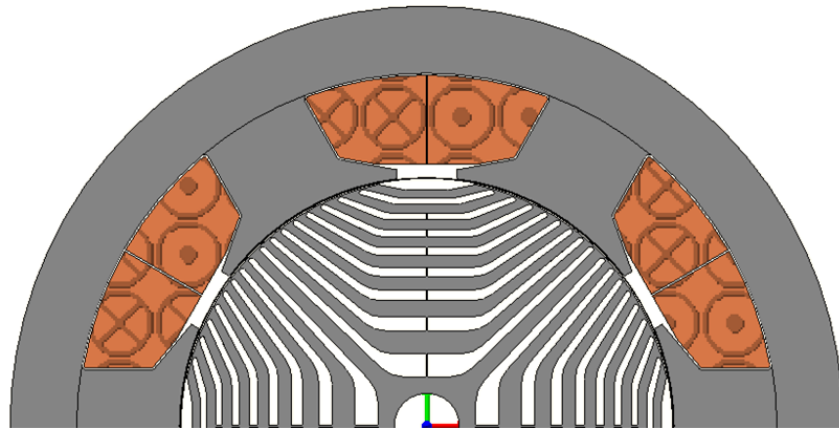


Figure 6.9: 6-slot 4-pole cSynRM - Initial motor cross-section

Figure 6.10 shows the FEA computed torque waveform. It is evident that there is considerable torque ripple when loaded (1500rpm, $I_{line} = 21.2A$, $V_{DC} = 590V$, MTPA control). The torque ripple as a percentage of the mean torque is 106%, whilst the magnitude of the mean torque is 22.6Nm, as determined from a 2D time stepping finite element model in Infolytica MagNet. This level of torque ripple is often unacceptable and is usually found in switched reluctance machines, but not synchronous reluctance machines

as they usually have distributed windings with low space harmonic content. Analysis must be performed and the issues mitigated through improved electromagnetic design in order to realize a practically viable machine, with improvements in the torque quality. In Fig 6.11, plotted over the finite element solution, is the calculation of the torque waveform based on the harmonically decomposed air gap fields according to Eq. 6.19 and implemented as presented in Fig. 6.8.

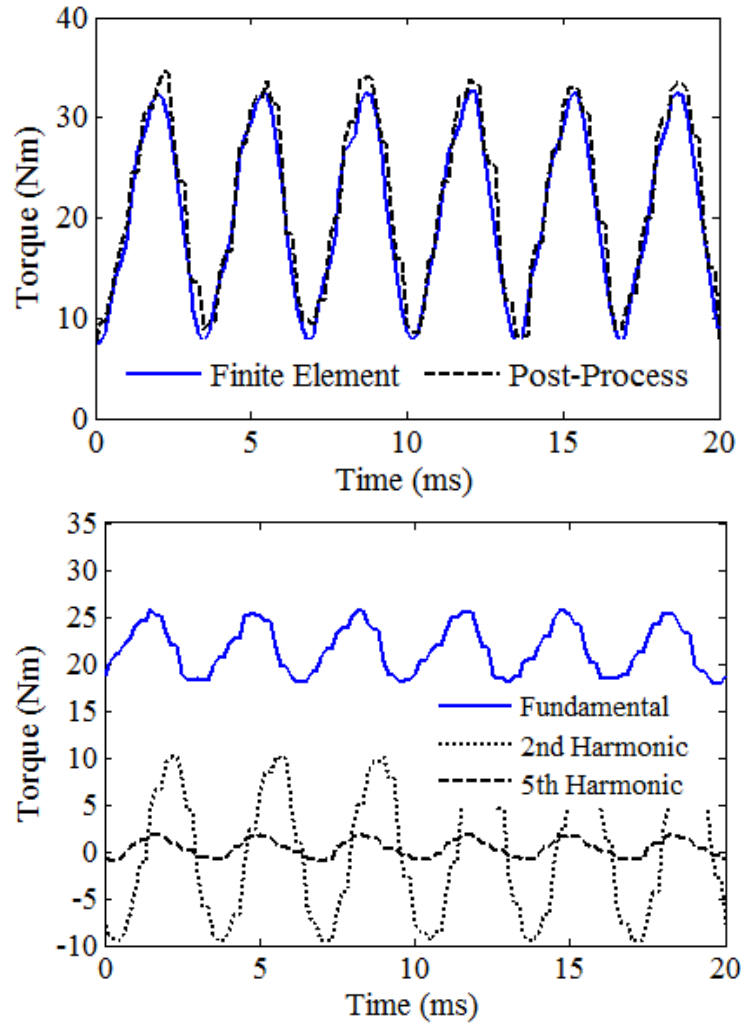


Figure 6.10: Initial machine design; Top: Reconstructed and FE torque waveforms Bot-
tom: Selected torque space harmonic components

The upper plot in Fig. 6.10 shows excellent correlation between the finite element software output and the post-processed torque waveform computed and reconstructed by the developed equations. This acts to validate the equation set Eq. 6.19 - 6.22, which form the developed post-processing method. In the lower plot of Fig. 6.10, the fundamental 4-pole component of the reconstructed waveform, which is based on the superposition of the computed harmonic torque components, is shown with two harmonic components of interest. It is evident that there is a large second order field component (the 5th harmonic interaction is also shown) which corresponds to a second order even MMF harmonic ($k = -2$) as shown in Figure. 6.3 - a counter-rotating 8-pole field with respect to

the fundamental 4-pole field. This 2nd order harmonic interacts with the rotor saliency (permeance function), which is designed for 4-pole operation, and a parasitic oscillatory torque is produced in the examined synchronous reluctance motor, leading to undesirably high torque ripple. The figures focus on the 2nd and 5th harmonics that contribute the most torque ripple in the machine.

The fundamental component is pulsating due to changes in the Carter factor and the influence of the spatial variation of saturation as the rotor rotates at its synchronous speed. Therefore, particular interest can now be paid to the second order field component due to its negative effect on the torque quality of the machine. To the author's knowledge such information is not readily obtained with conventional analysis methods and additional information in identifying a particular offending harmonic in the machine in order to improve the torque quality of the machine is useful to the machine designer. Reduction of the effect of this harmonic is a key objective in the rotor design by reducing the apparent saliency of the rotor for this harmonic field, without compromising the saliency for the main torque producing component. Consider the FE calculated flux patterns for the 8-pole field, presented in Fig. 6.11. These are calculated using a visual basic script in the finite element software to form a infinitesimally thin current sheet producing a 2nd order 8 pole field. Through the introduction of this current sheet, consideration of the points of maximum and minimum torque production of the travelling 8-pole field is possible. Figure 6.11 shows the 8-pole field plot at the zero and maximum torque positions.

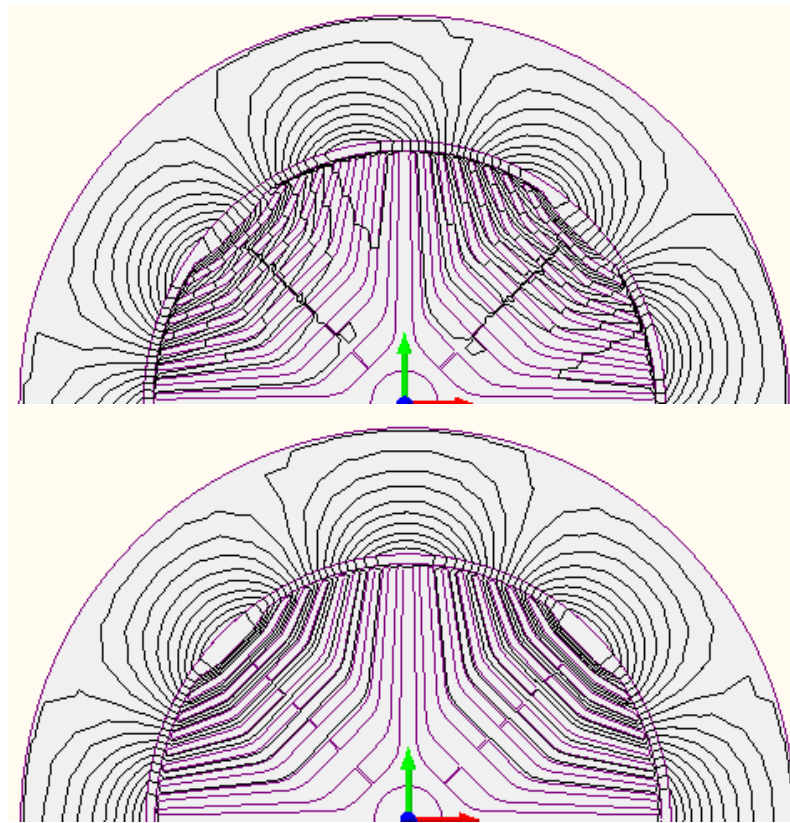


Figure 6.11: 8 pole field for maximum (upper) and zero (lower) torque positions

In order to produce a torque a tangential magnetic stress is required, whether it be the fundamental or any particular harmonic. The magnitude of the torque relates to the magnitude of that tangential magnetic stress and down to the magnitude and angle of the radial and tangential flux densities - determined in turn by the interaction of an MMF and a permeance and so a higher order harmonic field penetrates less into the iron than lower orders, a slight modification of the rotor in the form of a q -axis cutout, depending upon the harmonic order, could reduce the effective saliency (permeance function) for the harmonic of interest and therefore improve the torque quality of the machine.

6.6.2 Initial Rotor Design and Iterations

Initially, the rotor design has number of layers $N_l = 15$ for maximum performance, with the conception that with the possibility of q -axis cutouts, the number of layers would then be reduced. The barrier shape is chosen straight as the component will be wire eroded and this simplifies the cutting process. With EDM the preferred prototyping method and the negligible performance difference between hyperbolic and straight barriers [14], this is the best option for both machine performance and manufacturability. Figure 6.12 shows the initial rotor design used in the optimized FSCW stator configuration in the cSynRM.

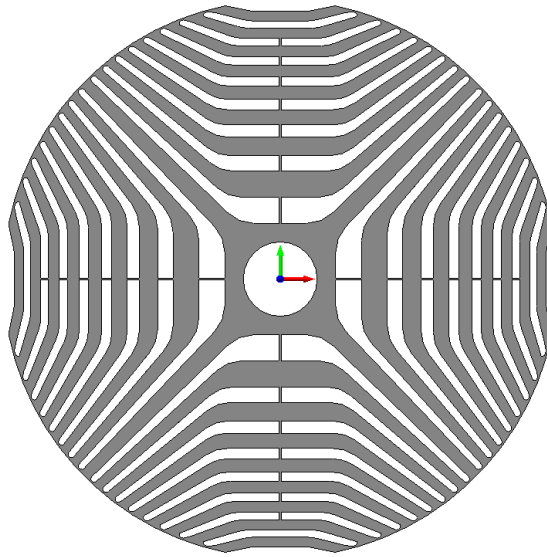


Figure 6.12: Initial rotor design (9 flux barriers)

Finite element analysis of the full machine incorporating the stator design previously reported and the initial rotor design is performed. The analysis is performed under maximum torque per Ampere control with sinusoidal current for a copper loss fixed at 300W. During finite element studies, it was evident that the machine exhibits a large torque ripple and presented in Figure 6.10. Introducing a q -axis cutout, the resulting mean torque and torque ripple can be evaluated through finite element solutions in Infolytica MagNet. The cutout depth is increased by simply removing flux guides from the initial rotor design, depicted in Fig. 6.13 as designs a), b) and c), design a) is the initial design and c) is the

design with three removed flux guides. This is a crude method of rotor improvement, but was used for its simplicity and for its good results, as will be shown.

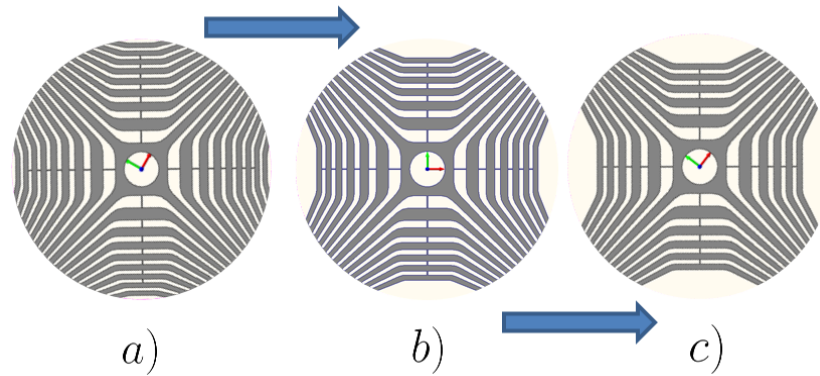


Figure 6.13: q-axis cutout rotor designs

The results for mean torque and torque ripple from finite element solutions for the cutout designs are presented in Table 6.1.

Cut-out depth (Barriers)	Mean Torque (Nm)	Torque Ripple (%)
0	22.7	106.00
1	21.36	46.41
2	19.93	38.39

Table 6.1: Effect of cutout depth on mean torque and torque ripple

Table 6.1 shows that the introduction of the q-axis cutout improves the torque ripple of the machine, but also reduces the mean torque of the machine. With the increasing cut out depth, the flux capturing capability of the d -axis is reduced, lowering the torque index somewhat. A simple way of re-establishing the d -axis flux is to 'fill in' the flux barriers, which acts to increase the d -axis inductance. The cutout depth is set at the level in design c) for maximum torque ripple reduction. With the cut-outs, the 4-pole flux is inhibited and thus designs a through h try to re-establish the fundamental flux to regain the mean torque that is lost due to the introduction of this q -axis cutout. The designs for the iterations a) through to i) are presented in Figure 6.14 and Figure 6.15.

So, by means of crude design iterations, an improved design, with significantly reduced torque ripple is achieved in the final design ' i '. A simple improvement process by trial and error has been used, in order to modify the initial rotor design which has good electromagnetic performance in a conventionally wound machine. The radial and tangential rib widths and barrier thicknesses have not been altered during this simple optimisation, the existence of the ribs is simply changed in iteration to find the best result. This applied method is a crude improvement process and superior results may be achieved by using specialist optimization software and techniques, however very good improvements

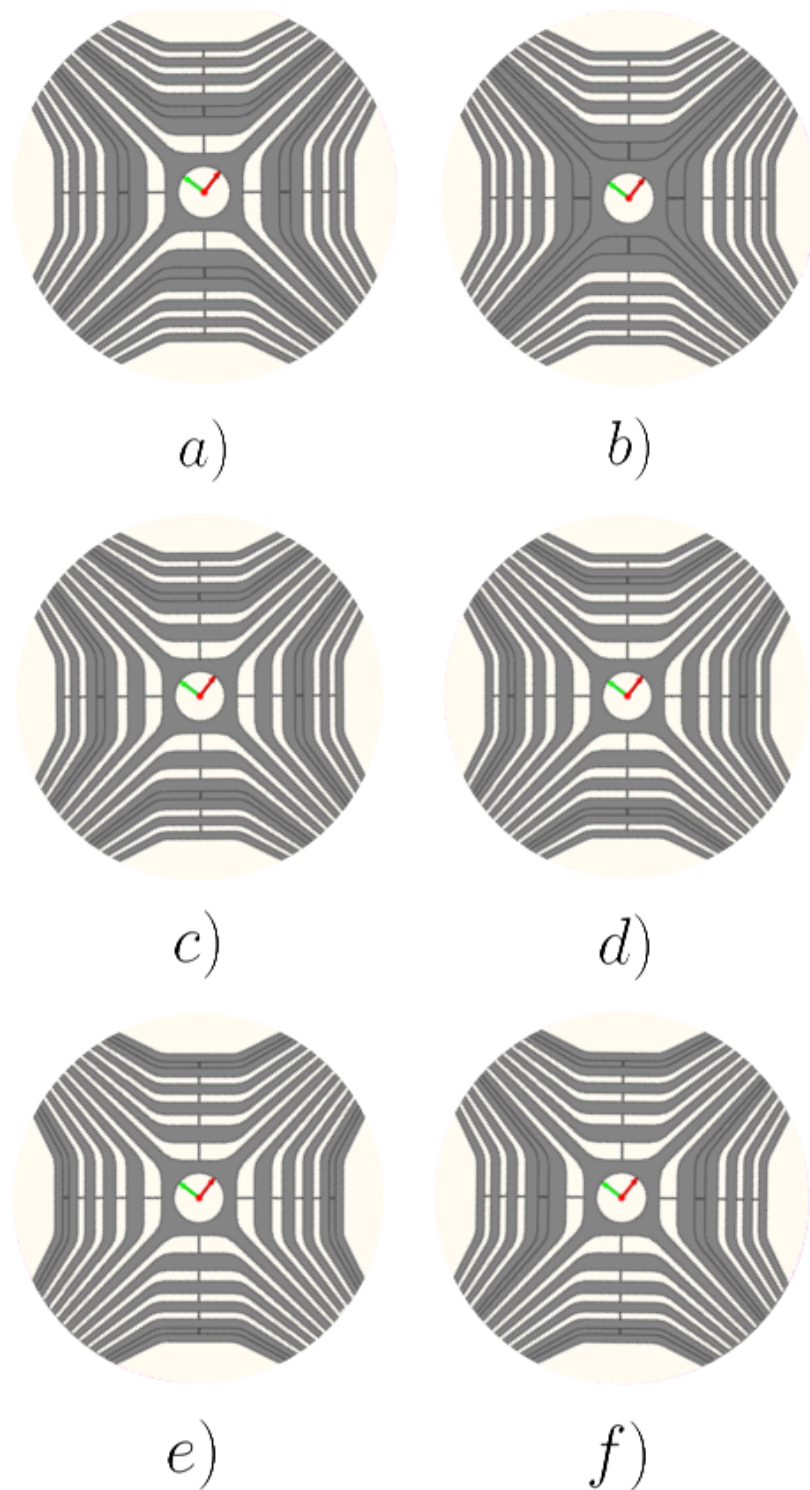


Figure 6.14: Iterative rotor designs a) through f)

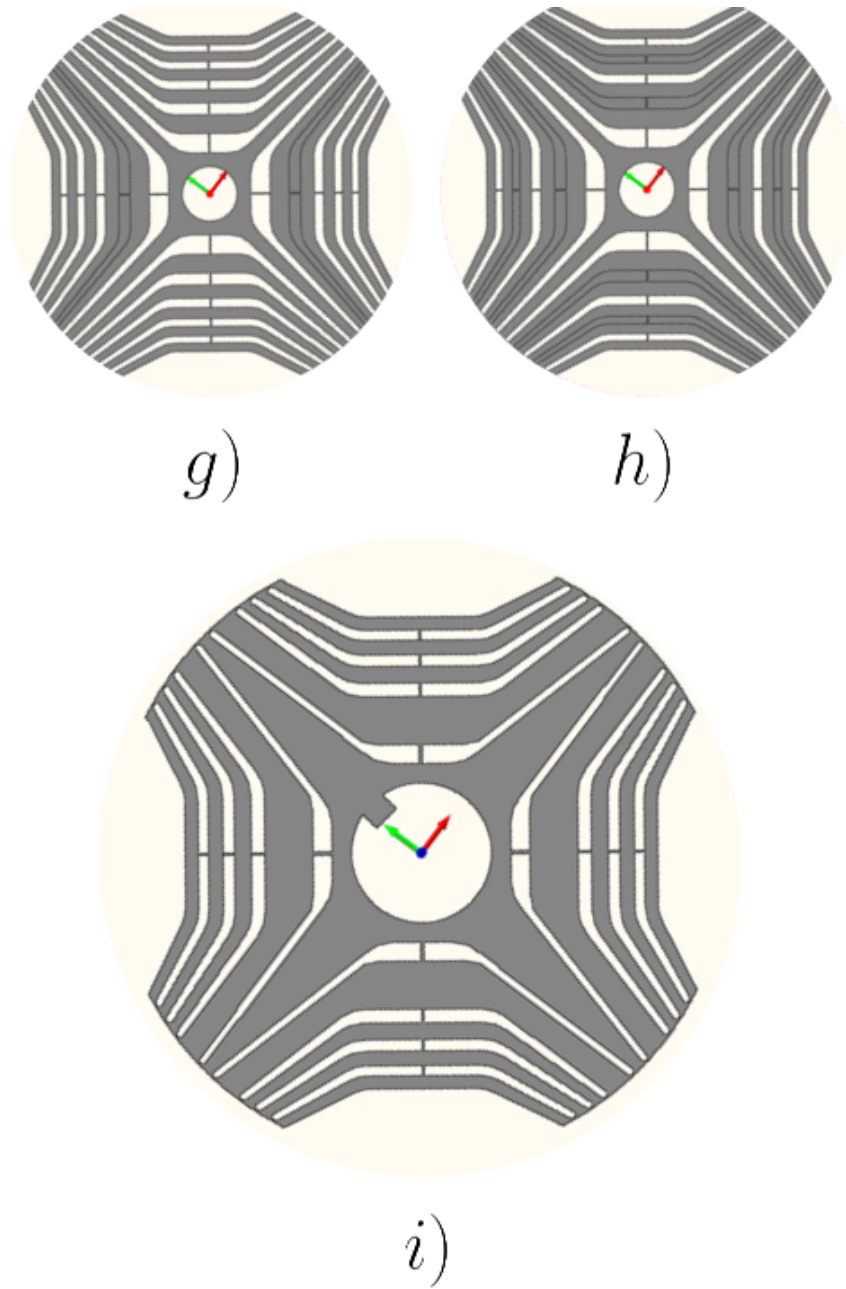


Figure 6.15: Iterative designs g) and h) with the final rotor design i)

in torque quality are achieved. A fitness function for a given design x such that the mean torque and torque ripple are equally weighted, is defined as;

$$f(x) = 1 - \left(\frac{T_m^x}{T_m^A} - \frac{T_r^x}{T_r^A} \right) \quad (6.23)$$

Where T_m^A is the mean torque of the original design, T_m^x is the mean torque of the design under analysis and T_r^x is the torque ripple of the design in percentage points. With this simple fitness function, the lower the result, the more fit the design. The mean torque, torque ripple and fitness calculations for the various design iterations are presented in Table 6.2.

Design	Mean Torque (Nm)	Torque Ripple (%)	Fitness
A	20.24	41.87	1
B	20.02	45.00	1.085
C	20.42	42.22	0.999
D	20.63	42.60	0.998
E	21.23	43.33	0.985
F	20.58	51.57	1.214
G	20.10	41.13	0.989
H	21.71	45.92	1.024
I	21.98	44.00	0.973

Table 6.2: Design iteration mean and ripple torque with rotor fitness

Significantly lower torque ripple is achieved, with the final design i having close to the same mean torque (21.98Nm opposed to the initial 22.7Nm) as the original rotor component, however only 44% torque ripple, opposed to the original 106% torque ripple. This is a significant reduction in torque ripple at the expense of little mean torque and therefore is a good result based on a simple torque improvement method of rotor design modification. However, it must be stated that even though a significant torque ripple reduction was achieved, a torque ripple of 44% is still unacceptable for many applications and further work is required to reduce it further. Figure 6.16 shows the torque ripple comparison between the original design and the optimized design: clearly the torque ripple is significantly reduced.

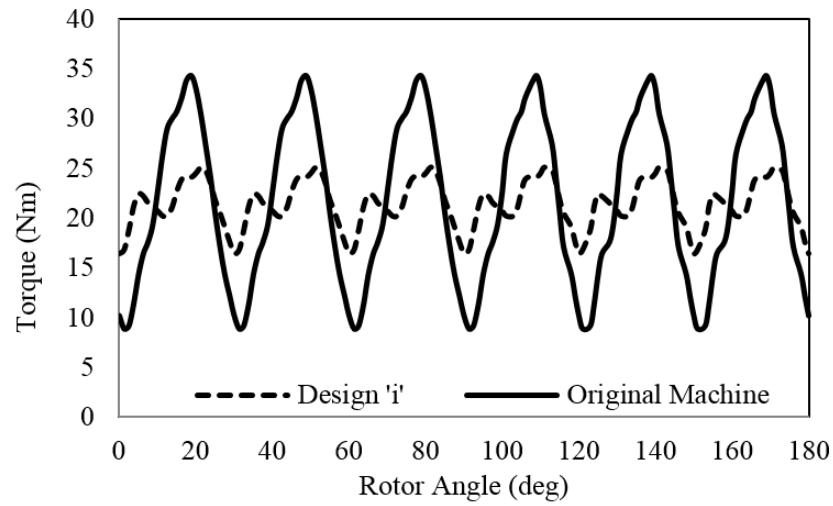


Figure 6.16: Torque quality comparison

The final design, *i*, is slightly adjusted by hand to provide the highest mean torque and power factor, whilst obtaining the lowest torque ripple. The hand adjustments slightly moved the inner-most barrier outwards to accommodate space for a 20mm shaft at the centre of the lamination profile.

6.6.3 Prototype Machine Design

Following the design of the prototype machine in Chapter 3 with fractional slot concentrated windings, and noting the previous section in this chapter, analysis and comparison between the original and final designs is now presented. The 6 slot, 4 pole final machine design with improved rotor as used in the prototype machine is analysed, the 2D motor cross-section is presented in Figure. 6.17.

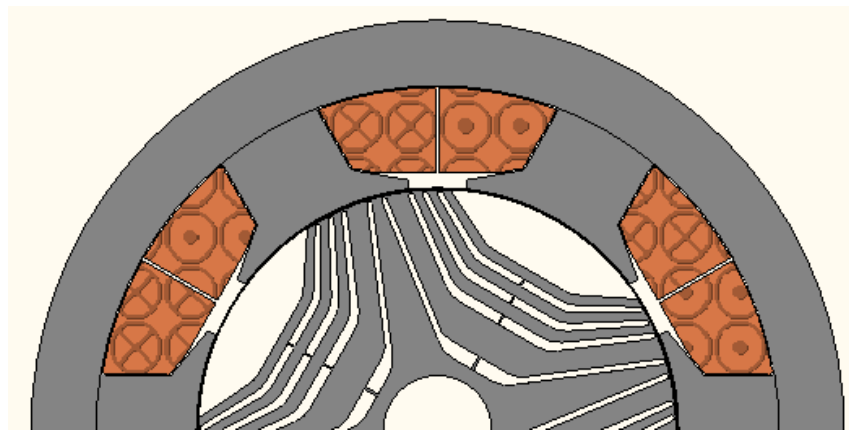


Figure 6.17: 6-slot 4-pole cSynRM - Prototype machine 2D model

The torque ripple at rated load (1500rpm, $I_{line} = 21.2A$, $V_{DC} = 590V$) has been reduced to 44% whilst the mean torque is maintained close to 22.6Nm at 21.9Nm in this machine, as determined from a 2D time stepping finite element modelling. The analysis

of this machine follows an identical process to that of the unoptimised machine. Again the harmonic torque components are calculated from Eq. 6.23 and those of interest are presented in Figure. 6.18. In the figure, the upper plot shows the the finite element solution of the torque waveform and is presented with the computed torque waveform based on the harmonically decomposed air gap fields, again showing excellent correlation between the finite element output and the developed equations. The lower plot shows the selected 2nd and 5th order torque contributions.

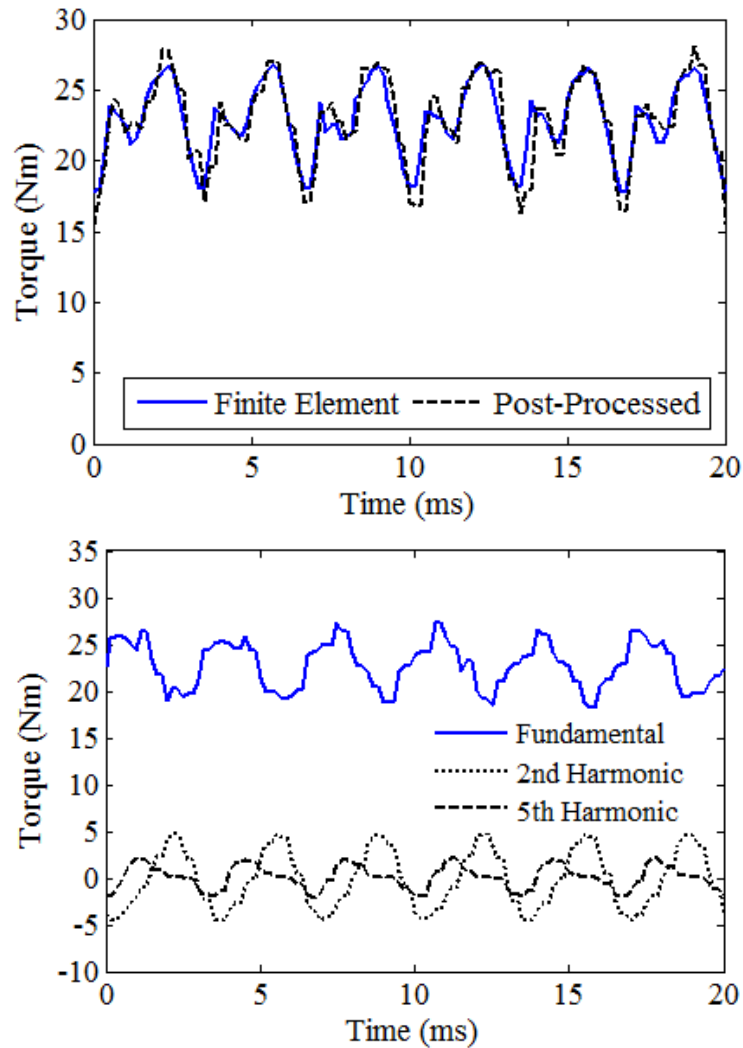


Figure 6.18: Prototyped machine; Top: Reconstructed and FE torque waveforms; Bottom: Selected torque harmonic components

Fig. 6.18 shows a greatly reduced (approximately by half) second order field harmonic torque component and more interestingly the phase relationship between the fundamental component and the second order component has changed such that superposition acts to further reduce the torque ripple in the machine, substantially improving torque quality. As the counter rotating 8 pole field harmonic torque component oscillates about the x-axis, it does not contribute to mean torque and thus its minimisation does not affect the mean torque capability of the machine, but its minimisation does improve torque quality. In the

initial machine design in Figure 6.10, the phase relationship allows for the superposition to exacerbate the torque ripple in that case. Therefore, it is clear that the torque quality of a machine can be improved in two ways;

1. Reduction of the magnitude of an offending harmonic torque component
2. Alter the phase of an offending harmonic torque component

How exactly to implement electromagnetic design changes in any given motor design to accomplish either of these tasks is not the focus of this chapter or the thesis as it will require further research. Rather, this chapter has provided a useful tool for acquiring knowledge about a particular design of machine. There is a phase change in the fundamental component waveforms but little change in mean and ripple levels of this mean torque producing component. However, there is a large difference in the peak to peak value of the second order field torque as it was the aim of the design improvements to reduce the amplitude of this offending torque harmonic to improve torque quality. This reduction effectively reduces the torque ripple in conjunction with the fundamental component phase shift.

6.6.4 Accuracy of Post-Processed Solutions

The developed equations use the solution of a single surface integral in the centre of the airgap to extract the airgap field, compute their respective components and the Maxwell stress tensor. This stress tensor evaluation method is only one technique. The commercial FEA software computes the Maxwell stress tensor using a different method than in Eq. 6.6. In using the single surface integral method (which is consequently reduced to a contour integral when the field is assumed to be invariant across the axial length of the rotor), sensitivity to local field errors is high and thus the computed stress tensor can sometimes be inaccurate, leading to errors and noise in the subsequent post-processed waveforms. This is why the FEA and post-processed torque waveforms are not 100% identical in Figure. 6.11. It is beyond the scope of this thesis to consider the optimal evaluation of the Maxwell stress tensor, however it is suggested that to improve the results of this post-processing method, in the case of 2D FEA, a method based on a volume integral over the entire airgap volume, reducing to a surface integral over the 2D airgap surface between the rotor outer diameter and the stator inner bore, in order to effectively average the forces would be advantageous. This would act to eliminate noise and errors in calculations due to local field errors by averaging the spatial field over a number of elements; such a method is described in [15] but it is beyond the scope of this thesis to examine this further.

6.7 Conclusions

Development of the Maxwell stress tensor leads to a simple algebraic expression for the calculation of torque components in electrical machines caused by air-gap field harmonics. Finite element analysis (FEA) is used to determine the equation variables by harmonically decomposing the radial and tangential air gap fields. It is shown that post-processing of the FE solution by scripting in MATLAB provides valuable information regarding the composition of the torque waveform, based upon individual airgap field harmonic contributions. A deeper insight can potentially be gained into more direct electromagnetic design changes to reduce torque ripple in synchronous machines, improving their torque quality, by showing the actual composition of the torque waveform due to individual air gap field harmonics. As an example, the developed method is applied to a synchronous reluctance machine with fractional slot concentrated windings that is known to exhibit high torque ripple and a large second order (8-pole) harmonic field was found to be the dominant cause of the torque ripple; this information was not possible to be obtained with conventional methods where only mean torque and percentage torque ripple are the figures of merit. In analysing and comparing the original design and the prototype motor, it was found that both a phase change in the fundamental torque producing component and a amplitude reduction of the offending second order field component act to reduce the machines torque ripple. This technique and the information it provides can be a useful tool in electromagnetic design.

6.8 References

1. Eason, Hong-Seok Ko; Kwang-Joon Kim, "Characterization of noise and vibration sources in interior permanent-magnet brushless DC motors," *Magnetics, IEEE Transactions on*, vol.40, no.6, pp.3482,3489, Nov. 2004.
2. Daohan Wang; Xiuhe Wang; Sang-Yong Jung, "Cogging Torque Minimization and Torque Ripple Suppression in Surface-Mounted Permanent Magnet Synchronous Machines Using Different Magnet Widths," *Magnetics, IEEE Transactions on*, vol.49, no.5, pp.2295,2298, May 2013
3. Chu, W.Q.; Zhu, Z.Q., "Investigation of Torque Ripples in Permanent Magnet Synchronous Machines With Skewing," *Magnetics, IEEE Transactions on*, vol.49, no.3, pp.1211,1220, March 2013
4. Alotto, P.; Barcaro, M.; Bianchi, N.; Guarnieri, M., "Optimization of Interior PM Motors With Machaon Rotor Flux Barriers," *Magnetics, IEEE Transactions on*, vol.47, no.5, pp.958,961, May 2011
5. Bianchi, N.; Bolognani, S.; Bon, D.; Pré, M.D., "Rotor Flux-Barrier Design for Torque Ripple Reduction in Synchronous Reluctance and PM-Assisted Synchronous Reluctance Motors," *Industry Applications, IEEE Transactions on*, vol.45, no.3, pp.921,928, May-june 2009
6. Arkadan, A.A.; ElBsat, M. N.; Mneimneh, M. A., "Particle Swarm Design Optimization of ALA Rotor SynRM for Traction Applications," *Magnetics, IEEE Transactions on*, vol.45, no.3, pp.956,959, March 2009
7. Lixin Tang; Limin Zhong; Rahman, M.F.; Yuwen Hu, "A novel direct torque controlled interior permanent magnet synchronous machine drive with low ripple in flux and torque and fixed switching frequency," *Power Electronics, IEEE Transactions on*, vol.19, no.2, pp.346,354, March 2004
8. Jezernik, K.; Korelic, J.; Horvat, R., "PMSM sliding mode FPGA-based control for torque ripple reduction," *Power Electronics, IEEE Transactions on*, vol.28, no.7, pp.3549,3556, July 2013
9. Hao Zhu; Xi Xiao; Yongdong Li, "Torque Ripple Reduction of the Torque Predictive Control Scheme for Permanent-Magnet Synchronous Motors," *Industrial Electronics, IEEE Transactions on*, vol.59, no.2, pp.871,877, Feb. 2012
10. Griffiths, David J. *Introduction to Electrodynamics*. Pearson, 2013.
11. Magnussen, F.; Sadarangani, C.; , "Winding factors and Joule losses of permanent magnet machines with concentrated windings," *Electric Machines and Drives Conference, 2003. IEMDC'03. IEEE International*, vol.1, no., pp. 333- 339 vol.1, 1-4 June 2003
12. Bianchi, N.; Bolognani, S.; Fornasiero, E., "An Overview of Rotor Losses Determination in Three-Phase Fractional-Slot PM Machines," *Industry Applications, IEEE Transactions on*, vol.46, no.6, pp.2338,2345, Nov.-Dec. 2010
13. Jacek F. Gieras, 'Noise of Polyphase Electric Motors', CRC Press, 2005
14. Moghaddam. R, 'Synchronous Reluctance Machines (SynRM) in Variable Speed Drive (VSD) Applications', Doctoral Thesis in Electrical Engineering, Stockholm, Sweden, 2011
15. McFee, S.; Webb, J.P.; Lowther, D.A., "A tunable volume integration formulation for force calculation in finite-element based computational magnetostatics," *Magnetics, IEEE Transactions on*, vol.24, no.1, pp.439,442, Jan 1988

Chapter 7

Inductance Characteristics and Modified dq Machine Model

In this chapter, the flux linkage, corresponding inductance characteristics and the governing equations of the developed cSynRM are explored in the rotating reference frame. Conventional dq theory is reviewed and the machine flux linkages are analysed, assessing the applicability of the model. The d and q -axis flux linkages in the abc frame and their transformation, including harmonics, into the $dq0$ frame is analysed and the conventional dq model is then revised. The modified dq axis equations and a machine model for the cSynRM is presented, taking account of the variations observed. The model includes parasitic effects by utilising the functional dependent characteristics of the flux linkages on rotor position and machine currents. Orthogonal axis equivalent circuits are developed based on the developed equations. The modified equations are then applied to the cSynRM in order to evaluate the developed torque of the machine in the dq frame that includes parasitic effects. As these parasitic effects are important in the cSynRM topology, a machine model in the dq frame would be useful in order to observe the machine variables, predict performance and aid design of both the motor and electric drive controller. The chapter aims to highlight some of the key features of the cSynRM in terms of its machine variables and pave the way for further research into machine analysis and controller design.

7.1 dq Theory Review

Conventional dq theory used in synchronous machine analysis assumes only the fundamental components of flux linkage are present. This corresponds to the machine self L_{ii} and mutual inductances M_{ij} in the stationary abc reference frame as a function of rotor electrical angle. The spatially varying inductances can be expressed [1];

$$L_{ii} = L_{s0} + L_{sv} \cos(2p\theta_m + \varphi_{ii}) \quad (7.1)$$

$$M_{ij} = -\frac{L_{s0}}{2} + L_{sv} \cos(2p\theta_m + \varphi_{ij}) \quad (7.2)$$

Where L_{s0} is the average inductance coefficient and L_{sv} is the amplitude of the fundamental variation. The angle θ_m is the mechanical electrical angle and p the number of rotor pole pairs. The angles φ_{ii} and φ_{ij} are related to the spatial distribution of the phases (120 elec. degree separation) and the indices $i, j \in \{a, b, c\}$ identify the phases concerned with the self- or mutual-inductances. The $2p\theta_m$ in the variation term is due to the geometrical configuration repeating $2p$ times in a complete rotor rotation. The essence of the abc to $dq0$ transform is to transform these spatially varying inductances in the *stationary* reference frame to that of the equivalent inductances in a *rotating* $dq0$ reference frame, effectively decoupling the inductance variation with spacial angle to produce equivalent inductances which are then constant in the synchronous reference frame. This acts to reduce the number of equations required to be solved (as the 0 -component can usually be disregarded) and also makes the variables more appropriate for use in control algorithms as PID controllers work well with DC values, rather than AC quantities. The $dq0$ transformation effectively enables high performance AC drives that implement schemes such as vector control. This transformation is performed using the Park Transformation matrix (abc to $dq0$). The conventional expressions therefore contain no information on saturation, cross coupling or harmonic effects. The conventional electric circuital equations for the synchronous reluctance motor in the dq rotating reference frame are explored in Chapter 1, Section 1.4.3; the scalar $dq0$ equations are repeated here for reference. The equivalent d and q axis circuit voltage equations are;

$$u_d = Ri_d + \frac{d\Psi_d}{dt} - p\omega_e \Psi_q \quad (7.3)$$

$$u_q = Ri_q + \frac{d\Psi_q}{dt} + p\omega_e \Psi_d \quad (7.4)$$

Where in the steady state all quantities are DC valued. The conventional dq model of a synchronous reluctance machine used for dynamic modelling and performance prediction has the following assumptions [1-3];

- Sinusoidally distributed windings energized with sinusoidal currents leading to sine distributed MMF profiles, inductances and air-gap fields.
- No airgap spatial harmonics
- Linear magnetic circuits
- Fully decoupled dq axis inductances (no cross coupling)

In the cSynRM, the first assumption is immediately violated as the coils are discretely positioned around the airgap and wound around single teeth. This invalidates assumption two, as high space harmonic content results from the winding arrangement, leading to

high odd and even harmonic content in the airgap fields. Saturation is a key operational requirement in any SynRM (particularly saturable radial and tangential ribs) and local saturation in tooth tips exists depending on rotor position, which is more pronounced in the cSynRM (as will be explored later in this chapter). This model is only accurate and useful if the described parasitic effects are minimal, which may not be the case in the cSynRM.

7.1.1 Winding Distribution

Usually in three phase machines, the coils are not infinitely thin filaments and there is more than one coil per phase (or conductor for that matter), thus with the appropriate distribution of those coils, any even harmonics can be eliminated and when the three phase system is employed the triplen harmonics sum to zero. In the cSynRM machine, the coils are short pitched and not distributed around the airgap periphery, they are discretely placed around the airgap. With fractional slot concentrated windings, the coil span is actually the tooth span, as the coils are wrapped around a single tooth - hence '*single tooth windings*'. The prototyped machine has a number of slots per pole equal to 1.5 (slots per pole per phase of 0.5) and, as such, the stator slot pitch is less than the rotor pole pitch. Therefore even harmonics are contained in the MMF and airgap field distributions as has been shown in previous chapters.

7.2 Flux Linkage Harmonics

Even airgap field (B-field) harmonics may exist in the cSynRM machine due to the coil arrangement [4], but do not feature in the phase flux linkage waveform due to the machines symmetries which act to produce half wave symmetric voltage waveforms (positive half cycle is symmetric with the negative half cycle); consequently, only odd harmonics feature in the phase flux linkages in symmetric and balanced machine's [5], as will now be shown.

7.2.1 cSynRM Phase Flux Linkages

As mentioned, even harmonics exist but do not feature in the phase flux linkage waveforms, therefore, the odd harmonics are of interest when analysing the phase flux linkages. Figure 7.1 shows an FFT of the MMF both with and without the even harmonics of the prototyped cSynRM machine.

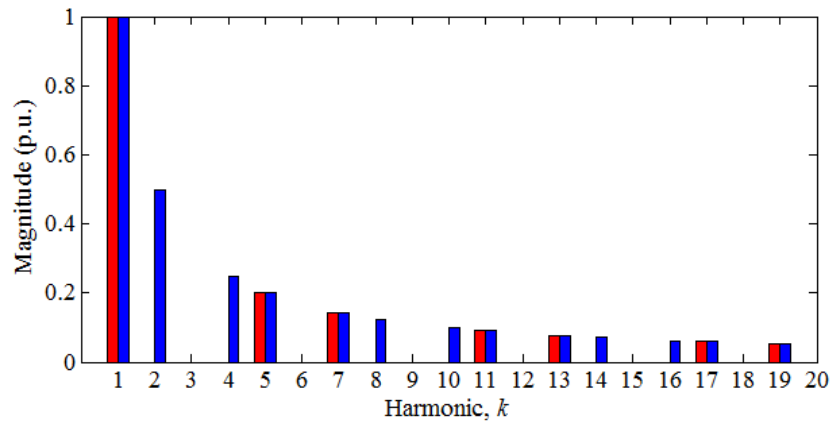


Figure 7.1: cSynRM MMF harmonic spectrum with and without even harmonics

Therefore, the harmonics likely to cause variation in the phase flux linkage waveforms are the 5th and 7th harmonics as these have the largest magnitudes. To demonstrate that the phase flux linkage waveforms of the cSynRM machine do indeed only contain these odd harmonics, Figure 7.2 shows the three phase flux linkage waveforms and their corresponding harmonic spectra - derived from the finite element machine model. These flux linkages are calculated by applying balanced three phase sinusoidal currents to the phases of rated magnitude.

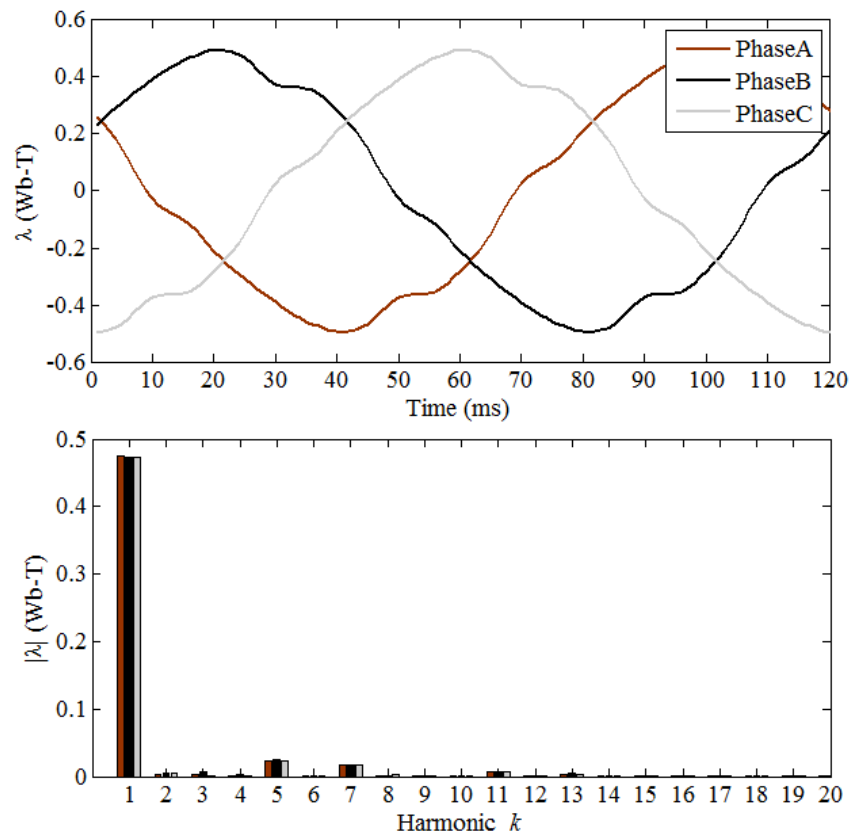


Figure 7.2: cSynRM 3ph flux linkage waveforms and corresponding harmonic spectra

It is clear that the flux linkage harmonic spectra contain mainly the -5th, +7th, -11th

and +13th odd harmonics, where the -ve indicates counter rotating negative sequence harmonics and +ve indicates forward sequence harmonics, with respect to the fundamental. The apparent non-zero magnitudes of the even harmonics is numerical noise both from the flux linkage calculation from the FEA field solution and the FFT computation. Therefore, the machine's phase flux linkage does contain harmonic content and it is only odd harmonics that feature.

Thus from Section 7.1, the $dq0$ transformation has difficulty due to the odd harmonic content in the phase flux linkage waveforms and all the parasitic effects in the machine caused essentially by the discrete placement of the coils around the airgap. This short pitching of the coils is a fundamental issue when it comes to parasitic effects and machine analysis, but on the other hand facilitates the short end windings and high fill factor coils leading to the benefits describes in this thesis.

7.2.2 SynRM Phase Flux Linkages

With the SynRM and its sinusoidally distributed wound stator, even harmonics are eliminated and the odd harmonics are greatly reduced. The low odd harmonics are of interest when analysing the phase flux linkages of a typical SynRM, they are obtained through FEA of the machine in the same manner as the cSynRM. Figure 7.3 shows the three phase flux linkage waveforms and an FFT of those waveforms for sinus currents.

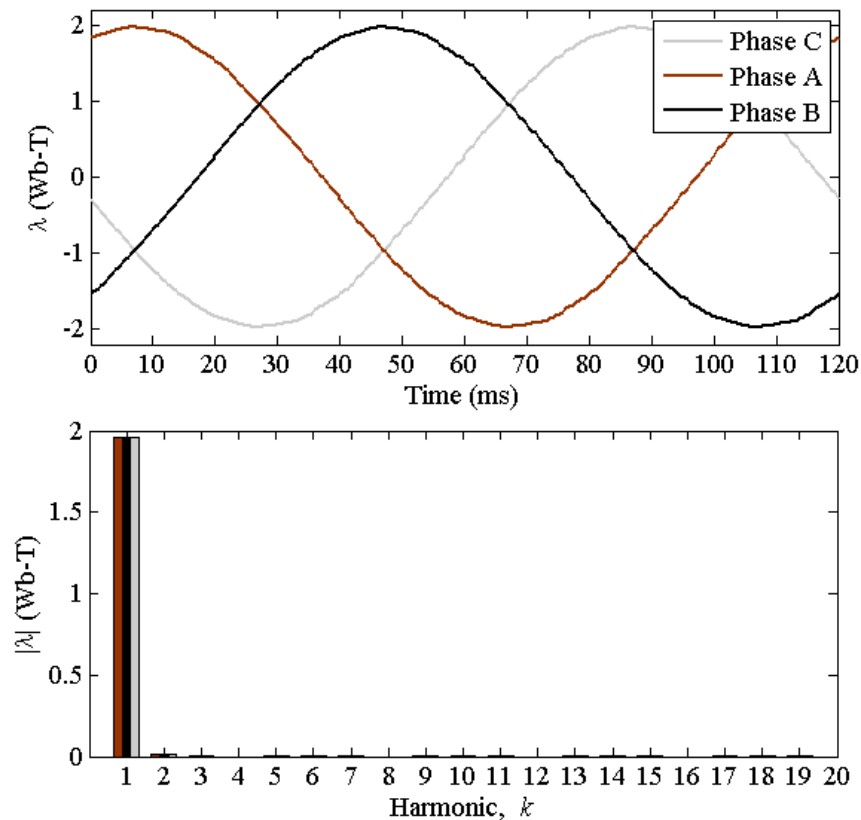


Figure 7.3: 3ph flux linkage waveforms of the SynRM and corresponding harmonics

It is clear that the flux linkage harmonic spectra contains very little harmonic content and the waves can be assumed perfectly sinusoidal, unlike the cSynRM. Therefore, the SynRM machine's phase flux linkage does not contain harmonic content and fulfils the fundamental assumption of sine distributions of conventional $dq0$ theory.

7.3 Machine Characteristics

With a distributed wound stator, the synchronous reluctance machine parameters (i.e. the flux linkages and inductances) in the abc frame vary with rotor position due to the relative position of the poles under the coils making up each phase. These coils form a balanced set. Usually, when the $dq0$ transform is employed to eliminate this spacial variation, the transformation is synchronous with the fundamental variation, yielding constant values for the $dq0$ machine parameters. If harmonics are present in the abc variables, these will then be asynchronous to the fundamental $dq0$ transformation and the $dq0$ parameters will no longer be smooth and will vary with rotor position. This section investigates position varying $dq0$ machine variables and compares the conventional SynRM to the cSynRM machine.

7.3.1 Flux Linkages

The abc frame flux linkages can be found easily through finite element studies as this is a standard computation. Three phase sinusoidal currents are applied to the phase windings and the rotor rotates at the synchronous frequency. Figure. 7.2 in Section 7.2 shows the three phase flux linkages at the machine's rated operating point. From these flux linkages, the $dq0$ flux linkages can be calculated via the following transformation equation [1];

$$\Psi_{dq0} = \mathbf{T}^{-1} \Psi_{abc} \quad (7.5)$$

This gives direct access to the orthogonal axis flux linkages in the rotating $dq0$ reference frame. If Ψ_{abc} contains harmonics, its matrix multiplication with the $dq0$ transform \mathbf{T}^{-1} does not yield constant flux linkages in that reference frame, as conventional theory would dictate - the transformed quantities are varying DC. Using the obtained abc frame flux linkages as in Fig. 7.2, the $dq0$ flux linkages are obtained and presented in Fig. 7.4. Here the $dq0$ flux linkages vary significantly with rotor angle about the average value dictated by the fundamental flux linkage, the variation $\Delta\Psi_d = 86.5\text{mWb-T}$ and $\Delta\Psi_q = 60.8\text{mWb-T}$ with mean values $\Psi_{1d} = 558\text{m Wb-T}$ and $\Psi_{1q} = 160\text{ Wb-T}$. The ripple as a percentage of the mean value is calculated to be 15.5% and 38% for the d - and q -axis respectively. Therefore the $dq0$ transformation based on the abc flux linkages at a current angle of 45 degrees suggests a saliency ratio of $\xi = 3.55$, which is in agreement with Chapters 3 and 4. The harmonic content of the d and q axis waveforms are shown in Fig. 7.5.

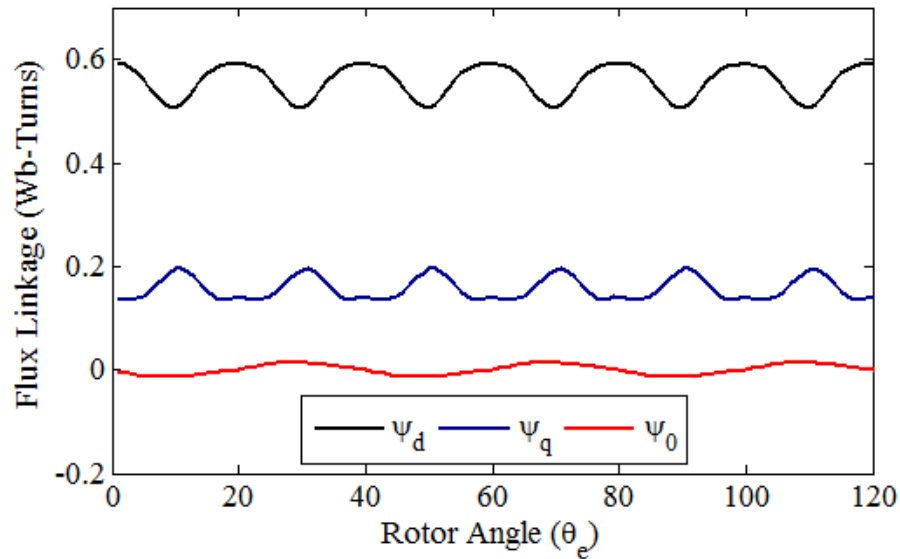


Figure 7.4: cSynRM flux linkages in the $dq0$ reference frame (rated current with a current angle of 45 degrees)

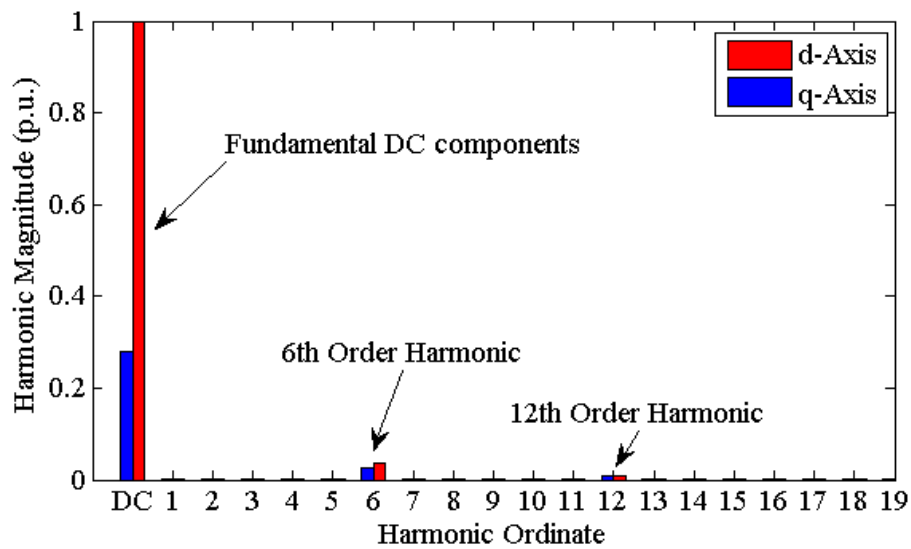


Figure 7.5: cSynRM flux linkage harmonics in the $dq0$ reference frame

Therefore a 6th order harmonic along with a 12th order harmonic are present in the $dq0$ waveforms, this is explored further in Section 7.3.1.1. The fractional slot concentrated winding cSynRM does not therefore have constant orthogonal axis inductances with rotor position. As a contrast, using the obtained abc frame inductances for the distributed wound SynRM as in Fig. 7.3, the $dq0$ flux linkages are obtained and presented in Fig. 7.6.

Here the $dq0$ flux linkages only slightly vary with rotor angle about the average value dictated by the fundamental flux linkage, the variation of the dq flux linkages is $\Delta\Psi_d = 34\text{mWb-T}$ and $\Delta\Psi_q = 29.2\text{mWb-T}$ with mean values $\Psi_{1d} = 2.37\text{ Wb-T}$ and $\Psi_{1q} = 0.36\text{ Wb-T}$. The ripple as a percentage of the mean value is calculated to be 1.43% and 8% for the d - and q -axis respectively. Therefore the $dq0$ transformation based on the

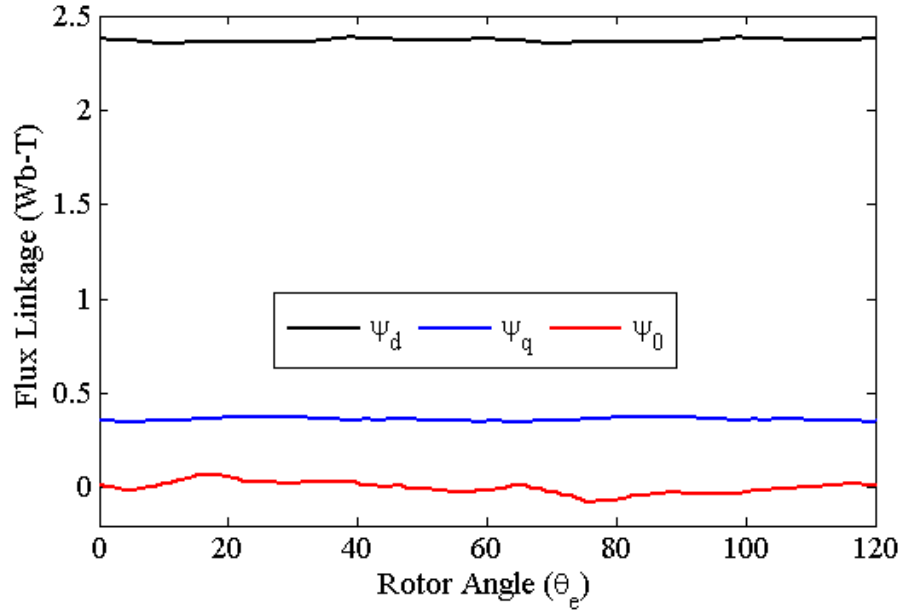


Figure 7.6: SynRM flux linkages in the $dq0$ reference frame (rated current with a current angle of 45 degrees)

abc flux linkages at a current angle of 45 degrees suggests a saliency ratio of $\xi = 6.6$, this is verified through standard FEA methods of determining the d and q -axis inductances which suggests a saliency ratio of $\xi = 6.79$. The distributed winding SynRM, for all purposes can generally be considered to have constant orthogonal axis inductances with rotor position, unlike the cSynRM.

It is interesting to note from Figs. 7.4 and 7.6 that the Ψ_0 flux linkages are non-zero. The current vector, $i_0 = 0$ and thus the associated flux linkage should be zero; this non-zero component may arise from numerical errors in the FEA solutions.

7.3.1.1 Post Transformation Harmonic Content

The $dq0$ transformation is a synchronously rotating reference frame. In other words, it is designed such that the fundamental component maintains a DC value with rotor rotation. With respect to higher order harmonics in the stationary abc frame, their orders upon $dq0$ transformation obey the rule;

$$k_{dq0} = k_{abc} - 1 \quad (7.6)$$

This ordinate transformation is sign sensitive, therefore, for the positive and negative sequence harmonics in the abc frame, the harmonic ordinates are transformed to unlikely ordinates. This is illustrated by Table 7.1.

<i>abc</i> Frame	<i>dq0</i> Frame
1	0 (DC)
-5	-6
7	6
-11	-12
13	12
-17	-18
19	18
-23	-24

Table 7.1: *abc* to *dq0* harmonic ordinate transformations

Thus the harmonic ordinates present in a *abc* to *dq0* transformed waveform are of the orders $k_{dq0} = 6h$ where $h \in \mathbb{Z}$. This explains the results in Fig. 7.5 where 6th order harmonics arise in the *dq0* transformed flux linkage waveform when only the 5th, 7th, 11th and 13th are present in the *abc* frame flux linkage waveform. A physical explanation is as follows: The 5th harmonic rotates backwards (counter rotating) as a negative phase sequence component with frequency $5\omega_s$ with respect to the stator, where ω_s is the synchronous angular velocity. The rotor (and the synchronous reference frame) is rotating with frequency ω_s in the opposite direction, giving a relative frequency of $6\omega_s$. The 7th harmonic rotates forwards as a positive phase sequence component with frequency $7\omega_s$ with respect to the stator. Again, the rotor (and the synchronous reference frame) is rotating at ω_s but this time in the same direction, therefore the relative frequency of the 7th order harmonic is again $6\omega_s$. Therefore, the 6th order variation in Fig. 7.4 is due to the combination of the 5th and 7th order harmonics and the 12th order variation a combination of the 11th and 13th. It can be concluded here that the harmonics with ordinates $6h \pm 1$ in the *abc* reference frame produce harmonics of the order $6h$ in the *dq0* or rotor reference frame, where $h \in \mathbb{Z}$. This deduction agrees with 3 phase power systems analysis where the *dq0* transformation can be used as a harmonic filter and identifier [6,7].

7.3.2 Inductances

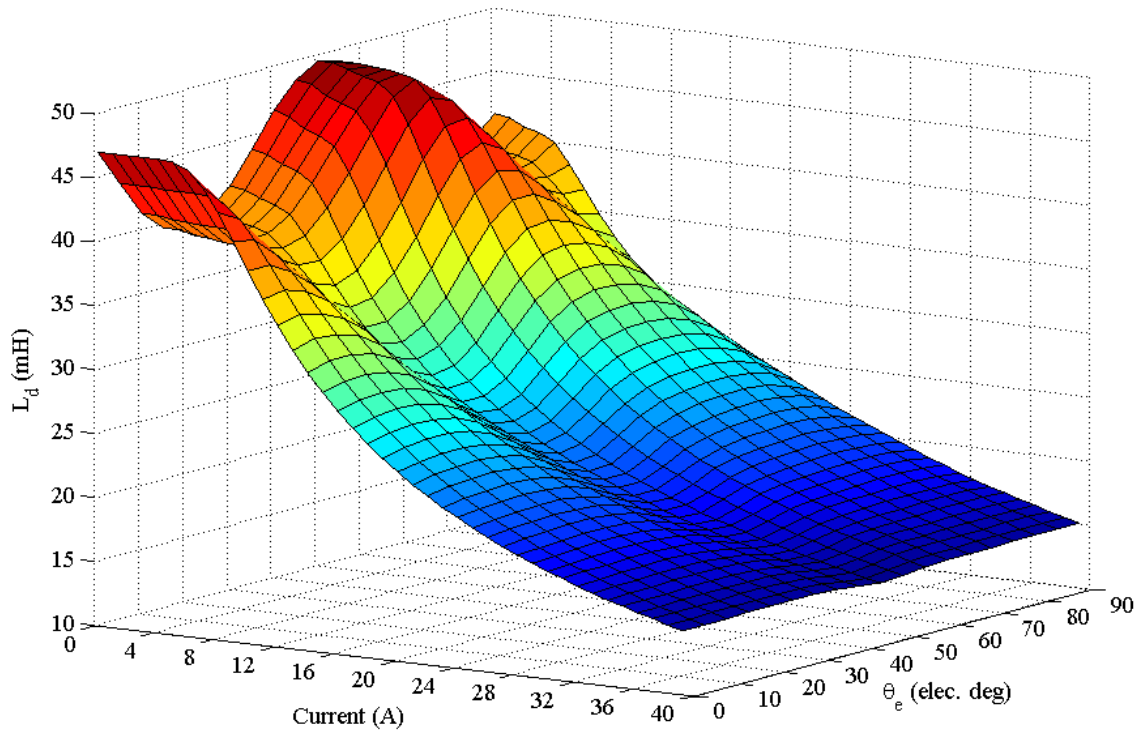
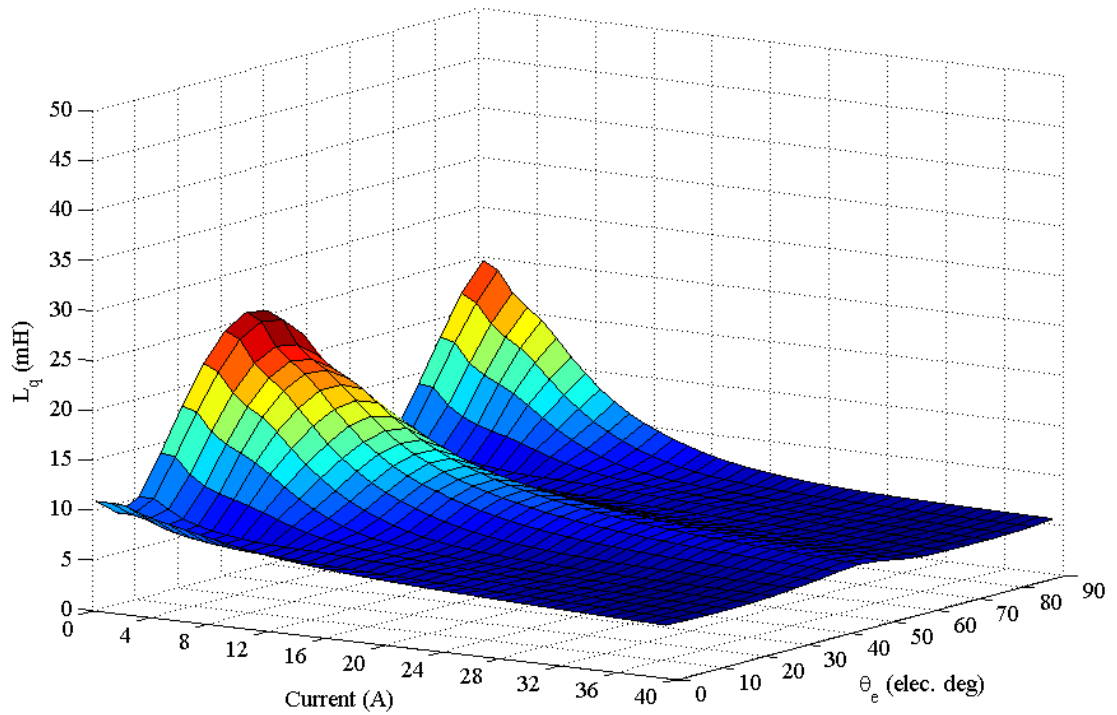
The machine inductances are derived either as apparent or incremental inductances from the flux linkages and the applied currents. They can be obtained in either the *abc* reference frame or the *dq0* reference frame through finite element studies, however localised saturation significantly affects the result in the *abc* method of determination. Usually one phase is energised with current at a time and the self and mutual flux linkages computed. Saturation is ignored due to the contributions of the other two phases during operation, thus accurate estimate is not practical unless permeability freezing techniques are used. Here the *dq0* inductances as a function of axis current and rotor angle are obtained through finite element studies by rotating the rotor and the current angle in synchronism

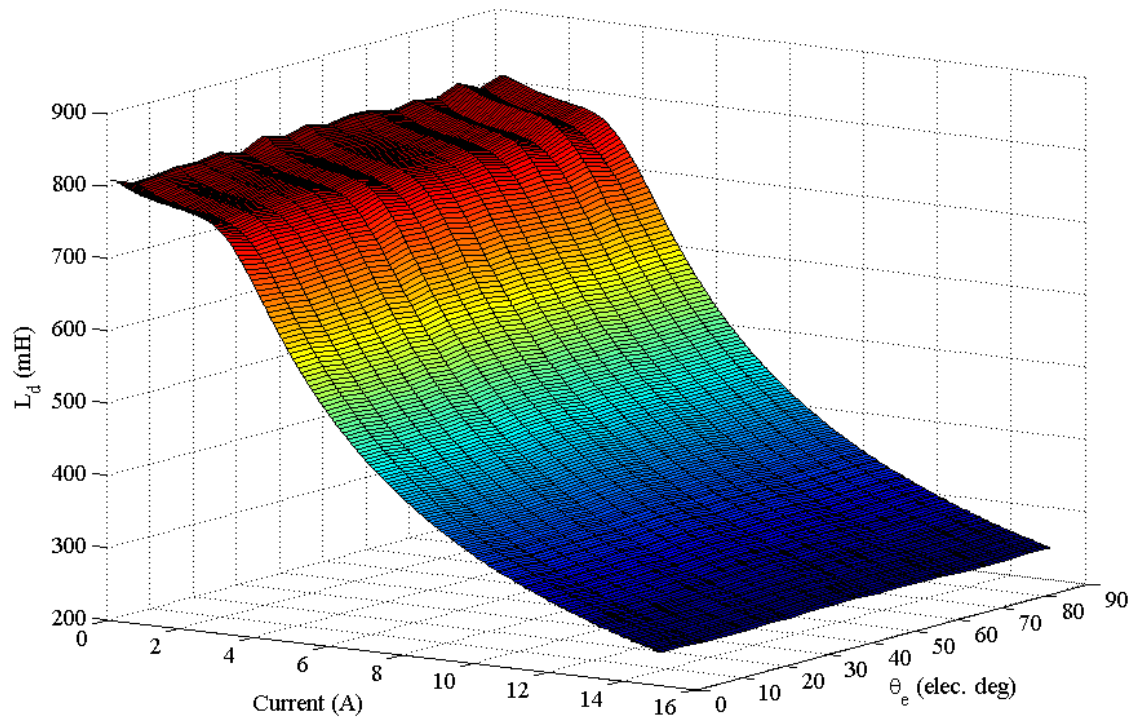
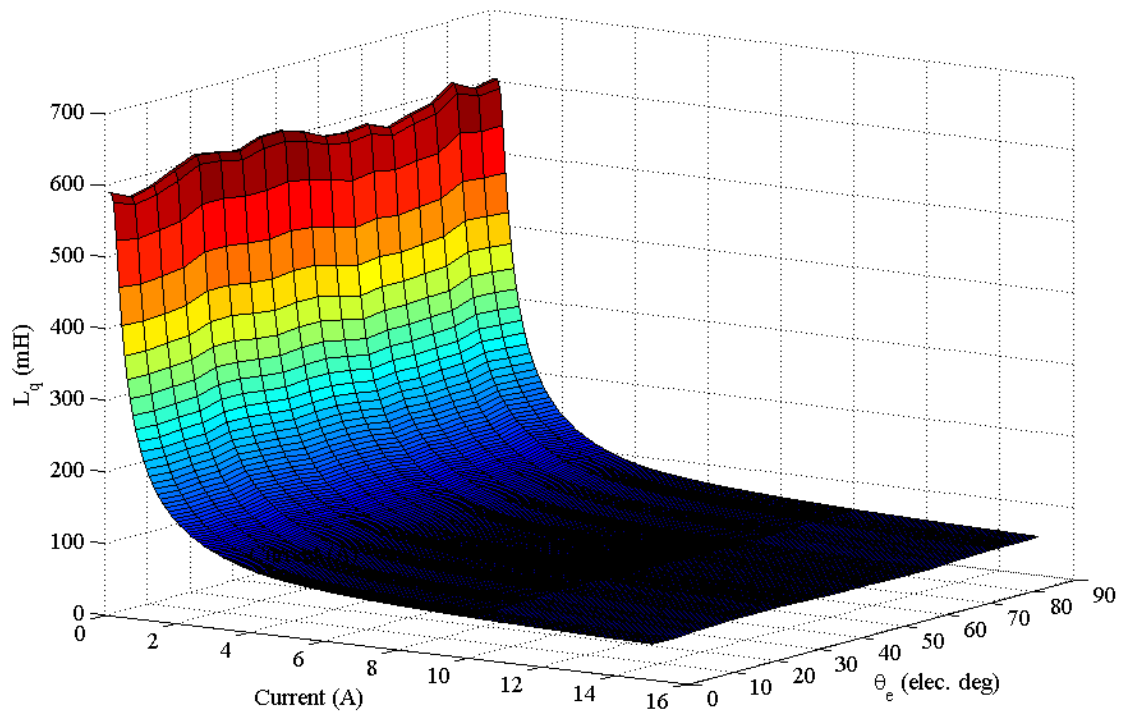
and then computing the axis flux linkages. The apparent inductances are then calculated and plotted as a surface. The software Infolytica MotorSolve is used for this analysis as it automates the process. Figures 7.7 and 7.8 show the inductances L_d and L_q as a surface plot for the prototyped cSynRM. From the figures it is clear that spatial variation of the inductances with rotor angle in the cSynRM is significant. For each current level, the inductances of the cSynRM machine can be written as;

$$L_d = L_{d0} + L_{d6} \cos(6p\theta) + L_{d12} \cos(12p\theta) + \dots + L_{d(6k)} \cos(6kp\theta)$$

$$L_q = L_{q0} + L_{q6} \cos(6p\theta) + L_{q12} \cos(12p\theta) + \dots + L_{q(6k)} \cos(6kp\theta)$$

Where L_{q0} is its DC component and $L_{d(6k)}$ are the harmonic variation terms. At rated phase current the variation of the inductances are almost sinusoidal – the overall variation $\Delta L_d \approx 4\text{mH}$ and $\Delta L_q \approx 6\text{ mH}$. This result suggests that the effective saliency ratio varies with rotor angle, whereas the saliency ratio is usually considered a constant figure of merit. As the currents used in the analysis are pure sinusoidal with no time harmonics present, the $dq0$ transformed currents are DC valued. This means that the harmonics in the abc frame of $6h \pm 1$ maintain harmonics of the order $6h$ in the inductance waveforms via spatial variation of the $dq0$ flux linkages. It is clear that the 6th harmonic is present in the inductance as over 90 electrical degrees inductance 1.5 cycles are present, $1.5 \times 4 = 6$. This harmonic content is derived from the discrete nature of the coils, as explained in Chapters 2 and 3. The influence of increased axis current reduces the inductance variation due to dominance of magnetic saturation in the main magnetic circuit. This variation needs to be considered in drive control schemes, requiring multidimensional lookup tables stored for each rotor angle - this suggests that very high performance drives with these machines may become increasingly complex and therefore costly. The machine model requires modification in order to take this variation into account. Again, as a contrast, Figure 7.9 shows the d -axis inductance surface of the distributed wound SynRM, Fig. 7.10 shows the q -axis inductance surface.

Figure 7.7: cSynRM - spatial variation of L_d with rotor angleFigure 7.8: cSynRM - Spatial variation of L_q with rotor angle

Figure 7.9: SynRM - spatial variation of L_d with rotor angleFigure 7.10: SynRM - spatial variation of L_q with rotor angle

Clearly the inductances of the SynRM are constant with rotor position and saturation reduces both the d - and q -axis inductances. The effective saliency ratio of the SynRM is therefore constant with rotor position but does change with current, as is expected and reported in the literature.

7.3.2.1 Saliency Ratios

The findings presented suggest that the orthogonal axis inductances vary with rotor position in the developed cSynRM, if then, by definition, the saliency ratio will also vary with rotor position. The saliency ratio is expressed (where the constituent inductances are a function of both current and rotor angle);

$$\xi = \frac{L_d(i_d, \theta)}{L_q(i_q, \theta)} \quad (7.7)$$

Therefore, based on the computed inductances of the prototype cSynRM machine, as depicted in Fig. 7.7 and Fig. 7.8, the saliency ratio as a function of current and rotor angle is presented in Fig. 7.11.

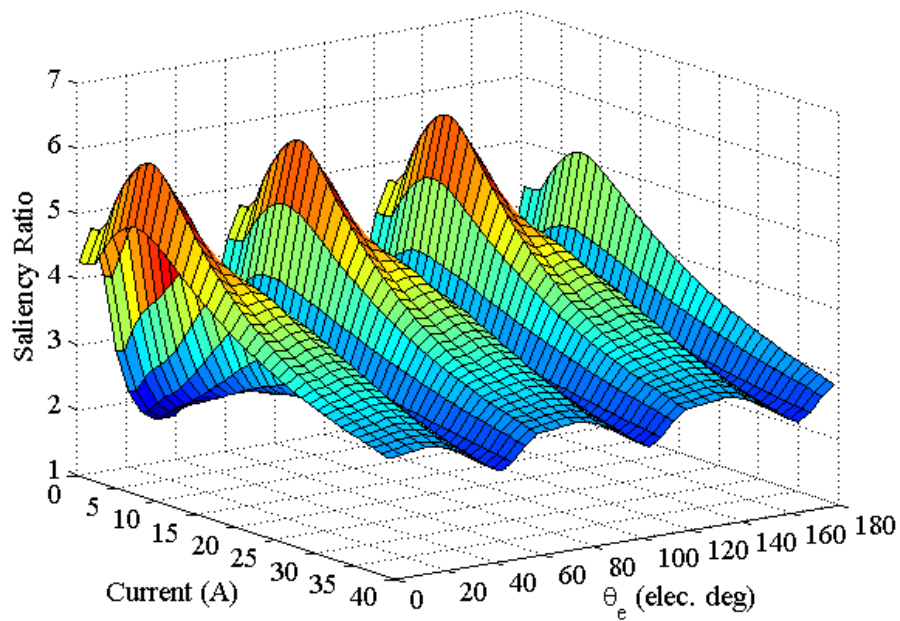
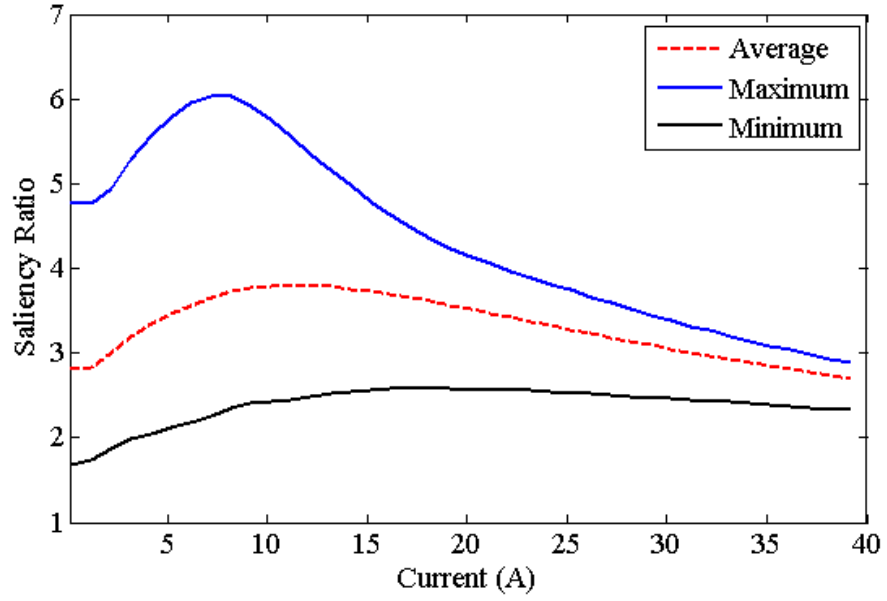
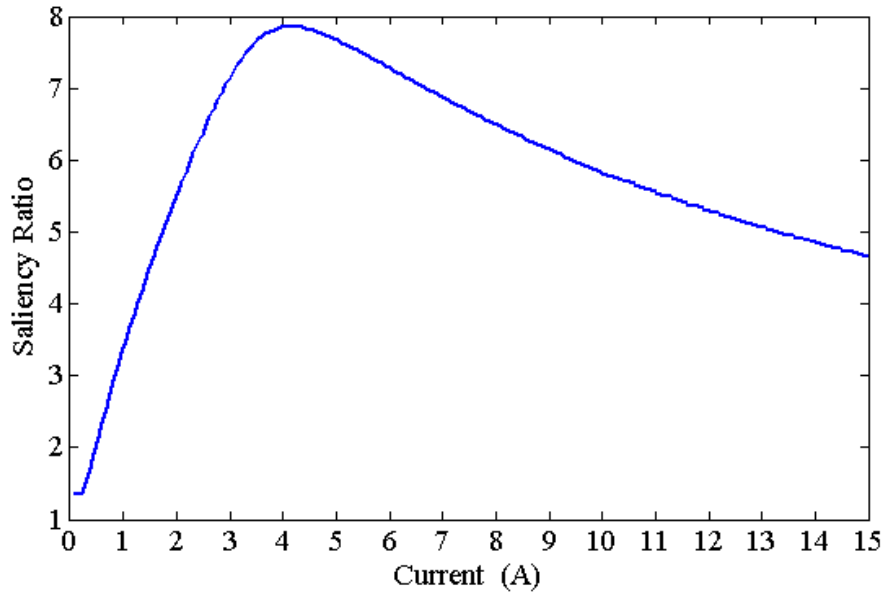


Figure 7.11: cSynRM - spatial variation of ξ_{true} with rotor angle

As can be seen from the figure, the variation in the saliency ratio due to the inductance harmonics is significant. Figure 7.12 shows the maximum, minimum and average saliency ratio as a function of current based on the saliency ratio surface data and Figure. 7.13 shows the saliency ratio as a function of current of the SynRM. The low saliency ratio at low current levels is due to the high q-axis inductance in this current range, this is before the radial and tangential ribs are saturated.

Figure 7.12: cSynRM - maximum, minimum and average ξ_{true} Figure 7.13: SynRM - ξ_{true} of the distributed winding motor

7.3.3 Summary

The odd harmonics of orders $6h \pm 1$ present in the phase flux linkages are transformed into the $dq0$ frame and maintain harmonics of the orders equal to $6h$. Therefore, contrary to standard use of conventional $dq0$ theory, the cSynRM exhibits orthogonal axis flux linkages that are dependent on rotor position and their variation with that position is significant. In this study, due to the sinusoidal nature of the applied currents, no additional current induced time harmonics are present and the $dq0$ flux linkage harmonics are carried into the orthogonal axis inductances of the machine. The largest variation is seen

in the unsaturated region of operation: this then tails off somewhat due to saturation in the main magnetic circuit. The variation in the cSynRM is much larger than in interior permanent magnet motors as the airgap in reluctance machines is smaller, allowing the harmonic fluxes to cross the airgap. This inductance variation induces a voltage in the dq frame voltage equations and it must be concluded that this affects the machine performance, the applicability of sensorless control and accuracy of dynamic simulations. This inductance variation (and corresponding flux linkage variation) must also have an implication on the machine electromagnetic torque - this is investigated later in this chapter. The dq transformation is usually applied with integral slot windings in mind, assuming no space harmonic content in the airgap. This transformation effectively reduces the spatially varying inductances to constants (neglecting saturation) attributed to the dq axes, this includes no spatial variation with the rotor angle. As with fractional slot concentrated windings high levels of space harmonics exist in the airgap and therefore a fundamental assumption of dq axis theory does, strictly, no longer apply. In machines with $q > 1$ the inductances L_d and L_q are constant and do not exhibit any spatial or temporal variation in linear or saturated machine operation. However, in machines with $q < 1$, such as the cSynRM, the inductances L_d and L_q are indeed dependant on rotor angle. Consequently, the machine's saliency ratio varies with rotor angle and the average saliency ratio over the period of rotation is required to be calculated to form a useful figure of merit.

7.4 Flux-Linkage Functions

There are machine models (IPM and SynRM) that incorporate saturation [8,9] and orthogonal axis cross coupling [10-11], which are shown to aid development of accurate sensorless control algorithms [12]. However, spatial variation, in order to accommodate spatially varying dq flux linkages, Ψ_d and Ψ_q in the cSynRM, is not found in the literature. The introduction of the cSynRM makes modification of the machine governing equations necessary in order to take the spatial effects into account. This section aims to go some way to achieving this. In this case the flux linkage function must be extended to a function of three variables and the equations of the dq theory relating to the synchronous reluctance motor modified accordingly. Table 7.2 outlines the flux linkage functions that relate to different models for the synchronous reluctance motor.

Model	Flux Linkage Function
With Saturation [3,4]	$\Psi_d = f(i_d)\Psi_q = f(i_q)$
With Cross-coupling [5-7]	$\Psi_d = f(i_d, i_q)\Psi_q = f(i_d, i_q)$
Rotor variation included	$\Psi_d = f(i_d, i_q, \theta)\Psi_q = f(i_d, i_q, \theta)$

Table 7.2: Flux linkage functional relationships

7.4.1 Reciprocity

In any following analysis assume a conservative system, *i.e.* iron loss in magnetic components is neglected and the following reciprocity condition must hold [13];

$$\frac{\partial \Psi_d(i_d, i_q, \theta)}{\partial i_q} = \frac{\partial \Psi_q(i_d, i_q, \theta)}{\partial i_d} \quad (7.8)$$

Thus the cross coupling, or mutual inductances between the two orthogonal axes are equal, $L_{dq} = L_{qd}$.

7.4.2 Cross Coupling vs Cross Saturation

Models for the synchronous reluctance machines with cross coupling and saturation are found in the literature. These are two 'cross-axis effects' between the orthogonal d and q axes;

- **Flux Linkage Cross Coupling** - flux generated by one axis current (d or q) links the other axis in a mutual inductance (cross coupling) manner.

$$\Psi_d(i_d, i_q, \theta) = L_{dd}(i_d, \theta) i_d + L_{dq}(i_q, \theta) i_q \quad (7.9)$$

$$\Psi_q(i_d, i_q, \theta) = L_{qq}(i_q, \theta) i_q + L_{qd}(i_d, \theta) i_d \quad (7.10)$$

- **Orthogonal Axis Cross Saturation** - the inductance in one axis is affected by the current in the other axis modifying the saturation level in that axis.

$$\Psi_d(i_d, i_q, \theta) = L_{dd}(i_d, i_q, \theta) i_d + L_{dq}(i_d, i_q, \theta) i_q \quad (7.11)$$

$$\Psi_q(i_d, i_q, \theta) = L_{qq}(i_d, i_q, \theta) i_q + L_{qd}(i_d, i_q, \theta) i_d \quad (7.12)$$

Both of these effects modify machine performance, and any of the two effects can be chosen to be modelled. These are not explored further here, only the spatial variation is investigated.

7.4.3 Inductance vs Flux Linkage

Usually, when modelling electrical machines the equations are written in terms of inductance [2,3,14,15]. However, when $\Psi = L(i_d, i_q, \theta) \cdot i$ the total derivative of the flux linkage and subsequent separation into the inductances to form an equation set that accounts for magnetic saturation, including cross saturation and the spatial variation, becomes a rather large set of equations. The dq axis voltage equations in terms of inductances are (neglecting spatial variation);

$$v_d = R i_d + \left(L_d + i_d \frac{\partial L_d}{\partial i_d} \right) \frac{di_d}{dt} + i_d \frac{\partial L_d}{\partial i_q} \frac{di_q}{dt} - i_q L_q \dot{\theta} \quad (7.13)$$

$$v_q = Ri_q + \left(L_q + i_q \frac{\partial L_q}{\partial i_q} \right) \frac{di_q}{dt} + i_q \frac{\partial L_q}{\partial i_d} \frac{di_d}{dt} + i_d L_d \dot{\theta} \quad (7.14)$$

The functional dependencies create additional terms, which results in an increased computational load and increased storage requirement in multidimensional lookup tables of data found by an increasing number of FEA studies. Models of this sort have been presented in the literature [16,17], however it is difficult to know if they have been applied wide scale in industry. It is the authors opinion is that it is preferable to form a model based on the maps of flux linkages only as all information can be encoded into a smaller set of lookup tables, increasing the efficiency of the model.

7.4.4 Flux Linkage Total Derivatives

The time rate of change of flux linkage as a function of three variables, as required in the machine circuit equation is expanded in the dq coordinate system as follows¹;

$$\dot{\Psi}_d(i_d, i_q, \theta) = \frac{\partial \Psi_d}{\partial i_d} \frac{di_d}{dt} + \frac{\partial \Psi_d}{\partial i_q} \frac{di_q}{dt} + \frac{\partial \Psi_d}{\partial \theta} \dot{\theta} \quad (7.15)$$

$$\dot{\Psi}_q(i_d, i_q, \theta) = \frac{\partial \Psi_q}{\partial i_d} \frac{di_d}{dt} + \frac{\partial \Psi_q}{\partial i_q} \frac{di_q}{dt} + \frac{\partial \Psi_q}{\partial \theta} \dot{\theta} \quad (7.16)$$

Magnetic energy is also converted into mechanical energy here and the partial derivatives containing the axis currents are the incremental inductances relating to the self and mutual inductances of the system. They can be determined numerically using the central difference method. With the total derivatives, the machine circuit equation must be modified accordingly as there will be additional terms in the dq axis voltage equations from the spatial variation terms $\frac{\partial \Psi_{d,q}}{\partial \theta} \dot{\theta}$.

7.4.5 Revision of SynRM abc -Frame Circuit Equations

In general for a synchronous machine, the fundamental circuit equation linking the terminal voltages, phase currents and flux linkages in the abc frame is a system of first-order differential equations in matrix form;

$$\mathbf{v}_{abc} = R_s \mathbf{i}_{abc} + \dot{\Psi}_{abc} \quad (7.17)$$

The non-linearities and spatial variation effects are considered in the Ψ_{abc} vectors;

$$\mathbf{v}_{abc} = \begin{bmatrix} u_a \\ u_b \\ u_c \end{bmatrix}; \quad \mathbf{i}_{abc} = \begin{bmatrix} i_a \\ i_b \\ i_c \end{bmatrix}; \quad \Psi_{abc} = \begin{bmatrix} \Psi_a(i_a, i_b, i_c, \theta) \\ \Psi_b(i_a, i_b, i_c, \theta) \\ \Psi_c(i_a, i_b, i_c, \theta) \end{bmatrix} \quad (7.18)$$

¹where $\left(\dot{f} = \frac{df}{dt} \right)$

The definition of $\Psi(i_a, i_b, i_c, \theta)$ allows construction of a non-linear model as the flux linkages are functions of both the stator currents and rotor position. The effects of saturation and other parasitic effects are included due to these current and position dependencies, however, knowledge of these functions is required in order for the model to be fruitful.

7.5 Modified dq Circuit Equations

With the general flux linkage function and the characteristics of the cSynRM machine requiring a spatially varying flux components in the synchronously rotating $dq0$ frame, the transformation of Eq. 7.17 into its $dq0$ equivalent form is performed by using the following transformation equations;²;

$$\mathbf{v}_{abc} = \mathbf{T}\mathbf{v}_{dq0}; \quad \mathbf{i}_{abc} = \mathbf{T}\mathbf{i}_{dq0}; \quad \Psi_{abc} = \mathbf{T}\Psi_{dq0} \quad (7.19)$$

$$\mathbf{v}_{dq0} = \begin{bmatrix} v_d \\ v_q \\ v_0 \end{bmatrix}; \quad \mathbf{i}_{dq0} = \begin{bmatrix} i_d \\ i_q \\ i_0 \end{bmatrix}; \quad \Psi_{dq0} = \begin{bmatrix} \Psi_d(i_d, i_q, i_0, \theta) \\ \Psi_q(i_d, i_q, i_0, \theta) \\ \Psi_0(i_d, i_q, i_0, \theta) \end{bmatrix} \quad (7.20)$$

With mathematical manipulation, the resulting matrix equation is written for a symmetrical winding;

$$\begin{bmatrix} v_d \\ v_q \\ v_0 \end{bmatrix} = R \begin{bmatrix} i_d \\ i_q \\ i_0 \end{bmatrix} + \begin{bmatrix} \frac{\partial \Psi_d}{\partial i_d} & \frac{\partial \Psi_d}{\partial i_q} & \frac{\partial \Psi_d}{\partial i_0} \\ \frac{\partial \Psi_q}{\partial i_d} & \frac{\partial \Psi_q}{\partial i_q} & \frac{\partial \Psi_q}{\partial i_0} \\ \frac{\partial \Psi_0}{\partial i_d} & \frac{\partial \Psi_0}{\partial i_q} & \frac{\partial \Psi_0}{\partial i_0} \end{bmatrix} \frac{d}{dt} \begin{bmatrix} i_d \\ i_q \\ i_0 \end{bmatrix} + \frac{d\theta}{dt} \left\{ \begin{bmatrix} \frac{\partial \Psi_d}{\partial \theta} \\ \frac{\partial \Psi_q}{\partial \theta} \\ \frac{\partial \Psi_0}{\partial \theta} \end{bmatrix} + \begin{bmatrix} -\Psi_q \\ \Psi_d \\ 0 \end{bmatrix} \right\} \quad (7.21)$$

Here $R_s = R_a = R_b = R_c$. The equation is greatly simplified if the machine winding is balanced and star-connected, as at the star-point: $\sum i = 0$ and $i_0 = f(i_a + i_b + i_c) = 0$, the machine circuit matrix equation in the dq frame can be contracted into the form³;

$$\mathbf{v}_{dq} = R\mathbf{i}_{dq} + \dot{\Psi}_{dq}(i_d, i_q, \theta) + \dot{\theta}\Lambda\Psi_{dq}(i_d, i_q, \theta) \quad (7.22)$$

Thus the following scalar circuit equations for the dq axes are extracted from the

$$^2\text{The Park transformation is written; } \mathbf{T} = \begin{bmatrix} \cos(\theta) & -\sin(\theta) & \sqrt{\frac{1}{2}} \\ \cos(\theta - \frac{2\pi}{3}) & -\sin(\theta - \frac{2\pi}{3}) & \sqrt{\frac{1}{2}} \\ \cos(\theta + \frac{2\pi}{3}) & -\sin(\theta + \frac{2\pi}{3}) & \sqrt{\frac{1}{2}} \end{bmatrix}$$

$$^3\text{The matrix } \Lambda = \begin{bmatrix} 0 & -1 \\ 1 & 0 \end{bmatrix} \text{ is the rotation matrix, cross-linking the axes.}$$

matrix;

$$v_d = Ri_d + \frac{\partial \Psi_d}{\partial i_d} \frac{di_d}{dt} + \frac{\partial \Psi_d}{\partial i_q} \frac{di_q}{dt} + \dot{\theta} \left(\underbrace{\frac{\partial \Psi_d}{\partial \theta}}_{\text{Spatial}} - \Psi_q \right) \quad (7.23)$$

$$v_q = Ri_q + \frac{\partial \Psi_q}{\partial i_d} \frac{di_d}{dt} + \frac{\partial \Psi_q}{\partial i_q} \frac{di_q}{dt} + \dot{\theta} \left(\underbrace{\frac{\partial \Psi_q}{\partial \theta}}_{\text{Spatial}} + \Psi_d \right) \quad (7.24)$$

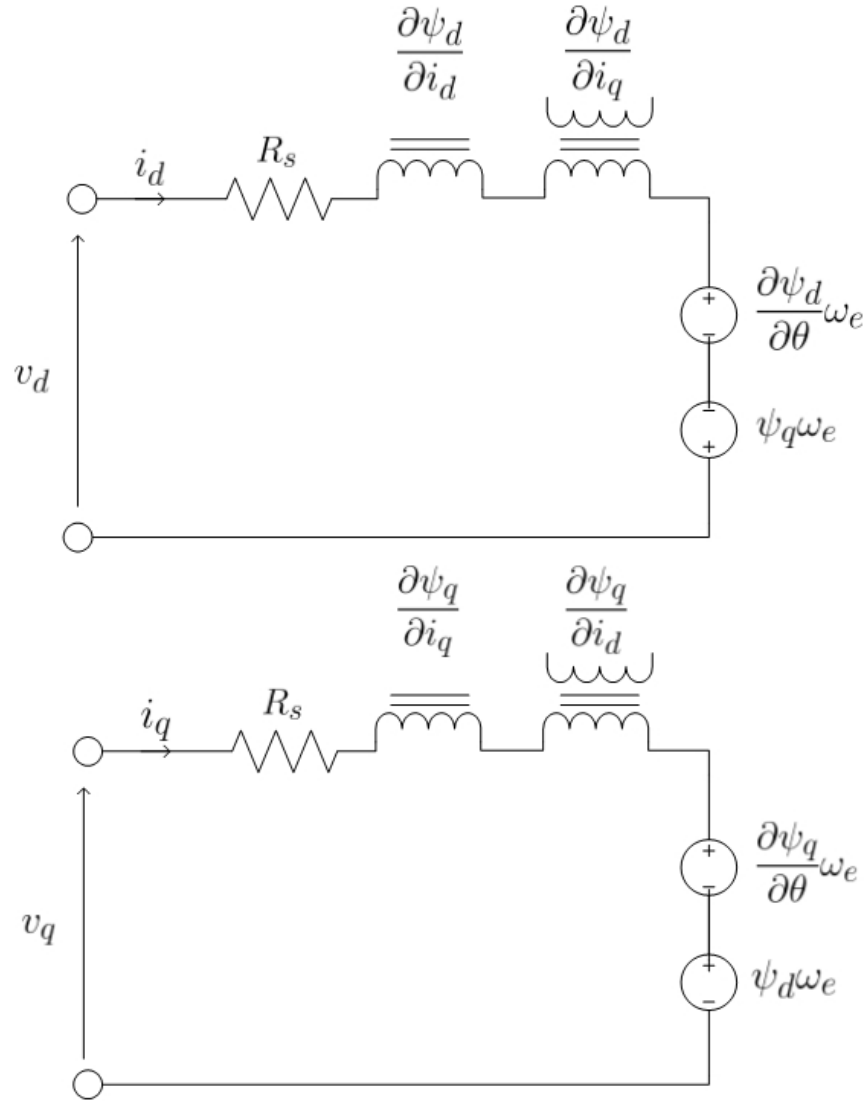
These equations contain additional terms involving spatial variation to the conventional equations previously presented in Chapter 1, consequently more information is encoded into them. These equations form a more advanced and complete model in the $dq0$ reference frame, applicable to the cSynRM. The equations reduce to that of the conventional equations if the spatial terms go to zero - they are then applicable for the SynRM topology. The spatial variation terms are either very small or zero in the SynRM topology.

7.5.1 Orthogonal Axis Equivalent Circuits

Equivalent circuit models are useful in prediction of machine performance [14] and visualization of machine circuit features, and they are also used to implement machine models in simulation software such as MATLAB/Simulink [15]. The machine equivalent models allow dynamic simulation for steady state and transient operation. However, as spacial variation is included in the new model, the direct and quadrature axis equivalent circuits must be redrawn to take this into account. Figure. 7.14 shows the d - and q -axis equivalent circuit diagrams taking into account axis-self and cross coupling inductances as well as the spatial variation terms developed in this chapter. These circuits incorporate both the cross coupling and spacial variation terms and saturation is also taken into account by the partial derivatives. For a sinusoidal winding, as in the SynRM, the equivalent circuits are reduced to the conventional circuit diagrams by dropping the spatial variation dependant circuit elements.

7.5.1.1 Implications for the cSynRM

In the case of the synchronous reluctance motor, as the airgap length is small due to its inverse relation with the machine magnetizing inductance, power factor and torque capability, the effects caused by the higher order MMF harmonics are increasingly pronounced on the dq axis inductances. In relation to the developed circuit equations Eq. 7.23 and Eq. 7.24, it is evident that this spatial inductance variation gives rise to additional induced voltages due to the partial derivative terms. As the variation is a higher order harmonic than the fundamental, additional harmonic content is found in the phase and line voltages in the abc frame; this could have complications for the attached voltage source inverter,

Figure 7.14: Modified dq equivalent circuits for the cSynRM

such as electromagnetic interference issues, possible control difficulty and an increased peak line voltage level. It was previously stated that it would be advantageous if the inductance variation could be neglected, as would be the case as in the SynRM. The harmonic induced voltage can be approximated due to the d -axis flux linkage variation (assuming fundamental only) of the prototype machine at rated operating current and speed, operating under maximum torque per Ampere control;

$$V_{ind,d} \approx \frac{d\theta_e}{dt} \left(\frac{d\Psi_{d1}}{d\theta_e} \right) \approx 2\pi f \frac{d}{d\theta_e} \{ \Delta\Psi_{d1} \sin(k\theta_e) \} \quad (7.25)$$

$$\therefore V_{ind,d(rms)} \approx \frac{2\pi f k \Delta\Psi_{d1}}{\sqrt{2}} = 39.9V \quad (7.26)$$

Thus an RMS voltage of around 40V is induced in the dq frame due to the inductance variation in the d -axis, equating to around 9.5% of the line voltage, this therefore cannot be ignored. The stator resistance voltage drop is calculated to be 3.29V in the case of the prototyped cSynRM, as a comparison.

7.6 Electromagnetic Torque Expressions

The mechanical model relating to the electromagnetic torque $\tau_{em(dq)}$ of the cSynRM is described by the following differential equation [18];

$$J \frac{d^2 \theta}{dt^2} + B \frac{d\theta}{dt} + \tau_l = \tau_{em(dq)}(i_d, i_q, \theta) = \tau_0 + \tau(\theta) \quad (7.27)$$

Where J is the polar moment of inertia of the system, B the friction coefficient and τ_l the load torque. In order to obtain accurate performance predictions during steady state and in transients, the electromagnetic torque $\tau_{em(dq)}(i_d, i_q, \theta)$ must be an accurate representation. Mean torque developed is important as well as the torque ripple as this can lead to speed ripple, depending upon the inertia of the machines rotor. Correct development of the expression of electromagnetic torque is therefore important in the cSynRM, taking into account the spatial variations in the $dq0$ frame and therefore correctly describing both the mean torque τ_0 and the torque ripple $\tau(\theta)$ components.

7.6.1 Development of Torque Expression

To obtain an expression for the electromagnetic torque in the dq reference frame, multiplication of the dq axis voltage equation by the respective current leads to an expression for the machine power [2,19];

$$p_m = v_d i_d + v_q i_q = p_{loss} + p_{stored} + p_{mech} \quad (7.28)$$

As it is the mechanical power developed by the machine that is translated into torque, interest is in terms that contain only $\frac{d\theta}{dt}$, thus the torque per pole pair can be written as;

$$\frac{\tau_{em(dq)}}{p} = i_d \left\{ \frac{\partial \Psi_d}{\partial \theta} - \Psi_q \right\} + i_q \left\{ \frac{\partial \Psi_q}{\partial \theta} + \Psi_d \right\} \quad (7.29)$$

This takes into account the spatial variation of the dq flux linkages. Expressions for the loss and stored power can also be derived easily but are of no concern here. It is possible to write the torque expression in a more familiar form;

$$\tau_{em(dq)} = p \left\{ \underbrace{(\Psi_d i_q - \Psi_q i_d)}_{\alpha} + \underbrace{i_d \frac{\partial \Psi_d}{\partial \theta} + i_q \frac{\partial \Psi_q}{\partial \theta}}_{\beta} \right\} = p \Psi_{dq} \times \mathbf{i}_{dq} + p \mathbf{i}_{dq}^T \frac{\partial \Psi_{dq}}{\partial \theta} \quad (7.30)$$

Now, contrary to the conventional equations, a new term denoted by β has arisen; this takes into account spatial variations of the orthogonal axis flux linkages. The conventional component α remains in the expression for the electromagnetic torque, but now α also varies spatially and is no longer constant and therefore no longer providing a smooth DC torque. If the flux linkages are DC valued, the partial derivatives go to zero, the

conventional torque equation is recovered, and the term denoted by α once again becomes a smooth constant DC valued function. This expression shows that the torque is not only modulated in the conventional sense but additional torque components are produced by the spatially varying orthogonal axis flux linkages.

7.6.2 Expansion To Machine Inductances

It follows that the dq flux linkages can be written in terms of the inductance matrix \mathbf{L}_{dq} and the current vector \mathbf{i}_{dq} ;

$$\Psi_{dq} = \mathbf{L}_{dq} \mathbf{i}_{dq} \quad (7.31)$$

Thus, by using Eq. 7.46 and 7.47, the electromagnetic torque per pole pair can be written in the form;

$$\frac{\tau_{em(dq)}}{p} = \mathbf{L}_{dq} \mathbf{i}_{dq} \times \mathbf{i}_{dq} + \mathbf{i}_{dq}^T \frac{\partial \mathbf{L}_{dq}}{\partial \theta} \mathbf{i}_{dq} \quad (7.32)$$

Where \mathbf{i}_{dq}^T is the transpose of the current vector. This matrix equation can be expanded into scalar form;

$$\frac{\tau_{em(dq)}}{p} = \underbrace{L_{dd}i_d i_q - L_{qq}i_d i_q - L_{qd}i_d^2 + L_{dq}i_q^2}_{\alpha} + \overbrace{\frac{\partial L_{dd}}{\partial \theta} i_d^2 + \frac{\partial L_{qd}}{\partial \theta} i_d i_q + \frac{\partial L_{dq}}{\partial \theta} i_d i_q + \frac{\partial L_{qq}}{\partial \theta} i_q^2}^{\beta} \quad (7.33)$$

This allows calculation of the torque in the dq frame that includes space harmonic effects and cross coupling in the synchronous reluctance machine. This is only workable if reliable data of the inductance characteristics as a function of rotor angle, current and current angle can be obtained. It requires the knowledge of the principal orthogonal axis inductances as well as the cross-coupling inductances. These are not readily obtained and would require numerous multidimensional lookup tables to be stored in simulation packages derived from FEA studies or in memory in a physical drive. Otherwise, the torque equation in terms of flux linkages is much easier to use in dynamic calculations as the number of lookup tables is significantly reduced. Equation 7.33 shows that torque is produced by not only the conventional components of inductance, but that the cross coupling inductances and the spatial variance introduces additional components through the partial derivatives if the inductances are non steady DC valued. The dq inductances are conventionally defined to be constant, providing a decoupling mechanism whereby we eliminate any space-time varying values in the machine. However, now, as there are harmonics, the flux linkages and inductances are not constant in this reference frame, but will vary slowly, depending upon the harmonic content. Again, usually the partial derivatives will be zero for constant inductances, but here they can have a value which

either increases or diminishes the torque mean value and also causes torque oscillations. The conventional torque equation for the synchronous reluctance motor can be recovered if the cross coupling terms and the partial derivatives go to zero, leaving;

$$\frac{\tau_{em(dq)}}{p} = (L_{dd} - L_{qq}) i_d i_q \quad (7.34)$$

Which is well known and is presented as part of conventional theory in Chapter 1. All torque expressions henceforth will be expressed in terms of the flux linkages.

7.6.3 Torque Harmonics

In terms of the harmonic content in the torque waveform of the machine, it is obvious that the torque can be expressed;

$$\tau_{em(dq)}(\theta) = \tau_0 + \tau(\theta) \quad (7.35)$$

Here, τ_0 is the fundamental DC component of torque produced by the fundamental flux linkage interacting with the fundamental current. The $\tau(\theta)$ contains harmonics, producing torque oscillations by the interaction of the harmonic flux linkages of orders $6k$ with the fundamental current. If time harmonics in the current existed, there would be other interactions present. Therefore, it can be concluded that the torque harmonics are of the orders $6k$.

7.6.4 Other Methods of Torque Calculation

The derived torque expression for the cSynRM takes into account the spatial variation when calculating the torque in the dq frame, however, the torque can be calculated by other techniques. As described in Chapter 6, the torque can be calculated by the finite element method described by Maxwell stresses in the airgap of the machine [5];

$$\tau_{em(FEA)} = \frac{r^2}{\mu_0} \int_0^{l_a} \int_0^{2\pi} B_\theta B_r d\theta dz \quad (7.36)$$

Where $\int_0^{l_a} \int_0^{2\pi} d\theta dz$ is a integral over the rotor surface. This numerical method through finite elements incorporates all non-linear and parasitic phenomena. The torque in the dq frame by using Eq. 7.29 and neglecting the partial derivatives, which reduces to the conventional dq model;

$$\tau_{em(DQ)} = \Psi_{dq} \times \mathbf{i}_{dq} = \Psi_d i_q - \Psi_q i_d = \alpha \quad (7.37)$$

The finite element method is the most accurate as this directly calculates electromagnetic torque based on the airgap fields. The FEA calculation and the conventional dq expressions can be compared to the developed torque equation, Eq. 7.29 in order to validate it and observe its accuracy.

7.6.4.1 Numerical Derivatives

The numerical evaluation of derivatives is performed using the central difference method. The torque equation, Eq. 7.29, is numerically evaluated by the following expression [20];

$$\tau_{em(dq)}^n = (\Psi_d^n i_q - \Psi_q^n i_d) + i_d \frac{\Psi_d^{n+1} - \Psi_d^{n-1}}{2\Delta\theta} + i_q \frac{\Psi_q^{n+1} - \Psi_q^{n-1}}{2\Delta\theta} \quad (7.38)$$

Using the central difference method provides a more accurate approximation of the derivative by eliminating the first order errors. It also eliminates any phase shift when calculating the derivatives.

7.6.5 Comparison of Torque Calculations

Here the torque equations, Eqns. 7.29, 7.36 and 7.37 are compared. The results are based upon the rated operating point of the prototyped cSynRM machine with sinusoidal currents applied to the phase windings, the flux linkages calculated through finite element studies and stored in lookup tables in MATLAB. The *abc* frame flux linkages are transformed using the Park transform into the *dq0* frame, as in Section 7.3. Figure 7.15 shows the resultant torque per pole pair waveform of $\Psi_d i_q - \Psi_q i_d$ for the machine, equivalent to the conventional *dq* theory torque expression.

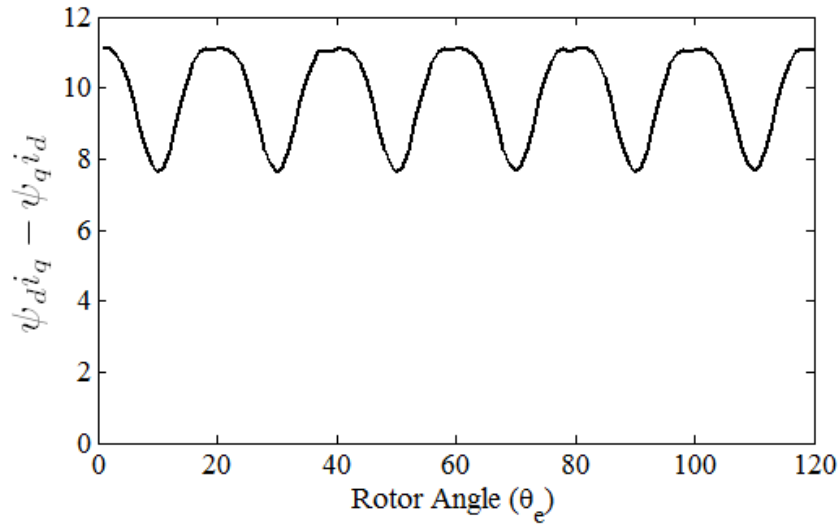
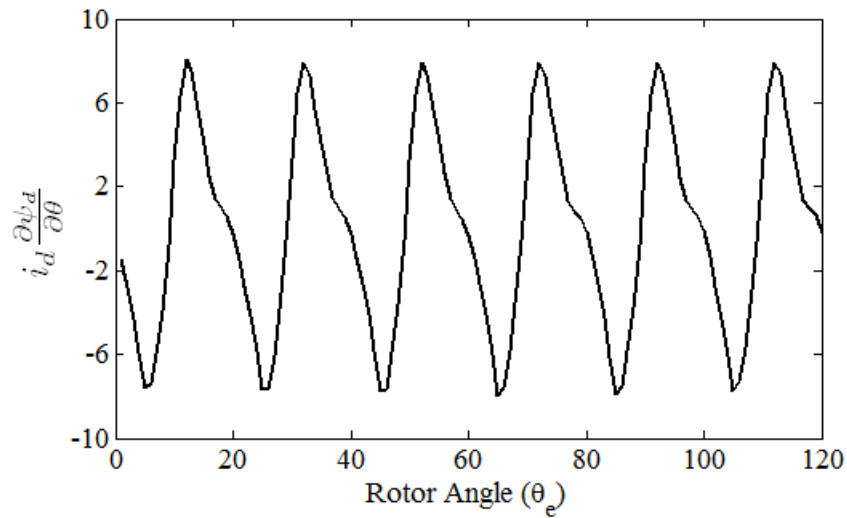
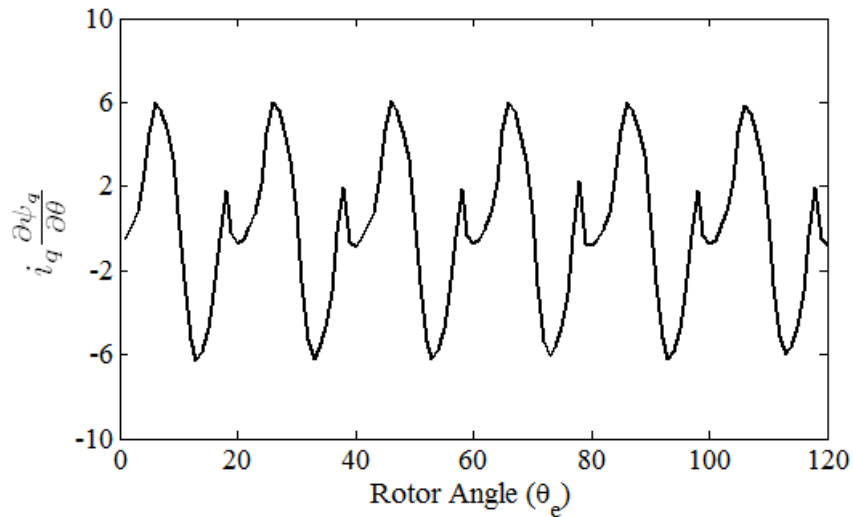


Figure 7.15: Torque per pole pair using only $\Psi i_q - \Psi_q i_d$

As the flux linkages are no longer single valued, the $\Psi i_q - \Psi_q i_d$ term does no longer yield a smooth torque, but contains oscillation due to the harmonic content in the *dq0* flux linkages, showing the torque quality of the machine to a certain degree. The main harmonic in the torque waveform is clearly the 6th harmonic, as expected. In order to predict the torque waveform more accurately, the derived partial derivative terms must be accounted for in the torque expression. Figures 7.16 and 7.17 show the individual torque contributions from the terms $i_d \frac{\partial \Psi_d}{\partial \theta}$ and $i_q \frac{\partial \Psi_q}{\partial \theta}$.

Figure 7.16: Torque due to the d -axis flux linkage spatial partial derivativeFigure 7.17: Torque due to the q -axis flux linkage spatial partial derivative

As is clearly seen from the figures, the partial derivative terms contribute large oscillatory torques to the resultant torque developed in the machine. They effectively modulate the conventional torque term about its mean value, affecting the torque quality and to a much lesser extent the mean torque. Figure 7.18 shows the contribution from $\alpha = \Psi i_q - \Psi_q i_d$, the sum $\beta = i_d \frac{\partial \Psi_d}{\partial \theta} + i_q \frac{\partial \Psi_q}{\partial \theta}$ and the resultant torque waveform $= p(\alpha + \beta)$.

It is clear that the partial derivative terms are not negligible and thus must be included for accurate performance prediction in dynamic simulation or advanced drive systems. It is clear from the figures that the d -axis flux variation torque produces a slightly larger torque oscillation component and the partial derivative terms influence the torque ripple more than the variation in the conventional term. The partial derivative torques also are asymmetric about the x -axis and thus they contribute to mean torque over an electrical cycle, but only by a very small amount. It is observed from Figure 7.16 and Figure 7.17

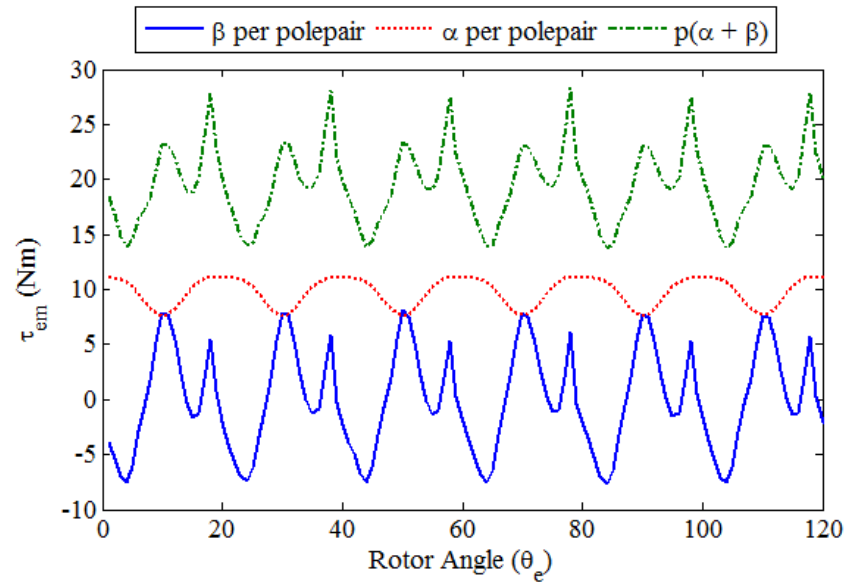


Figure 7.18: Torque component waveforms

that the large peaks in the partial derivative torques are largely out of phase with respect to the axes, diminishing their impact on torque oscillation. The mean torque contribution of the conventional term is 19.65Nm and the mean torque of the d - and q -axis partial derivatives is -0.0028 Nm and -0.0162 Nm respectively. So, the partial derivatives mainly contribute to torque ripple in the cSynRM, degrading torque quality. Figure 7.19 shows the comparison between the conventional Eq. 7.37, the developed Eq. 7.29 and the FEA calculated torque via the Maxwell Stress Tensor method. The conventional theory with single valued axis flux linkages (or axis inductances) with respect to rotor angle would yield a single valued torque waveform over the rotor rotation cycle. Figure 7.19 clearly shows the the developed equation models the instantaneous electromagnetic torque to a greater degree of accuracy than that of the conventional equation, replicating more harmonic content, which is derived from the new partial derivative terms. Therefore, it is reinforced that the spatial variation of inductance with rotor angle cannot be ignored. In the conventional dq model, with static values of L_d and L_q , the torque would be represented by a horizontal straight line with no variation over the electrical cycle. There is some discrepancy between the FEA torque waveform based on Maxwellian stress and the dq calculated method, this is most likely to be due to the fundamental differences in calculation method, especially when the FEA uses discrete volume integrals in the air-gap to evaluate the stress and then the torque. It is clear however, that the derived dq torque equation follows this FEA result relatively closely compared to any other method - especially conventional single valued theory.

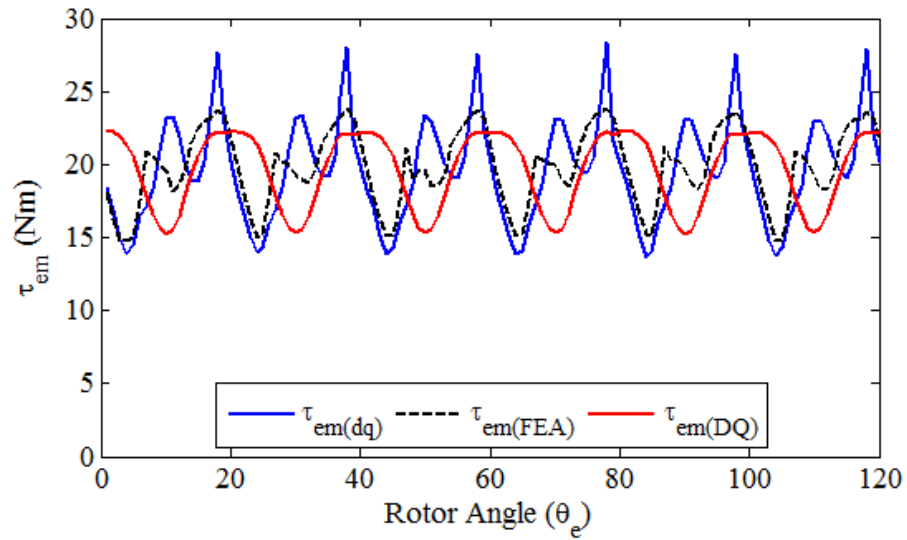


Figure 7.19: Torque waveform comparison (computed results)

7.6.6 Summary

It is important to develop complete torque equations for the cSynRM machine for accurate performance calculation. A torque equation is derived from the dq frame power balance that includes spatial variation terms and does not assume DC valued orthogonal axis flux linkages or inductances - the developed torque equation reduces to the conventional equation if the flux linkages are assumed as DC quantities. Based on the new torque equation it is clear that cross axis coupling contribute to torque production and spatial variation of inductances contributes to torque oscillation. The partial derivative terms due to the spatial variation cannot be neglected in the cSynRM; their main contribution is to reduce torque quality in the machine. The developed torque equation with the addition of the partial derivatives provides a much more accurate representation of the torque waveform when compared to the finite element derived waveform - this shows that the partial derivative terms are significant in performance prediction and that the spatial variation in either flux linkages or inductances produces parasitic torque quality issues in the cSynRM. The developed equation could be implemented in a MATLAB-Simulink model, along with the new orthogonal axis equivalent circuit models and equations, this is an area of further investigation.

7.7 Applicability of DQ Theory

In the steady state of machine operation, the conventional phasor diagram generally presented for the synchronous reluctance machine requires single valued quantities in the rotating reference frame. This allows constant length phasors to be drawn and therefore all quantities rotate with constant magnitude. If the orthogonal axis inductances do not maintain a single value, the phasors magnitude varies with rotor position, of course

this introduces new components into the phasor diagram also - as indicated in Section 7.5.1 by the orthogonal axis equivalent circuit diagrams. The equations derived from the phasor diagram, such as the saliency ratio and the machine power factor also require single valued functions across all rotor angles. This means that the dq theory derived from the phasor diagram or indeed the phasor diagram itself is not directly applicable without modification. As an alternative to modifying the existing equations, it is suggested here that the mean value of any varying quantity be taken and substituted into the dq equations. As an example, here the mean values of the rotor position dependant quantities are used in order to calculate the machine's saliency ratio, its mean torque capability and its power factor. They are then compared to that of FEA calculations. The equations used in the performance calculations are;

$$\xi_{eff} = \frac{\overline{L_d}}{\overline{L_q}} \quad (7.39)$$

$$\cos(\varphi) = \frac{\xi_{eff} - 1}{\sqrt{2}} \sqrt{\frac{1}{1 + \xi_{eff}^2}} \quad (7.40)$$

$$t_{em} = p (\overline{L_d} - \overline{L_q}) i_s^2$$

Where ξ_{eff} is the effective saliency ratio, $\overline{L_d}$ is the mean direct axis inductance, $\overline{L_q}$ is the mean quadrature axis inductance, $\cos(\varphi)$ the machine power factor. The terms t_{em} is the machine electromagnetic torque capability and i_s is the stator phase current. The machine is simulated and calculated for its rated operating point with $i_s = 21.2\text{A}$ under maximum torque per ampere control (equal d - and q -axis currents). Table 7.3 shows the calculated results in comparison to the FEA derived results. The 'Averaged dq ' results are obtained by calculating the mean values of the required quantities based on the FEA derived flux linkages and subsequent inductances from Figures 7.7, 7.8 and 7.11.

	Averaged dq	FEA
Saliency Ratio, ξ_{eff}	3.55	3.11
Power Factor, $\cos(\varphi)$	0.488	0.455
Torque, t_{em}	21.39	21.9

Table 7.3: Machine performance comparison between averaged dq and FEA

As the harmonic variation components are relatively small compared to the fundamental DC component resulting from the fundamental and contribute mainly an oscillatory response - it is apparent that the effects in terms of calculating steady state performance characteristics of the machine are 'averaged out' and thus the dq prediction for mean torque, machine power factor and its effective saliency ratio are relatively accurate. In control schemes however, this luxury may not be able to be used as instantaneous control is required.

7.8 Conclusion

The MMF profile in electrical machines with short pitched coils indicated that both odd and even harmonics can be present, as in the developed cSynRM machine. These harmonics can have large magnitudes and therefore parasitic effects are amplified in the cSynRM compared to that of the SynRM with distributed windings. Despite the existence of even airgap B-field harmonics, the phase flux linkages can only contain odd harmonics as the even harmonics cancel due to symmetry and are therefore not present in any voltage waveforms - they are symmetrical waveforms. Large magnitude odd harmonics can still exist in the flux linkages of the cSynRM, in contrast to the SynRM which has near sinusoidal flux linkages and voltages. On transformation of the flux linkages into the rotating dq reference frame, the 5th and 7th harmonics both manifest 6th order harmonics, one forwards rotating and one backwards rotating, in the flux linkages. Large oscillations in the dq flux linkages are observed in the cSynRM whilst the transformed flux linkages for the SynRM remain essentially DC valued - a contrast between the machines. The flux linkage harmonics give rise to spatially varying direct and quadrature axis inductances in the cSynRM machine and therefore based on conventional theory the machine's saliency ratio also varies with rotor position in this case. The mean value of the saliency ratio function is the effective saliency ratio of the machine. The distributed winding machine (conventional SynRM) has constant inductances with rotor position in the dq frame and therefore a constant saliency ratio. Variation in the dq flux linkages and inductances contravenes the fundamental assumptions of the dq theory and transformation - the machine equations and corresponding equivalent circuit diagrams must be modified to reflect the spatial variation. The modified circuit equations show that the spatial variation terms provide a reasonable contribution to machine dynamics and therefore cannot be ignored in any dynamic simulation of the cSynRM. The developed electromagnetic torque is no longer governed by conventional expressions and again must be modified. Torque harmonic ordinates follow that of the flux linkage and inductance harmonics; it is shown that the derived spatial partial derivative terms contribute largely to the machine torque ripple. Finally it is shown that the developed electromagnetic torque equation models the instantaneous torque more accurately than the conventional equations and follows the FEA results reasonably well. The developed circuit equations and electromagnetic torque expression take into account the additional variation in the machine parameters and can be applied to dynamic simulation and controller development which is an area of further research.

7.9 References

1. P.C. Krause, 'Electromechanical Motion Devices', Wiley-Blackwell; 2nd Edition (27 July 2012)
2. I Boldea, 'Reluctance Synchronous Machines and Drives', Clarendon Press, 1996
3. Honsinger, V.B., "The Inductances L_d and L_q of Reluctance Machines," Power Apparatus and Systems, IEEE Transactions on , vol.PAS-90, no.1, pp.298,304, Jan. 1971
4. Bianchi, N.; Bolognani, S.; Pr , M.D.; Grezzani, G., "Design considerations for fractional-slot winding configurations of synchronous machines," Industry Applications, IEEE Transactions on , vol.42, no.4, pp.997,1006, July-Aug. 2006
5. Juha Pyrh nen, 'Design of Rotating Electrical Machines', Wiley-Blackwell, 2008
6. Sang-Hyub Han; Tack-Hyun Jo; Jong-Hyoung Park; Heung-Geun Kim; Tae-Won Chun; Eui-Cheol Nho, "Dead time compensation for grid-connected PWM inverter," Power Electronics and ECCE Asia (ICPE & ECCE), 2011 IEEE 8th International Conference on , vol., no., pp.876,881, May 30 2011-June 3 2011
7. Ewald F. Fuchs and Mohammad A.S. Masoum , 'Power Quality in Power Systems and Electrical Machines', Elsevier, 2008
8. Zengcai Qu; Tuovinen, T.; Hinkkanen, M., "Inclusion of magnetic saturation in dynamic models of synchronous reluctance motors," Electrical Machines (ICEM), 2012 XXth International Conference on , vol., no., pp.994,1000, 2-5 Sept. 2012
9. Gerada, C.; Bradley, K.J.; Sumner, M.; Asher, G., "Non-linear dynamic modelling of vector controlled PM synchronous machines," Power Electronics and Applications, 2005 European Conference on , vol., no., pp.10 pp.,P.10, 0-0 0
10. Pacas, M.; Morales, R., "A predictive torque control for the synchronous reluctance machine taking into account the magnetic cross saturation," Industrial Electronics Society, 2005. IECON 2005. 31st Annual Conference of IEEE , vol., no., pp.6 pp.,, 6-10 Nov. 2005
11. Morales-Caporal, R.; Pacas, M., "Impact of the magnetic cross-saturation in a sensorless Direct Torque controlled Synchronous Reluctance Machine based on test voltage signal injections," Industrial Electronics, 2008. IECON 2008. 34th Annual Conference of IEEE , vol., no., pp.1234,1239, 10-13 Nov. 2008
12. Guglielmi, P.; Pastorelli, M.; Vagati, A., "Impact of cross-saturation in sensorless control of transverse-laminated synchronous reluctance motors," Industrial Electronics, IEEE Transactions on , vol.53, no.2, pp.429,439, April 2006
13. Melkebeek, J.A.; Willems, J.L., "Reciprocity relations for the mutual inductances between orthogonal axis windings in saturated salient-pole machines," Industry Applications, IEEE Transactions on , vol.26, no.1, pp.107,114, Jan/Feb 1990
14. Slemon, G.R., "Equivalent Circuits for Cylindrical-Rotor, Reluctance, and Salient-Rotor Synchronous Machines," Power Apparatus and Systems, Part III. Transactions of the American Institute of Electrical Engineers , vol.81, no.3, pp.219,224, April 1962
15. <http://www.mathworks.co.uk/help/physmod/sps/powersys/ref/permanentmagnetsynchronousmachine.html>: Accessed 20/05/2014 8:21.am

16. Jong-Bin Im; Wonho Kim; Kwangsoo Kim; Chang-Sung Jin; Jae-Hak Choi; Ju Lee, "Inductance Calculation Method of Synchronous Reluctance Motor Including Iron Loss and Cross Magnetic Saturation," *Magnetics, IEEE Transactions on* , vol.45, no.6, pp.2803,2806, June 2009
17. Kilthau, A.; Pacas, J.M., "Appropriate models for the control of the synchronous reluctance machine," *Industry Applications Conference, 2002. 37th IAS Annual Meeting. Conference Record of the* , vol.4, no., pp.2289,2295 vol.4, 13-18 Oct. 2002
18. 2. Gieras, Jacek F. Permanent magnet motor technology: design and applications. CRC press, 2002
19. P. Vas, *Sensorless Vector and Direct Torque Control*, Oxford University Press, 1998
20. K. F. Riley, M. P. Hobson, S. J. Bence, 'Mathematical Methods for Physics and Engineering (3rd edition): A Comprehensive Guide', Cambridge University Press, 2006

Chapter 8

Conclusion and Further Work

The main aim of this work was to conceive and design a novel synchronous reluctance motor topology that improves upon the current technology and disseminate that research. The key objectives of the work to achieve this aim were; to perform a literature review and develop a concept motor topology in an area that has not been widely researched, produce a machine design based upon that concept leading to the manufacture and assembly of a prototype machine for experimental validation. Therefore, in this thesis, the fractional slot concentrated winding synchronous reluctance machine with segmental stator concept is explored and developed resulting in the experimental validation of a designed prototype motor, meeting the aims and objectives of the research project. The literature review covers current technology and surrounding material, identifying the general lack of research in synchronous reluctance technology, compared to other machine types and finds that almost exclusively the synchronous reluctance motor, as found in the literature, employ polyphase distributed windings which is the standard construction for industrial motors, including the traditional induction motor. Research into the synchronous reluctance motor in the literature typically focuses on the rotor design of such machines. It was noted that the switched reluctance machine, as well as modern low speed permanent magnet machines are found to enjoy benefits attributed to fractional slot concentrated windings. The work contained in this thesis presents the concept, design, analysis, manufacture and experimental validation of a fractional slot concentrated wound synchronous reluctance machine with segmental stator. The work in this thesis contributes to the understanding of synchronous reluctance motor technology, particularly when equipped with fractional slot concentrated windings - with a novel machine presented and compared with existing synchronous reluctance and induction motor technology. Insights gained into the parasitic effects introduced by adopting single tooth span coils in this type of machine are also explored as part of the machine's analysis. The prototype four pole six slot motor utilizes a segmented core-back structure and tooth-wound stator coils, obtaining a high slot fill factor and high efficiency. Novel FEA post-processing techniques have been developed for machine analysis and more applicable d - q equivalent circuits have been derived to take into account the spatially varying inductance characteristics of the cSynRM topology. The

key advantages of adopting fractional slot concentrated windings and segmental stators in synchronous reluctance machines are;

- Improved slot fill factors
- Increased torque density
- High efficiency machines
- Ease of stator coil winding
- Improved thermal properties

The main drawbacks can be considered to be;

- Increased space harmonic effects
- Lower power factor
- Higher torque ripple
- Increased leakage inductance

Of the advantages, the ability to increase the slot fill factor to 60% or higher is key. Short end turns with single tooth coils and high fill factors facilitate low copper losses, which are the dominant loss mechanism in low speed synchronous reluctance motors - such as those used in industry. This thesis has presented an introduction to the cSynRM machine topology and presents a list of topics of future research at the end of this chapter.

8.1 General Conclusions

In the development of the presented cSynRM motor topology, each chapter in this thesis has its own conclusion. Therefore, here, general conclusions and key specific outcomes relating to new knowledge in each stage of the study are made. Conclusions relating to the development of the initial concept, producing a detailed design and predicting performance through simulation, then through the prototyping of that design and its experimental verification and advanced electromagnetic modelling are now presented in a concise manner.

8.1.1 Motor Concept

In general, the conventional synchronous reluctance motor design has remained relatively unchanged over the last 100 years. The cSynRM concept has been developed by selecting an appropriate alternative winding scheme to that conventional choice for synchronous reluctance motors in order to dictate the direction of research. The machine is essentially

a hybrid of the switched reluctance and synchronous reluctance motors, taking the advantages of each machine and synthesizing the fractional slot-concentrated winding synchronous reluctance motor with segmental stator arrangement. Particular attention is paid to the relevance of increased fill factor to reduce copper loss and improve machine efficiency and to the advantages and disadvantages of adopting a fractional slot-concentrated winding arrangement. The conceptual design of the topology resulted in presentation of design guidelines, to be observed during the design phase. A low pole number with suitable slot combination to provide a good fundamental winding factor and low air-gap harmonic leakage is desirable - this allows good electromagnetic design flexibility, good mechanical integrity and allows maximum potential for the topology to be achieved. Due to the increased parasitic effects, the thesis presents a trial and error based, but effective, optimization technique to improve the torque quality in the designed machine. As of the commencement of this research project, to the author's knowledge, there was no literature detailing the design, analysis, prototyping and validation of such a machine topology and therefore this thesis contributes to new engineering knowledge in advancing synchronous reluctance motor technology.

8.1.2 Design and Performance

The design phase considered the initial design of a cSynRM with a fixed stack length and outer diameter for an optimal rotor outer-diameter, producing a machine in a standard Newcastle University research machine frame size of approximately 3.5kW. The design utilizes a segmented coreback arrangement in order to facilitate ease of winding and obtaining a high slot fill factor. The inter-segment airgaps are shown to not impair machine performance for gaps of the length that would occur in practice. The fractional slot concentrated winding was chosen with a slot fill factor of 60% desired, the estimate was based on a model of individual turn placement into the stator slot. It is first shown that the cSynRM topology has inherently high torque ripple due to MMF space harmonic parasitic effects and a improved rotor electromagnetic design is presented that maintains high mean torque but with significantly reduced torque ripple - showing that simple electromagnetic design changes can produce good results. The magnetizing and leakage inductance components were analytically calculated and it is shown that the airgap harmonic leakage is the dominant leakage component due to the airgap space harmonic content. This was shown to reduce the power factor of the machine and is one of the major barriers for this machine. Two- and three-dimensional FEA analysis was performed on the machine geometry showing that it has potential for high efficiency, despite its low power factor: the key enabler for this high efficiency is achieving a high slot fill factor. The electromagnetic simulation results and comparison with the induction motor and a conventionally wound synchronous reluctance motor show that for equal loss, the designed cSynRM exhibits superior energy conversion efficiency and torque density than its rivals for a lower mass and with no increase in raw material costs. Rotor-dynamic and mechanical stress studies

suggested that the designed machine is safe to operate up to 10krpm - rotor stress and resonant modes are found to be of no concern within its operating range, despite the small rib thicknesses. Full electromagnetic, mechanical and electrical design work was undertaken by the author.

8.1.3 Prototyping and Experimental Verification

The work in prototyping the machine showed that electro-discharge-machining, if performed correctly, can produce prototype rotor designs with fine features and no or minimal magnetic damage to the laminations - as indicated by the standstill DC testing of the magnetic circuit. It is best to perform the machining in smaller stack lengths to be subsequently assembled onto a keyed shaft and axially clamped between a flange and locking nut. It also proved that neat, high fill factor stator coils with short end windings can be produced with ease due to the segmental nature of the coreback and by introducing end winding supports to the end of the stator stack. Using a coil winding machine to wrap the coils on individual stator segments a high slot fill factor of 58% was achieved, compared to industrially wound machine of the same size between 35 and 40%. This acts to improve the thermal performance of the machine by eliminating air in the slot; the thermal soak test confirms good thermal performance of the prototyped motor. Assembly of the complete motor was not an issue and any inter-segment air-gaps introduced by the segmental nature of the machines stator coreback did not pose any great difficulty in assembly or in the performance of the machine, again verified by the magnetic measurements. Dynamic testing showed that 3D effects reduced the machine performance slightly, an increased q-axis inductance lead to a reduction in torque capability and therefore also efficiency but the machine still compared favorably with the other technologies considered. The maximum speed was limited to only 3000rpm due to the capability of the testing equipment. The prototype machine was manufactured using low volume techniques - for mass manufacture a different approach is required. Stamping of the laminations would be required for mass manufacture, with the possibility of introducing some magnetic damage to the laminations. The manufacture of the stator segments lends itself to automated assembly with needle winding and subsequent stator assembly performed entirely without manual operations. The experimental measurements matched well to the FEA predicted results.

8.1.4 Analysis

Two forms of analysis are presented in this thesis, an air-gap field based analysis and a electrical parameter based analysis. It is shown through analytical development and application of the Maxwell stress tensor for individual air-gap field harmonics, that the individual harmonic torque components can be computed with relative ease from a solved FEA model for a synchronous motor. The developed cSynRM has a particularly rich harmonic content in the airgap stresses leading to a degradation in torque quality. The

developed post-processing technique identified the air-gap field harmonic responsible for the high contribution of oscillatory torque. A good reconstruction of the FEA torque waveforms from the individual torque components was achieved using the developed technique. It was identified that time varying space harmonics exist in the prototyped motor, caused by parasitic effects. Electromagnetic design changes were made to the rotor design in order to reduce the identified torque component, resulting in a significant torque ripple reduction but maintaining mean torque. The parasitic effects due to space harmonics in terms of the machine's orthogonal axis flux linkages and inductances were also explored - the developed machine does not have single values d- and q-axis inductances and as such, the dq model and orthogonal axis equivalent circuits were required to be modified accordingly. Finite element studies showed that unlike the conventionally wound machine, the cSynRM saliency ratio varies with rotor position and its mean value is attributed to the steady state performance of the machine. Novel torque equations based on the modified dq theory were shown to provide improved accuracy compared to the conventional dq model and finite element predictions - the new torque terms attributed to spatial variation of the motor dq axis inductances cause unwanted oscillatory torques. This inductance characteristics provides valuable information for subsequent studies of the cSynRM topology, especially in its dynamic simulation and development of practical control algorithms.

8.2 Suggested Further Work

The work contained within this thesis has introduced the concept of the cSynRM with its slot concentrated windings and its segmental stator structure, a demonstrator machine has been constructed and the design experimentally verified. A number of useful extensions and ideas for the expansion of the work presented in this thesis in order to more fully understand and progress the application of cSynRM technology are outlined here;

- Investigate and apply methods to reduce the space harmonic content in the airgap but maintain a segmental stator structure with high fill factor coils and short end windings. A higher number of winding layers could potentially be used or unequal tooth widths may be applied - a method to simultaneously increase the fundamental winding factor and reduce the space harmonic content should be an area for further advancement.
- Apply more advanced optimization schemes with the objective of increasing the motor power factor and reducing torque ripple further. Achieving a higher power factor and lower torque ripple in a low cost, robust machine such as the cSynRM would increase their applicability both in industry and in higher performance applications.
- Reformulate the novel post processing technique by the use of airgap volume integ-

rals to provide increased accuracy in the estimation of the harmonic torque contributions and also re-write the equations to include time harmonic effects - formally reconcile the 'field' and 'circuit' perspectives of the same phenomenon. This would give a more accurate and complete understanding of the torque ripple and any necessary electromagnetic design changes.

- Develop high performance control schemes incorporating the spatially varying flux linkage components based on the developed dq equivalent circuit model of the cSynRM. Specifically the sensorless control aspect and the impact of spatially varying inductances and any cross-coupling effects. High performance sensorless control of the cSynRM would be highly desirable, as well as a direct control algorithm to reduce torque ripple through software.
- Investigate the use of grain oriented (GO) material for use in the rotor for a TLA type synchronous reluctance motor. A segmental rotor with the grains aligned in the d -axis of the rotor design could increase saliency by promoting this d -axis flux but simultaneously hindering any q -axis flux due to the anisotropic nature of the permeability in GO laminations. Increasing saliency whilst maintaining low eddy current losses could lead to cSynRM technology with higher efficiency, power factors and torque capability - at the cost of increased rotor complexity. Specific investigation into the electromechanical inter-dependencies of such a rotor would be useful.
- Develop and validate a more accurate method of experimentally determining the leakage inductance of electrical machines with fractional slot concentrated windings and high levels of space harmonic content.

A future direction may be to use permanent magnet material to increase the torque density and also the power factor of the machine, however with uncertainty in the rare earth market and the poor magnetic performance of ferrite type permanent magnets (despite their low cost), coupled with the associated environmental and ethical issues, maintaining 'magnet free' research in the field of synchronous reluctance technology is the author's preference. Advanced materials and novel electromagnetic designs could provide a route forward for low cost, magnet free, industrially oriented electrical machines for both high performance and high energy efficiency applications. Here the discovery of a material with *negative magnetic permeability* could be very useful in relation to increasing the saliency of reluctance machines.

8.3 Closing Remarks

This work was inspired by the idea of combining the long-standing work on single tooth switched reluctance motors at Newcastle University and under-researched area of Synchronous Reluctance motor technology to synthesize a novel motor that aims to possess

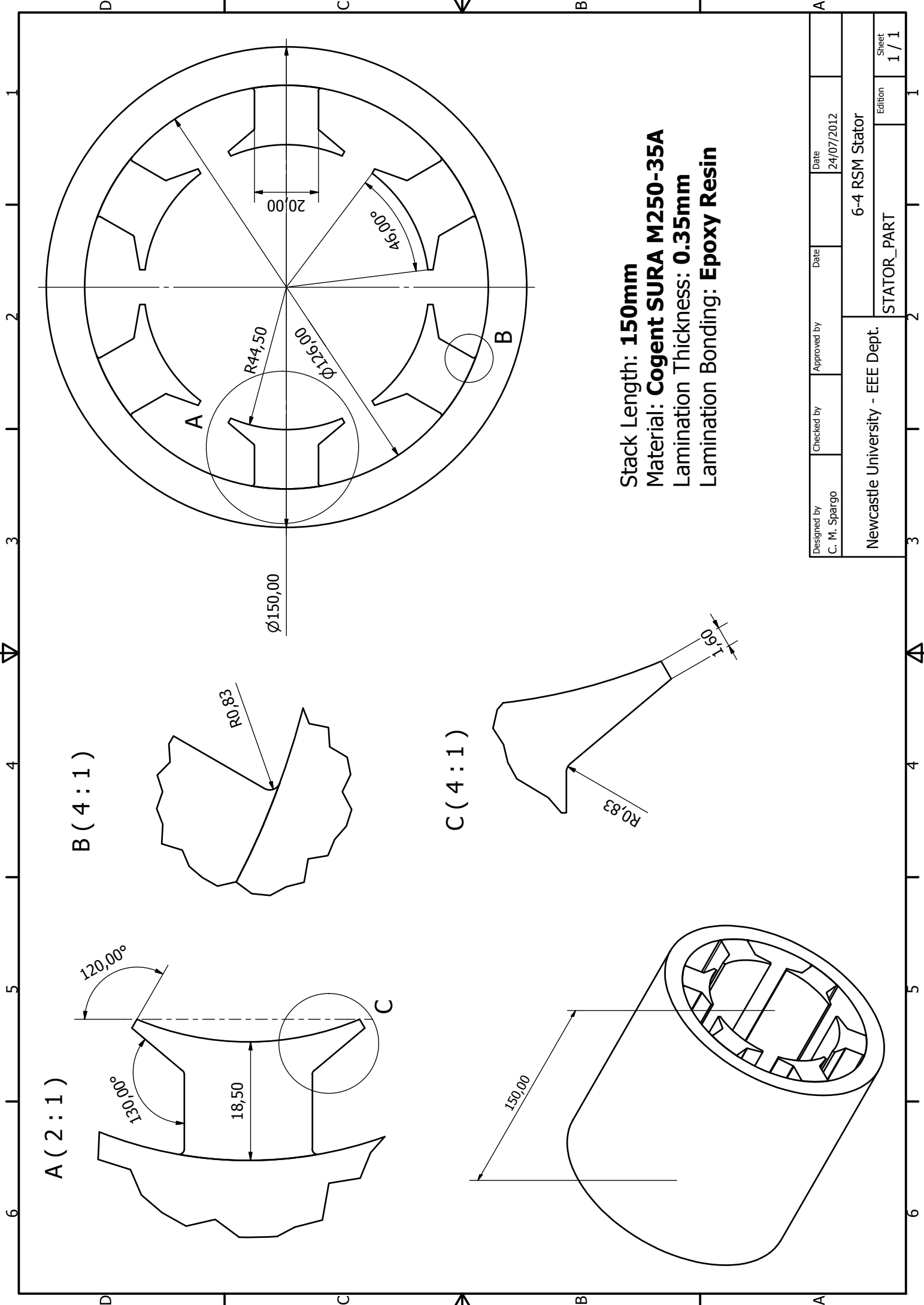
the benefits of both machine topologies. It was noted that whilst the switched reluctance motor has some specific advantages due to its robust construction and single tooth wound coils, its drawbacks of using a non-standard off-the-shelf converter topology and its acoustic noise and vibration have prevented it from mainstream success. The synchronous reluctance motor operates on the same reluctance torque principle but using off-the-shelf converters and arguably has had much greater success. This thesis has successfully demonstrated a synchronous reluctance motor with fractional slot concentrated windings by design, construction and its experimental validation - a high efficiency, high torque density and low cost machine was produced, compared to the induction motor and a conventionally wound synchronous reluctance machine. There were some drawbacks to utilizing fractional slot concentrated windings identified in this thesis; the low power factor and high torque ripple pose a design and application challenge for the developed machine. As an indication of the value of the research contained within this thesis, 3 peer-reviewed IEEE journal papers were successfully published and 5 international conference papers presented around the world. ABB has brought conventional synchronous reluctance motor technology to mass market, this thesis has brought the cSynRM to the prototyping and validation stage - It is hoped by the author that the future development of synchronous reluctance motor technology can be realized without the inclusion of permanent magnet material and that the fractional slot concentrated winding configuration can be the subject for further research and potential commercialization in either niche or mass markets.

Appendix A

Prototype: Mechanical Drawings

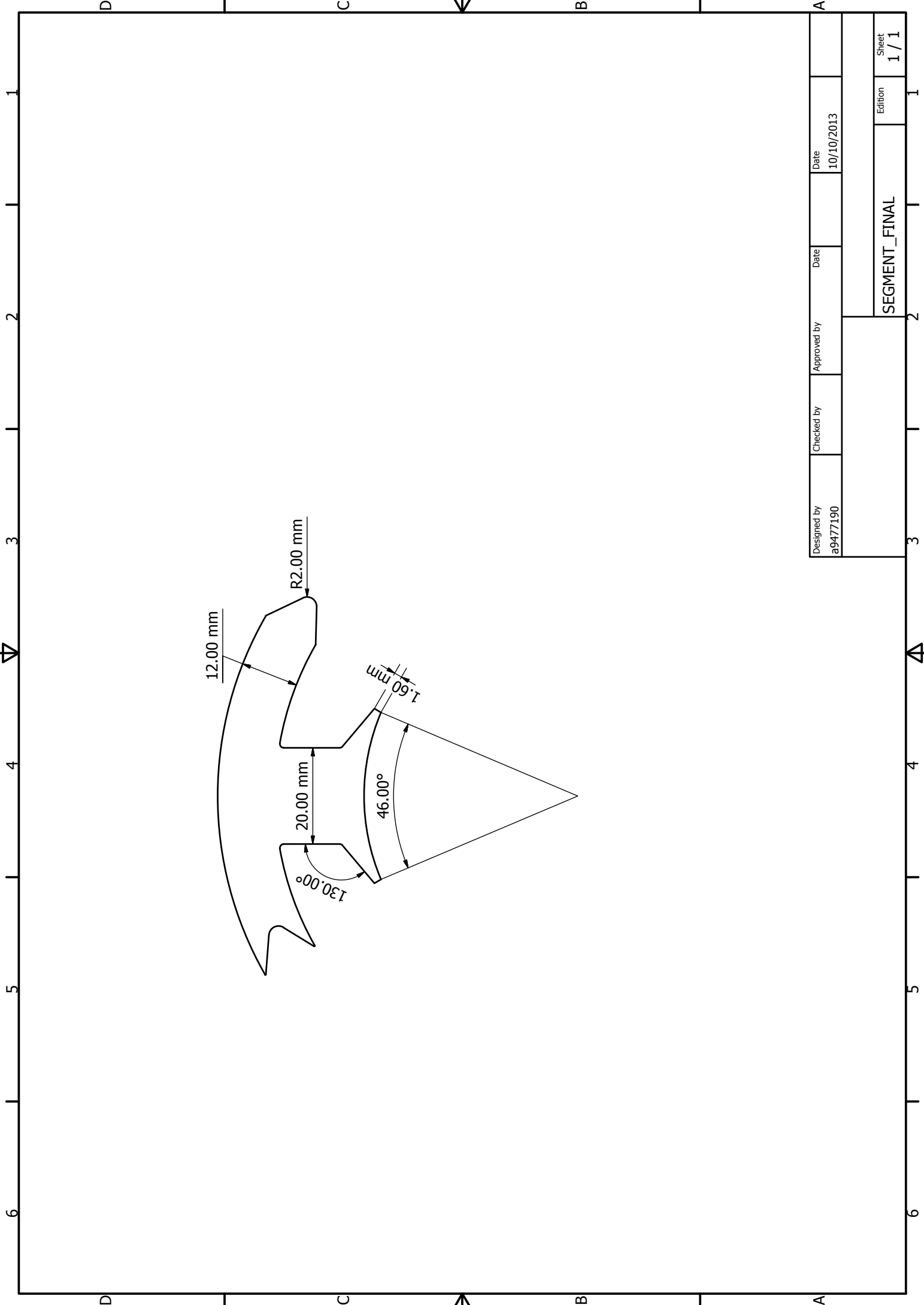
Overleaf, the principal mechanical drawings of the prototype machine are presented. These drawings were used to guide the manufacture of the prototype machine in the Mechanical Workshop at Newcastle University. Drawings included are;

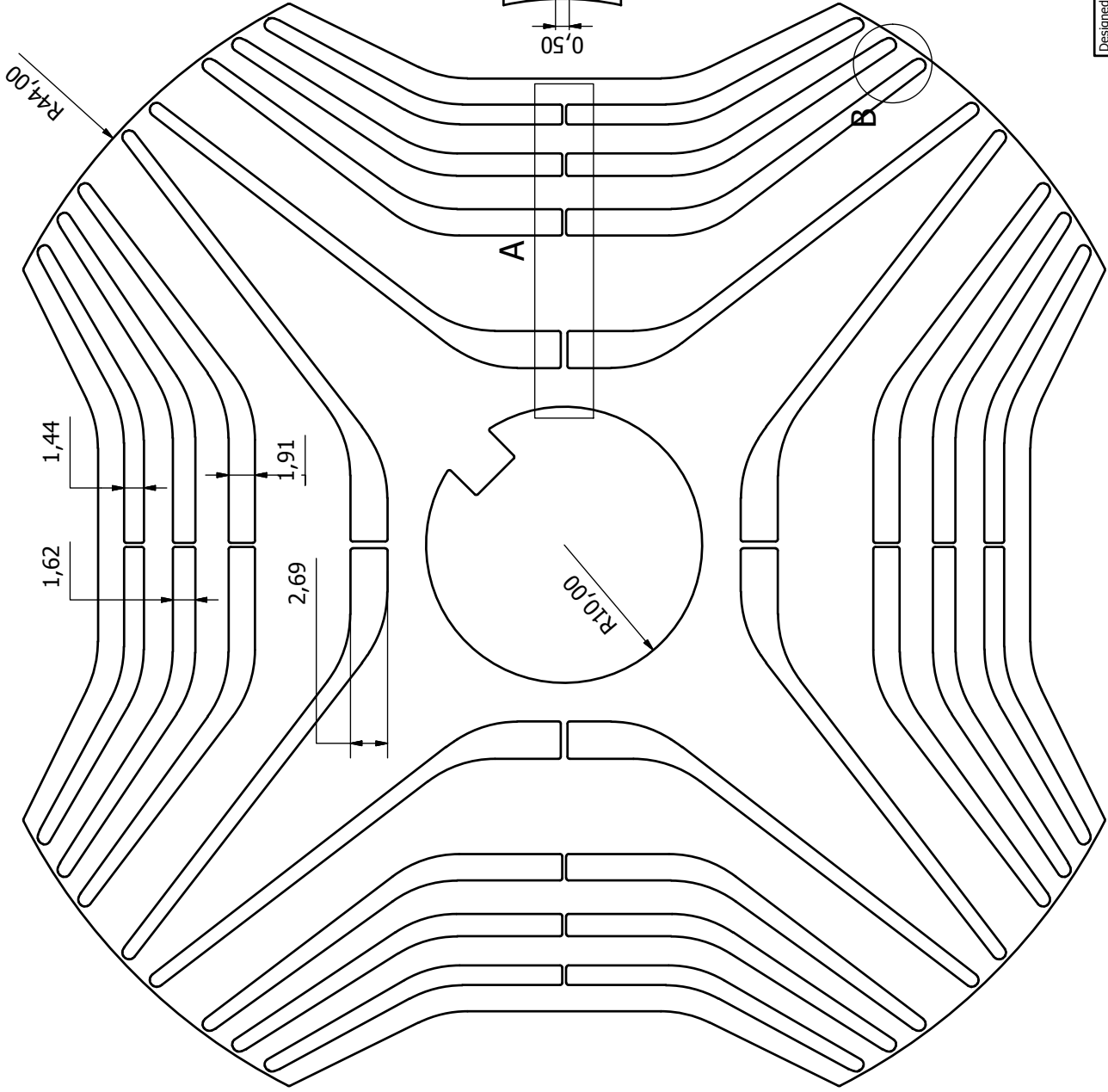
- Motor Assembly (cross-section)
- Stator Lamination Profile
- Stator Segment Dimensions
- Rotor Lamination Profile
- Shaft Design
- End Winding Support Design



Stack Length: **150mm**
Material: **Cogent SURA M250-35A**
Lamination Thickness: **0.35mm**
Lamination Bonding: **Epoxy Resin**

Designed by C. M. Spargo	Checked by	Approved by	Date 24/07/2012	A
Newcastle University - EEE Dept.				6-4 RSM Stator
STATOR_PART				Sheet 1 / 1





Material: Cogent SURA M250-35A Fully
Processed Non-Oriented Electrical Steel

Min Corner Radius: 0.16mm

Stack Length: 150mm (z-axis)

Bonding: Epoxy Resin

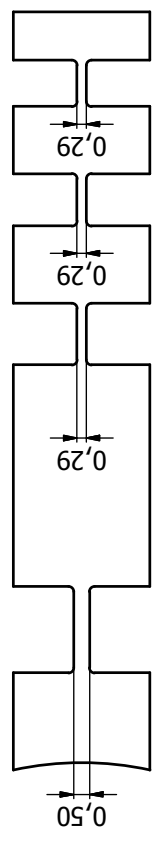
Lamination Number: Approx 420

Lamination Thickness: 0.35mm

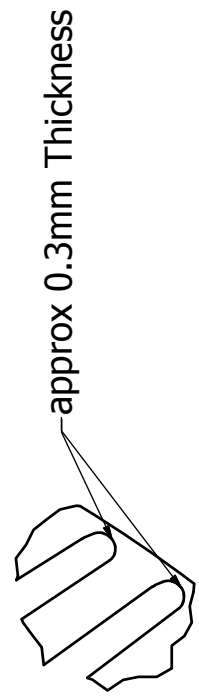
Stacking Factor: 0.98 approx

Manufacture: EDM Wire Erosion

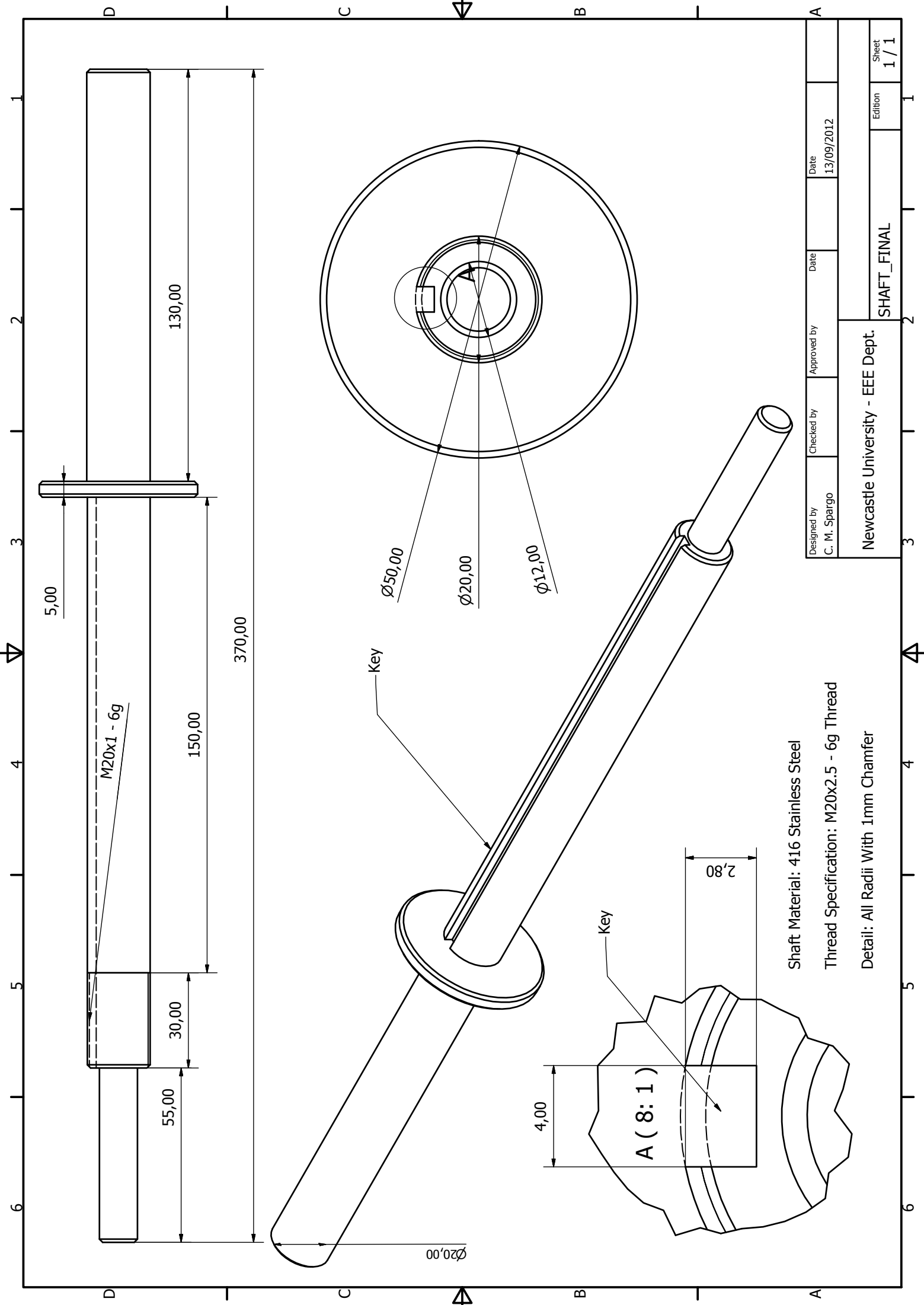
A (6 : 1)



B (6 : 1)



Designed by C.M. Spargo	Checked by	Approved by	Date	Date	
Newcastle University - EEE Dept.			RSM Rotor		
			Edition		Sheet
			5		1 / 1

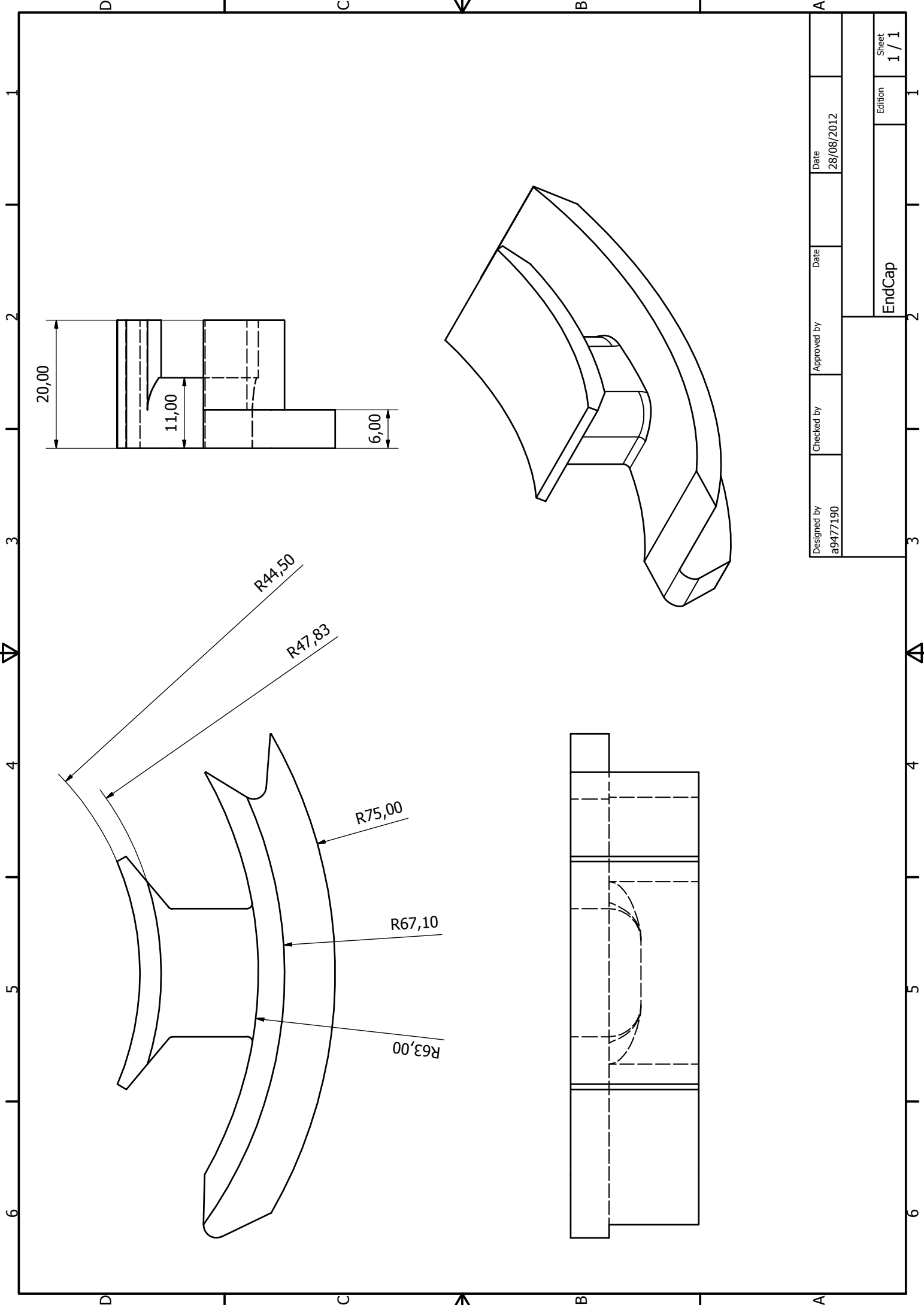


Shaft Material: 416 Stainless Steel

Thread Specification: M20x2.5 - 6g Thread

Detail: All Radii With 1mm Chamfer

Designed by C. M. Spargo	Checked by	Approved by	Date 13/09/2012	Date 13/09/2012	
Newcastle University - EEE Dept.				SHAFT_FINAL	Sheet 1 / 1



Designed by a9477190	Checked by	Approved by	Date 28/08/2012	Date 28/08/2012	A
EndCap				Edition	1
				Sheet	1 / 1